Single particle studies of vesicular stomatitis virus assembly

Single particle studies of vesicular stomatitis virus assembly

A dissertation presented

by

Timothy Kinshiong Soh

to

The Division of Medical Sciences

in partial fulfillment of the requirements

for the degree of

Doctor of Philosophy

in the subject of

Virology

Harvard University

Cambridge, Massachusetts

May 2015

Dissertation Advisor: Dr. Sean P. J. Whelan Timothy Kinshiong Soh

Single particle studies of vesicular stomatitis virus assembly

Abstract

The formation of viral particles requires the coordinated assembly of both nucleic acids and proteins. In the case of Rhabdoviruses, such as vesicular stomatitis virus (VSV), the particles display a characteristic bullet-shape. VSV virions consist of the matrix protein (M), glycoprotein (G), and viral ribonucleoprotein (RNP), which contains the nucleocapsid protein (N) coated RNA bound to the large polymerase protein (L) through the phosphoprotein (P). During assembly, these components are recruited to the plasma membrane where the viral RNP undergoes condensation by M and envelopment with G containing membranes. To address whether formation of the bullet-shape requires a consistent packaging of the viral proteins, the composition of single virions was measured with fluorescence microscopy. We generated autonomously replicating VSV bearing up to 3 fluorescent protein fusions in the disordered N-terminal region of M and N-terminus of P and G. Quantification of single particles reveals that VSV assembles with a range of M, P, and G molecules, suggesting a flexible packaging mechanism. The maintenance of the bullet-shape with significantly less M proposes that condensation does not require the particle to be saturated with M. Our fluorescent VSV clones permit the tracking of viral components in live cells. We observed that assembly of M into particles requires ~2 min and can be broken into 4 stages. First, M forms a small preassembly complex. Second, M rapidly assembles into particles where its incorporation initiates before P, although they are packaged concurrently. This is followed by a delay before final release of particles into the supernatant. Late domains in M were thought to only recruit the endosomal sorting complexes required for transport (ESCRT) pathway to mediate fission. However, using

our M fusions we demonstrate that these motifs are required for efficient competition into released particles and a step in assembly prior to pinching off. These constructs have permitted the study of viral assembly at the single particle level and are useful tools for studying viral entry and egress. Specifically, VSV containing M-eGFP and the lassa virus glycoprotein instead of G was used to demonstrate the requirement of a host factor for lassa virus fusion.

Table of Contents

List of Tables

List of Figures

Acknowledgements

My PhD has been a journey to become a better scientist and contribute to the scientific community. It would not have been possible without the advice, care, and support of those around me. My advisor, Sean P. J. Whelan, provided me with the independence and freedom to pursue my own project and ideas. His input has helped to develop both my scientific and critical thinking skills. Most importantly, he has taken on a number of people that have contributed to a productive lab environment. Lab members, both present and past, have helped me develop scientifically and professionally.

There are also many people that have acted like an advisor to me. I am grateful to Jennifer C. Waters for all of the time that she has spent discussing ideas and teaching me about microscopes. Josh Rosenberg, Talley Lambert, and Lauren Alvarenga have been more than helpful during my time at the Nikon Imaging Center. I want to thank Eric Marino who was also always willing to answer my microscope questions. My training as a microscopist would not be where it is without their time and support. Connie L. Cepko has provided me with much advice, and I have always felt welcome in her lab. Maria Ericsson, Elizabeth Benecchi, and Louise Trakimas have been a pleasure to learn electron microscopy from and were wonderful to work with.

The people outside of lab have been equally important. Those that I know for non-scientific reasons have provided the perspective and distraction that was sometimes needed. I want to thank David L. Cardozo for his consideration and thoughtfulness and my colleagues and friends for their positive influence.

Chapter 1

Introduction

Assembly of viral particles requires not only temporally and spatially coordinated localization of the viral structural proteins but that these proteins associate in the correct order, position, and orientation. Non-enveloped viruses form structures with a characteristic triangulation number, but enveloped viruses can be either amorphous or a reproducible 3D structure. The interlocking nature of the capsid protein in non-enveloped viruses explains their symmetrical organized structure. How enveloped viruses generate asymmetrical macromolecular complexes is less clear. The family *Rhabdoviridae* of the order *Mononegavirales* produces enveloped virions with a characteristic bullet-shape. These particles are a consistent length and width, and the internal components of the Rhabdovirus vesicular stomatitis virus (VSV) form 2 regular helices (1). One helix is composed of the nucleocapsid protein (N) coated genomic RNA, and the second is of the matrix protein (M). The bullet-shape could be generated through the formation of the N or M helix or an interaction between them. Regardless, the trigger that induces the generation of the bullet-shape is unclear. After assembly is triggered the viral proteins must be recruited, but the consistency in the amount of protein packaged is unknown. The content of particles may be variable and the role this could play in the formation of the structure is uncertain. A deeper knowledge of the composition of particles and the features of viral proteins that mediate their incorporation will further the understanding of the assembly mechanism of VSV.

VSV is a member of the order *Mononegavirales* that forms a fixed-sized structured virion

The order *Mononegavirales* is characterized by a nonsegmented negative-sense RNA genome (2). Genomic RNA that is coated with the viral nucleocapsid protein serves as the template for the virally encoded RNA-dependent RNA polymerase (RdRp) (2). Genome

replication occurs through a positive-sense antigenome intermediate, and mRNA synthesis occurs *via* a start-stop mechanism where the viral genes are transcribed sequentially following polymerase binding at the 3' end of the genome (2). The viral genome is organized in the following order: 3' untranslated region (UTR) – core proteins – envelope proteins – polymerase – 5' UTR. Assembly of viral genomes into particles occurs by budding of the N-RNA bound to the RdRp complex at membrane sites that contain the envelope protein (2).

Viruses from the *Mononegavirales* order (Table 1.1) have similar virion components, but the particles have different morphologies (3, 4). Virions must contain the envelope protein, to mediate entry, as well as the genome with associated RdRp, for gene expression and genome replication. The other virion component, the matrix protein, drives assembly and is sufficient for formation of virus-like particles (5-7). Some families of the order *Mononegavirales, e.g. Bornaviridae*, *Nyamiviridae*, and *Paramyxoviridae*, form spherical particles while *Filoviridae* form filamentous particles that are variable lengths and *Rhabdoviridae* form bullet-shaped particles with consistent dimensions (4). This suggests that the assembly mechanism of Rhabdoviruses is ordered. Since the bullet-shape is asymmetrical, initiation must proceed differently than the bulk of the assembly process. Furthermore, consistent dimensions imply that release of the virus occurs at a specific point during assembly. The best studied member of the family *Rhabdoviridae* is VSV, which grows to high titres in cell culture. In combination with the robust reverse genetics systems (8, 9) and tolerance of the genome to a large degree of manipulation, VSV is a tractable virus for studying assembly.

Table 1.1. Members of the order *Mononegavirales* (10).

Family	Subfamily	Genus	Type Species
Bornaviridae		Bornavirus	Mammalian 1 bornavirus
Filoviridae		Cuevavirus	Lloviu cuevavirus
		Ebolavirus	Zaire ebolavirus
		Marburgvirus	Marburg marburgvirus
Nyamiviridae		Nyavirus	Nyamanini nyavirus
Paramyxoviridae	Paramyxovirinae	Aquaparamyxovirus	Atlantic salmon paramyxovirus
		Avulavirus	Newcastle disease virus
		Ferlavirus	Fer-de-Lance paramyxovirus
		Henipavirus	Hendra virus
		Morbillivirus	Measles virus
		Respirovirus	Sendai virus
		Rubulavirus	Mumps virus
	Pneumovirinae	Metapneumovirus	Avian metapneumovirus
		Pneumovirus	Human respiratory syncytial virus
Rhabdoviridae		Cytorhabdovirus	Lettuce necrotic yellows virus
		Ephemerovirus	Bovine ephemeral fever virus
		Lyssavirus	Rabies virus
		Novirhabdovirus	Infectious hematopoietic necrosis virus
		Nucleorhabdovirus	Potato yellow dwarf virus
		Perhabdovirus	Perch rhabdovirus
		Sigmavirus	Drosophila melanogaster sigmavirus
		Sprivivirus	Spring viraemia of carp virus
		Tibrovirus	Tibrogargan virus
		Tupavirus	Durham virus
		Vesiculovirus	Vesicular stomatitis Indiana virus

VSV replication cycle

VSV replication consists of an extracellular virion and intracellular replication stage (Figure 1.1). Virions are assembled from 3 major components, the glycoprotein (G), viral ribonucleoprotein (RNP), and matrix protein (M). After binding to the plasma membrane, VSV enters cells by clathrin-dependent endocytosis (11). A subsequent pH triggered G-mediated fusion of the endosomal and viral membranes results in the delivery of the viral core into the cytoplasm (12, 13). Release of the viral RNP initiates the process of intracellular replication with the commencement of transcription (14). The 3 components, the viral RNP, M, and G, are synthesized and transported to assembly sites at the plasma membrane through independent pathways (15). During assembly, the viral RNP undergoes condensation by M to form a compact nucleocapsid-matrix protein (NCM) complex (16) that acquires G by budding through the plasma membrane (15). Fission releases these particles into the supernatant, and these newly formed virions can bind and infect new cells.

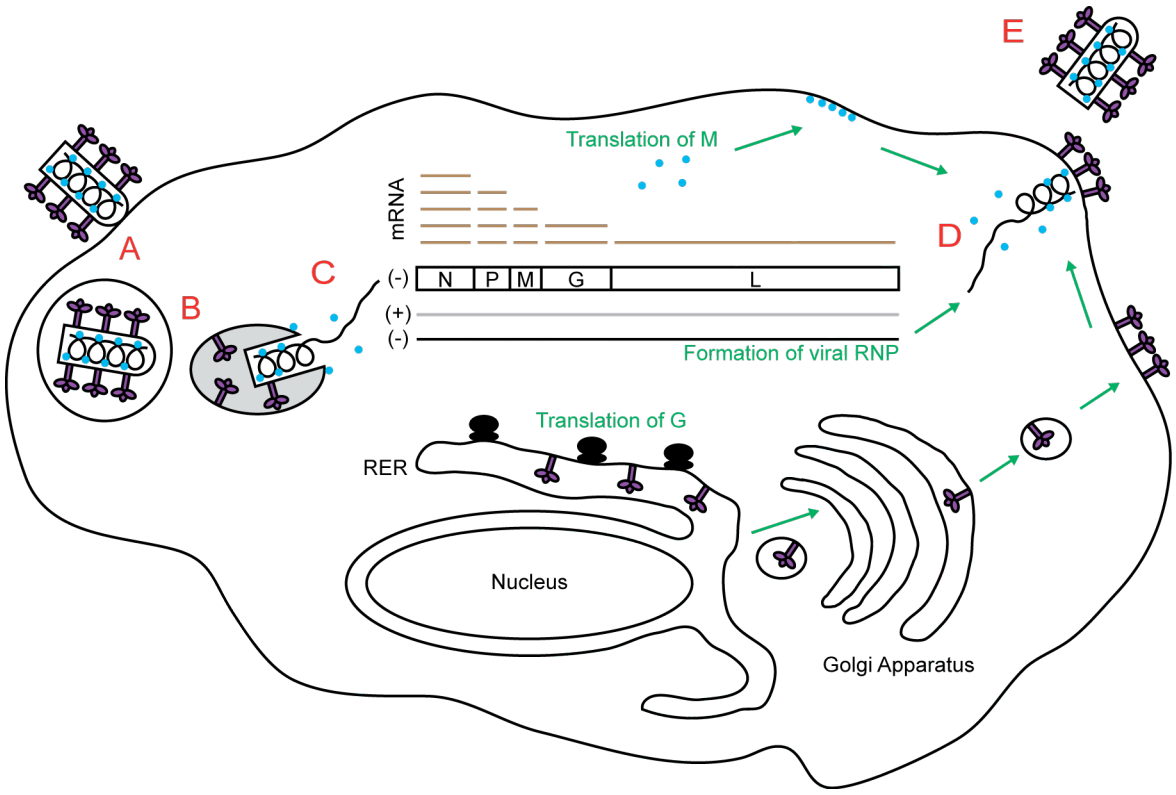

Figure 1.1. VSV replication cycle.
(A) A VSV particle binds to the target cell and undergoes endocytosis. (B) The particle is trafficked to the correct compartment and fusion is triggered by low pH (grey area). (C) Uncoating of the NCM complex releases the viral RNP which initiates viral transcription *via* a transcription cascade and genome, (-), replication through an anti-genome, (+), intermediate. (D) G (purple trimer) is transported to the plasma membrane through the RER and Golgi apparatus. The viral RNP (black helix/string) is transported to G microdomains. M (blue circle), which is synthesized in the cytoplasm, forms microdomains at the plasma membrane and is recruited to assembly sites to mediate condensation. (E) Fission of the viral and cellular membranes results in the release of the newly assembled VSV particle.

Entry of VSV

An essential step in the viral replication cycle is entering the cell. As an enveloped virus, VSV must fuse its membrane with the cellular membrane to deposit the virion's internal components into the cytoplasm. This process begins with the binding of the particle to the cell surface. This is mediated by the viral protein G, but the specific receptor on the cell is controversial. The receptor was suggested to be proteins due to the observation that treatment of cells with trypsin prevented VSV infection (17, 18). It was shown that G binds to members of the low-density lipoprotein receptor (LDLR) family. Soluble LDLR protects mammalian but not insect cells from infection, suggesting that insect cells are infected by other means (18). Other studies have shown that VSV can bind to cells through a nonsaturable target, proposing that binding is nonspecific (19), and it was demonstrated that G binds nonspecifically to membranes through electrostatic interactions between the positively charged G surface and negatively charged phospholipids (20). The plasma membrane lipid phosphatidylserine (PS) was proposed to be the receptor due to its ability to bind to G and protect cells from infection (21). It has also been suggested that the PS in the VSV envelope (22) may enhance binding through PS receptors on the cell surface (23). The extent to which these multiple mechanisms contribute to viral entry requires additional clarification.

After VSV has bound to the target cell, the membranes must undergo fusion and deliver the replication machinery into the cytoplasm. For VSV, this requires clathrin-mediated endocytosis (11) followed by acidification to trigger fusion mediated by G (12, 13). Fusion may occur in early endosomes and result in the immediate release of the internal components into the cytoplasm (24), or fusion may occur in multivesicular bodies (MVBs) and require back-fusion for release into the cytoplasm (25). In both cases, the released viral core undergoes uncoating to

release M from the replication machinery (26), and the open viral RNP will initiate viral transcription and genome replication.

The VSV virion components

Synthesis and transport of G

Generation of infectious VSV particles requires the incorporation of G, the protein that mediates binding to cells and fusion of the cellular and viral membranes. Since G is a single-pass transmembrane protein that is cotranslationally inserted into the rough endoplasmic reticulum (RER), it must pass through the secretory pathway before reaching the plasma membrane (27) where it is incorporated into assembling particles (15). Proper folding of G and oligomerization into non-covalently linked trimers is required for transport through the Golgi apparatus (28, 29). During this transport, G undergoes posttranslational modifications that are required for efficient processing. Glycosylation of G (30, 31) is required for binding to chaperone proteins that facilitate folding (32). In addition to this quaternary structure, the cytoplasmic tail is required for rapid and efficient transport to the plasma membrane (33). Once G reaches the cell surface, it organizes into microdomains that facilitate assembly (34).

Viral transcription and genome replication by the viral RNP

The viral RNP is the functional unit for viral transcription and genome replication and consists of nucleocapsid protein (N) coated RNA bound to the large polymerase protein (L) through the phosphoprotein (P) (35). The functions of N, P, and L are intimately coordinated. N-RNA and not naked RNA is the active template for transcription and replication (36). This

results in the dependence of genome replication on the expression of N (37) so that newly synthesized genomic RNA can be encapsidated. The crystal structure of N-RNA demonstrates that N consists of an N-terminal and C-terminal lobe that hold the RNA between them (38). A transient remodelling or displacement of the N protein is thus required for access of L to the RNA template (38). P mediates the access of L to the RNA by virtue of binding N and L *via* opposite termini, C-terminus and N-terminus respectively (35). L contains the catalytic machinery for transcription, namely RNA polymerization (14, 39), capping (40, 41), methylation (42-44), and polyadenylation (45), but requires P as a cofactor (46) to engage the template-bound N (35), rearrange the conformation of L (47), and increase the processivity of the RdRp (46, 48).

The VSV genes are transcribed *via* a transcriptional cascade that results in higher expression of genes proximal to the promoter. The VSV genome encodes 5 genes that generate 5 structural proteins. The genes are ordered linearly and are flanked by a leader (Le) and trailer (Tr) sequence, 3' Le-N-P-M-G-L-Tr 5'. The Le and Tr are necessary and sufficient for replication of the RNA by VSV and serve as promoters for replication of the genome and antigenome, respectively (49-51). The viral genes are transcribed sequentially based on their genomic order (52), and transcription occurs *via* a stop-start mechanism (53), where at each gene junction the polymerase adds a poly(A) tail to the mRNA by "slippage" on a U-rich sequence (54), releases the mRNA (55), and reinitiates on the next gene start sequence (53). Transcription of the following gene is decreased by 29-33%, resulting in a gradient of transcript abundance (53).

In a VSV infected cell, N, P, and L colocalize in cytoplasmic inclusions (56), but the viral RNP must be transported to the plasma membrane for incorporation into assembling particles. Transport of viral RNPs to the periphery is dependent on microtubules (57), but how individual

genomes are selected for this transport is unknown. A *cis*-acting sequence in Tr is thought to be required for incorporation into particles, although the assay used was indirect and relied on measuring the infectivity of released particles (58).

Assembly and host shutoff by M

In infected cells, M is responsible for mediating host shutoff (59) in addition to its role in particle formation. M is required for the assembly and budding of VSV, and when expressed alone, it is sufficient for the release of lipid vesicles (5, 6). This suggests that during assembly M oligomerizes at membranes and mediates fission from the cell. The ability of M to self-associate has been mapped to the N-terminal 48 amino acids, and full length M will oligomerize under low salt conditions (60). However, this oligomerization requires nucleation by a complex of 3-4 molecules of M (61). This dependence on nucleation suggests that during VSV assembly, small amounts of M may nucleate the oligomerization of the majority of M into the forming virion. Budding at the membrane also requires that M can bind to lipids. There are 2 characterized membrane binding domains in M, residues 1-50 and 75-106 (62), but only the N-terminal 19 amino acids are in close proximity to the membrane (63). Once associated with the plasma membrane, M forms microdomains that are recruited to assembly sites (64). During assembly, the viral RNP must also be incorporated into the particle. Another role of M is to bridge the viral RNP with the membrane (65, 66). M that is associated with membranes requires the N-terminal 16 amino acids to bind to N (65).

The cellular endosomal sorting complexes required for transport (ESCRT) pathway is recruited to mediate fission of the virus from the cell (67). This requires late domains in M, which are named after the “late” stage in the viral replication cycle that is blocked when these

domains are mutated (68, 69). VSV M contains 2 late domain motifs at residues 24 PPPY 27 (68) and 37 PSAP 40 (69). While mutating only PPPY, *e.g.* Y27A, results in a decrease in the amount of released infectious virus (68-70), mutating only PSAP, *e.g.* 37 AAAA 40, does not have a measureable effect (69, 70). However, mutating both motifs generates a virus that is more attenuated than the PPPY mutant alone (69). This redundancy emphasizes the importance of late domains and their role in mediating fission. These functions illustrate the critical role that M plays in the assembly of VSV particles.

Host shutoff by VSV leads to an increased expression of viral genes (71). The ability of VSV to mediate host shutoff was mapped to M (59), which is sufficient to inhibit host transcription (72) as well as nuclear export of cellular mRNA (73). These functions are mediated by the ability of M to bind to mRNA export factor 1 (Rae1) (74) and form a complex with nucleoporin 98 kDa (Nup98) (75). Rae1 and Nup98 are components of the nuclear pore complex that facilitate nuclear export of host mRNA (76, 77). A crystal structure of this complex confirms the M-Rae1-Nup98 interactions and illustrates how M binding to Rae1 displaces the normal nucleic acid substrate (78). The mechanism of inhibition of Rae1 by M may be through its ability to outcompete the normal substrate for binding to Rae1 (78). Binding of M to Rae1 forms scaffolds that are necessary for the inhibition of RNA polymerase (RNAP) I, II, and III (79). While the exact mechanism of how this inactivation occurs is unclear, for RNAP II it involves the inhibition of transcription factor IID (TFIID) (80). A mutation in M which eliminates its interaction with Rae1, *e.g.* M51R, abolishes the inhibition of nuclear export (74, 75). In contrast, siRNA knockdown of Rae1 does not restore nuclear export in VSV infected cells, but impedes inhibition of cellular transcription (79). This difference could be due to insufficient knockdown

of Rae1, but it suggests that the M-Rae1 scaffold is more efficient at inhibiting host transcription than nuclear export.

The disordered nature of the N-terminus of M may permit the adoption of multiple conformations to facilitate its numerous interactions (Table 1.2). Crystal structures of M have demonstrated a disordered N-terminal domain, 1-57, and structured C-terminal domain, 58-229 (78, 81, 82). A loop that is disordered in purified M (82) binds tightly to Rae1 (78), demonstrating the stabilization of this loop through the formation of a complex. The ability of distinct conformations to perform different functions has been illustrated by ebola virus virion protein 40 (VP40) (83), which has similar functions to VSV M in assembly. VP40 can adopt multiple conformations, and each has a different function in the viral replication cycle. The ability of M to bind to its numerous interacting partners may be due to the unstructured nature of the N-terminus.

Table 1.2. Characteristics and functions of M.

Function	Residues
M Oligomerization	1-48 (60)
Membrane Binding	1-50, 75-106 (62)
Membrane Proximal	1-19 (63)
N Binding	2-16 (65, 66)
NCM Affinity	121-124 (84)
Late Domain	24-27 (68), 37-40 (69)
Bind Rae1	49-61 (78)
Bind Dynamin 2	1-10 (85)
Translational Start Sites	1, 33, 51 (86)
Nuclear Localization Signals	23-57, 47-229 (87)
Phosphorylation	20-34 (88)
Disordered Region	1-57 (82)
Globular Domain	58-229 (78, 81, 82)

Assembly of VSV virions

In vivo assembly of particles

Assembly of infectious VSV requires that all of the structural proteins come together. Each component is transported to the plasma membrane through a distinct pathway (15). G is cotranslationally inserted into the RER and traffics through the Golgi apparatus to the plasma membrane where it is incorporated into assembling particles (15, 27). The viral RNP proteins are synthesized as soluble components in the cytoplasm but are quickly assembled with RNA into this complex (15). During assembly, the viral RNP only associates with the plasma membrane immediately before being incorporated into particles and released into the supernatant. M is also synthesized as a soluble cytoplasmic protein, but a portion of the population associates with membranes (15). The binding of M to the viral RNP rapidly proceeds to incorporation into released particles, suggesting that condensation at the plasma membrane is a fast process that leads to particle release. The variations in transport of the viral components reflect the differences in the maturation and function of these proteins.

While the distinct transport of each VSV component from synthesis to virion is known, the initiation and progression of assembly of individual particles is unclear. Prior to the initiation of assembly, G (34) and M (64) form microdomains at the plasma membrane (Figure 1.2). However, these microdomains are independent and do not colocalize significantly (64). In contrast, N was found to colocalize with G but not M, suggesting a model where assembly is initiated by the transport of the viral RNP from cytoplasmic inclusions to G microdomains (64). Consistent with this model, regions of G that enhance virus release have been mapped to the cytoplasmic tail (89) and ectodomain (90). However, G is not essential for assembly since a virus

lacking G (VSV ΔG) is released from cells (90, 91). Once the viral RNP has translocated to G, M microdomains are recruited to condense the viral RNP into the NCM complex (64). This M recruitment and oligomerization could be initiated by the creation of M nucleation sites (61) induced by the association of the viral RNP with G. These data suggest a model where interactions of G with internal components facilitate, but are not essential for, assembly.

During assembly, the open viral RNP must be condensed by M into the bullet-shaped NCM complex before budding and particle release (16). While purified N-RNA can be induced to adopt an NCM complex-like structure (92), M also likely plays a role in the generation of the characteristic bullet-shape of VSV particles. In addition to the presence of M correlating with the formation of the NCM complex (93), the temperature sensitive mutant tsO23, which maps to M (94), forms spherical particles at the non-permissive temperature (95). Furthermore, a deletion of M from the rabies virus genome results in particles that are filamentous and round instead of bullet-shaped (96). These data support a critical role for M in proper assembly of VSV particles.

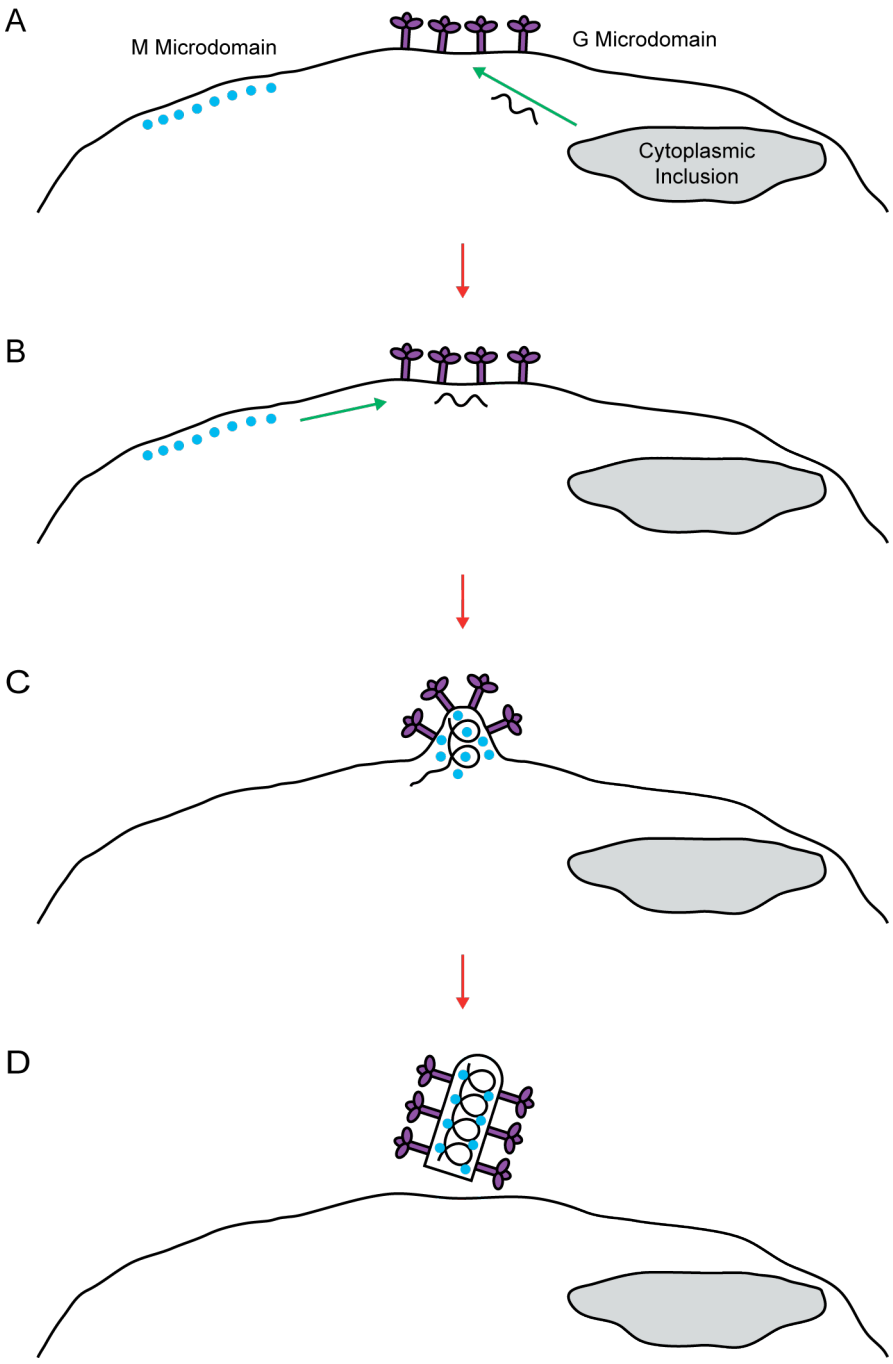

Figure 1.2. Order of assembly of VSV proteins into particles
(A) Prior to assembly, M (blue circles) and G (purple trimers) form microdomains at the plasma membrane and the viral RNPs (black helix/string) are in cytoplasmic inclusions. During the initiation of assembly, the viral RNP is recruited to G microdomains (green arrow). (B) After translocation of the viral RNP, M microdomains are recruited to mediate condensation of the viral RNP into the NCM complex. (C) Budding and (D) fission result in the release of the newly formed VSV particle.

In vitro formation of NCM complexes

After recruitment of the open viral RNP to assembly sites, it must be condensed into the NCM complex before budding through the membrane. However, this intermediate has not been identified in infected cells, leaving a gap in the understanding of assembly. The inability to observe this intermediate is likely due to the short time that M associates with the viral RNP in cells before it is released as a completed particle (15). The requirements for condensation have predominantly been inferred from *in vitro* reassembly studies. The NCM complex derived from virions is held together by non-covalent M interactions (16). Disruption of these interactions causes the NCM complex to adopt a confirmation that is similar to the open viral RNP, and likewise conditions that favor protein-protein interactions can trigger spontaneous reassembly of the NCM complex (93). A caveat to this study is that the reassembled NCM complex disassembles with faster kinetics than isolated NCM complexes (97). This demonstrates that the interactions of M with the complex are fundamentally different after *in vitro* reassembly. While a bullet-shaped structure with similar protein composition and dimensions as the NCM complex can be assembled *in vitro* (93), this reformed structure is not identical to *in vivo* assembled complexes. These differences propose that there is a crucial step in condensation that changes how M associates with the viral RNP.

Even though M and viral RNPs are abundant in the cytoplasm of infected cells, condensation only occurs at assembly sites. This inconsistency has been attributed to a higher affinity of M for NCM complexes than viral RNPs (98). Careful *in vitro* studies have shown that that M from the cytosol, cellular membranes, and virions all favor binding to NCM complexes over cytosolic viral RNPs as well as NCM complexes stripped of M (97, 98). The conversion of the high affinity NCM complex to the low affinity stripped NCM complex suggests that a

reversible step in assembly is responsible for initiating condensation of the viral RNP. The identity and trigger of this step has remained elusive.

While M has been thought to drive condensation, the N-RNA may also play an intrinsic role. Purified recombinant N-RNA can adopt a bullet-shaped structure under low salt and acid conditions (92). Whereas VSV particles contain a tip with 7 turns and a trunk with 37.5 monomers per turn (1), the N-RNA bullet contains only 5 turns in the tip and 33 monomers per trunk turn. This study suggests that the formation of the VSV bullet-shape is an intrinsic property of N but interactions of N with other viral proteins are important for generating the correct structure in virions. The N-RNA bullets form under non-physiological conditions that are unlikely to be found in infected cells. Perhaps interactions with viral proteins, such as M, generate local environments that mimic these conditions.

Constant versus variable incorporation of proteins into particles

The homogeneous bullet-shape of VSV suggests that the viral proteins are packaged through a regulated mechanism to ensure that a consistent amount of protein is incorporated to construct this structure. The amount of N that is incorporated into the particle is likely constant since N coats the packaged genomic RNA (38), which is a fixed length. This regularity is consistent with the defined N helix in virions (1) that accounts for the expected number of N molecules (99). In contrast, a variable amount of P and L may be incorporated into particles. The incorporation of P and L may be dependent on the binding of L to P and P to N (35). Therefore, the binding of P and L to the viral RNP would be in an equilibrium, which would result in a variable amount being associated during assembly. Particles contain a distinct M helix of ~1200 molecules (1), but 1826 molecules of M are packaged per particle (99). The remaining ~600

monomers are likely in the central "cigar" (100) that did not appear in the reconstruction. The absence of a structure suggests that it is amorphous and would contain a variable amount of protein. Perhaps a consistent amount of M in only the helix is necessary for formation of the virion shape. It is unclear if G is specifically incorporated into virions. While G enhances the efficiency of budding (89, 90) and colocalizes with N at the plasma membrane (64), it is not essential for assembly (90, 91). G may play an accessory role in assembly, which would lead to the incorporation of a variable amount per particle. While all 5 viral proteins must be incorporated into particles in order for them to be infectious, perhaps a consistent amount of only some of the proteins is required.

CryoEM reconstruction of VSV virions

A cryo-electron microscopy (cryoEM) reconstruction of VSV virions illustrates the locations of N and M inside assembled particles (1). N and M form discrete concentric helices that adopt the bullet-shape (Figure 1.3). The inner helix contains N oriented radially with its N-terminal lobe facing M and its C-terminal lobe facing the interior (1). This orientation proposes that the N-terminus interacts with M (1) and allows for interactions of P with the C-terminal lobe (101). M forms the outer helix that is immediately under the membrane (1), and this location accounts for the ability of M to bridge the viral RNP with membranes (65, 66). The electron density attributed to M contains 2 lobes, which were interpreted to be the N-terminal disordered "hub" domain that did not appear in the crystal structures and the C-terminal domain (CTD) from the solved structures. M was oriented with its N-terminus away from the membrane, which would allow for interactions with N (65). Knowing the correct orientation of M would emphasize those interactions that stabilize the assembled particle.

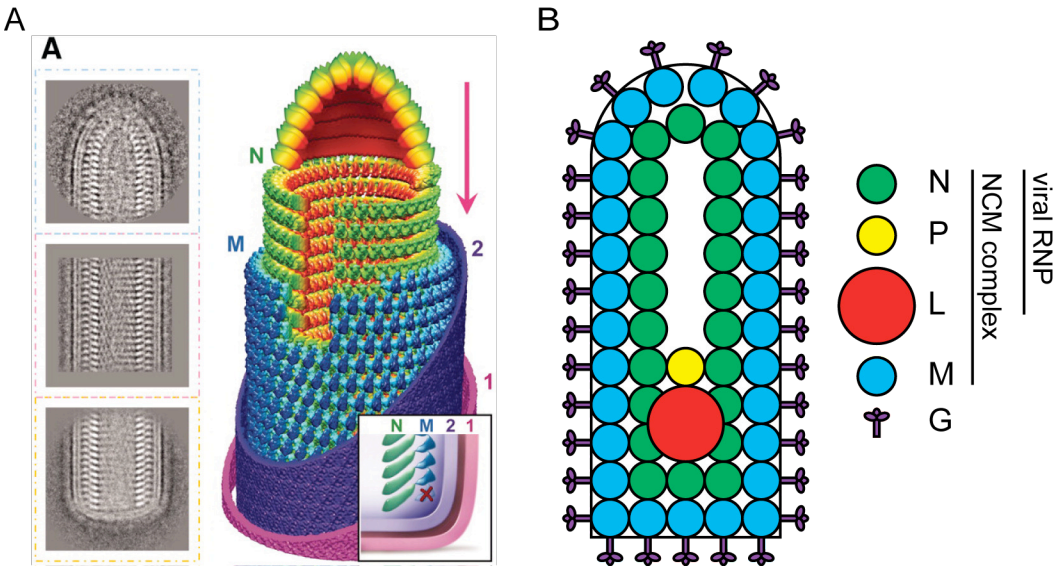

Figure 1.3. Composition and organization of VSV virions.
A cryoEM reconstruction of VSV particles was generated (1). (A) CryoEM class averages of the tip, middle, and blunt end of VSV particles, and a 3D model of the electron density map of a VSV particle. (B) A schematic of the localization of the VSV proteins in a particle. N and M form helices under the membrane (1) and L and P are found near the blunt end (102). (A) is from Cryo-EM model of the bullet-shaped vesicular stomatitis virus. Ge P, Tsao J, Schein S, Green TJ, Luo M, Zhou ZH. Science. 2010 Feb 5;327(5966):689-93. Reprinted with permission from AAAS.

The orientation of M described above is inconsistent with some published data. The sequences of M that are important for membrane binding are oriented away from the membrane. Residues 1-50 and 75-106 of M have each been demonstrated to be sufficient for binding to the plasma membrane (62). Since these experiments were performed with deletion mutants, a caveat is that perhaps these regions mediate membrane binding indirectly. However, using the hydrophobic photoreactive probe 3-(trifluoromethyl)-3-(m-[^{125}1]iodophenyl)-3Hdiazirine (^{125}I-TID), a probe that only labels amino acids that penetrate the lipid bilayer, it was shown that residues 1-19 are in close proximity to the membrane (63). The fitting of M in the cryoEM reconstruction positions these resides on the opposite site of M from the membrane (1).

The published orientation of M may not be the best fit in the electron density map since the correlation value is similar between multiple orientations. To analyze this, we used UCSF Chimera v1.7 (University of California San Francisco; San Francisco) to fit the full length M crystal structure (82) into the cryoEM reconstruction (1). M was fit in the published orientation with a contour map of 1.7 σ (1) and generated a correlation value of 0.828 (Figure 1.4 A). To test the accuracy of this fit, M was rotated 180°, and this orientation generated a correlation value of 0.839 (Figure 1.4 B). Ge P. *et al.* (1) fit M into a contour map of 1.15 σ and generated a correlation value of 0.63, and when they fit M upside-down obtained a correlation value of 0.41. While we found that M fit equally well in both orientations, which suggests that the density map is not at a high enough resolution for accurate fitting, Ge P. *et al.* (1) found better correlation in 1 orientation. These differences could be due to the contour level used, highlighting the need for further studies.

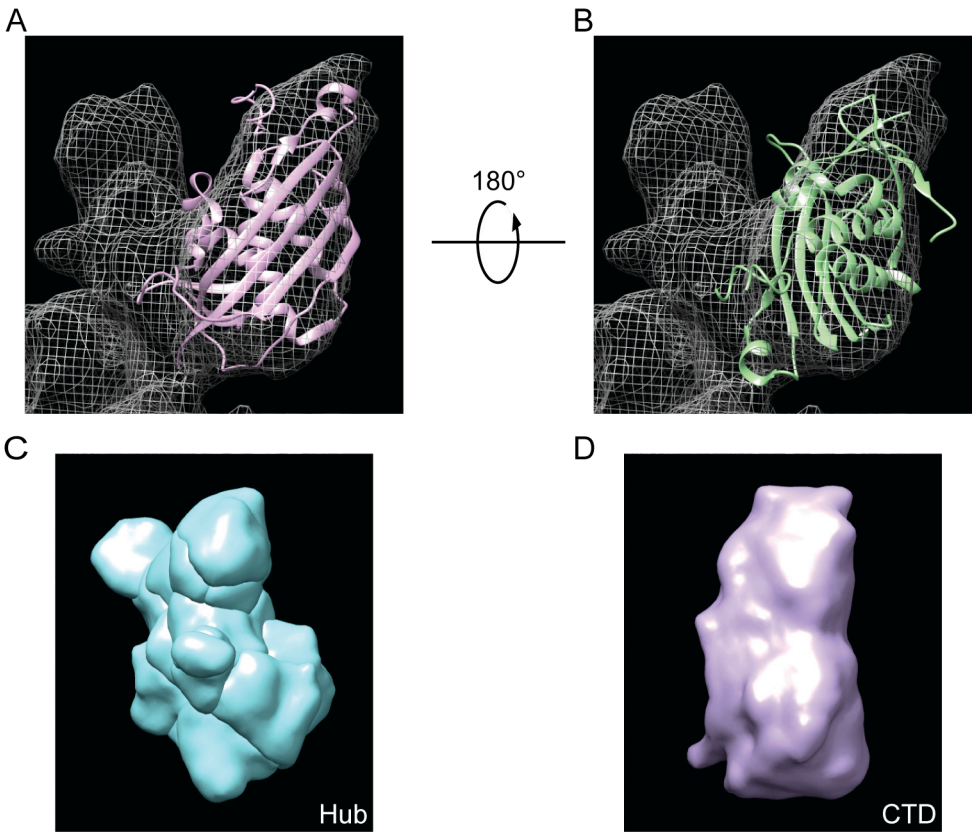

Figure 1.4. Fitting of the M crystal structure into the VSV cryoEM reconstruction.
The VSV M crystal structure, PDB 2W2R (82), was fit into the VSV cryoEM M density, EMD 1663 (1) with UCSF Chimera v1.7. Correlations were calculated with a map simulated from the M crystal structure at a resolution of 10.6 Å, the cryoEM resolution. The M crystal structure coordinates are shown as ribbon diagrams, and the M cryoEM densities are shown as mesh surfaces at contour level 1.0, which corresponds to 1.7 σ above mean. (A) M is oriented as in the publication and fit with UCSF Chimera v1.7. It generated a correlation value of 0.828. (B) M is rotated 180° relative to the publication and fit again. This orientation generated a correlation value of 0.839. The M electron density was segmented at σ = 1.7 with UCSF Chimera v1.7 to isolate the hub domain (C) and CTD (D), shown on the left and right of the mesh surface (A-B), respectively. The volume of the hub domain and CTD were measured to be 31 510 and 33 850 in arbitrary units, respectively. The CTD is 0.93-fold the volume of the hub domain.

The electron densities attributed to the hub domain and CTD are inconsistent with the anticipated molecular weights of these protein domains. The crystal structure of full length M identified the N-terminal disordered domain as residues 1-57 and the C-terminal globular domain as residues 58-229 (82). The calculated molecular weight of the hub domain is 6.2 kDa and the CTD is 19.8 kDa, and the ratio of the CTD to hub domain is 3.2:1. To measure the volumes of the predicted hub domain and CTD in the cryoEM reconstruction (1), UCSF Chimera v1.7 (University of California San Francisco) was used to segment the map at a contour level of 1.7 σ (Figure 1.4 C-D). The ratio of the CTD to hub domain volume in the cryoEM reconstruction is 0.93:1. The crystal structure predicts that the CTD is ~3-fold the size of the hub domain, but the ratio of the volumes of the predicted M lobes is only ~1.

A possible explanation for the inconsistencies in the fitting of M into the helix is that M may assemble in 2 orientations. The N-terminus of M is responsible for both binding to membranes (62) as well as N (65), but in virions, N and the membrane are on opposite sides of M (1). It is possible that in particles, some M has the N-terminus oriented towards the membrane and other monomers have the N-terminus oriented towards the N helix (1, 82). However, the monomers in the crystal structure filaments displaying this flipping organization are closer together than the electron densities in the cryoEM reconstruction (1). This could be reconciled if M is loosely tethered together and farther apart in virions than in the crystal (82). Such a flipping organization could explain why the hub domain and CTD are of similar volume; if half of the M is in each orientation, then the average would generate a 2 lobed structure.

While some viral proteins did not appear in the cryoEM reconstruction, their organization and function in assembled particles can be inferred (1). Although M could be localized to the outer helix, this helix only accounts for ~1200 (1) of the expected 1826 monomers of M (99).

Since M is known to be in the central "cigar" (100) that did not appear in the reconstruction, M may also form an amorphous structure that does not assemble with the same regularity as the helices. Perhaps the helices play an active role in creation of the bullet-shaped structure but the "cigar" is only required for structural integrity. P and L, which could not be localized, may also be in this central amorphous core (102). Alternatively, P and L may bind randomly along the length of the N-RNA and thus be averaged out in the reconstruction (1). P binds to N in a 1:2 ratio (103), but the ratio of P:N in the virion is 1:2.7 (99). Therefore, P and L would be bound to different N in each virion. Since P and L must be incorporated into particles in order for them to be infectious, a possible mechanism to ensure this is if the polymerase is frozen on the N-RNA template during assembly (104). This mechanism would also result in the random distribution of P and L along the genome. While entire G trimers did not appear in the reconstruction, a density protruding from the membrane towards each M monomer was suggested to be the cytoplasmic tail (1), and the number of protrusions would account for the expected number of G monomers (99). This interpretation proposes that the ectodomain is flexible but that the cytoplasmic tail is stabilized through its interactions with M (105), and such interactions are known to facilitate budding (89). The cryoEM reconstruction has revealed a wealth of information about the organization of the VSV proteins inside virions. Further studies may demonstrate how the N and M helices interact with the other viral proteins during assembly.

Late domains and the ESCRT pathway

For enveloped viruses, the final step of assembly is fission from the cellular membrane. Recruitment of the cellular endosomal sorting complexes required for transport (ESCRT) pathway by viral motifs named late domains appears to be required for this step. These motifs

were originally identified as position independent motifs in the group-specific antigen protein (Gag) of the retrovirus human immunodeficiency virus type 1 (HIV-1) (106, 107), but have since been found in a number of virus families (Table 1.3) (108). In cells, the ESCRT pathway is normally involved in the scission that occurs during cytokinesis and the generation of MVBs (109). These cellular processes are topologically equivalent to budding viruses where proteins in the cytoplasm must induce the release of a membrane-bound compartment on the opposite side of the membrane. This pathway is initiated by ubiquitination of the cargo (110), which leads to the sequential recruitment of the ESCRT complexes, ESCRT-0, -I, -II, -III, and finally the vacuolar protein sorting 4 (Vps4) complex (111) (Table 1.4).

Three types of late domain motifs have been identified that each bind directly to a different ESCRT protein to recruit this pathway (Figure 1.5). The late domain motif PPXY binds to the neural precursor cell expressed developmentally down-regulated 4-like E3 ubiquitin protein ligase (Nedd4) (112, 113), and viral proteins with this motif are ubiquitinated to initiate ESCRT recruitment (114, 115). The P(S/T)AP motif binds to tumor susceptibility gene 101 (Tsg101) (116), and this leads to recruitment of the ESCRT-I complex (117). The $LYPX_nLXXLF$, where n = 1-3, motif binds to apoptosis-linked gene-2 interacting protein X (Alix), which recruits the ESCRT-III complex (118, 119). The reason why viruses recruit the ESCRT pathway through different ESCRT complexes is unknown. While 3 late domain motifs and corresponding ESCRT protein binding partners have been identified, there may be others yet to be discovered. Whether binding early in the pathway to Nedd4 versus late in the pathway to Alix provides an advantage or disadvantage is unclear. HIV-1, which can bind to Alix (118, 120), is unaffected by siRNA knockdown of some components of the ESCRT-III complex (121) that are required for cytokinesis (122).

Table 1.3. Viral late domains.

Family	Virus	Protein	Late Domain
Rhabdoviridae	vesicular stomatitis virus	M	PPPY (68), PSAP (69)
Paramyxoviridae	Sendai virus	M	YLDL (123)
Filoviridae	ebola virus	VP40	PTAPPEY (124, 125)
Arenaviridae	lymphocytic choriomeningitis virus	Z	PPPY, PTAP (126)
Retroviridae	human immunodeficiency virus type 1	Gag	PTAP (127), YPDL (118)

Table 1.4. ESCRT complex compositions.

Complex	Components		Intercomplex Interactions
	Yeast	Human	
ESCRT-0 (128)	Vps27	Hrs	Hrs (P(S/T)AP motif) binds Tsg101 (129)
	Hse1	STAM 1/2	
ESCRT-I (117)	Vps23	Tsg101	hVps28 binds EAP45 (130)
	Vps28	hVps28	
	Vps37	hVps37 A/B/C	
	Mvb12	hMvB12 A/B	
ESCRT-II (111)	Vps36	EAP45	EAP20 binds Chmp6 (131)
	Vps22	EAP30	
	Vps25	EAP20	
ESCRT-III (132)	Vps20	Chmp6	Chmp1, Chmp2, and Chmp3 (MIM domain) bind Vps4 (MIT domain) (133) Chmp6 binds Vta1 (134)
	Snf7	Chmp4 A/B/C	
	Vps24	Chmp3	
	Vps2	Chmp2A/B	
	Vps46	Chmp1	
Vps4 Complex (128)	Vps4	SKD1	
	Vps60	Chmp5	
	Vta1	LIP5	

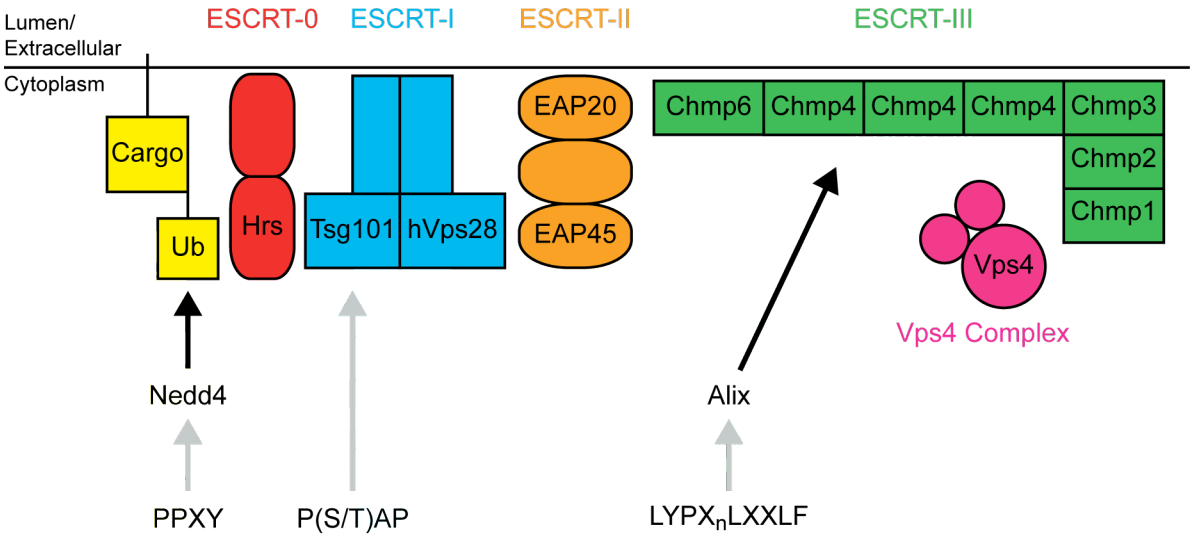

Figure 1.5. Recognition of late domains by the ESCRT pathway.
Late domains mediate recruitment of the ESCRT pathway to the site of viral assembly (128). The 3 identified late domain motifs are PPXY, which is ubiquitinated by Nedd4, P(S/T)AP, which binds to Tsg101, and LYPX$_n$LXXLF, where n = 1-3, which binds to Alix. Each of these cellular proteins connects to the ESCRT pathway. For clarity, only the ESCRT proteins directly involved in complex recruitment are labelled.

HIV-1 assembly

HIV-1 is an enveloped retrovirus whose assembly has been extensively studied with live cell fluorescence microscopy. Like VSV, the main components of the HIV-1 particle are Gag, the genome, and envelope glycoprotein (Env). Gag has similar functions as VSV M in assembly, and the creation of fluorescent Gag (135-137) permits the study of *de novo* assembly of HIV-1 particles (138, 139). The egress of particles occurs through 3 distinct stages (Figure 1.6) (139). During stage I, Gag rapidly assembles into the particle and the viral components are packaged. After completion of assembly, there is a pause, stage II, before fission and release of the particle into the supernatant, stage III. The separation into multiple phases suggests that assembly, budding, and fission are not concomitant processes, but rather steps that require completion before egress progresses. The ability to observe Gag assembly allows for the study of how the genome and Env are recruited. The genomes are recruited to assembly sites after particle formation is initiated by Gag, and the function of Gag to anchor the genome to the membrane illustrates a role in packaging the genome (140). Like VSV G, Env can form microdomains at the plasma membrane, but this is dependent on the presence of Gag (141). The interaction between Env and Gag is required for the incorporation of Env into assembly sites, suggesting an active mechanism of incorporation. Fission of HIV-1 particles from the cellular membrane requires recruitment of the ESCRT pathway. While the late domain binding protein Tsg101 is recruited gradually during Gag assembly (142), Alix and the ESCRT-III complex only associate transiently with the completed HIV-1 particle (143, 144). Consequently, Tsg101 may be involved in Gag assembly, but the majority of ESCRT machinery is recruited after assembly is finished. The kinetics and order of assembly of HIV-1 particles has been deciphered with fluorescence microscopy, and this methodology can be applied to studying VSV assembly.

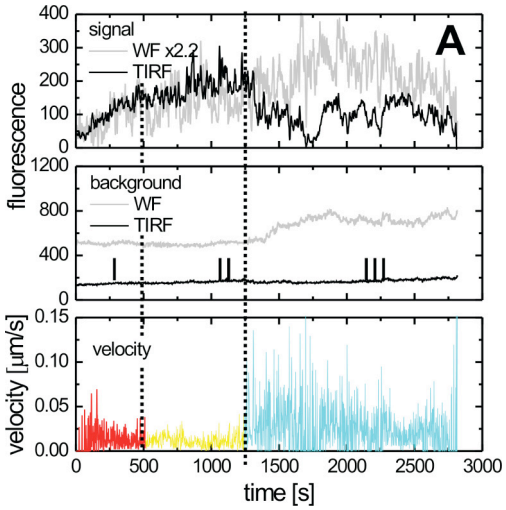

Figure 1.6. Stages of assembly of HIV-1 particles.
Fluorescent intensity and speed traces of assembling HIV-1 particles illustrate 3 stages of assembly (139). In stage I, an increasing Gag fluorescent intensity demonstrates rapid assembly into the particle. Stage II is a plateau in Gag intensity that likely represents the association of Gag with cellular machinery. At the end of stage II, fission occurs between the viral and cellular membranes, leading to stage III, where the particle is released into the supernatant. During the final stage, the speed increases and the fluorescent intensity varies as the particle moves in and out of the total internal reflection fluorescence (TIRF) field. This figure is from Dynamics of HIV-1 assembly and release. Ivanchenko S, Godinez WJ, Lampe M, Kräusslich HG, Eils R, Rohr K, Bräuchle C, Müller B, Lamb DC. PLoS Pathog. 2009 Nov; 5(11).

Open questions in VSV assembly

Formation of viral particles requires the coordinated association of the structural proteins. While the proteins that are required at each stage of VSV assembly have been identified, the triggers for individual steps remain to be ascertained. Creation of the bullet-shaped virion requires both M and the N-RNA (16, 92), but how much M is required to trigger the formation of this structure is unclear. The cryoEM reconstruction demonstrates that the average structure of particles has a complete helix of N and M, but whether this is true for individual virions is not known (1). Condensation of the viral RNP into the NCM complex requires a trigger whose identity has remained elusive (98). This process could be mediated by an interacting partner of M, but the involvement of many of these proteins in assembly is not fully understood. While the order that viral proteins are recruited to assembly sites has been difficult to determine, colocalization of proteins in fixed cells proposes a model (34, 64), but the static nature of these experiments prevents the determination of which sites lead to productive assembly.

Steps in VSV egress have been observed by fluorescence microscopy. During assembly, the viral RNP must be transported from cytoplasmic inclusions to the plasma membrane. Fluorescent protein fusions to viral RNP proteins, *e.g.* P (57, 145) and L (146), have allowed visualization of the subcellular distribution of these proteins (56, 146) prior to assembly and the microtubule-dependent transport of the viral RNP to the periphery (57). VSV particles must also contain G in order to be infectious. The fusion of eGFP to the G cytoplasmic tail does not prevent incorporation into particles, demonstrating that the packaging of G can tolerate large additions, *e.g.* 27 kDa, to the normally small tail, 29 amino acids (147). M is required for assembly and was shown to be predominantly synthesized in the cytosol but transported to the

membrane in < 30 min through pulse labelling with a fluorescent dye (148). Fluorescent protein fusions allow for the tracking of viral proteins during assembly.

A limitation of studying VSV assembly has been the difficulty in examining the contents of single particles as well as the formation of particles in live cells. To begin to address this problem, we generated fluorescent fusions to viral proteins and used fluorescence microscopy to quantify the contents of virions. Specifically, we measured the variation in incorporation of structural proteins into single particles and evaluated how mutations that inactivate the late domains of M alter its incorporation into particles. The tools we developed were used to study viral replication in 3 ways: (i) imaging the process of assembly of single virions in live cells, (ii) evaluating the protein composition of single viral particles, and (iii) imaging the process of viral entry and uncoating. This work provides important advances on each of those fronts and sets the stage for future studies to examine the kinetics of assembly of single viral particles.

Chapter 2

Vesicular stomatitis virus incorporates a range of M and P per virion

Abstract

A defining characteristic of Rhabdoviruses is the bullet-shape of the virion. How this reproducible structure is generated is unclear. A cryo-electron microscopy (cryoEM) reconstruction of particles reveals a discrete helix of the nucleocapsid protein (N) and matrix protein (M). This suggests that a constant amount of N and M are incorporated into particles to form these helices. While this is expected for N, which coats the fixed length genomic RNA, the amount of M may not be constant since only a fraction of the M monomers are accounted for. Since the cryoEM is an average and previous measurements of the protein content of particles have been on bulk populations, the variation in the incorporation of each viral protein into single virions has not been evaluated. To address this question, we measured the content of single particles with fluorescence microscopy and fluorescent fusions. A functional M-eGFP was identified through a forward genetics screen of a library with eGFP inserted into random positions in M. The M protein tolerates insertion after residue 37 without abolishing M function in assembly and budding of an infectious particle. An autonomously replicating virus containing this M-eGFP fusion is attenuated in cell culture replication but assembles virions that maintain the typical bullet-shape. By measuring the fluorescent intensity of individual VSV M-eGFP particles, we obtain evidence for a range of M molecules per particle. Using a previously described eGFP fusion to the polymerase cofactor phosphoprotein (P), we show that virions also contain a variable amount of P. By generating a dual labelled virus in which both M and P are tagged with separate fluorophores, we show that the incorporation of M and P are not correlated. These data suggest that the incorporation of M and P into particles is through a flexible mechanism, and that the shape of the virion does not depend on a specific amount of either of these proteins.

Introduction

Vesicular stomatitis virus (VSV) is an enveloped virus that assembles into a reproducible bullet-shape. Such a homogeneous structure suggests that there are strict regulations on the incorporation of the viral proteins, but the consistency in packing has not been tested. A cryo-electron microscopy (cryoEM) reconstruction demonstrates discrete concentric helices of the nucleocapsid protein (N) and matrix protein (M) within the bullet-shaped particle (1). The fact that N coats the RNA and a monomer binds to exactly 9 nucleotides (1, 38) suggests that a consistent amount of N is packaged into particles. Since only ~1200 molecules (1) of the expected 1826 (99) of M were identified in the reconstruction, the remaining M is likely in the central "cigar" (100). This "cigar" does not appear in the cryoEM reconstruction, suggesting an amorphous structure that would package a variable amount of M. The polymerase components, phosphoprotein (P) and large polymerase protein (L), were not visible in the cryoEM reconstruction (1), suggesting a lack of symmetry in their incorporation and perhaps a flexible amount of those proteins. P functions to link L to the N-RNA (35) and binds to L to form the active polymerase complex (46, 47). During assembly, the polymerase may be "frozen" randomly along the genome (104), leading to an inconsistent location in the virion. In addition, there is a ratio of 1 L:9.3 P in virions (99), but *in vitro* the active polymerase complex consists of 1 L:2 P (47). Therefore inside particles, some P is not bound to L. Since P binds tightly to the viral ribonucleoprotein (RNP) (149), the excess free P may be in the amorphous "cigar" or may also be bound to the N-RNA. Since the ratio of P:N is 1:2.7 in virions but only 1:2 *in vitro*, the P in particles would be bound to the N-RNA at inconsistent locations. If VSV particles contain a variable amount of protein, this variation does not affect the overall structure of the virion.

To determine how much the protein content of bullet-shaped virions varies, the composition needs to be measured at the single particle level. This can be accomplished with quantitative fluorescence microscopy, but this requires that the protein of interest is fluorescently tagged. Given the role of M in assembly (16), the consistency in packaging of M would be informative about the flexibility of the assembly mechanism. While a functional terminal fluorescent protein fusion to M has not been reported, M has been fluorescently tagged with the tetracysteine motif/biarsenical dye (148). However, the use of a dye could introduce variations in the fluorescent intensity since binding is in an equilibrium, and this could mask the consistency in the number of M molecules. Therefore, a dye is non-ideal and a fluorescent protein fusion would be preferable.

The structural features of M and its functions in assembly and host cell shutoff likely place constraints on the locations where a fluorescent protein could be inserted. The N-terminus of M contains multiple in-frame translational initiation sites that lead to the generation of multiple N-terminal truncation variants (86). These are thought to be generated through "leaky scanning" by the ribosome (150), and thus large insertions in this region would prevent the expression of the M truncation variants. While these truncated proteins induce the cytopathic effect (CPE), they are not essential for VSV viability (86) and are not competent for assembly (151). Disruption of the expression of these M variants may not be detrimental to the viability of an M fusion. The N-terminus also plays a role in engaging the endosomal sorting complexes required for transport (ESCRT) pathway for viral particle budding through the 2 late domains of M, located at residues 24 PPPY 27 (68) and 37 PSAP 40 (69). The crystal structures of M (78, 81, 82) provide an opportunity for rationale design for creation of a functional fusion. However, this is complicated by the multiple interaction partners of M (Table 1.2). For example, the region

around M51 is engaged in direct contact with Rae1 and insertion of eGFP may disrupt this interaction. To mediate assembly, M must be able to oligomerize, bind to membranes, and bind to the viral RNP. These functions map to the disordered N-terminus of M (82). The N-terminus may be a permissible site due to the disordered nature, or it may be a disruptive site due to the high density of M functions associated with it.

In this study, we generated a function fluorescent fusion to M through forward selection of a library with eGFP inserted randomly in M. A replication competent VSV containing exclusively fluorescent M was generated. The single particle protein content of VSV M-eGFP as well as the dual fluorescent virus VSV M-mCherry P-eGFP demonstrate that a variable amount of M and P are incorporated into particles, demonstrating a flexible packaging mechanism, and that this does not affect the overall bullet-shaped structure of VSV.

Results

A functional M-eGFP fusion identified from a screen

To generate a functional M-eGFP, we took the approach of creating an internal fusion protein. Transposon (Tn) mutagenesis was used to generate random insertions within M (Figure 2.1 A). The Tn was subsequently replaced with eGFP and the resulting M-eGFP library was cloned into a VSV genomic analog comprising 3' Leader-M-G-Trailer 5'. The diversity of the library was verified by restriction enzyme digestion using enzymes that excise M and Tn (Figure 2.1 B). Each insertion site creates a unique sized fragment representing the distance of the Tn from the start of M. The smear of DNA on the agarose gel (Figure 2.1 B, lane 4) suggests Tn insertions at multiple locations throughout M. Consistent with this, sequence analysis shows the presence of secondary peaks in the chromatogram (Figure 2.1 C). To determine whether any of the M variants are functional for particle budding, the genomic analog was transfected into cells along with the necessary trans-acting replication machinery N, P, and L (Figure 2.2 A). Functional M fusions permitted the assembly and budding of particles that were subsequently amplified by low MOI infection of cells expressing N, P, and L. Sequence analysis of the released genomic analogs identified a permissive site for insertion of eGFP in M after residue 37 (Figure 2.2 B). This site is located within the disordered N-terminus (82) and near a number of mapped characteristics and functions of M (Figure 2.3 A). The crystal structures of M (82) and GFP (152) illustrate their similar sizes and globular structures and how the disordered region of M allows for the fusion to GFP to not interfere with the M structure (Figure 2.3 B). Other sites in the disordered region identified from the screen, *e.g.* after residue 46 and 50, did not successfully generate replication competent virus.

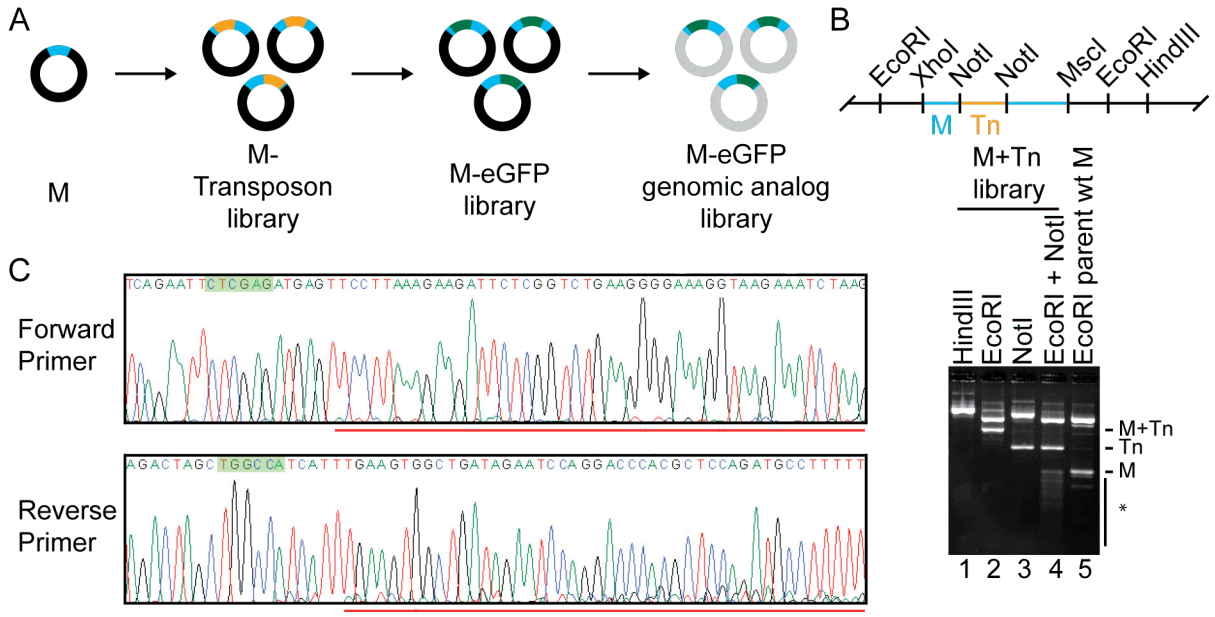

Figure 2.1. Generation of M-eGFP fusion library.
(A) A cDNA of VSV M (blue) was subjected to transposon mutagenesis. The Tn (orange) was replaced with eGFP (green), and the resulting M-eGFP library was cloned into a VSV genomic analog consisting of 3' Leader-M-G-Trailer 5' (grey). (B) Diversity of the library was verified by restriction enzyme digestion. A schematic of the cDNA highlighting the position of restriction sites, including upstream XhoI and downstream MscI, is shown. The library was digested with HindIII, EcoRI, NotI, or EcoRI + NotI, and compared to wild type M (digested with EcoRI), lanes 1-5 respectively. Multiple Tn insertion sites are indicated by the smear of DNA (*) in lane 4 that are smaller than the size of wild type M. (C) Sequence analysis of the M-eGFP library. Primers upstream and downstream of the highlighted (green) XhoI and MscI sites, which flank the coding sequence, were used to sequence the cDNA, and the extent of diversity is indicated by the secondary peaks in the chromatogram, underlined in red.

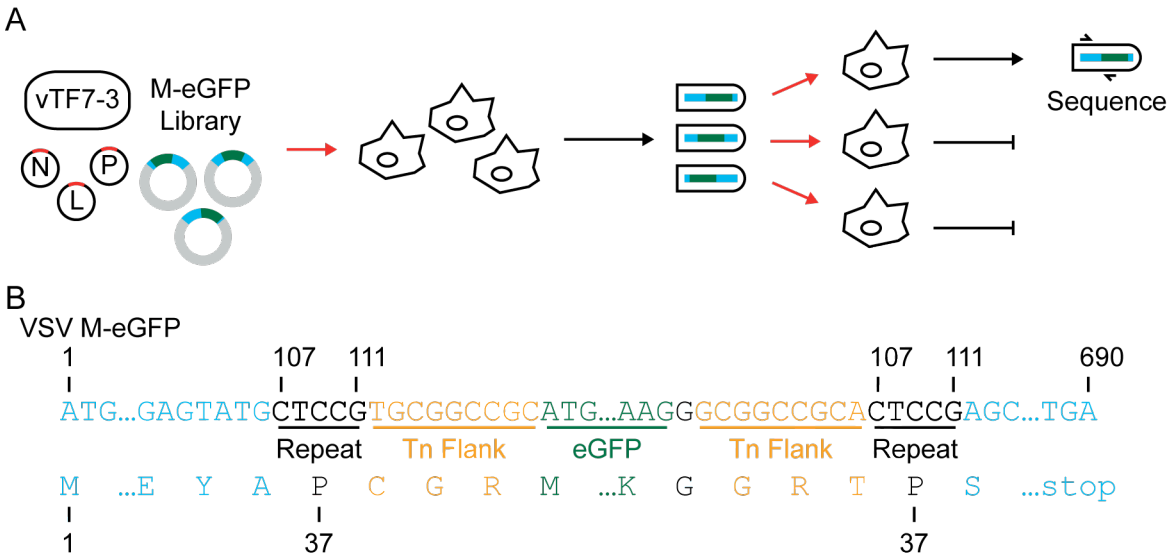

Figure 2.2. Selection of viable M-eGFP fusion proteins.
(A) Selection of viable M-eGFP fusions. VSV genomic analog particles were recovered from the library by infecting cells with a T7 expressing vaccinia virus (vTF7-3) and transfecting the cells with the library and plasmids encoding the trans-acting viral replication machinery, N, P, and L (red arrow). The resulting produced (black arrow) particles were used to infect cells at low MOI that were also infected with vTF7-3 and transfected with N, P, and L. The sequences of the genomic analogs of the released virions were obtained. (B) The sequence of the viable fusion selected for further analysis is shown. The numbers listed above represent the nucleotide position and below represent the amino acid position in the cDNA of wild type M.

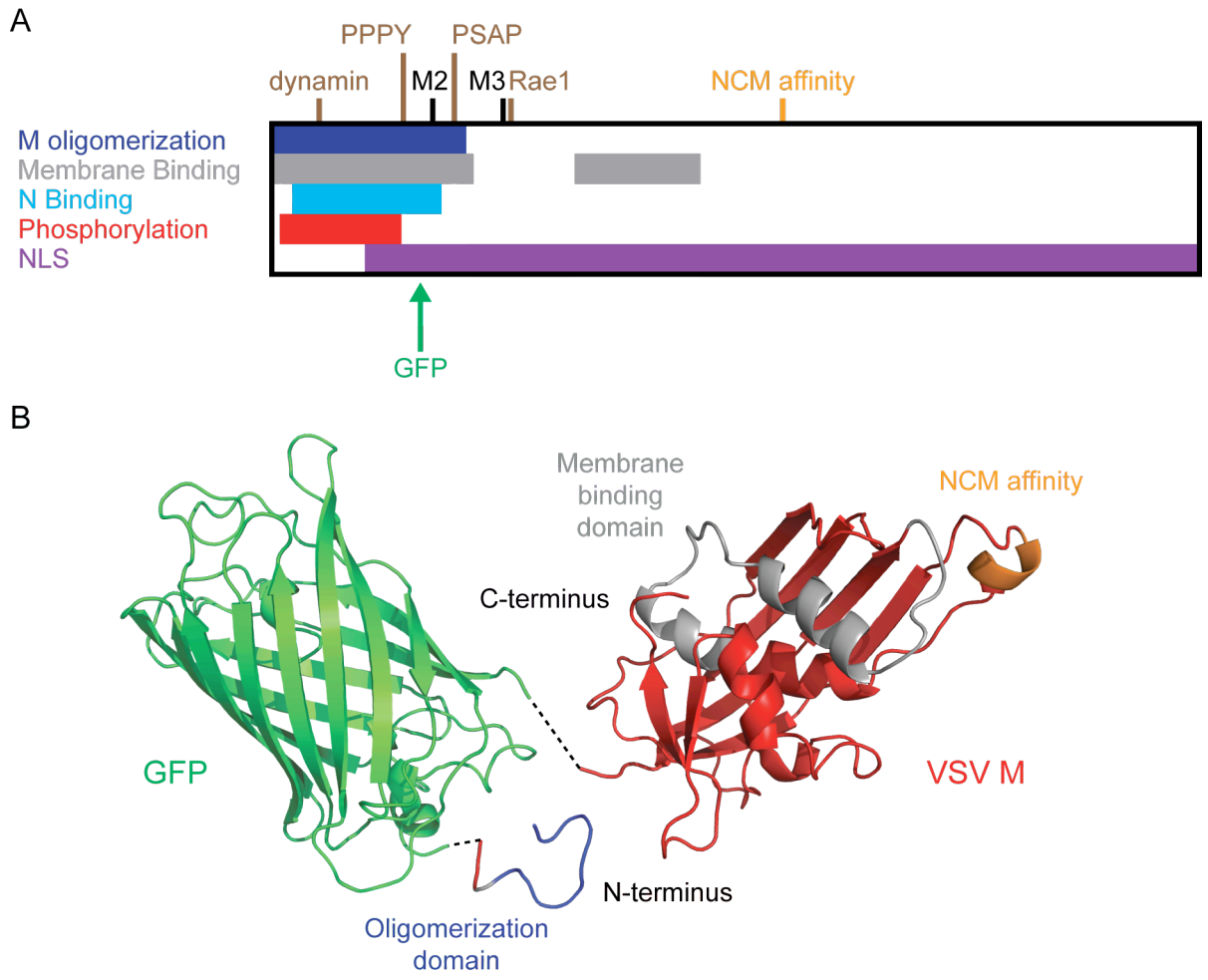

Figure 2.3. Location of the permissive site of eGFP relative to characteristics of M.
(A) A schematic of the location of the permissive insertion site of eGFP, the M oligomerization domain (60), membrane binding domain (62), N binding domain (65, 66), residues that affect nucleocapsid-matrix protein (NCM) complex affinity (84), late domains (PPPY, PSAP) (68, 69), Rae1 binding domain (78), dynamin binding domain (85), alternate translational start sites (M2, M3) (86), nuclear localization signals (NLS) (87), and phosphorylation sites (88) in M are shown to scale. (B) The crystal structure for M (82) and GFP (152) are positioned in approximately the correct orientation. The functional domains of M that appeared in the crystal structure are highlighted, *e.g.* oligomerization domain (blue) (60), membrane binding domain (grey) (62), and NCM complex affinity (orange) (84).

Fusion of M with eGFP attenuates virus replication in cell culture

To determine the impact of the M fusion on virus replication, we inserted this M-eGFP into an infectious cDNA clone. We also engineered a clone of VSV where M was fused to mCherry instead of eGFP and combined this fusion with a previously published P-eGFP fusion (145) to generate a dual fluorescent VSV. The reduced plaque size and single-step growth curves of the resulting viruses demonstrate that the fusion of M-eGFP attenuates replication (Figure 2.4 A-B). While VSV M-eGFP and VSV P-eGFP replicate at 37°C, VSV P-eGFP M-mCherry grows better at lower temperatures (Figure 2.4 C). Analysis of the protein composition of purified particles demonstrates that the insertion of a fluorescent protein is associated with the loss of the wild type proteins on an SDS PAGE and appearance of bands consistent with the fusion proteins, *i.e.* a protein 27 kDa larger (Figure 2.4 D). As expected, M-eGFP is larger than M and reacts with antibodies against both M and eGFP, and no degradation products of M-eGFP are observed (Figure 2.4 E). To estimate the relative infectivity of VSV M-eGFP particles versus wild type VSV, the relative genome to plaque forming unit (PFU) ratio was calculated with quantitative PCR (qPCR) for the genome and plaque assay for titre. The genome to PFU ratio of VSV M-eGFP relative to wild type was found to be 3.9 ± 1.1 ($n = 3$). Since M is known to migrate to the nucleus where it inhibits host messenger RNP export (73), we examined the intracellular distribution of M-eGFP. No gross difference in the distribution of M-eGFP was observed when compared to wild type M (Figure 2.5).

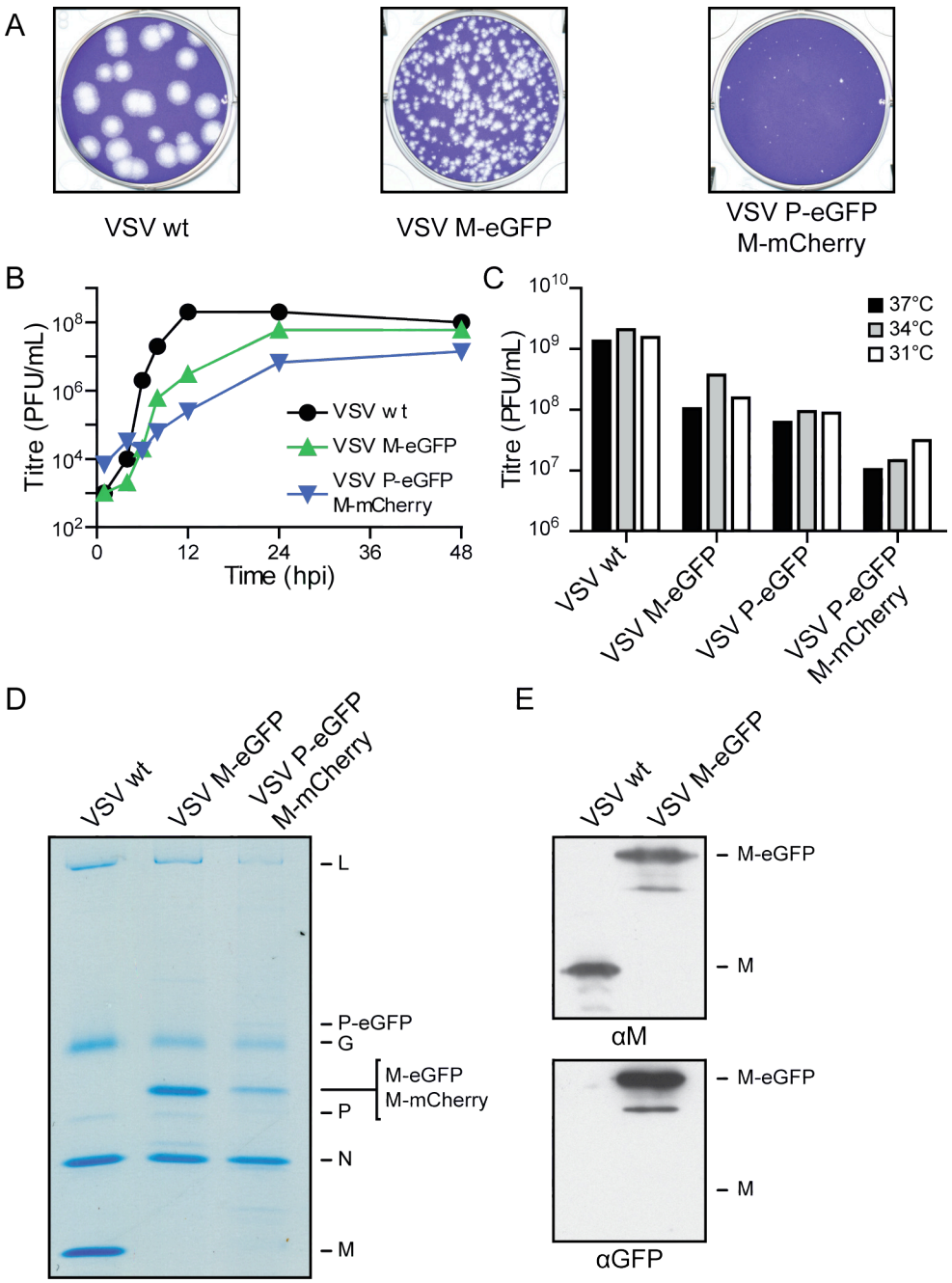

Figure 2.4. VSV M-eGFP and VSV P-eGFP M-mCherry replicate with slower kinetics.
(A) Plaque assays of viruses fixed and stained 48 hpi. (B) Single-step growth curves of the recombinant viruses containing the indicated fluorescent fusions of M and P. BsrT7 cells were infected at MOI 3 and the supernatant was sampled at the indicated times. (C) BsrT7 cells were infected at MOI 3 with wild type VSV, VSV M-eGFP, VSV P-eGFP, or VSV P-eGFP M-mCherry. Cells were grown at 31°C, 34°C, or 37°C. At 1 dpi the supernatant was harvested and titred. Purified viruses were analyzed on an SDS PAGE and stained with Coomassie blue (D) or followed by a western blot for M or eGFP (E).

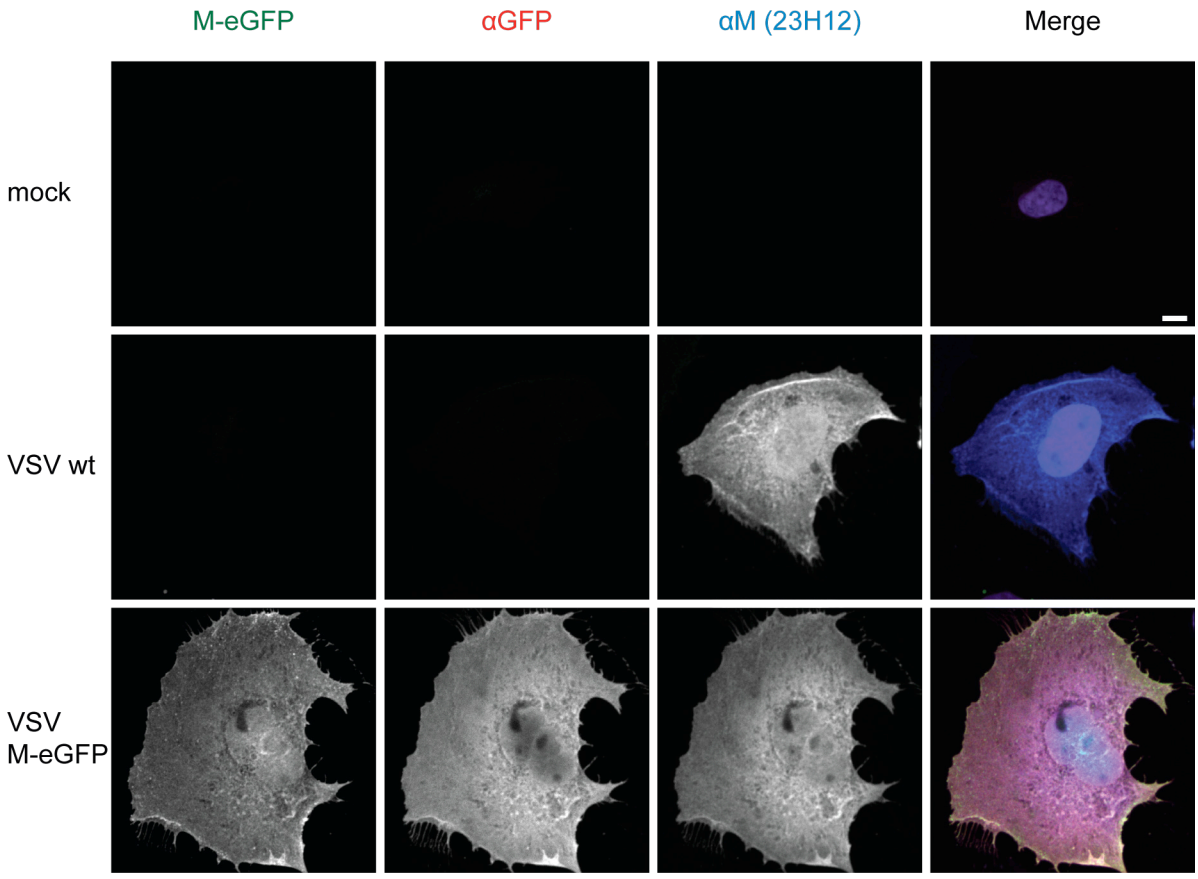

Figure 2.5. Subcellular localization of M-eGFP in infected cells.
BS-C-1 cells were infected with wild type VSV or VSV M-eGFP at MOI 3, fixed at 8 hpi, and stained with antibodies against eGFP (red) and M (blue). The merge image also includes DAPI (purple). Images were acquired under the same microscope settings and renormalized to the same values. Scale bar represents 10 μm.

Kinetics of maturation and assembly of VSV M-eGFP are not grossly perturbed

To determine if the M-eGFP fusion perturbs particle formation and release, the kinetics of assembly of VSV M-eGFP was compared to wild type VSV (Figure 2.6). VSV infected BsrT7 cells were pulse labelled with ^{35}S, and the supernatant virus was analysed by SDS PAGE. The total time required for VSV proteins to complete synthesis, transport, and assembly was measured for wild type VSV and VSV M-eGFP. The kinetics for M and M-eGFP are the same, appearing after 10 min, and the other viral proteins had similar kinetics regardless of whether they are in the wild type VSV or VSV M-eGFP backbone. Note however, that the extent of host protein labelling was higher in cells infected with VSV M-eGFP, suggesting less efficient host shutoff or reflecting a delay in the kinetics of replication.

M-eGFP alters virion protein composition but not shape

Using negative stain transmission electron microscopy (TEM), we found that VSV M-eGFP virions retain the classic bullet-shape (Figure 2.7 A) but are slightly longer (Figure 2.7 B) and the same width (Figure 2.7 C) as wild type VSV. Particle length is dependent on genome length (153) and the M-eGFP genomes are 7% larger leading to an increase in length of 12%. Analysis of populations of purified virions by SDS PAGE (Figure 2.7 D) shows similar moles of P, but less L and glycoprotein (G) and 56% less M-eGFP than M (Figure 2.7 E). Previous estimates indicate that there are 1826 molecules of M per virion on average (99), which suggests that there are 800 ± 30 molecules of M-eGFP.

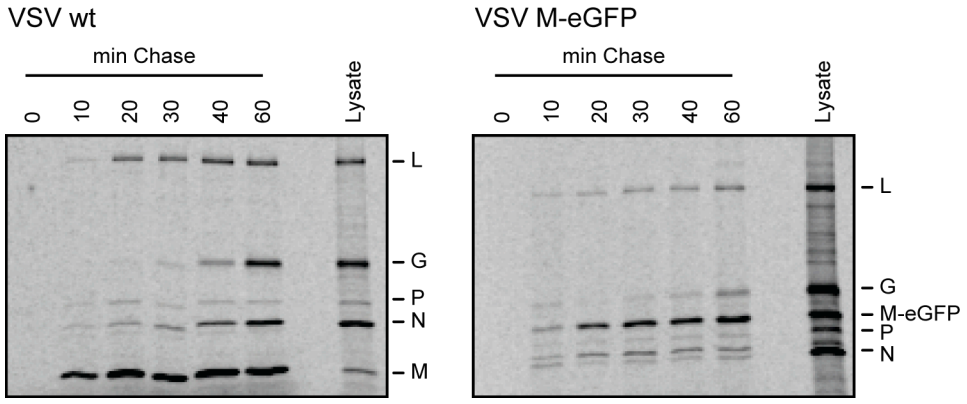

Figure 2.6. Incorporation kinetics of M-eGFP into released particles.
BsrT7 cells were infected at MOI 10 and pulse-labelled with ^{35}S at 6 hpi. Supernatant virus was collected every 10 min. Virus was concentrated by ultracentrifugation and analysed by SDS PAGE and autoradiography. Images are renormalized to the same values.

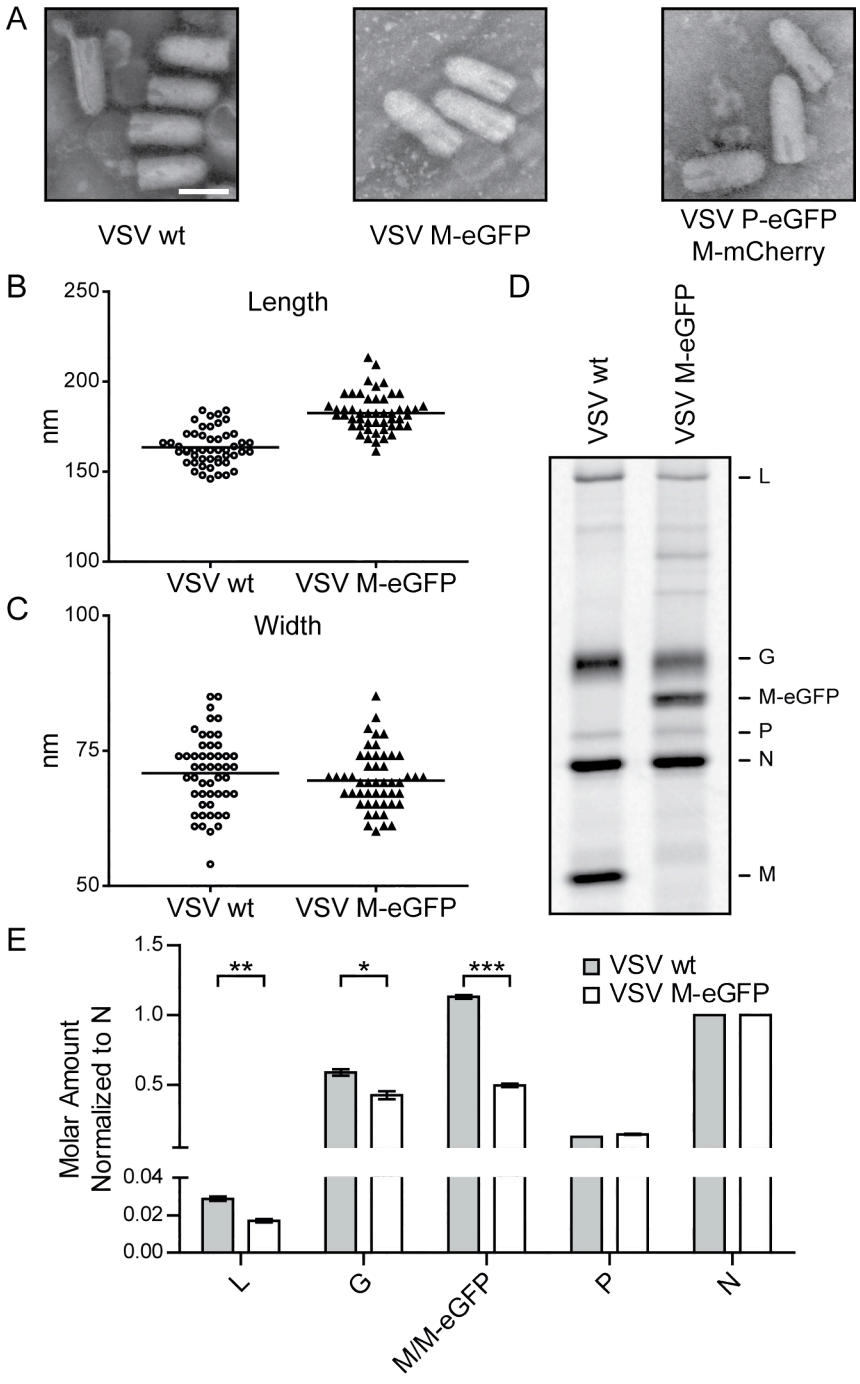

Figure 2.7. Dimensions and contents of VSV M-eGFP particles.
(A) Purified viruses were negatively stained and imaged by TEM. Scale bar represents 100 nm. The length (B) and width (C) of 50 virions was measured, and the length but not width is significantly different (Student's t-test p-value = 10^{-14} and 0.3, respectively). (D) ^{35}S labelled viruses were analyzed on an SDS PAGE and the viral bands quantified by densitometry. (E) The intensities were normalized to the number of cysteines and methionines in each protein and then normalized to N. SEM for n = 3 are shown. ***p-value < 10^{-5}, **p-value < 10^{-2}, *p-value < 0.05 (Student's t-test).

To examine the composition of individual particles, we performed fluorescence confocal microscopy on gradient purified particles (Figure 2.8 A). Single viral particles show a distribution of intensities of M-eGFP (Figure 2.8 B-C). A similar quantification of VSV P-eGFP M-mCherry particles (Figure 2.9 A) also illustrates a distribution of M-mCherry (Figure 2.9 B) and P-eGFP (Figure 2.9 C) per particle. The M-mCherry content of VSV P-eGFP M-mCherry has a wider distribution than M-eGFP in VSV M-eGFP. This larger variation was also found in VSV M-mCherry, suggesting that it is due the fusion of mCherry instead of eGFP to M. A scatter plot of VSV P-eGFP M-mCherry particles displays a single population and no correlation between M and P intensities (Figure 2.9 D). This demonstrates that a range of the fusion proteins is incorporated into particles.

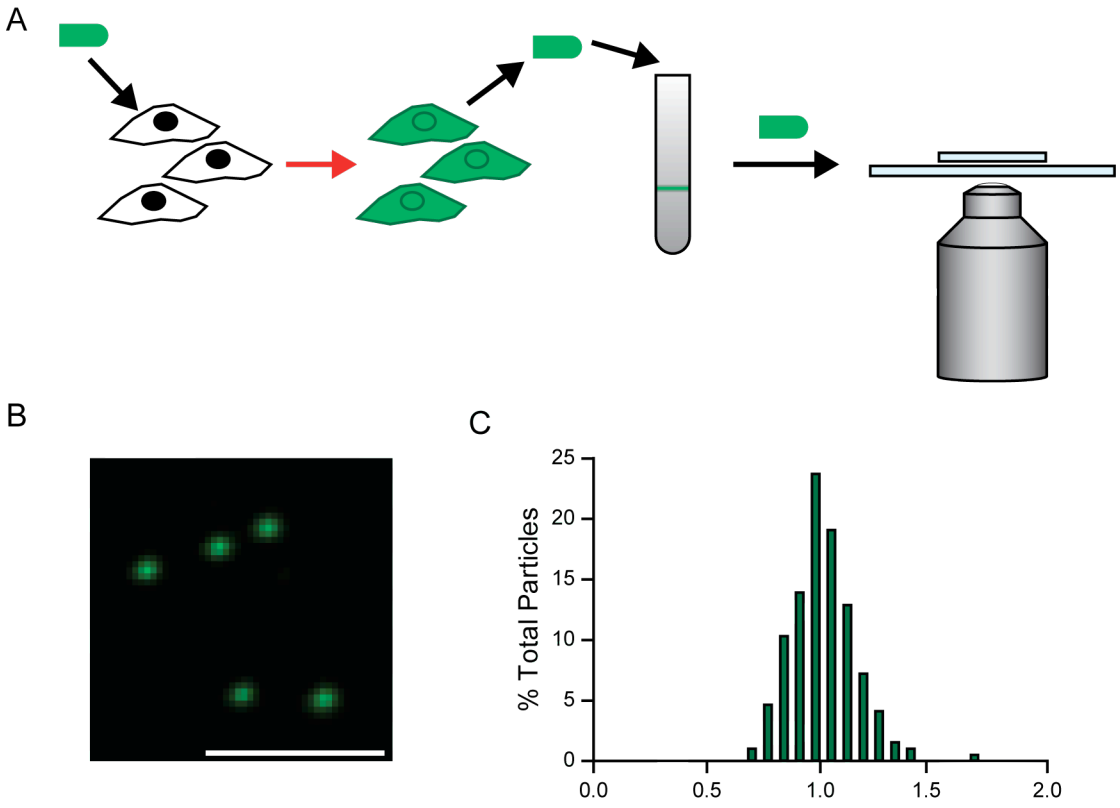

Figure 2.8. Fluorescent intensity of VSV M-eGFP particles.
(A) Gradient purified VSV was imaged with a fluorescence confocal microscope. The fluorescent intensities of individual VSV M-eGFP particles (B) were plotted to generate a histogram (n = 194) (C). The scale bar represents 5 μm. Histogram intensity is normalized to the peak. A control dataset measuring the acquisition error was determined by calculating the variation in intensity of the particles between multiple acquisitions. The distribution of M-eGFP is significantly different from its control dataset (Kolmogorov-Smirnov test p-value < 10^{-8}).

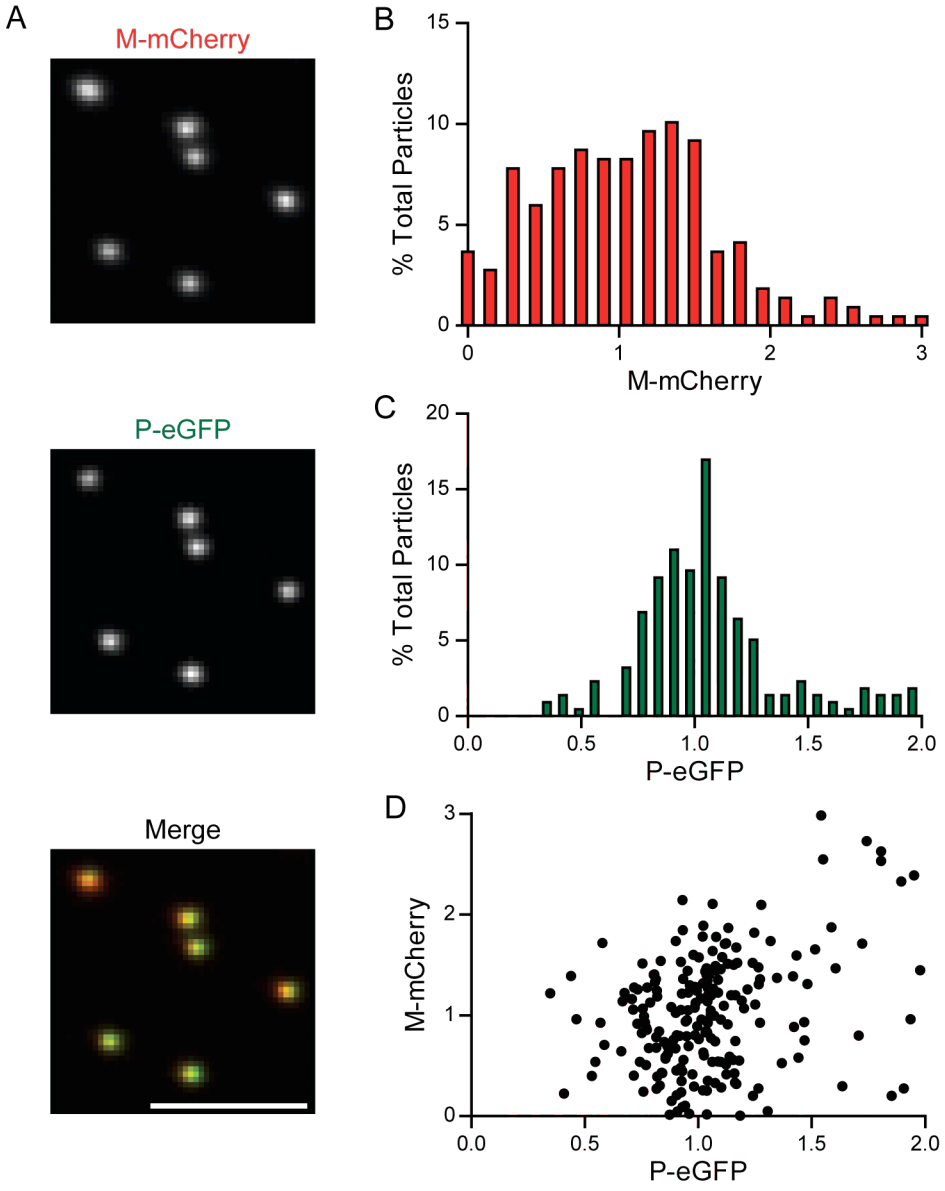

Figure 2.9. Fluorescent intensity of VSV P-eGFP M-mCherry particles.
(A) VSV P-eGFP M-mCherry particles (n = 219) were imaged as in Figure 2.8 and used to generate a histogram of M-mCherry intensities (B), a histogram of P-eGFP intensities (C), and a scatter plot (D). The scale bar represents 5 μm. The distributions of M-mCherry and P-eGFP are significantly different from their control datasets, which were acquired as described in Figure 2.8 (Kolmogorov-Smirnov test p-value < 10^{-14} and 10^{-3}, respectively).

Discussion

A functional fluorescent protein fusion to M could be generated by insertion into the disordered N-terminus. Fluorescence microscopy reveals that VSV particles contain a variable amount of M and P, but the amounts of these proteins that are packaged are independent of each other. A fraction of the M content of wild type particles is sufficient for the formation of the characteristic bullet-shape, suggesting that M may play a nucleating role in the creation of this structure.

The permissive site for insertion of fluorophores is in the disordered N-terminus of M

Given the crystal structures of M (81, 82), rational design would suggest inserting a fluorophore into the disordered N-terminus or loops between β sheets. Our screen demonstrates that the disordered region is a permissive site. However, not all positions in this region are functional, *e.g.* virus could not be recovered with eGFP inserted after residue 46 or 50, illustrating that there are additional constraints on this domain.

VSV M-eGFP with eGFP inserted after residue 37 in M can replicate autonomously. This insertion site disrupts expression of the M variant synthesized from the alternate translational start site at residue M51 (86). This N-terminally truncated M induces CPE and host shutoff but is non-essential (86, 154). This eGFP insertion site is also in close proximity to residues 49-61, which mediate host shutoff through binding to mRNA export factor 1 (Rae1) (71, 78, 79). These characteristics may contribute to the decreased host shutoff in infected cells (Figure 2.6). However, the most important feature of this virus is that the M-eGFP fusion is competent for assembly and generates fluorescent virions.

The genome to PFU ratio of VSV M-eGFP was found to be higher than for wild type VSV, suggesting a defect in the assembled particles. If VSV M-eGFP particles are less stable, then a higher ratio could be explained if the particles are more prone to lysis. This could be due to a reduced structural integrity caused by the reduced number of M molecules per particle (Figure 2.7). Alternatively, the particles could be less infectious. Given the reduced number of M monomers per virion, the interactions between the membrane, M, and N in the nucleocapsid-matrix protein (NCM) complex may be perturbed. These interactions could be important for proper uncoating during entry, leading to premature uncoating or uncoating in the wrong location.

VSV M-eGFP produces fewer particles per cell than wild type VSV (Figure 2.6). Since VSV M-eGFP infected cells produce 10-fold less infectious virus but the genome to PFU ratio is only 4-fold higher, this suggests that 2.5-fold fewer particles are assembled. Given the close proximity of the eGFP insertion, residue 38, to the sequences that are important for N-binding, resides 1-15 (65), and M-oligomerization, 1-48 (60), M-eGFP could be less capable of mediating assembly, which would be consistent with the observed decrease. While this is a possibility, defects in M-eGFP unrelated to assembly could also indirectly cause the decrease in yield.

While VSV containing only an M or P fusion grows equally well at multiple temperatures, VSV P-eGFP M-mCherry grows better at lower temperatures (Figure 2.4). This suggests that the M and P fusions are temperature sensitive and that combining them into a single virus leads to a more dramatic phenotype. The fluorescent protein fusion may generate a temperature sensitive phenotype through an effect on protein stability or folding. The additional protein domain may inhibit efficient folding and lead to misfolding of the fusion protein at higher temperatures. Alternatively, the fusions could be attenuating a protein interaction. The N-terminus of P, where eGFP is fused (145), interacts with L (35), and the fluorescent proteins are inserted into the

disordered domain of M, which mediates a number of interactions (Table 1.2). The fusion could be inhibiting a protein interaction that is stabilized at lower temperatures.

VSV particles contain a variable amount of M and P which do not alter overall virion shape

VSV virions are highly-ordered structures with a characteristic bullet-shape, suggesting the formation of an ordered structure inside the particle. By comparing the amount of M versus M-eGFP in particles and using the measurement of 1826 molecules of M per particle on average (99), we determined that VSV M-eGFP particles contains 800 ± 30 molecules of M-eGFP on average (Figure 2.7). This number of M-eGFP monomers is insufficient to fill the ~1200 positions in the M helix (1), which suggests that assembly of the bullet-shape tolerates some flexibility in the content of the M helix. Alternatively, while the reconstruction suggests that all ~1200 positions are occupied, since it is an average this may not be true for individual virions. Single particles may normally contain only a partially filled helix, and this is how the number of M-eGFP molecules per particle can maintain the bullet-shape. The absolute amount of M per particle may not be relevant for the formation of this structure; only a small amount of M may be necessary for triggering this arrangement.

We have found that VSV with a range in the number of M molecules maintains the bullet structure. The variation in the amount of M-eGFP molecules per virion could be due to a variation in the number of M-eGFP molecules in the helix, core, or both. If the helix is not completely occupied in virions containing the average amount of M, then particles that contain more M than average could insert M into these empty positions. The core did not appear in the cryoEM reconstruction (1), and this absence suggests that the core is unstructured, which could

accommodate a variable amount of M. Our data suggests that VSV assembles through a flexible mechanism that incorporates varying numbers of M molecules per particle but still generates structurally similar particles. This suggests that M is not the driving force for creation of the bullet-shape. Since N-RNA alone can adopt a similar structure (92), perhaps only a small amount of M is required to trigger the formation of the bullet-shape.

While infectious particles must contain the viral RNP, the amount of the viral proteins incorporated per particle is not known. We have demonstrated that a variable amount of P is packaged into particles, which suggests a variable binding of P to the viral RNP. While a fixed amount of N may be incorporated into particles due to its coating of the fixed length genomic RNA with regular spacing (38), the packaging of P and L may be dependent on the tethering of L to P and P to N (35). Since they form a non-covalent complex (35, 47), the proteins are in a binding equilibrium and thus a variable amount of protein is associated with the viral RNP at any given moment. In addition, the ratio of L:P in virions is 1:9.3 (99) but only 1:2 *in vitro* in the active polymerase complex (47). This suggests that some P in the virion is not involved in bridging L to N. While this free P may be bound to the N-RNA as well, it could also be in the central core and not be interacting with its binding partners. A variable amount of this free P in the core would account for the observed inconsistent packaging.

M and P are not co-packaged

We observed that the amounts of M and P in particles are not correlated, revealing that their packaging is not dependent on each other. Specifically, this demonstrates that particles that contain more M do not contain less P and *vice versa*. This suggests that either a constant amount of protein is not incorporated into particles or packaging of other proteins, viral or cellular,

maintains a constant total mass of virions. The total mass of single VSV particles was measured and found to be a distribution, but whether this is due to microscope acquisition variations or a true variation in the content of virions was not addressed (99). P and some M are not localized in the cryoEM, and a portion of these proteins may be incorporated into the amorphous central "cigar" (1). Proteins could be incorporated into this unstructured core through nonspecific packaging, leading to the observed variable and uncorrelated amounts of M and P.

Limitations of studying particle composition with fluorescent fusions

The quantification of the protein composition of single virions was performed with fluorescent fusions. This method assumes that every fluorophore emits the same amount of signal. There is evidence that single eGFP molecules emit a normal distribution of fluorescence (155). However, given the large number of eGFP molecules, 800 ± 30, the standard error of the mean becomes negligible. Variations in fluorescence could also be caused by self-quenching due to the high density of proteins inside virions. Although, fluorescent proteins have not been found to exhibit this characteristic (156). A caveat of using fusions is that they may not function identically to the wild type protein. VSV clones containing exclusively the fluorescent variant, VSV P-eGFP and VSV M-eGFP, are attenuated in yield and have a higher genome to PFU ratio, demonstrating a partial dysfunction of the fusion protein. This dysfunction may lead to the observed variation in the amount of protein packaged per particle, and it is possible that wild type VSV does not incorporate variable amounts of viral proteins. Nevertheless, these studies demonstrate that VSV particles are at least able to tolerate variations in the number of molecules per particle and still maintain the overall bullet-shape.

Materials and Methods

Generation and selection of M-eGFP library.

The VSV M coding sequence was mutagenized using a Mutation Generation System F-701 (Finnzymes; Vantaa, Finland) according to the manufacturer. The transposon was replaced with eGFP *via* the NotI sites, and the M-eGFP library was cloned into a VSV genomic analog comprising 3' Leader-M-G-Trailer 5'. Infectious particles were recovered from this genomic analog as previously described (9).

Cells and viruses.

Vero, BS-C-1 (CCL-26; American Type Culture Collection; Manassas, VA) and BsrT7 (a kind gift from Conzelmann KK (157)) cells were grown at 37°C with 5% CO_2. Cells were infected in Dulbecco's modified Eagle's medium (DMEM) (Invitrogen, Life Technologies Corporation; Carlsbad, CA), but maintained in DMEM supplemented with 10% fetal bovine serum (FBS) (Tissue Culture Biologicals; Tulare, CA). Plaque assays were performed by overlaying infected Vero cells with 0.25% (w/v) agarose 10% (v/v) FBS DMEM. They were fixed in 3.75% formaldehyde in phosphate buffered saline (PBS) and stained with 0.5% crystal violet (w/v) 10% ethanol (v/v) in water. Recombinant VSV was generated using the infectious clone pVSV1(+) (9).

VSV single-step growth kinetics and temperature sensitivity

Growth curves were determined by infecting BsrT7 cells at MOI 3 in serum-free DMEM for 1 h at 37°C with 5% CO_2. Cells were then washed 3× with PBS and recovered in 2% (v/v) FBS DMEM at 37°C with 5% CO_2. A 20 μL aliquot of the supernatant was taken at the specified

time points. The samples were titred simultaneously on Vero cells as described above. To test for temperature sensitivity, BsrT7 cells were inoculated as described above, and then recovered at 31°C, 34°C, or 37°C with 5% CO_2.

PAGE for western blot, Coomassie, and radioactive samples

VSV was purified *via* a 15-45% sucrose gradient as previously described (158), and virion composition was analyzed by low-bis SDS PAGE, 10% (w/v) acrylamide 0.13% (w/v) bis-acrylamide. Protein was visualized by 70 μg/ml pH 1.5 Brilliant Blue G Coomassie (Sigma; St. Louis, MO) or western blot with monoclonal anti-VSV M 23H12 (a kind gift from Lyles DS (159)), anti-mouse horseradish peroxidase (Sigma), and BioMax MR film (Kodak; Rochester, NY). Radioactive protein was visualized with a storage phosphor screen (Amersham Biosciences, General Electric (GE) Healthcare; Piscataway, NJ) and Typhoon 9400 Variable Mode Imager using control software Typhoon Scanner Control v4.0 build 4.0.0301.2100 (Amersham). Quantification was performed with ImageQuant TL v7 (GE Healthcare).

Measurement of genome to PFU ratio

Wild type VSV and VSV M-eGFP were gradient purified as described above (158). Genomic RNA was extracted from virions with QIAamp Viral RNA kit (Qiagen; Venlo, Netherlands). Quantitative PCR was performed with the SYBR ® Select Master Mix and Prism 7300 sequence detection system (Applied Biosystems Life Technologies; Grand Island, NY). Equal volumes of RNA were loaded in duplicate, and relative numbers were determined from a standard curve. No RNA wells were used as negative controls. The relative genome to PFU ratio of VSV M-eGFP to wild type was calculated by:

$$\frac{\frac{\text{Genome [M - eGFP]}}{\text{PFU [M - eGFP]}}}{\frac{\text{Genome [wt]}}{\text{PFU [wt]}}} = \frac{\frac{\text{RNA [M - eGFP]}}{\text{Titre [M - eGFP]}}}{\frac{\text{RNA [wt]}}{\text{Titre [wt]}}}$$

$$= \frac{\frac{\text{RNA [M - eGFP]}}{\text{RNA [wt]}}}{\frac{\text{Titre [M - eGFP]}}{\text{Titre [wt]}}}$$

Immunofluorescence

BS-C-1 cells were seeded on #1.5 Micro-cover glass (Electron Microscopy Sciences; Hatfield, PA), infected at MOI 3, fixed in 2% paraformaldehyde in PBS at 8 hpi, permeabilized with 0.2% Triton X-100, and blocked with 1% bovine serum albumin (w/v) in PBS. They were stained with 2 μM 4',6-diamidino-2-phenylindole (DAPI), anti-M 23H12 (159), anti-GFP (Abcam; Cambridge, MA), anti-mouse (Molecular Probes Life Technologies; Grand Island, NY), and anti-rabbit (Molecular Probes) and mounted on Micro slides (VWR; Radnor, PA) with ProLong Gold (Invitrogen).

Samples were placed in a computer controlled Piezo 'Z' PZ-2000 and linear encoded X&Y Stage MS-2000 (Applied Scientific Instrumentation; Eugene, OR) and imaged with a Marianas system (Intelligent Imaging Innovations (3i); Denver, CO) with a Zeiss Axio-Observer (Carl Zeiss AG; Oberkochen, Germany) and control software SlideBook v5.0 (3i). A LASER Launch light source (3i) with a 405 nm, 488 nm, 561 nm, and 640 nm laser and the Semrock CF HQE filter sets (Chroma Technology Corp; Rockingham, VT) Ex 405/3 Em 452/45, Ex 488/3 Em 525/50, Ex 561/3 Em 607/36, and Ex 640/3 Em 680 long-pass were used for DAPI, eGFP, AF594, and AF647, respectively. The system is equipped with a Plan-Apo 63× Oil objective NA

1.40 with additional 1.2× magnification lens for 0.212 μm/pixel (Carl Zeiss AG), Spherical Abberation Correction (3i), Model CSU-X1 spinning disk unit (Yokogawa Electric Corporation; Tokyo, Japan), and QuantEM: 512SC electron multiplication camera (Photometrics; Tucson, AZ).

Incorporation kinetics of M into released particles

Kinetics of incorporation were determined as previously described (15). Briefly, BsrT7 cells were infected at MOI 10, starved of methionine and cysteine 5 hpi, and labelled for 2.5 min with 150 μCi ^{35}S/mL 6 hpi. The supernatant was harvested 0, 10, 20, 30, 40, and 60 min post-label, and cell debris was removed by microcentrifugation of 16 000 ×g for 1 min at 4°C. Virions were isolated by ultracentrifugation at 100 000 ×g for 1 h at 4°C. The pellet was resuspended in SDS sample buffer and analyzed by SDS PAGE and autoradiography.

TEM analysis of particle dimensions

Purified virus (158) was adhered to glow discharged formvar and carbon coated copper grids. Samples were stained with 2% phosphotungstic acid (w/v) pH 7.5 in H_2O and imaged with a Tecnai G^2 Spirit BioTWIN TEM (FEI; Hillsboro, OR) with AMT 2k CCD camera (Advanced Microscopy Techniques Corp.; Woburn, MA). Particle dimensions were measured in ImageJ (U.S. National Institutes of Health; Bethesda, Maryland; http://rsb.info.nih.gov/ij/). Statistical Student's t-tests were performed with R (The R Foundation for Statistical Computing; Vienna, Austria; http://www.r-project.org/).

Quantification of virion fluorescent intensities

BsrT7 cells were infected with the specified viruses at MOI 3 in serum-free DMEM for 1 h at 37°C with 5% CO_2. Cells were then washed 10× with PBS and recovered in 2% (v/v) FBS DMEM at 37°C with 5% CO_2. Supernatant was harvested 2 dpi and gradient purified as described above (158).

Purified virus was placed between 2 #1.5 Micro-cover glasses loaded into an Attofluor Cell Chamber (Invitrogen) and used in a modified heated stage insert (20/20 Technology; Wilmington, NC) in a computer controlled Piezo 'Z' PZ-2000, X&Y Stage MS-2000 (Applied Scientific Instrumentation). The Marianas system (3i) with a Zeiss 200M (Carl Zeiss AG) and control software SlideBook v5.0 (3i) was used to acquire images. A LASER Launch light source (3i) used a 491 nm and 561 nm laser with Semrock CF HQE filter sets (Chroma Technology Corp) Ex 491/3 Em 525/50 and Ex 561/3 Em 620/60 to image eGFP and mCherry, respectively. The system is equipped with a Plan-Apo 63× Oil objective NA 1.40 with additional 1.5× magnification lens for 0.169 μm/pixel (Carl Zeiss AG), Model CSU-22 spinning disk unit (Yokogawa Electric Corporation), and QuantEM: 512SC electron multiplication camera (Photometrics). Z-stacks 7 μm tall with 0.1 μm spacing were acquired and averaged to compensate for slanted samples. Single particle intensities were measured with a custom MATLAB (MathWorks, Natick, MA) script (Innovative Microscopy Applications for Biology (IMAB (160)) and normalized to the peak of the histogram. To control for fluorophore and microscope noise, data sets were determined by imaging the same field of view twice, and for each particle calculating the ratio of the intensity between the images. Statistical Kolmogorov-Smirnov tests were performed with R (The R Foundation for Statistical Computing).

Chapter 3

Detection of VSV assembly events with viral fluorescent fusion proteins

Abstract

The vesicular stomatitis virus (VSV) virion components are transported independently to the plasma membrane for assembly. The matrix protein (M) is synthesized as a soluble protein but is found in the cytosol and bound to membranes, the viral ribonucleoprotein (RNP) assembles in the cytoplasm, and the glycoprotein (G) is transported through the secretory pathway to the plasma membrane. While the transport has been characterized, it has not been possible to define the order and kinetics of their incorporation into assembling particles. Using a combination of viruses that contain fluorescently tagged M, the viral RNP core component phosphoprotein (P), and G, we set out to image the egress of virions. Assembling VSV virions are expected to show a rapid accumulation of M followed by a sharp increase in speed, and events that meet these criteria were identified in infected cells. To test the identity of the M-eGFP puncta as VSV virions, mutations in the late domains of M were used to induce the accumulation of virions at the plasma membrane. While the build up of particles could be verified by electron microscopy, fluorescent puncta did not accumulate significantly. Using fluorescence recovery after photobleaching (FRAP), we similarly observe a small number of M-eGFP puncta that appear to be released. To identify assembling particles, diffraction limited puncta were screened for colocalization of M, P, and G. However, few puncta display colocalization or an accumulation of protein over time. Alternatively, condensed nucleocapsid-matrix protein (NCM) complexes were screened for by looking for protein-protein interactions with förster resonance energy transfer (FRET). Assembly of M into particles was found to occur in 18 ± 2 s, n = 11, and the process from initiation to fission requires 127 ± 29 s, n = 5. M and P may be packaged concurrently with M initiating first, n = 2. The relatively small number of VSV assembly events limits this approach and tempers our conclusions.

Introduction

As an enveloped non-segmented negative-strand RNA virus, vesicular stomatitis virus (VSV) particles must contain the machinery for a number of functions in order to be infectious. The virions must contain the viral ribonucleoprotein (RNP) to perform viral transcription and genome replication and the glycoprotein (G) to mediate membrane fusion. In addition, the particles contain the matrix protein (M), which drives assembly and particle formation. Each of these components are synthesized and transported to the plasma membrane for assembly through independent pathways (15). The viral RNP proteins are synthesized in the cytosol as soluble proteins but rapidly assemble with RNA into the RNP complex. In infected cells, they will form large cytoplasmic inclusions (56) and only associate with the plasma membrane shortly before assembly (15). G is a transmembrane protein that is cotranslationally inserted into the rough endoplasmic reticulum (RER) and must be transported through the Golgi apparatus before reaching the plasma membrane (15, 27). M is translated as a soluble cytoplasmic protein, but a portion of the population will bind to membranes and lead to a ubiquitous distribution in the cell (15, 161, 162). While the viral components have distinct subcellular distributions, they must come together during assembly.

How the viral components are incorporated into assembling particles is unclear. Prior to initiating assembly, the viral RNP is in the cytoplasm and G and M are at the plasma membrane, where assembly occurs. G and M both form microdomains at the membrane, although they do not colocalize (34, 64). In fixed infected cells, the viral RNP was found to colocalize with G but not M microdomains (64). While it is unknown if the association of the viral RNP with G leads to productive assembly, it suggests that assembly is initiated by the recruitment of the viral RNP to the membrane by G. This is consistent with the ability of G to enhance the budding efficiency

of VSV (89, 90). However, the generation of ΔG virions demonstrates that G is not essential for assembly (90, 91). These data suggest a model where G facilitates assembly through nonessential interactions with the internal components. Subsequent to the localization of the viral RNP to the membrane, M is recruited to mediate condensation of the viral RNP into the nucleocapsid-matrix protein (NCM) complex (16) that will bud through the membrane. While fixed cell studies have built a model for assembly, live cell studies would permit the confirmation that these interactions lead to productive assembly and particle release and would allow for the examination of which viral and cellular interactions are required for each step of assembly.

Fluorescence microscopy is compatible with live cells and has been used to study assembly of the retrovirus human immunodeficiency virus type 1 (HIV-1) (138, 139). The essential components of HIV-1 virions have similar functions to the VSV components. In addition to the genome, particles must contain the envelope glycoprotein (Env) to mediate membrane fusion and the group-specific antigen protein (Gag) to drive assembly. Live imaging of Gag assembly reveals 3 stages in this process (139). Gag is rapidly incorporated into particles, which is followed by a pause before the particle is finally released into the supernatant. Live imaging also allows for the determination of the order the proteins are packaged in and viral protein domains required for incorporation (140, 141).

This methodology can be applied to study VSV assembly if the viral components can be fluorescently tagged. The viral RNP contains multiple proteins, and functional fusions have been generated to the phosphoprotein (P) (57, 145) and large polymerase protein (L) (146). The ability of P to bridge L to the nucleocapsid protein (N) coated RNA (35) permits the tracking of the genome with either of these fluorescent fusions. A G fusion (147) permits the evaluation of which step in assembly G mediates and why this role is not essential. We have described the

generation and characterization of a fluorescent fusion to M (Chapter 2) to allow the tracking of condensation and assembly. Simultaneously tracking the VSV components in live cells will allow for the determination of how assembly is initiated and the proteins are recruited.

Here, we report our endeavour to verify single particle assembly events in infected cells. Identification of assembling particles through genetic mutation and colocalization suggests that the majority of fluorescent viral protein is not actively involved in assembly, although sites of VSV condensation were implicated. Putative assembly events could be identified, but the low number of total observed events mean that a thorough investigation of VSV assembly has proven challenging.

Results

Live-cell imaging of VSV M-eGFP assembly

BS-C-1 cells were infected with VSV M-eGFP and imaged by total internal reflection fluorescence (TIRF) microscopy. Fluorescent events meeting the criteria for an assembling particle as describe for HIV-1 (139), *i.e.* increase in fluorescent intensity followed by a sharp increase in speed, were quantified (Figure 3.1). When compared to HIV-1, VSV appears to have an additional step in assembly (Figure 3.2). M forms a puncta of stable low intensity for 60 ± 18 s, n = 5, before initiating rapid incorporation of M over 18 ± 2 s, n = 11. Few events could be identified in cells 6-9 hpi, and the majority of puncta at the plasma membrane did not display a gradual increase in intensity. Instead, they would either "blink" or remain static in both position and fluorescent intensity.

After the observation of putative assembling VSV particles, HIV-1 was used as a control to confirm the capability to measure assembly events. The biogenesis of HIV-1 virus-like particles (VLPs) was performed as previously published (138). HeLa cells were transfected with Gag:Gag-eGFP at a ratio of 5:1, and VLPs were found to assemble rapidly in 9 ± 1 min (Figure 3.3), consistent with the published average of 8.5 min (138). The ability to reproduce the assembly kinetics of HIV-1 VLPs suggests that the VSV events represent assembling particles.

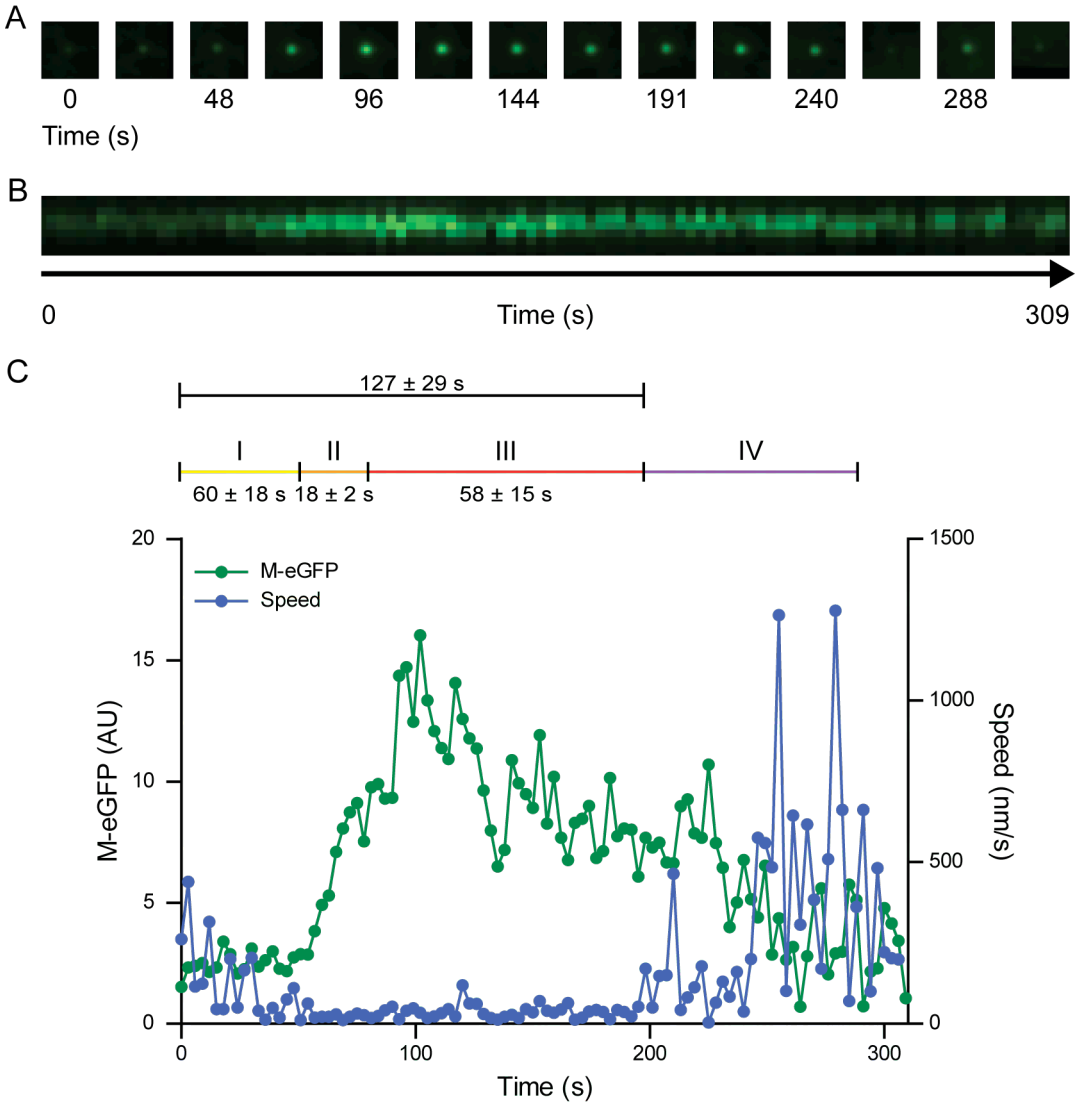

Figure 3.1. Live single particle VSV M-eGFP assembly events.
BS-C-1 cells were infected at MOI 3 with VSV M-eGFP and imaged with TIRF microscopy 9 hpi. Images were taken every 3 s for 15 min. A tile view (A), kymograph (B), and intensity and speed trace (C) of an assembling VSV particle are shown. The eGFP intensity is in arbitrary units. The average time ± SEM of each stage are stated above (n = 5 for stage I and total time and n = 11 for Stage II and III).

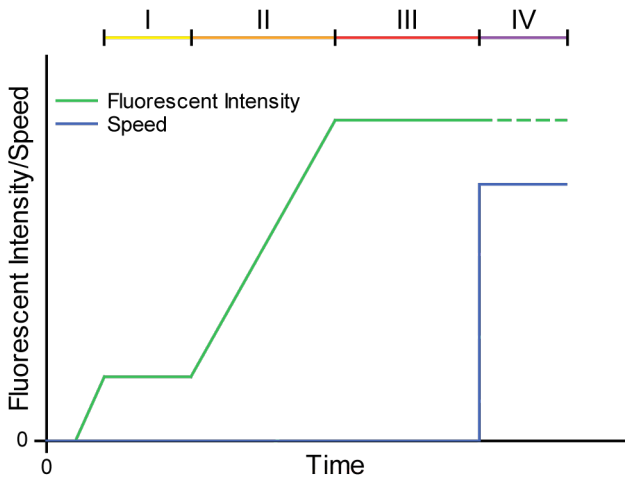

Figure 3.2. Theoretical profile of VSV assembly events.
Theoretical M intensity and speed trace for an assembling VSV particle. Assembly proceeds through 4 stages: I) assembly initiates with the formation of an M preassembly complex, II) M is rapidly incorporated into the particle, III) delay before fission occurs, and IV) after fission, the particle diffuses freely in the supernatant and the intensity will vary as the particle moves in and out of the TIRF evanescent wave, denoted by a dashed line.

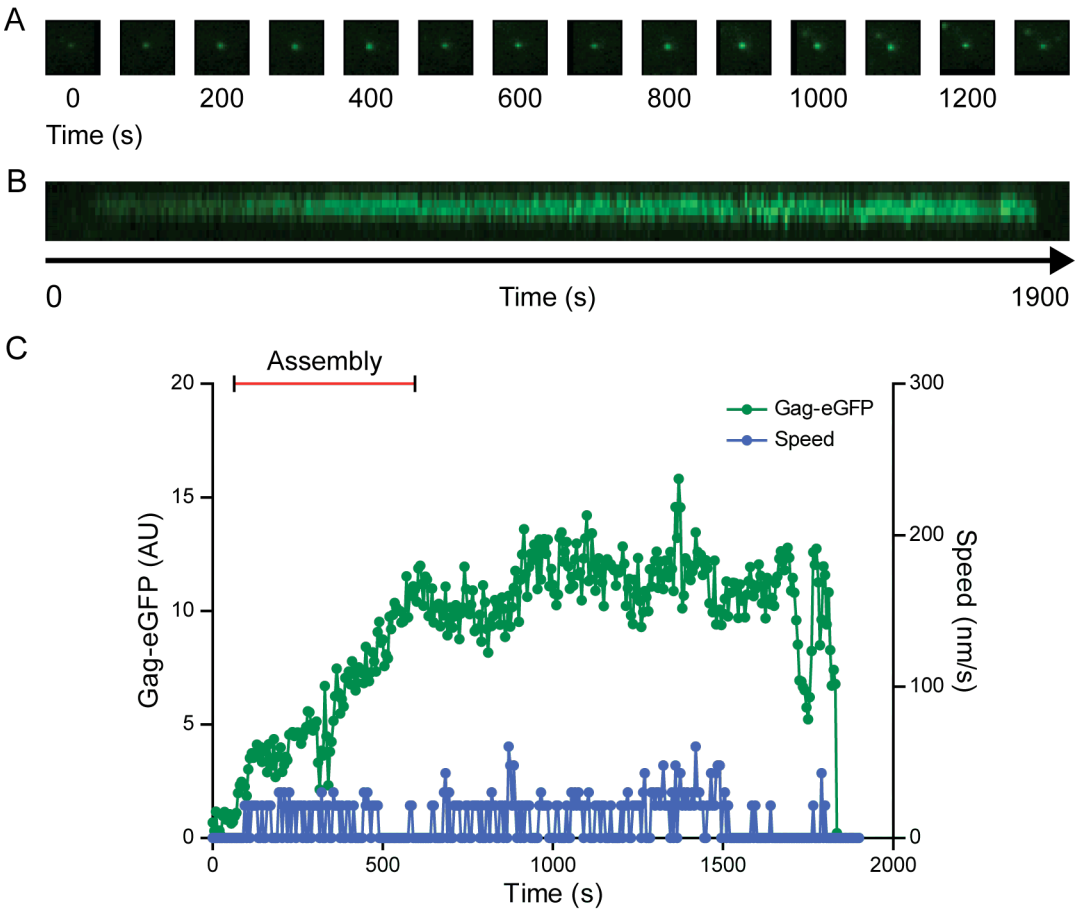

Figure 3.3. Live single particle HIV-1 VLP assembly event.
HeLa cells were transfected with Gag:Gag-eGFP at a ratio of 5:1 and imaged with a TIRF microscope 7 hpt. Images were taken every 5 s for 1 h. A tile view (A), kymograph (B), and intensity and speed traces (C) of an assembling HIV-1 VLP are shown. The eGFP intensity is in arbitrary units.

Since HIV-1 Gag-eGFP must be coexpressed with wild type Gag in order for VLPs to form properly (136), we tested whether coexpressing M-eGFP and wild type M in cells would enhance assembly. Cells were coinfected with VSV M-eGFP and wild type VSV. An MOI of 1 was used for VSV M-eGFP, but the MOI for wild type VSV varied from 1 to 10. At 6-9 hpi, the cells looked similar, in terms of eGFP intensity and cell morphology, regardless of the wild type VSV MOI. Fluorescent puncta could be identified that demonstrated a gradual increase in intensity and then plateau (Figure 3.4). However, there was no rapid movement after the plateau, suggesting a lack of fission.

The rate of virus production increases over the course of infection, but the cells will eventually retract and detach from the glass. Live-cell imaging, particularly TIRF microscopy, requires that the cells are well adhered to the glass surface. This cytopathic effect (CPE) can be partially alleviated by an M51R mutation in M (71), which prevents the association of M with mRNA export factor 1 (Rae1) and subsequent shutoff of host transcription (72) and messenger RNP export from the nucleus (73). We therefore generated a VSV M-eGFP M51R mutant so that imaging could be performed later in infection when the maximum number of particles was being released. BS-C-1 cells were infected with this virus and imaged 9-12 hpi. However, M-eGFP puncta demonstrated the same blinking or static fluorescent intensity traces.

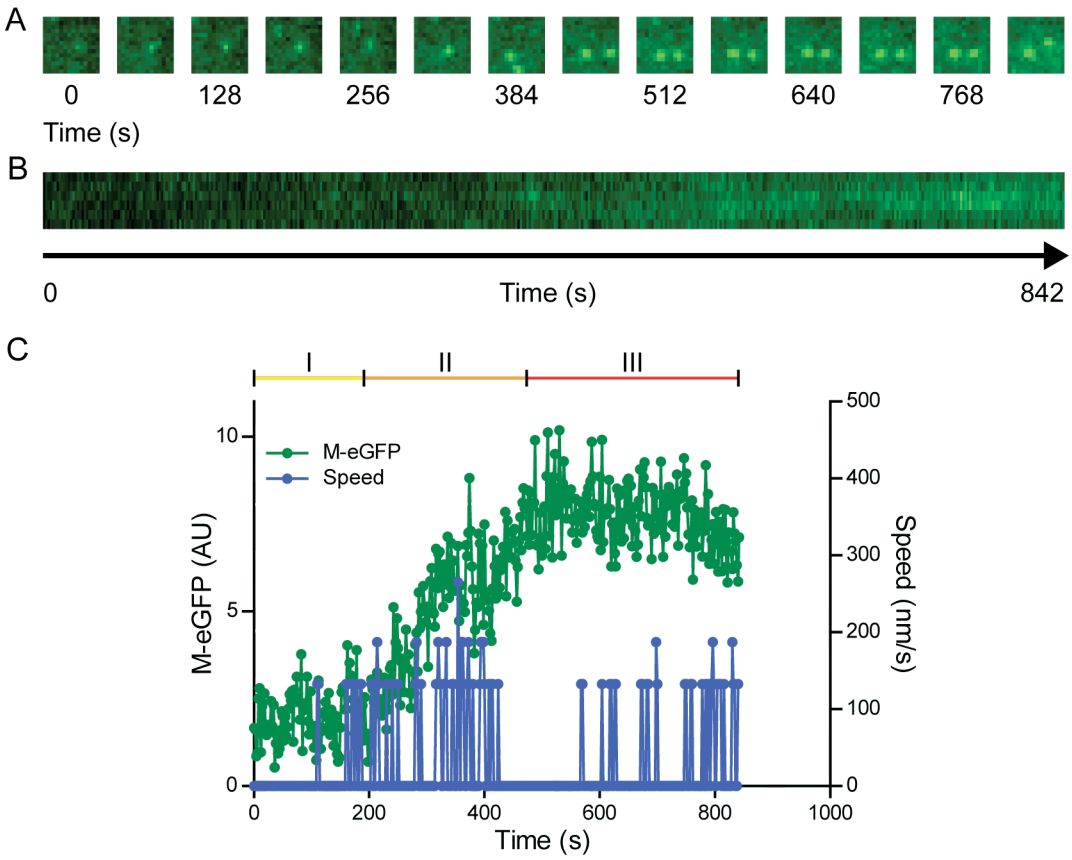

Figure 3.4. Live formation of M-eGFP puncta with wild type M.
BS-C-1 cells were infected at MOI 1 of each VSV M-eGFP and wild type VSV and imaged with a TIRF microscopy 6 hpi. Images were taken every 3 s for 15 min. A tile view (A), kymograph (B), and intensity and speed trace (C) of the formation of an M-eGFP puncta are shown. The eGFP intensity is in arbitrary units.

Fission of M-eGFP puncta from the plasma membrane

The final step in viral egress is fission from the cellular membrane, and consequently inhibition of this step results in the accumulation of particles at the cell surface. Fission can be inhibited by mutating the motifs in M, termed late domains, which mediated recruitment of the host endosomal sorting complexes required for transport (ESCRT) pathway that performs this function. Late domain mutations were introduced into M-eGFP, 24 PPPY 27 to AAPA (68) and 37 PSAP 40 to AAAA (69) (LD^-). Cells infected with VSV M-eGFP M51R LD^- display the expected accumulation of particles when imaged by ultra-thin cell section transmission electron microscopy (TEM) 12 hpi (Figure 3.5 A-B). However, live TIRF images of infected cells 9-12 hpi do not show an accumulation of fluorescent puncta at the plasma membrane (Figure 3.5 C-D). The ESCRT pathway can also be inhibited by a dominant negative (DN) vacuolar protein sorting 4 (Vps4), the final enzyme in this pathway that is recruited to the site of fission (143, 163). BS-C-1 cells were transfected with wild type Vps4A-mCherry or the DN variant (143) 24 h prior to infection with VSV M-eGFP. Vps4A-mCherry DN did not lead to an accumulation of M-eGFP puncta as the plasma membrane, and neither functional nor DN Vps4A-mCherry demonstrate colocalization with M-eGFP (Figure 3.5 E-F).

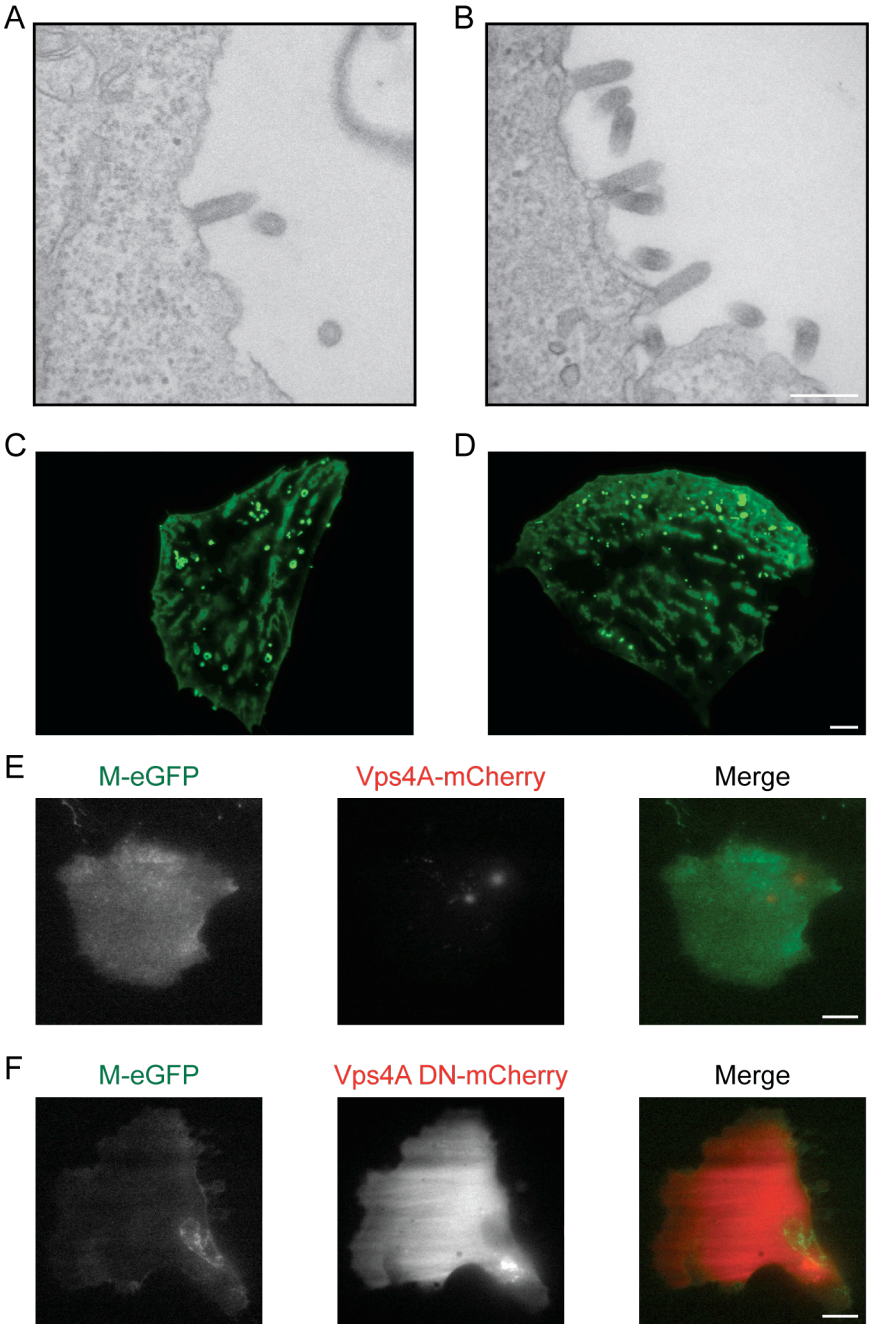

Figure 3.5. Inducing the accumulation of VSV M-eGFP particles at the plasma membrane. Ultra-thin cell section of BS-C-1 cells infected with VSV M-eGFP (A) and VSV M-eGFP LD$^-$ (B) 12 hpi. Scale bar represents 500 nm. TIRF images of BS-C-1 cells infected with VSV M-eGFP (C) and VSV M-eGFP LD$^-$ (D) 12 hpi. Scale bar represents 10 µm. TIRF images of BS-C-1 cells transfected with Vps4A-mCherry wt (E) or Vps4A-mCherry DN (F) 24 h prior to infection with VSV M-eGFP at 5 hpi. Scale bars represent 10 µm. Image pairs C-D and E-F were acquired under identical microscope settings and renormalized to the same values.

To determine if individual fluorescent puncta had undergone fission from the plasma membrane, we tested if the M-eGFP was still exchangeable with the cytoplasm. Fluorescence recovery after photobleaching (FRAP) can be used to determine if 2 volumes are continuous. BS-C-1 cells were infected with VSV M-eGFP and imaged 12-15 hpi. M-eGFP puncta were chosen for FRAP measurements (Figure 3.6). The bleaching efficiency varies between puncta, but they all demonstrate a large immobile fraction, *i.e.* bleached protein that is not replaced. Only some puncta display fluorescence recovery, suggesting that a population of puncta have undergone fission (Figure 3.6 C-D).

Colocalization of viral proteins in diffraction limited puncta

Infectious VSV particles must contain the viral RNP, M, and G, and thus productive assembly events could be screened for by identifying regions where these proteins colocalize. Since VSV virions are smaller than the diffraction limit of light microscopy, only the colocalization regions that are diffraction limited could be single VSV particles. A P-eGFP fusion has been previously described (145) and combined with an M fusion (Chapter 2). BS-C-1 cells were infected with VSV P-eGFP M-mCherry M51R and imaged by TIRF microscopy 9-12 hpi. Colocalization between M-mCherry and P-eGFP demonstrate that assembly of M initiates before P but that their recruitment occurs concurrently, n = 2 (Figure 3.7).

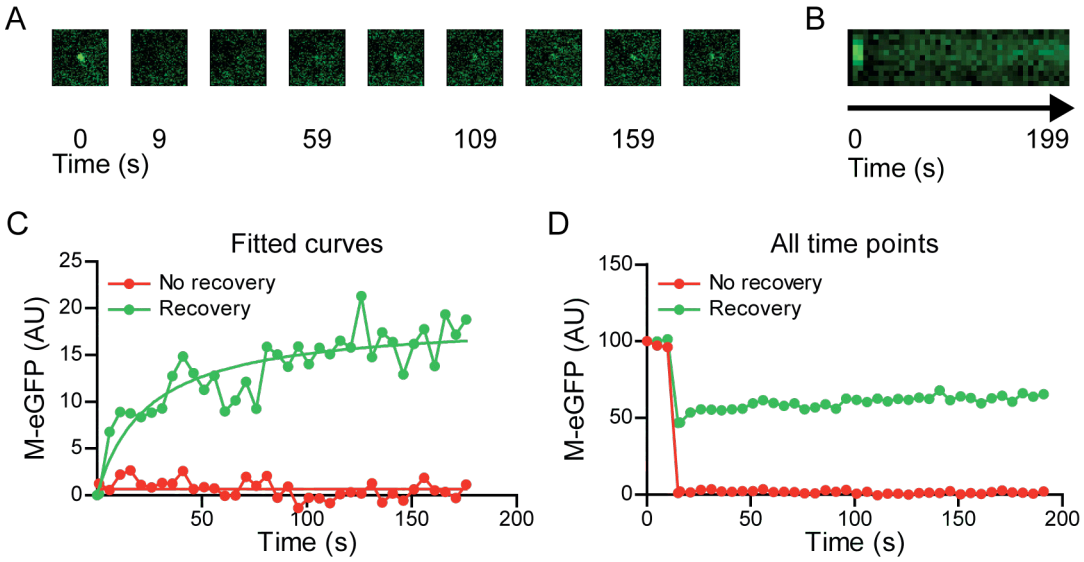

Figure 3.6. FRAP of M-eGFP puncta in cells.
BS-C-1 cells were infected with VSV M-eGFP and imaged with a FRAP confocal microscope 14 hpi. A tile view (A) and kymograph (B) of a punctum that demonstrates fluorescence recovery are shown. Intensity traces for the fitted curves (C) and all time points (D) of puncta that do and do not show fluorescence recovery are shown. The eGFP intensity is in arbitrary units.

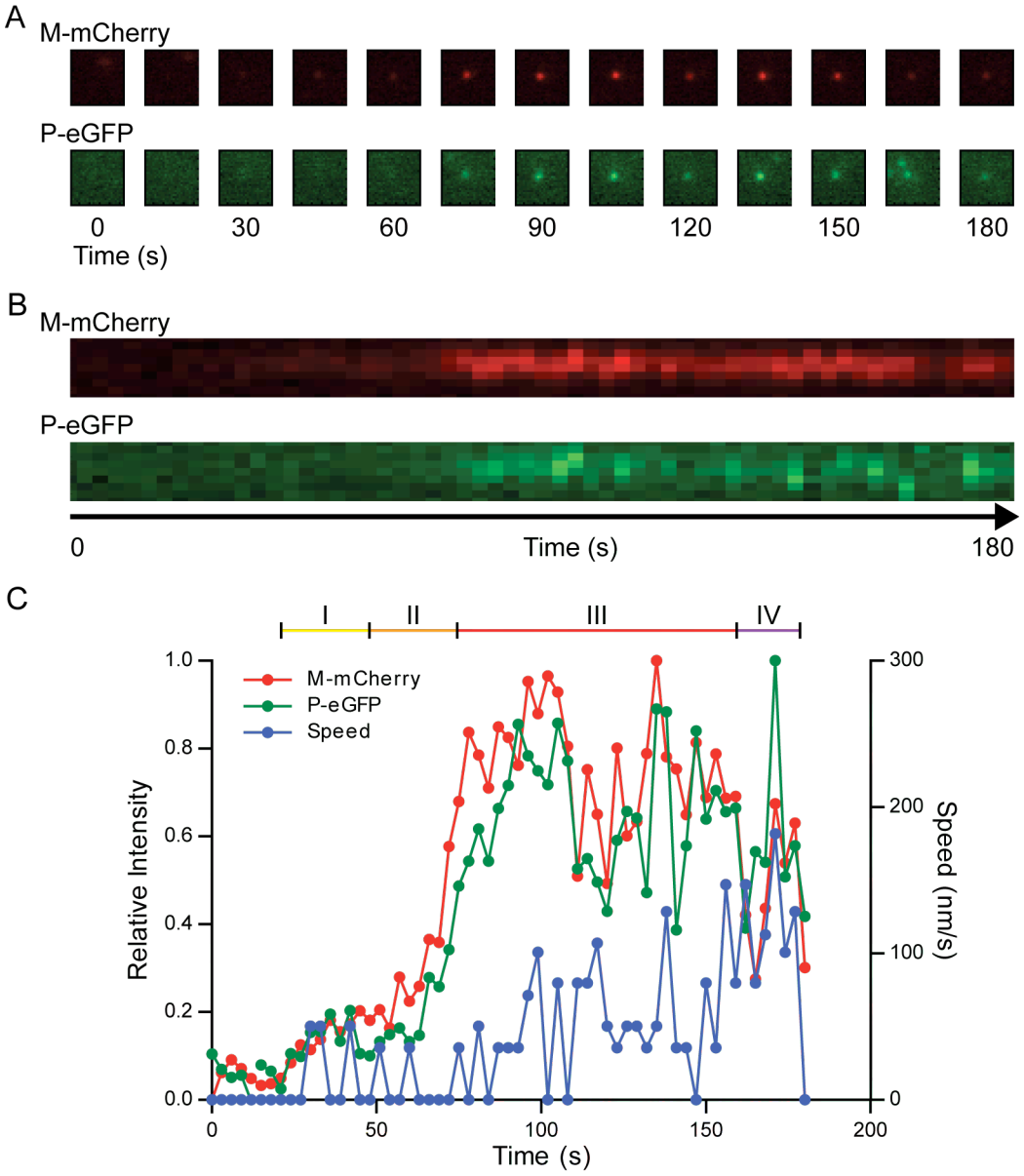

Figure 3.7. Live single particle VSV P-eGFP M-mCherry assembly event.
BS-C-1 cells were infected with VSV P-eGFP M-mCherry M51R and imaged with a TIRF microscopy 12 hpi. Images were taken every 3 s for 15 min. A tile view (A), kymograph (B), and intensity and speed trace (C) of an assembling VSV particle are shown. The eGFP and mCherry intensities are relative to their maximums (n = 2).

While a functional genetically unstable C-terminal fusion has been generated to G (147), we created a viable stable N-terminal fusion (Figure 3.8 A). The insertion was made after the signal peptide, and the crystal structures of G (164, 165) suggest that there is sufficient space between the monomers in the trimer to accommodate mCherry (166). In the pre-fusion (164) (Figure 3.8 B) and post-fusion (165) (Figure 3.8 C) structures, the N-terminus is near the periphery of G pointing towards the side of the trimer. VSV G-mCherry is replication competent and genetically-stable, but it is attenuated and grows better at lower temperatures (Figure 3.9 A). Incorporation of G-mCherry into particles can be demonstrated at the population (Figure 3.9 B) and single particle level (Figure 3.9 C). Quantification of the contents of VSV M-eGFP G-mCherry particles reveals that a variable amount of fluorescent M and G are incorporated into particles (Figure 3.9 D-E) (Chapter 2). Comparison of the M and G contents illustrates a positive correlation in the amounts packaged into single particles (Figure 3.9 F). Unlike the mCherry fusion, VSV G-eGFP is genetically unstable and the majority of eGFP is deleted from the genome by passage 3. Therefore, the fluorophore combination of M-eGFP with G-mCherry was chosen for further study. BS-C-1 cells were infected with VSV M-eGFP G-mCherry and imaged 6-9 hpi with a confocal (Figure 3.10 A) and TIRF (Figure 3.10 B) microscope. Colocalization was observed between M and G in both large structures and diffraction limited puncta. However, the puncta do not show changes in intensity over time.

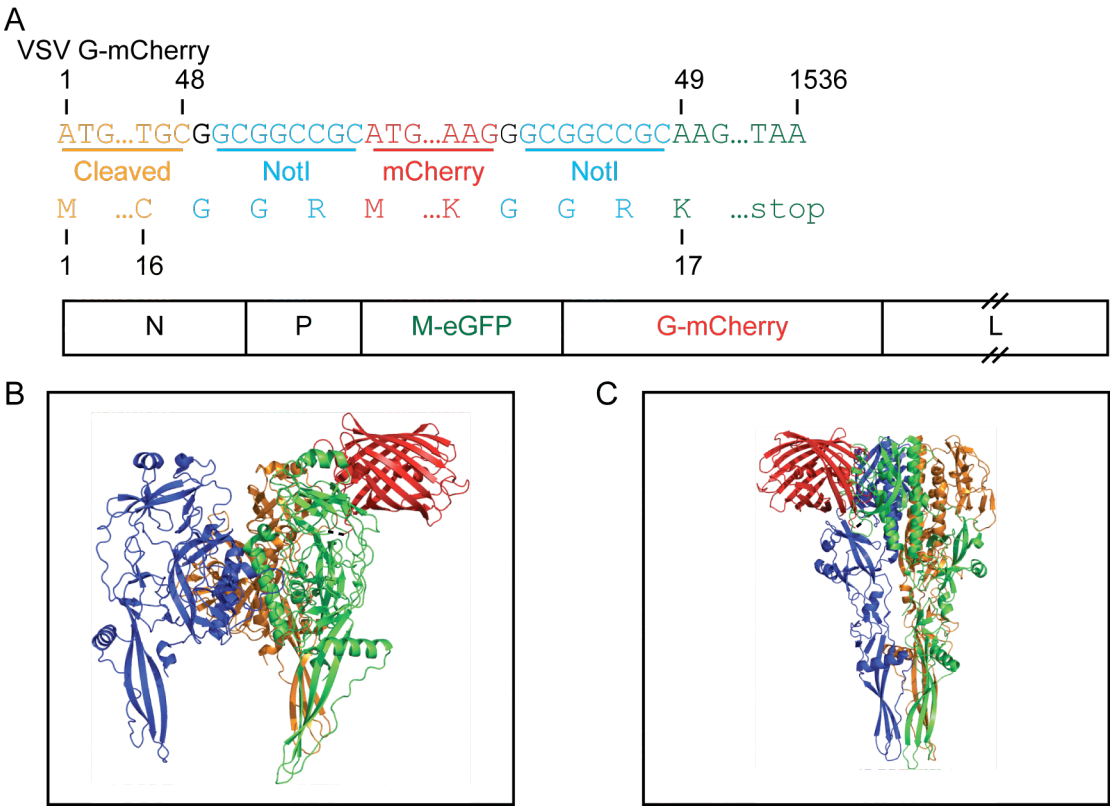

Figure 3.8. Generation of a viable and genetically-stable G-mCherry fusion protein.
(A) Schematic of the G-mCherry fusion and viral genome. The fluorescent protein is inserted after the signal peptide, residues 1-16 (167), to generate an N-terminal fusion to the mature G protein. The G fusion can be combined with and M fusion to generate a viable virus. The crystal structure for mCherry (166) in approximately the correct orientation relative to the pre-fusion (164) (B) and post-fusion (165) (C) G trimers.

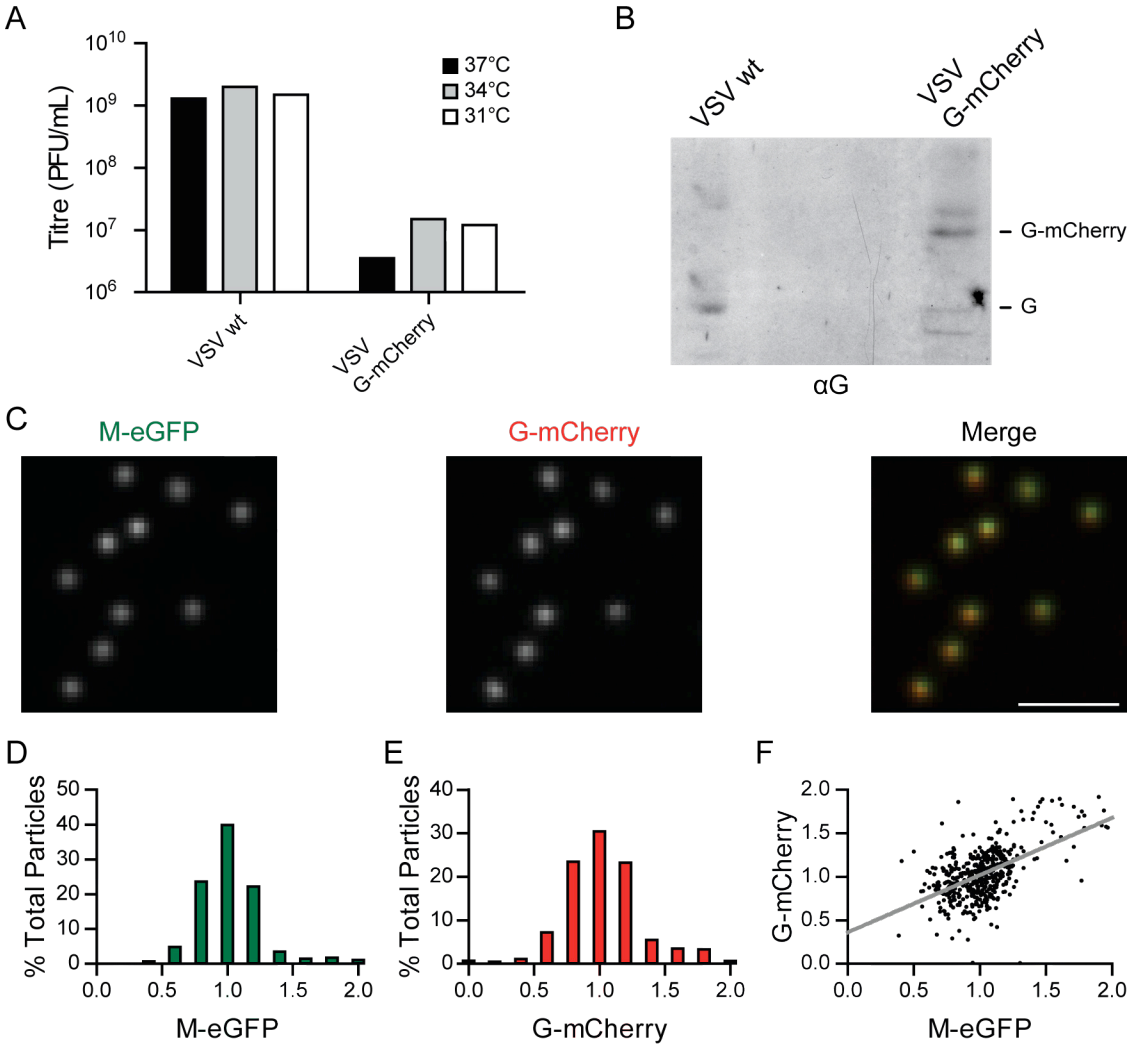

Figure 3.9. G-mCherry generates an attenuated virus but is incorporated into particles. (A) BsrT7 cells were infected at MOI 3 with wild type VSV or VSV G-mCherry. Cells were grown at 31°C, 34°C, or 37°C. At 1 dpi the supernatant was harvested and titred. (B) Purified viruses were analyzed on an SDS PAGE and followed by a western blot for G. (C) Gradient purified VSV M-eGFP G-mCherry was imaged with a fluorescent confocal microscope. The scale bar represents 5 µm. Quantification of the fluorescent intensities of particles (n = 456) was used to generate histograms of M-eGFP (D) and G-mCherry (E) intensities. The distributions of M-eGFP and G- mCherry are significantly different from their control datasets that measure the microscope acquisition error as described previously (Chapter 2) (Kolmogorov-Smirnov test p-value < 10^{-15} for both). (F) A scatter plot demonstrates a positive correlation between eGFP and mCherry intensities (Pearson's product-moment correlation r = 0.35, p-value < 10^{-12}). The line of best fit is shown in grey.

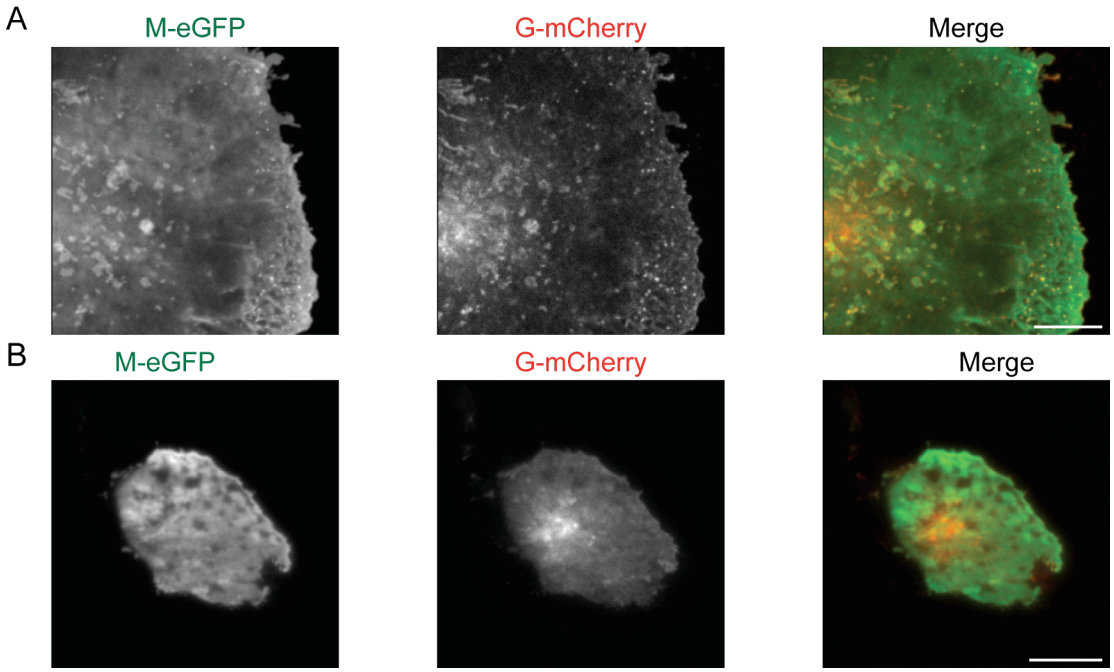

Figure 3.10. VSV M-eGFP G-mCherry infected cells.
Confocal (A) and TIRF (B) images of BS-C-1 cells infected with VSV M-eGFP G-mCherry 8 hpi. Scale bars represent 10 μm.

Fluorescent fusions to all 3 VSV components can be combined into a single virus that is replication competent and generates infectious particles, VSV P-eGFP M-mTagBFP G-mCherry (Figure 3.11 A). BS-C-1 cells infected with this virus were imaged 16-19 hpi with a confocal (Figure 3.11 B) and TIRF (Figure 3.11 C) microscope. At this later time point, the cells showed high expression of all 3 proteins. Colocalization was seen between M and G in structures larger than the diffraction limit, but P did not show colocalization with M or G.

Identification of condensed NCM complexes

During VSV assembly, the open viral RNP is condensed into the NCM complex. Since the mature particle is organized into a regular structure (1), the viral proteins in virions may be close enough to each other for förster resonance energy transfer (FRET) (138). We hypothesize that FRET could occur between adjacent M molecules or between M and P (Figure 3.12 A). BS-C-1 cells were coinfected at MOI 3 each for VSV M-eGFP and VSV M-mCherry (Figure 3.12 B) or VSV P-eGFP M-mCherry (Figure 3.12 C) and imaged 8 hpi. Ratiometric FRET was used to calculate FRET efficiencies and generate images displaying FRET efficiency on a per pixel basis. Diffraction limited puncta of high FRET efficiency could be identified, suggesting the presence of condensed individual NCM complexes.

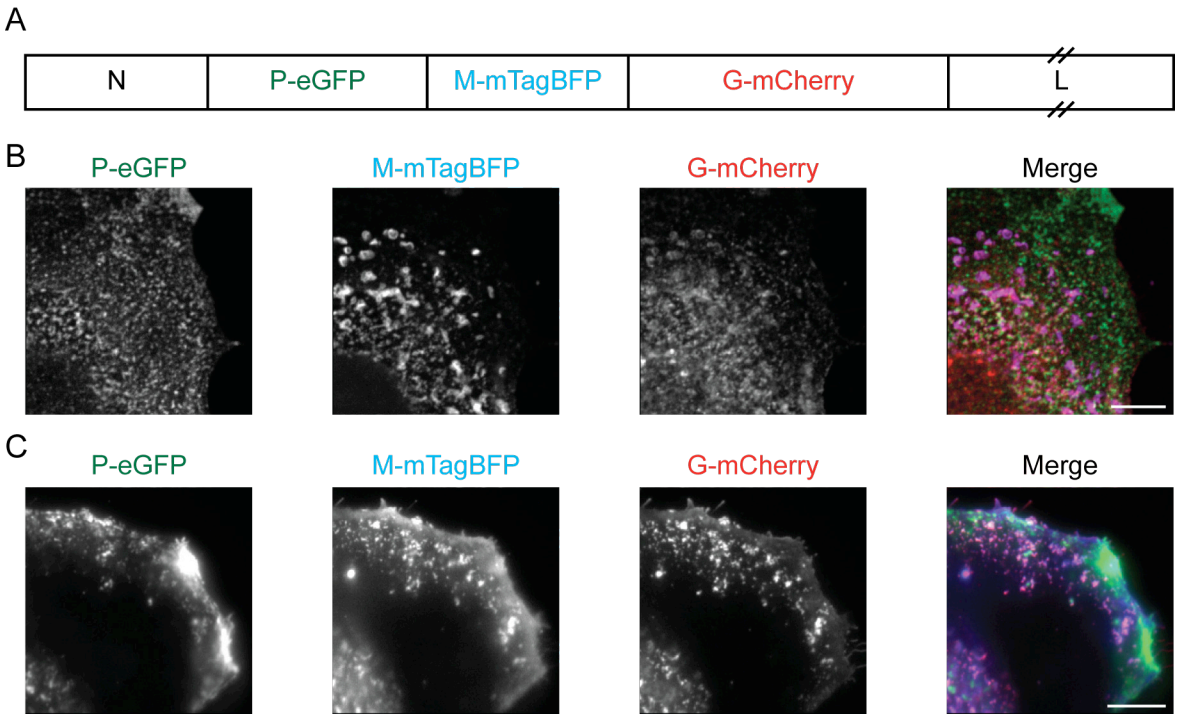

Figure 3.11. VSV P-eGFP M-mTagBFP G-mCherry infected cells.
(A) Schematic of VSV P-eGFP M-mTagBFP G-mCherry viral genome. Confocal (B) and TIRF (C) images of BS-C-1 cells infected with VSV P-eGFP M-mTagBFP G-mCherry 17 hpi. Scale bars represent 10 μm.

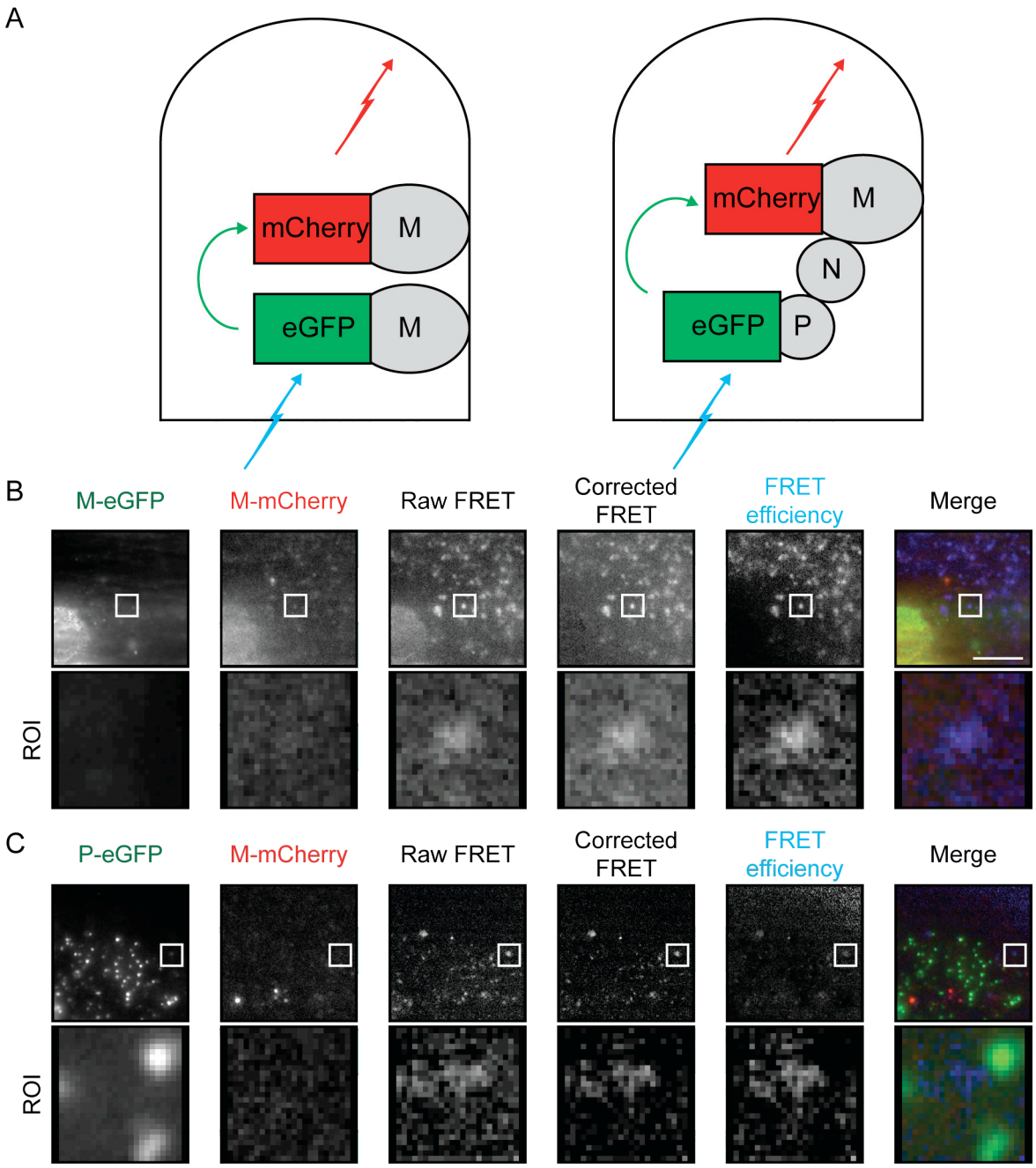

Figure 3.12. FRET efficiency between viral proteins in infected cells.
(A) Schematic of hypothesized FRET between adjacent M molecules or between adjacent M and P molecules. BS-C-1 cells were (B) coinfected at MOI 3 with VSV M-eGFP and VSV M-mCherry or (C) infected with VSV P-eGFP M-mCherry and imaged 8 hpi. The eGFP, mCherry, and Raw FRET images of infected BS-C-1 cells are shown along with Corrected FRET images, which are Raw FRET images after bleedthrough correction based on the eGFP and mCherry channels, and FRET efficiency images, which are the ratio of the Corrected FRET image to the eGFP channel. The merge image only shows M-eGFP or P-eGFP (green), M-mCherry (red), and FRET efficiency (blue). Regions of interest (ROI) displaying potential FRET sites are marked with a white box and are enlarged below. Scale bar represents 10 μm.

Discussion

Assembly of viral particles requires the coordinated recruitment of multiple proteins. The transport of the VSV components to the plasma membrane is known, but how they are incorporated into assembling particles is less clear. Through the generation of fluorescent protein fusions to viral proteins, we attempted to analyze the packaging of viral components in real time. While some events could be identified, they are rare, which is inconsistent with the viral yields. The enhancement of virus production was attempted by the coexpression of wild type M and imaging later in infection, and assembling particles were screened for by blocking fission and identifying colocalization of multiple viral proteins. However, only a small number of assembling virions were identified through these methods, demonstrating a difficulty in observing VSV assembly in real time.

Assembly kinetics of VSV in infected cells

Cells infected with VSV M-eGFP display events consistent with the criteria for assembling virions (Figure 3.2). M initiates assembly through the formation of a small structure (I). Subsequently, M assembles rapidly (II) and then there is a delay (III) before particle release into the supernatant (IV). The rapid assembly of M (II) likely represents condensation of the viral RNP and the recruitment of M to form the NCM complex. In this case, stage I could be the previously unidentified separate step in assembly that initiates high affinity binding of M to the genome (98). Since M oligomerization requires nucleation by an M complex (61), the small M structure formed during this stage could be the complex that induces oligomerization of M and condensation of the viral RNP into the NCM complex. The total assembly time measured for

single VSV particles, 127 ± 29 s, n = 5, is consistent with the bulk measurement, < 10 min (Chapter 2).

Comparison of the assembly kinetics of VSV and HIV-1 can deduce which stages of assembly are dependent on viral or common cellular functions. Stages I and II represent oligomerization of the viral protein, and consequently the kinetics are likely virus specific. As expected, stage II for HIV-1 was found to be 8.5 min (138) and 8-9 min (139), compared to 18 ± 2 s, n = 11, for VSV. Stage III represents the time required for recruitment of the cellular ESCRT machinery by viral late domains to mediate fission. Since these are cellular proteins, the time for this stage should depend on which late domain motif(s) the virus contains. HIV-1 Gag contains the P(S/T)AP (124) and $LYPX_nLXXLF$ where n = 1-3 (118) motifs. In contrast, VSV contains the PPXY (114) and P(S/T)AP (69) motifs. For HIV-1 VLPs, stage III requires a few minutes (143) while HIV-1 virions require 47 min (163). This is in sharp contrast to VSV, where stage III is 58 ± 15 s, n = 11, long. Given the differences in composition of these particles, perhaps the structure and content of the virion affects the recruitment and efficiency of the ESCRT pathway. Stage IV represents the time from when the virion is released from the cell to when it is no longer in the TIRF microscope field of view. Since this is not dependent on a biological function, it is expected to be inconsistent between events and viruses.

Wild type M and M-eGFP form a structure that does not undergo fission

Since HIV-1 Gag-eGFP is non-functional without wild type Gag, we tested if co-expressing M-eGFP with wild type M would generate more assembly events. While events showing the appearance, gradual accumulation, and plateau of M-eGFP signal could be identified, these puncta did not show the rapid movement indicative of release (Figure 3.4). The

assembly time for these structures, stage II, was significantly longer, ~300 s, than for VSV M-eGFP, 18 ± 2 s, n = 11. Since these events were numerous in the presence of wild type M, it suggests that they are a productive function of M and that appending eGFP to M decreases the number of assembly events. Perhaps M gradually forms structures at the plasma membrane, *e.g.* microdomains (64), that are not immediately incorporated into assembling particles.

Conclusions regarding observed VSV assembly events

The number of assembly events of VSV M-eGFP per cell is lower than predicted. Based on the burst size, 200 plaque forming unit (PFU) per cell, and genome to PFU ratio, 500 (168)(Chapter 2), of VSV M-eGFP, the average infected cell should produce 1×10^5 particles over the course of infection, and the growth curve of VSV M-eGFP (Chapter 2) predicts that between 6-19 hpi, the rate of particle release should be 200-4500 particles per h. In contrast, only a few events were observed per cell per hour even though ~½ of the plasma membrane is visible in the TIRF experiments, suggesting that imaging is missing the majority of events. An explanation is that the image acquisition rate of every 3 s is to slow. If M is rapidly incorporated into particles on a similar timescale, then the puncta in the time lapse movies would appear suddenly and not be scored as an assembling particle. Therefore, only the few slow events would be identified. Alternatively, the experiments may not have been performed over a long enough timescale. If assembly requires longer than the experiment, *i.e.* 15 min, then they would be missed. While the minimum time for VSV assembly is < 10 min (15), the assembly time is likely a distribution and the majority of events may take longer.

Single particle studies permit the analysis of how variable a process is and can be used to identify a minor population that is hidden in a bulk assay. The genome to PFU ratio of VSV M-

eGFP is 500 (168)(Chapter 2), therefore if the infectious nature of a particle is due to a step in assembly, it could only be identified through single particle analysis. However, discovery of this population would require the study of significantly more than 500 events to obtain replicates of the infectious particle. The low number of VSV assembly events observed, n = 11, implies that these are particles that will not lead to productive infection, which is a limitation of the conclusions from this study.

Identification of assembling particles

Since inhibiting fission of VSV did not result in the accumulation of fluorescent puncta at the plasma membrane, individual M-eGFP puncta were tested for whether they had undergone fission from the cell. FRAP was used to determine if the M-eGFP was exchangeable and thus continuous with the cytoplasm (Figure 3.6). Some puncta do not demonstrate fluorescence recovery, and since the M content of NCM complexes are exchangeable with the environment (98), this suggests that these puncta are not continuous with the cytoplasm and have undergone fission. These may be released particles that have remained stuck to the plasma membrane. A trivial explanation for the lack of fluorescence recovery is that the puncta are aggregates that do not exchange. On the contrary, large M-eGFP regions that are not diffraction limited demonstrate fluorescence recovery. While this does not completely rule out the possibility of an aggregate, it suggests that the M-eGFP structures remain exchangeable. The particles that demonstrate fluorescence recovery illustrate a large immobile fraction, which may reflect at least two different states of M in the particle, an exchangeable and non-exchangeable fraction. Perhaps this correlates with the location of some M in the central "cigar" (100) vs the surrounding helix (1), where 1 structure is immobile and the other is dynamic.

Colocalization between viral proteins was used to identify assembling particles. Incorporation of M and P into particles, n = 2, proposes that packaging of M is initiated before P, but that they are packaged concurrently (Figure 3.7). M and G colocalized in diffraction limited puncta, but did not appear to be actively assembling during the experiments. They may represent the previously described microdomains (34, 64). M and G also colocalized in large fluorescent bodies (Figure 3.10, Figure 3.11). Given the size of these structures and that M is associated with membranes (62) and G is a transmembrane protein (15), they are likely part of the Golgi apparatus and secretory pathway. The increased yield of VSV G-mCherry at lower temperatures suggests that the G fusion is temperature sensitive (Figure 3.9). Possible defects in folding or oligomerization due to the addition of mCherry could lead to accumulation of G in the Golgi apparatus (29).

Putative sites of NCM complex formation were identified through FRET analysis (Figure 3.12). M-M interactions were numerous and detected at locations where M signal was not measureable above background. This suggests that M forms small complexes at the membrane that could be important for initiating assembly, such as those found in stage I. M-P interactions are also found at the membrane but not in P cytoplasmic inclusions, consistent with a role in assembly. These protein-protein interactions identify sites where condensation and assembly may be occurring. While condensation should generate electron-dense bullet-shaped NCM complexes, TEM images of infected cells do not show the expected amount of these structures at the plasma membrane (Figure 3.5). Perhaps some FRET signal is from interactions that have not yet led to the formation of condensed structures that are readily observable by TEM.

Limitations of the study of virus assembly using fluorescent fusions

An assumption when using fluorescent protein fusions is that they function equally well as the wild type protein. For the VSV protein fusions, this is likely not true given the attenuated nature of the recombinant viruses. The fluorescent protein fusions may be less function and possibly prone to entering a non-productive pathway or generating a non-functional complex, such as an aggregate. This would result in a portion of the fluorescent proteins not being involved in assembly. These dysfunctional proteins could be very dense or cover a large area and obscure the VSV assembly events.

Detecting virion signals in cells

In order to detect assembling particles in infected cells, the protein signals must be higher than the background. P, M, and G in purified virus particles can be detected by the TIRF microscope, demonstrating that sensitivity is not a problem. However, in infected cells there is background signal that may obscure the assembling virions. In cells, P forms dense cytoplasmic inclusions and only associates with the membrane during assembly (15, 56). The inclusions contain a significant amount of protein and even with TIRF illumination at a high angle, they can still be detected. M binds to membranes (15, 64, 161, 162) and G is a transmembrane protein (27, 34), which leads to both M and G labelling the plasma membrane. The illumination of proteins not actively involved in assembly could obscure assembling particles. Detection of virions is compounded by movement in live cells, which causes the signal to be distributed over multiple lateral pixels. These circumstances lead to a decreased signal to background ratio that could contribute to the difficulty in detecting productive assembly events.

A variable amount of G is packaged into particles through a mechanism that involves M

VSV particles package a variable amount of M and P (Chapter 2), and this is may also be true for G (Figure 3.9 D-E). Since G is not essential for the assembly and release of VSV particles (90, 91), it may play an accessory role in this process and consequently not be specifically incorporated into particles, leading to variable incorporation. While our data demonstrate that an inconsistent amount of fluorescent G is incorporated into virions, it is possible that after particle release G-mCherry undergoes cleavage and becomes nonfluorescent, since some cleavage products may be present (Figure 3.9 B). Further analysis of the protein composition of G-mCherry containing virions is required to confirm the variable incorporation of G into particles.

The packaging mechanisms for at least some M and G into particles may be related. The amounts of M and G that are present in virions are positively correlated (Figure 3.9 F), demonstrating that the incorporation of M affects G and *vice versa*. Since M stabilizes G trimers (105), M and G may form a complex that is incorporated into particles, and thus the amounts of M and G packaged would be positively correlated. Alternatively, if G is present at assembly sites first (64) and recruits M through a stoichiometric interaction, then M and G incorporation would also be positively correlated. A trivial explanation is that these particles are a variable size, and the content correlation arises since larger particles contain proportionately more of all proteins. Quantification of the dimensions of VSV M-eGFP G-mCherry particles is necessary to confirm a related packaging mechanism between M and G.

Materials and Methods

Cells and viruses.

BsrT7, BS-C-1, and HeLa cells and VSV clones were maintained as previously described (Chapter 2 Materials and Methods). VSV mutants and fluorescent derivatives were based on the VSV M-eGFP backbone (Chapter 2). The M51R mutation was generated through site-directed mutagenesis using the primer (only (+) sense is reported and point mutations are underlined) GGAGTTGACGAGCGCGACACCTATGATCCG. The late domain mutants contained the point mutations 24 PPPY 27 to AAPA (68) and 37 PSAP 40 to AAAA (69), annotated for wild type M. These mutations were generated with the primers CTAAGAAATTAGGGATCGCAGCAGCCCCTGCTGAAGAGGACACTAGCATGG for PPPY and GCTGTACAAGGGCGGCCGCACTGCTGCTGCTGCAATTGACAAATCCTATTTTGG for PSAP. Recovery of VSV clones containing G fluorescent fusions also included wild type VSV G in the initial recovery transfection. HIV-1 Gag, Gag-eGFP, Vps4A-mCherry DN, and Vps4A DN in the pCR3.1 vector were kind gifts from Bieniasz PD (138). Vps4A wild type was generated from Vps4A DN through site-directed mutagenesis using the primer CCATCATCTTCATCGATGAGGTGGATTCCCTCTGC. HeLa cells were transfected with Lipofectamine® 2000 (Life Technologies Corporation; Carlsbad, CA) according to the manufacturer's instructions with 2 μg per 6 well of HIV-1 Gag:Gag-eGFP at a ratio of 5:1.

TIRF microscopy

Hela and BS-C-1 cells were seeded on #1.5 glass bottom Fluorodishes (World Precision Instruments; Sarasota, FL). Cells were infected asynchronously by adding virus directly to the

media and changing the media to 10% FBS 50 mM HEPES pH 7.4 DMEM without phenol red immediately before imaging, or synchronously by infecting in 400 μL 10% FBS DMEM for 1 hour and replacing the media with 10% FBS 50 mM HEPES pH 7.4 DMEM without phenol red.

The dishes were loaded into a Ti-E (Nikon; Melville, NY) inverted microscope with a heated stage and environment chamber warmed to 37°C. It is equipped with the Perfect Focus System (Nikon), motorized TIRF illuminator (Nikon), and 60× Plan Apo NA 1.4 objective lens (Nikon). The laser merge module with AOTF (Spectral Applied Research; Richmond Hill, Ontario, Canada) controls the 404 nm, 491 nm, and 561 nm solid state lasers. A Proscan III (Prior; Rockland, MA) controls the stage, filter wheels, and shutters. The excitation filter is a multi bandpass filter 405/491/561/642 and the emission filters are 470/24, 525/50, and 636/60 (Chroma Technology Corporation; Rockingham, VT). Images were acquired with an ImagEM C-9100-13 EM-CCD camera (Hamamatsu; Shizuoka, Japan) and ORCA-D2 CCD camera (Hamamatsu) with Metamorph 7.7 (Molecular Devices; Sunnyvale, CA).

Ultra-thin cell section TEM

Infected cells were fixed in 1.25% paraformaldehyde 2.5 % glutaraldehyde 0.03% picric acid 100 mM sodium cacodylate pH 7.4 and processed for ultra-thin cell section as previously described (169). Cell sections were imaged with a Tecnai G2 Spirit BioTWIN TEM (FEI; Hillsboro, OR) with AMT 2k CCD camera (Advanced Microscopy Techniques Corp.; Woburn, MA).

Confocal microscopy

Confocal images of cells were taken with the same microscope as previously described for immunofluorescence (Chapter 2 Materials and Methods). Quantification of single virus particles was performed as described previously with the automated MATLAB (MathWorks) script IMAB (160) (Chapter 2 Materials and Methods).

FRAP confocal microscopy

BS-C-1 cells were seeded on #1.5 glass bottom Fluorodishes (World Precision Instruments). Cells were synchronously infected, and the media was replaced with 10% FBS 50 mM HEPES pH 7.4 DMEM without phenol red. Cells were imaged every 1 s for 5 time points, with photobleaching occurring after time point 3. Fluorescence recovery was measured by subsequent imaging every 5 s for 200 s.

Dishes were placed in Bionomic Controller stage heater insert (20/20 Technology; Wilmington, NC) in a linear-encoded motorized stage (Prior) in a Ti-E inverted microscope with the Perfect Focus System (Nikon). It is equipped with a Yokogawa CSU-10 spinning disk (Yokogawa Electric Corporation; Tokyo, Japan), emission filter wheel (Sutter Instrument; Novato, CA) containing a 488/568 dual dichroic mirror (Chroma Technology Corp), and 60× NA 1.4 DIC optics objective lens (Nikon). Illumination used a fibre-optic delivery system with fast excitation wheel (Sutter) with a 100mW 488 nm Ar-Kr laser (Melles Griot; Rochester, NY) and Micropoint dye-tunable FRAP laser (Photonic Instruments; Belfast, Northern Ireland). Metamorph 7.7 (Molecular Devices) controlled galvos for FRAP beam positioning was used for image acquisition with an ORCA-AG cooled CCD camera (Hamamatsu). The microscope was

mounted on a vibration-isolation table (Technical Manufacturing Corporation Ametek; Peabody MA).

The background corrected intensities (I) of the objects were calculated by:

$$I(t)_{corrected} = 100\% \times \frac{\frac{I(t)_{object} - I_{background}}{I(t)_{cell} - I_{background}}}{\frac{I(0)_{object} - I_{background}}{I(0)_{cell} - I_{background}}}$$

The following equation was fit to the data (170), where A is a constant and $t_{1/2}$ is the half time of recovery, with GraphPad Prism 5 (GraphPad Software, Inc; La Jolla, CA).

$$I(t) = A \times \frac{t}{t_{1/2} + t}$$

Temperature sensitivity of VSV

The effect of temperature on the production of virus by VSV G-mCherry was performed as previously described (Chapter 2 Materials and Methods).

Western blot of purified virus

Western blots were performed on purified virus as previously described (Chapter 2 Materials and Methods) with a monoclonal anti-VSV G (Sigma; St. Louis, MO).

FRET Calculations

Bleedthrough corrections for the FRET images were performed with a custom macro in ImageJ (U.S. National Institutes of Health; Bethesda, Maryland; http://rsb.info.nih.gov/ij/). All

images were acquired with the same microscope parameters for each FRET pair. A background image was generated by averaging 10x black level images, *e.g.* no light going to the camera. Bleedthrough coefficients, C, were calculated from puncta in samples containing only the donor or acceptor. The pixel FRET efficiency was calculated with the following equations:

$$I(x,y)_{\text{D-corrected}} = \frac{I(x,y)_{\text{Donor}} - I(x,y)_{\text{Acceptor}}}{1 - C_{\text{DtoA}} \times C_{\text{AtoD}}}$$

$$I(x,y)_{\text{A-corrected}} = I(x,y)_{\text{Acceptor}} - C_{\text{DtoA}} \times I(x,y)_{\text{D-corrected}}$$

$$I(x,y)_{\text{FRET-efficiency}} = \frac{I(x,y)_{\text{FRET}} - C_{\text{DtoF}} \times I(x,y)_{\text{D-corrected}} - C_{\text{AtoF}} \times I(x,y)_{\text{A-corrected}}}{I(x,y)_{\text{Donor}}}$$

Chapter 4

Late domains in M mediate its efficient incorporation into released particles

Abstract

Enveloped viruses can take advantage of the host endosomal sorting complexes required for transport (ESCRT) pathway to mediate fission of the assembled particle from the cell. Late domain motifs are required for recruiting this pathway, and the vesicular stomatitis virus (VSV) matrix protein (M) contains 2 identified motifs. Disruption of the late domains results in the accumulation of bullet-shaped particles at the plasma membrane which appear fully formed due to the presence of an electron-dense core, although this conclusion has not been proven. To determine if the late domains play a role in the assembly of VSV, M with functional and disrupted late domains were tagged with different fluorescent proteins. We demonstrate that cells coinfected with viruses containing these M variants release particles that contain predominantly wild type M. This bias is not due to differences in protein expression or plasma membrane localization of the late domain mutant versus wild type M since the steady state levels are the same. We propose that the late domains play a role in assembly prior to fission of the VSV particle.

Introduction

Assembly of vesicular stomatitis virus (VSV) requires condensation of the viral ribonucleoprotein (RNP) by the matrix protein (M) to form the nucleocapsid-matrix protein (NCM) complex (16). How this process is initiated is unknown, and it is unclear how much M is required for the formation of the characteristic bullet-shape since the nucleocapsid protein (N) coated RNA can be induced to form a similar structure on its own (92). In addition, Chapter 2 demonstrates that an absolute amount of M is not required for the formation of the bullet-shape and suggests that M may not be the driving force for creation of this structure. This proposes a model where condensation of the viral RNP is triggered with a small amount of M to form the bullet-shaped structure, and subsequent to this formation, the majority of M is recruited to complete assembly.

Efficient release of VSV particles from cells requires recruitment of the host endosomal sorting complexes required for transport (ESCRT) pathway. In cells, this pathway is normally involved in the scission of membranous vesicles that bud away from the cytoplasm (110), and for VSV it is important for release of the enveloped virions into the supernatant. The ESCRT pathway is recruited to assembling virions through late domain motifs. M contains 2 late domains, 24 PPPY 27 (68) and 37 PSAP 40 (69), that recruit the ESCRT pathway by binding to the neural precursor cell expressed developmentally down-regulated 4-like E3 ubiquitin protein ligase (Nedd4) (68) and tumor susceptibility gene 101 (Tsg101) (116), respectively. The majority of the late domain function, *i.e.* release of virions, has been attributed to PPPY (69, 70), but whether these 2 motifs are simply redundant or have independent functions is unclear. The group-specific antigen protein (Gag) of the retrovirus Mason-Pfizer monkey virus (MPMV) also contains both a PPPY and PSAP motif (171). Like VSV, the majority of the late domain function

is attributed to the PPPY motif (171). However, both motifs play a role in the maturation of the procapsid, and PPPY is important for efficient Gag processing and may act upstream of PSAP in assembly (171). This suggests that the late domains and possibly ESCRT pathway play a role in the assembly of viruses, not just fission. Furthermore, angiomotin (AMOT) plays a role in the assembly of human immunodeficiency virus type 1 (HIV-1) (172), and the binding of Nedd4 to AMOT is required for efficient virus release (172). While late domains are important for mediating fission, they may also play a role in the assembly of VSV.

Mutation of the late domains in M results in an accumulation of electron-dense bullet-shapes at the plasma membrane, demonstrating the "late" block in the replication cycle (68, 69). These bullets are generally assumed to be fully assembled particles that have not yet pinched-off from the plasma membrane (68). The assembling particles appear to be "trapped" and not progress to fission, which is consistent with the accompanied decrease in amount of released particles and plaque forming units (PFU) into the supernatant (68, 69).

Here, we identify a previously unappreciated role of late domains in mediating efficient incorporation of M into released VSV particles. A competition assay was created where wild type and mutant M are fused to different fluorescent proteins, and the protein content of virions released from coinfected cells is quantified with fluorescence microscopy. When wild type and late domain mutated M are coexpressed in VSV infected cells, released particles preferentially contain wild type M. These findings propose that the late domain motifs mediate efficient packaging of M into particles and potentially play a role earlier in assembly than previously understood for VSV.

Results

Incorporation of genetically distinct M proteins into single particles

Late domains, first identified as position independent motifs in Gag of retroviruses (106, 107), facilitate virus release. Disruption of late domain motifs results in assembly of particles that remain trapped during pinching-off from the plasma membrane, but coexpression of wild type Gag was found to partially rescue the decrease in the amount of released retroviral particles (124, 171, 173). For VSV, electron micrographs of cells infected with late domain mutants also show the accumulation of viral particles at the plasma membrane that appear fully assembled. While Gag assembles into immature procapsids that undergo maturation, VSV assembles into a bullet-shape with a likely amorphous core (1). These dramatically different structures may have different effects on the ability of late domains to recruit the ESCRT pathway. Since VSV virions contain 1826 molecules of M (99), but the late domain motifs can bind to the ESCRT proteins in a 1:1 ratio (113, 116), a few molecules of wild type M may be sufficient to bind to and recruit the ESCRT pathway to complement the late domain phenotype. To investigate if VSV and retroviruses utilize late domains in the same manner, the ability of wild type M to complement late domain mutants can be examined. However, wild type and late domain point mutants of M are approximately the same molecular weight. Therefore, the genetic origin of the released M and whether wild type M is assembling with the late domain mutant or independently cannot be determined. A solution is to tag wild type and mutant M with different fluorescent proteins. To confirm that the different fluorescent fusions co-package and compete for incorporation into particles, cells were coinfected with VSV M-eGFP and VSV M-mCherry, generated previously (Chapter 2). Analysis of the contents of released particles with confocal fluorescence microscopy (Figure 4.1 A) demonstrates that virions co-package the different M variants (Figure 4.1 B). A

symmetrical distribution of each fluorescent fusion is incorporated into particles (Figure 4.1 C-D), and the amounts of M-eGFP and M-mCherry are negatively correlated (Figure 4.1 E).

Functional late domains are required for efficient incorporation into particles

Since M-eGFP and M-mCherry compete for incorporation into particles, complementation can be assessed. If wild type M is able to complement the late domain mutation, then the ratio of wild type to mutant M in particles should be the same as when both M are wild type. Cells were coinfected with VSV M-eGFP and VSV M-mCherry where 1 or neither M contained mutated late domains. Quantification of the M content of released particles demonstrates that mutation of the late domains of M reduces the amount of that M in the released virions, regardless of whether the mutation is engineered in the M-eGFP or M-mCherry background (Figure 4.2). Reduced incorporation of the late domain mutants was not due to reduced expression in cells, since both variants of M were expressed at similar levels as measured by western blot (Figure 4.3 A). The late domain mutant is also not defective in transport to the cell surface as equivalent amounts of M are transported to the plasma membrane (Figure 4.3 B). Taken together, these results demonstrate that late domain mutants are efficiently synthesized and transported to the plasma membrane but are not efficiently incorporated into released virions in the presence of wild type M.

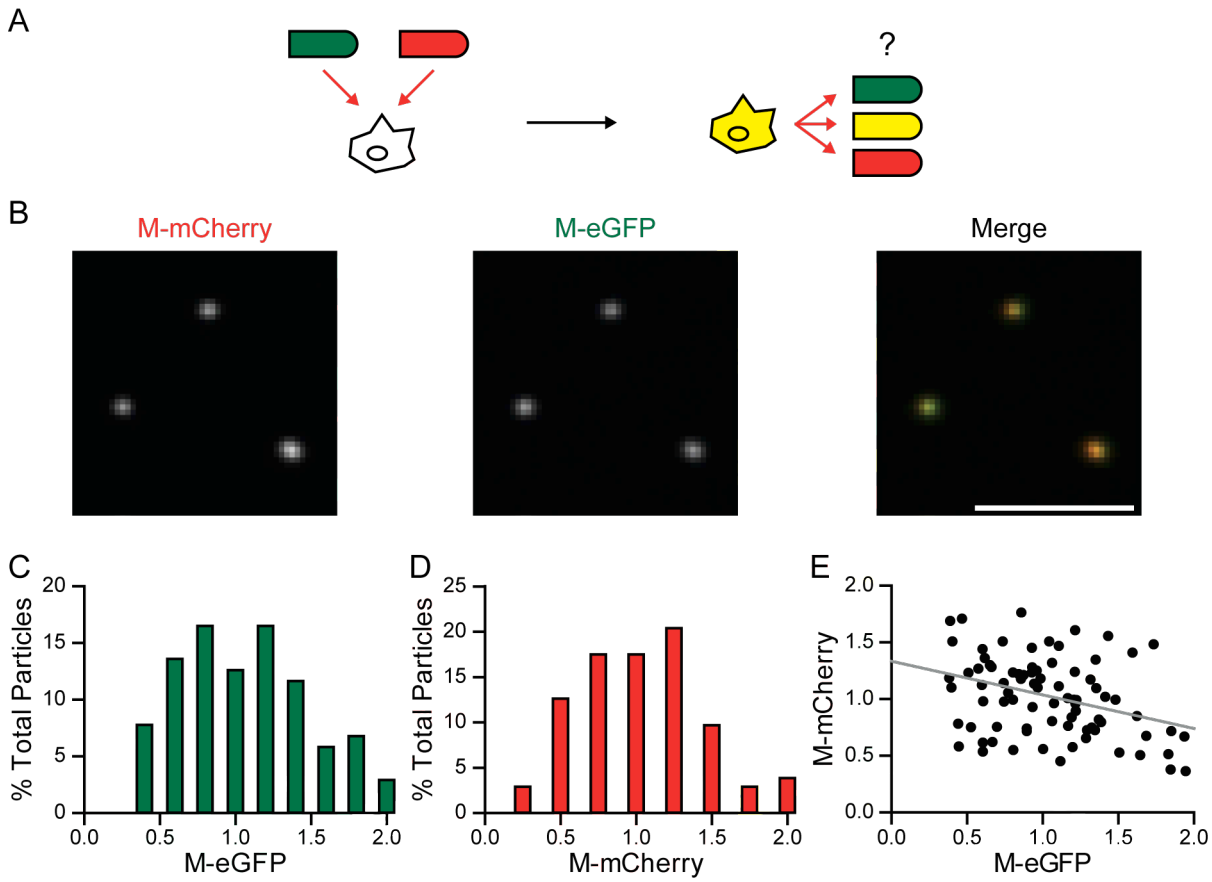

Figure 4.1. Fluorescent intensity of particles released from VSV infected cells expressing M-eGFP and M-mCherry.

(A) Schematic of experimental setup. BsrT7 cells were coinfected at MOI 10 each of VSV M-eGFP and VSV M-mCherry. The virus that is produced is assayed for whether it contains equal or unequal amounts of M-eGFP and M-mCherry. (B) Raw images of particles. Scale bar represents 5 μm. Histograms (n = 103) of the eGFP (C) and mCherry (D) intensities are shown. (E) A scatter plot demonstrates a negative correlation between eGFP and mCherry intensities (Pearson's product-moment correlation r = -0.34, p-value < 10^{-3}). The line of best fit is shown in grey.

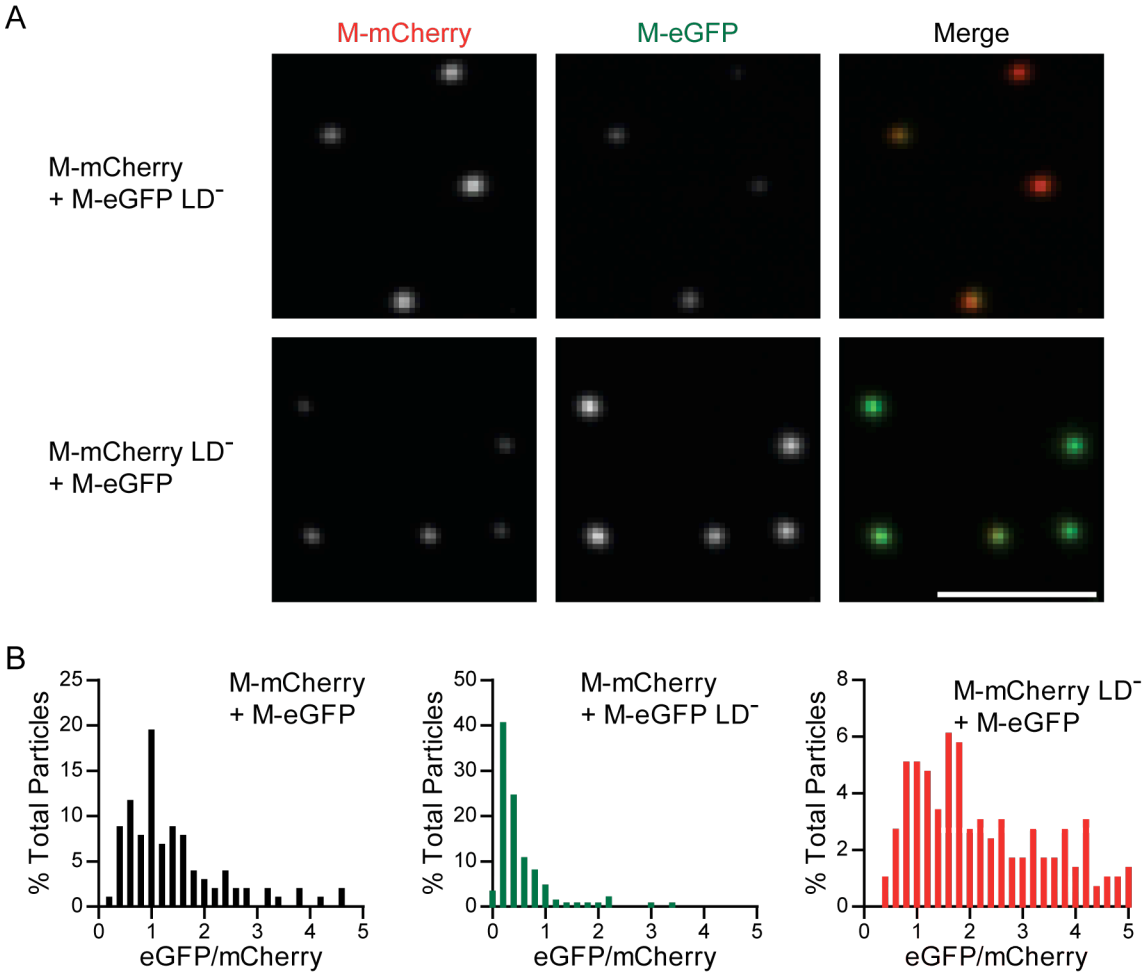

Figure 4.2. Competition between M with and without functional late domains into particles. The same experimental setup as Figure 4.1 was used except that the late domains in 1 of the viruses in the coinfection were mutated. (A) Raw images of particles that were acquired under the same microscope settings and renormalized to the same values. Scale bar represents 5 μm. (B) Particles were quantified, and the ratio of eGFP to mCherry was calculated for each particle and graphed on histograms (n = 103, 151, and 295 for coinfection with functional late domains, M-eGFP mutated, and M-mCherry mutated, respectively). The ratio values are normalized to the peak of the coinfection where both viruses have functional late domains. The coinfection with M-eGFP mutated is shifted to the left and the coinfection with M-mCherry mutated is shifted to the right (Kolmogorov-Smirnov test p-value < 10^{-15} and 10^{-13}, respectively).

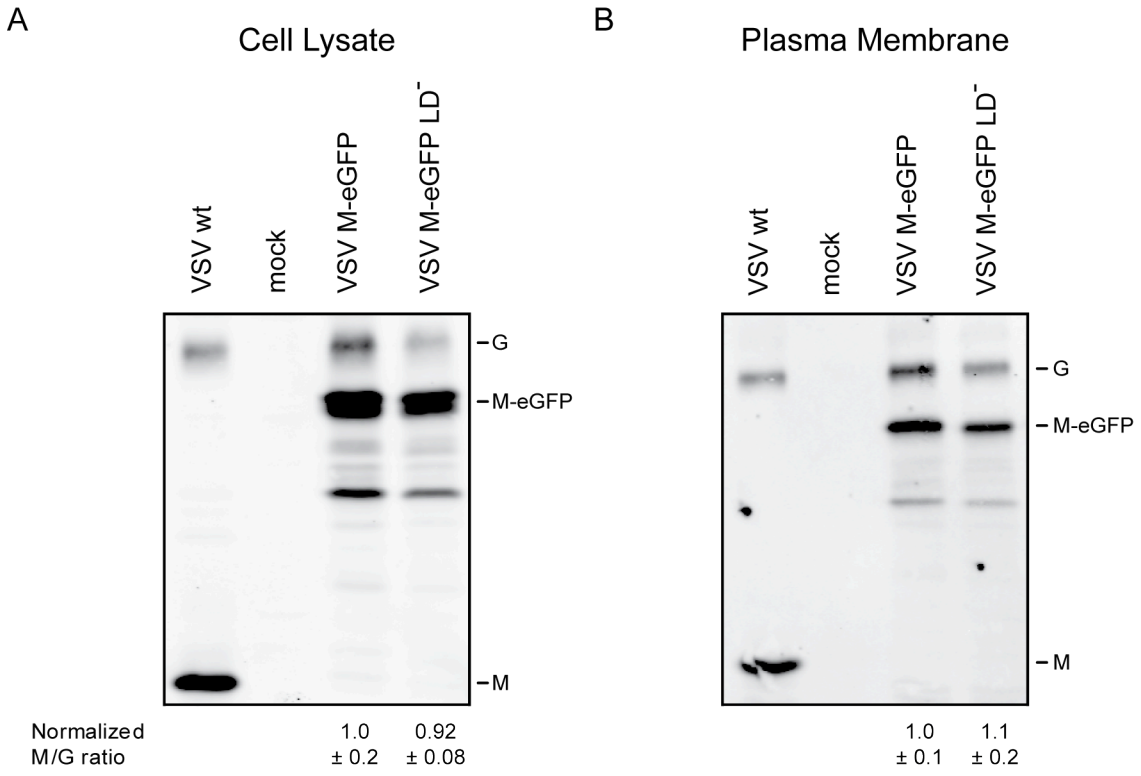

Figure 4.3. Comparison of M-eGFP and M-eGFP LD$^-$ cellular expression and presence at the plasma membrane.

BsrT7 cells were infected at MOI 20, and the whole cell extract (A) or plasma membrane (B) was extracted 7 hpi. The amount of M and G present were determined by western blot. Using G as a loading control, the amount of M expressed in cells or present at the plasma membrane was quantified. SEM for n = 3 is shown. The amount of M-eGFP versus M-eGFP with mutated late domains (M-eGFP LD$^-$) present in lysate and at the plasma membrane are not significantly different (p-value = 0.7 and 0.8, respectively, n = 3, Student's t-test).

Late domain mutations in M are not completely complemented *in trans*

The biased incorporation of wild type M over a late domain mutant of M suggests that the late domain mutation cannot be complemented *in trans*. To determine if coexpression of wild type with the mutant leads to a partial rescue as seen for MPMV (171), cells were coinfected and examined for a late domain phenotype. When wild type and mutant M are present, ultra-thin cell section transmission electron microscopy (TEM) of coinfected cells displays the accumulation of particles at the plasma membrane (Figure 4.4 A). To determine if there is a difference in the amount of released particles, M in the supernatant and cell lysate of coinfected cells were quantified by western blot (Figure 4.4 B and C). This illustrates that significantly less particles, 2-fold, are released when M with mutated late domains is present. Additionally, the amount of infectious units released was compared by titration of the supernatant at 24 hpi. The late domain coinfection had a burst size, *i.e.* released particles per cell, 2-fold lower than that of the double wild type coinfection (p-value = 0.06, n = 5, 1 sample t-test). To more carefully evaluate the amount of released infectious virus, growth curves for the coinfections were compared, and the presence of M with late domain mutations results in a lower yield of infectious virus (Figure 4.4 D).

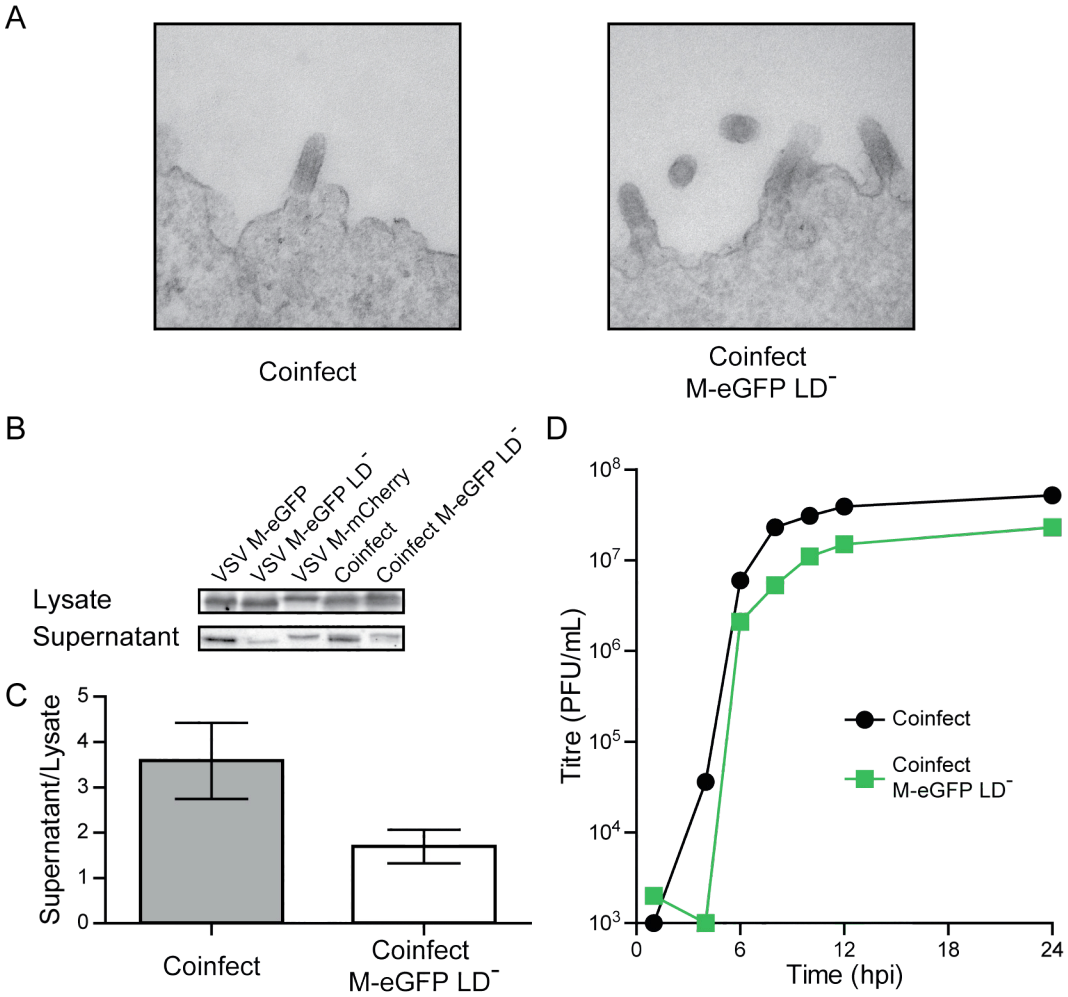

Figure 4.4. Inspection of coinfected cells for the late domain phenotype.
BsrT7 cells were coinfected with VSV M-mCherry and VSV M-eGFP (Coinfect) or VSV M-eGFP LD$^-$ (Coinfect M-eGFP LD$^-$) at MOI 10 each. (A) Cells were analyzed by ultra-thin cell section TEM 8 hpi. Lysate and supernatant of cells were harvested 24 hpi. Particles were isolated from the supernatant of coinfected cells by ultracentrifugation. Lysates and particles were analyzed by western blot for M (B) and quantified (C). The ratio of particles to lysate was averaged, and the SEM is shown. The late domain coinfection produced significantly less particles (p-value = 0.03, n = 3, paired Student's t-test). (D) A growth curve was determined by sampling the supernatant of coinfected cells at the indicated times. The curves are significantly different (p-value < 0.03, 2-way ANOVA).

HIV-1 Gag VLPs are highly pleomorphic

Given the unexpected results with the VSV late domains, we wanted to determine if the biased incorporation is also true for other viruses that contain late domains and use the ESCRT pathway. The late domains in HIV-1 Gag have been well studied (106, 107), and fluorescent fusions to Gag have been generated (135, 138). Therefore, the tools for studying the HIV-1 Gag late domains in a similar competition assay are available. HIV-1 Gag virus-like particles (VLPs) were generated by transfecting 293 T cells with wild type Gag with or without Gag-eGFP and harvesting the supernatant. To optimize gradient purification of the VLPs, radioactive particles were generated, fractionated over a continuous gradient, and analyzed by SDS PAGE and autoradiography (Figure 4.5 A). The Gag bands were quantified by densitometry and fraction 5 was identified to contain purified VLPs (Figure 4.5 B). VLPs made from Gag, Gag-eGFP, and Gag-mCherry were purified, and their fluorescent intensities were quantified with a confocal fluorescence microscope (Figure 4.5 C-E). The intensity histograms display a right-skewed distribution, *i.e.* the histogram extends to the right, and the scatter plot does not show a population with a negative correlation between eGFP and mCherry intensities, as shown by VSV (Figure 4.1). To test if this was due to low Gag expression, a more efficient transfection was performed and the quantification was repeated (Figure 4.5 F-G). These particles contain more Gag and still do not display a symmetrical distribution or negative correlation, suggesting the formation of an uneven structure and a pleomorphic nature of the VLPs.

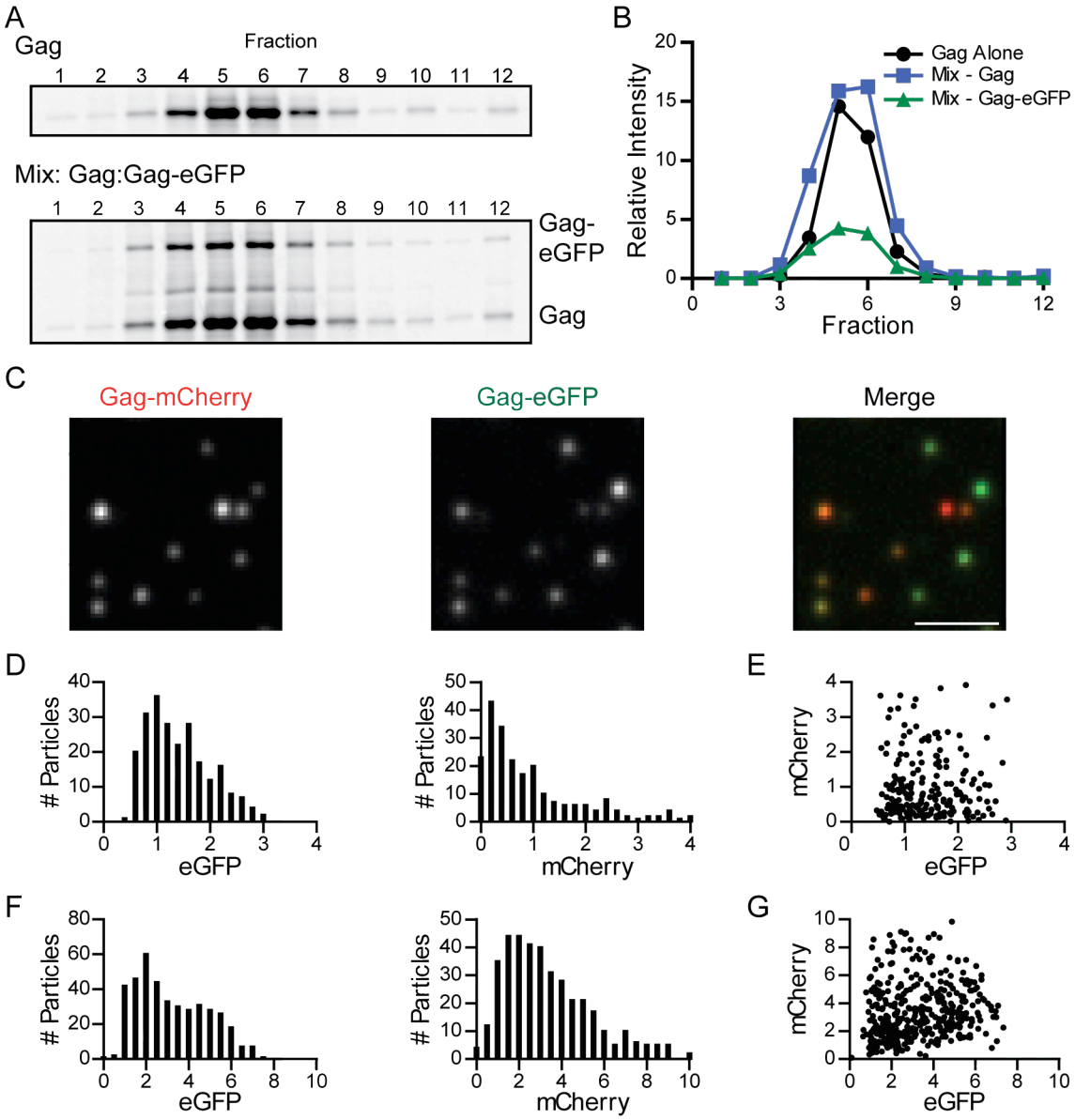

Figure 4.5. Quantification of Gag content of purified HIV-1 VLPs.
(A) 293 T cells were transfected with HIV-1 Gag or Gag:Gag-eGFP at a ratio of 5:1 (Mix) and labelled with ^{35}S. The supernatant was concentrated and then fractionated over a continuous 20-60% sucrose gradient. The fractions were analyzed by SDS PAGE and autoradiography. Fraction 1 is the top and 12 is the bottom. (B) The Gag and Gag-eGFP bands were quantified by densitometry. 293 T cells were transfected with HIV-1 Gag:Gag-eGFP:Gag-mCherry at a ratio of 10:1:1. The supernatant was imaged with a confocal microscope (C). Scale bar represents 5 µm. (D) Histograms and (E) a scatter plot (n = 406) of the fluorescent intensities of the particles in (C). HIV-1 Gag VLPs were generated and quantified as in (A) except that a higher efficiency transfection reagent was used. Fraction 5 was quantified and used to generate histograms (F) and a scatter plot (G). Note the scale change in fluorescent intensity axes.

Discussion

We demonstrate a role of late domains in facilitating the incorporation of M into released particles. Mutating the late domain motifs does not affect M expression or translocation to the plasma membrane. However, even though assembly occurs at the cell surface, late domain mutants of M are not efficiently incorporated into the released virions. The accumulation of bullet-shaped structures at the plasma membrane when the late domains are disrupted suggests that these motifs do not have a role in assembly. However, we show that late domain motifs affect which M are released from the cell.

M competes for incorporation into a finite structure inside virions

M-eGFP and M-mCherry compete for incorporation into VSV particles. This is illustrated by the negative correlation between the amounts of each fluorescent variant within each particle (Figure 4.1 E). The increased incorporation of 1 variant corresponds to a decreased incorporation of the other variant, demonstrating that particles can accommodate only a finite amount of M. The competition of the M variants for incorporation into this structure demonstrates that this system can be used to study how mutations affect competition into particles.

Late domains in M facilitate incorporation into released particles

When provided with equal opportunity for incorporation into released particles, wild type M has a greater presence than M with late domain mutations. This bias could be due to a role of the late domains in the assembly of M into particles. PPPY and PSAP are both important for the assembly of MPMV Gag into particles (171), creating the precedent that these motifs can play a

role in viral assembly and are not only required for recruitment of the ESCRT pathway for fission. In addition, expression of AMOT and its binding to Nedd4, an ESCRT ubiquitin ligase, were found to be required for HIV-1 assembly (172), substantiating involvement of the ESCRT pathway in particle assembly. The late domains or ESCRT pathway may facilitate assemble of M into VSV virions.

Mutating the MPMV Gag late domains or inhibiting AMOT expression leads to morphological defects in virions that are observable by ultra-thin cell section TEM (171, 172), but such an obvious assembly block is not seen for VSV (68-70). Disrupting PPPY or PSAP causes the accumulation of immature MPMV particles at membranes (171), and depletion of AMOT leads to HIV-1 assembly to arrest with the particles only partially formed (172). In contrast, late domain mutants of VSV in PPPY, PSAP, or both assemble bullet-shaped particles at the plasma membrane. Since these structures look similar to released VSV virions, it has been assumed that late domains do not play a role in assembly. However, perhaps the role of late domains for VSV is more subtle than for retroviruses. If the bullet-shape is formed by viral RNPs that have been triggered to undergo condensation, then the late domains could be affecting the packaging of M into these structures. Also, the dimensions of the trapped bullet-shapes have not been quantified, and since purified N-RNA can adopt a similar structure with altered dimensions (92), the internal organization could be malformed in these mutants.

The partial complementation of the late domain mutants suggests that these motifs mediate a *cis*-acting effect. While VSV with late domain mutations produces 98% less virus, the complemented coinfection produces only 51% less. This is similar to MPMV where Gag with late domain mutations releases 80% less particles but complemented mutant Gag releases only 40% less (171). The role of PPPY in MPMV Gag processing (171) is consistent with a *cis*

function. Perhaps a similar role of these motifs in M mediates efficient incorporation into particles. If M with functional late domains is packaged into particles at a higher rate, then assembling particles would contain predominantly wild type M. This would account for the non-exclusive incorporation of wild type M for VSV and Gag for Rous sarcoma virus (173) over the late domain mutant. Since the mutants are less efficient at assembly but not defect for this function, particles would contain mostly wild type protein but also a minor amount of the mutant.

HIV-1 Gag VLPs are too pleomorphic to test the effect of late domains on incorporation

Late domains are found in a number of enveloped viruses (Table 1.3), and whether the biased incorporation of wild type protein over late domain mutant is a general phenomenon could be examined with other viruses. HIV-1 is a well-studied model, and fluorescent VLPs have been generated (138). VLPs were produced, gradient purified, and then analyzed by confocal fluorescence microscopy for Gag incorporation. The histograms of the Gag-eGFP and Gag-mCherry content of VLPs were right-skewed instead of symmetrical, demonstrating that the VLPs are irregular and do not form a consistent structure. This is corroborated by the fact that the amount of Gag packaged is dependent on the transfection efficiency; the VLPs can accommodate more Gag if a higher concentration is present. This suggests that Gag VLPs form a variable sized uneven structure rather than a finite regular structure like VSV. In addition, the scatter plot does not show a population where eGFP and mCherry intensities negatively correlate, which would indicate competition. Therefore the pleomorphic HIV-1 Gag VLP system cannot be used in the competition assay as described above for VSV.

Materials and Methods

Cells and viruses.

BsrT7 cells, 293 T cells, and VSV clones were maintained as previously described (Chapter 2 Materials and Methods). Statistical Kolmogorov-Smirnov test, for comparing competition ratios, and 1 sample t-test, for comparing viral burst size, was performed with R (The R Foundation for Statistical Computing; Vienna, Austria; http://www.r-project.org/). Student's t-test, for comparing M present in cell lysate versus plasma membrane and M budding assay, and 2-way ANOVA, for comparing growth curves, was performed with GraphPad Prism 5 (GraphPad Software, Inc; La Jolla, CA).

Quantification of virion fluorescent intensity

Quantification of purified particles was performed as previously described (Chapter 2 Materials and Methods). Briefly, BsrT7 cells were coinfected with the specified viruses at MOI 10 each, and gradient purified particles were imaged on a fluorescent confocal microscopy, and the intensities of the particles were quantified with the automated MATLAB (MathWorks) script IMAB (160).

Isolation of plasma membrane

Plasma membrane was isolated as previously described (174) with minor modifications. Briefly, BsrT7 cells were infected at MOI 20, and at 7 hpi cells were harvested in 10 mM EDTA in PBS, resuspended in homogenization buffer (HB) (10 mM Tris, pH 7.4, 10 mM NaCl, 0.25 mM $MgCl_2$), and subject to 30 strokes in a Dounce chamber. Following centrifugation at 2,000 ×g for 5 min at 4°C, the 500 µl post-nuclear fraction was mixed with 2.5 ml 66% (w/v) sucrose

in HB, transferred to a SW 41Ti tube and overlaid with 6 ml 40% (w/v) sucrose in HB followed by 3 ml 10% (w/v) sucrose in HB. Following centrifugation at 160,000 ×g for 16 h at 4°C, the plasma membrane was collected from the 10-40% interface, diluted to 12 ml in HB, and subsequently recovered by centrifugation at 160,000 ×g for 1 h at 4°C. The resulting pellet was resuspended in SDS sample buffer and analyzed by SDS PAGE followed by western blot with monoclonal anti-VSV M 23H12 (a kind gift from Lyles DS (159)), monoclonal anti-VSV G (Sigma; St. Louis, MO), anti-mouse IRDye 680RD (LI-COR; Lincoln, NE), and Odyssey Classic (LI-COR). Quantification was measured relative to a standard curve with ImageQuant TL v7 (General Electric (GE) Healthcare; Piscataway, NJ).

Ultra-thin cell section TEM

Fixation and imaging of VSV infected BS-C-1 cells was performed as previously described (Chapter 3 Materials and Methods).

M budding assay

BsrT7 cells were infected with VSV at MOI 3. At 24 hpi, the cells were scraped, and the supernatant was microcentrifuged of 16 000 ×g for 1 min at 4°C. The pellet was resuspended in SDS sample buffer to generate cell lysate. The virions in the supernatant were isolated by ultracentrifugation at 100 000 ×g for 1 h at 4°C and resuspended in SDS sample buffer. Quantitative western blots were performed as described above for isolated plasma membranes.

VSV single-step growth kinetics

Growth curves of VSV in BsrT7 cells were determined as previously described (Chapter 2 Materials and Methods) except that a coinfection was performed at MOI 10 of each virus.

Purification of HIV-1 Gag VLPs

293 T cells were transfected with 2 μg per 6 well of HIV-1 Gag or Gag:Gag-eGFP:Gag-mCherry at a ratio of 10:1:1. Lipofectamine® 2000 (Life Technologies Corporation; Carlsbad, CA) was used according to the manufacturer's instructions for transfections, except when Lipofectamine® 3000 (Life Technologies) was used for more efficient transfections. At 48 hours post transfection, the supernatant was harvested, passed through a 0.22 μm filter, ultracentrifuged at 90 000 ×g for 2 h at 4°C, and resuspended in PBS. This was purified on a continuous 20-60% sucrose in PBS gradient by ultracentifugation at 100 000 ×g for 16 h at 4°C. The fractions were diluted up to 5 mL in PBS and the VLPs were collected by ultracentrifuged at 100 000 ×g for 2 h at 4°C. The resulting pellet was resuspended in PBS for quantification with fluorescence microscopy or SDS sample buffer for analysis by SDS PAGE and autoradiography, as previously described (Chapter 2 Materials and Methods).

Chapter 5

General discussion

State of field prior to this work

Many of the stages of VSV assembly have been investigated. The synthesis and transport of the virion components, *i.e.* the viral ribonucleoprotein (RNP), matrix protein (M), and glycoprotein (G), to the plasma membrane are known (15). The viral RNP must be assembled from the genomic RNA, nucleocapsid protein (N), phosphoprotein (P), and large polymerase protein (L), and G must oligomerize during transport, but how each component is recruited into assembling particles is unclear. Studies with fixed cells have generated a model where the viral RNP is recruited to the plasma membrane through G to initiate assembly (64). M is subsequently recruited to mediate condensation of the viral RNP into the compact nucleocapsid-matrix protein (NCM) complex (16). While M is essential for particle formation, the trigger for assembly has remained elusive. The final step in egress is fission of the particle from the cell, which is mediated by the host endosomal sorting complexes required for transport (ESCRT) pathway. This pathway was thought to be recruited only after particles are fully assembled through late domain motifs on viral proteins. While the proteins necessary for each step of assembly have been identified, their roles at these stages are not firmly established.

Contributions to the field

Our approach to studying VSV assembly was through the generation of fluorescent protein fusions and fluorescence microscopy. A functional fusion to M was generated by insertion after residue 37 in the disordered region (Chapter 2), and a viable genetically-stable fluorescent G was generated through an N-terminal fusion (Chapter 3). VSV containing exclusively fluorescent M or G is replication competent but attenuated. Quantification of the M,

P, and G content of particles reveals that a variable amount of each protein is packaged per virion. While M and P are incorporated independently of each other, the packaging mechanism of M and G are related. Virions contain a discrete helix of M (1), although formation of the bullet-shape does not require M to occupy all of the positions in this arrangement (Chapter 2). Assembly of M into virions begins with the formation of a complex with a small amount of M, which may be viral RNPs that have been triggered with M to undergo assembly (Chapter 3). Then there is a delay before M is rapidly assembled into the particle. Release of particles into the supernatant requires recruitment of the host ESCRT machinery through late domains to mediate fission. These motifs are also required for efficient incorporation of M into released particles, but the mechanism of how this occurs is unclear (Chapter 4). We have investigated multiple stages in assembly, which has led to implications for these processes.

Implications

M is required for triggering but not mediating the formation of the bullet-shaped virion

The characteristic bullet-shape of VSV has been thought to be formed through the oligomerization of M, but a significant amount of M may not actually be required. While M is necessary for the formation of the bullet-shaped NCM complex (93), how much is required has not been determined. A mutation that disrupts the bullet-shape (95) has been mapped to M (94), demonstrating that a function of M mediates the creation of this structure. However, we demonstrate that VSV particles contain a symmetrical distribution of M, revealing that the majority of particles are not saturated with M, and that formation of the VSV structure does not depend on the presence of M at every position in the M helix (1)(Chapter 2). We propose that the

majority of M is not critical for the assembly of this structure, but a minor amount of M is required for triggering the formation of the bullet-shape. Since N-RNA can adopt a bullet-shape (92) but M is essential for release of infectious particles (50), perhaps the triggering of assembly requires M but the formation of the structure is dependent on the viral RNP.

Models for the role of late domains in VSV assembly

The late domains in M may play a role in the assembly of VSV particles (Chapter 4). It was previously thought that the function of these motifs was only to recruit the ESCRT pathway to mediate fission of the virion from the cell. This was based on the observation that when these motifs are mutated, particles that appear fully formed due to the presence of an electron-dense core accumulate at the plasma membrane (68, 106, 107). However, the assumption that these structures are complete virions has not been demonstrated directly, and they may be an assembly intermediate due to a defect in a function of M. Our data is consistent with the latter case where late domains have a role earlier in assembly than fission and are required for efficient incorporation of M into assembling particles (Figure 5.1). VSV virions contain M in 2 locations, an outer helix (1) and central "cigar" (100). A differential role of late domains in the assembly of these structures could explain the nonexclusive bias of wild type M over the late domain mutant (Chapter 4). A function of these motifs in assembly is implicated for Mason-Pfizer monkey virus (MPMV), where late domain mutations in the group-specific antigen protein (Gag) lead to a defect in particle formation and maturation (171). However, the mechanism of how this occurs is unclear. Perhaps for VSV, the late domains increase the affinity of M for the NCM complex, which would lead to an increased rate of incorporation into particles. Wild type M would be incorporated faster and more often than mutant M and consequently make up a larger proportion

of M in the released particles. This role could be mediated through a *cis*–acting function that affects the intrinsic affinity of M or recruitment of proteins that facilitate assembly. M is ubiquitinated by the neural precursor cell expressed developmentally down-regulated 4-like E3 ubiquitin protein ligase (Nedd4) (114), and tumor susceptibility gene 101 (Tsg101) is recruited to human immunodeficiency virus type 1 (HIV-1) virus-like particle (VLP) assembly sites concomitantly with Gag (142). Ubiquitination or Tsg101 binding could facilitate M incorporation into assembling NCM complexes. In addition, angiomotin (AMOT) was found to be required for HIV-1 assembly, and the binding of AMOT to Nedd4 was necessary for this activity (172). If AMOT is also involved in VSV assembly, it may be recruited through direct binding to M, as it does to HIV-1 Gag (172), or binding to Nedd4, which binds to the PPPY motif in M (114). The latter case would explain the importance of late domains in VSV assembly. Perhaps recruitment of the ESCRT proteins by late domains mediates the association of other factors that are required for VSV assembly.

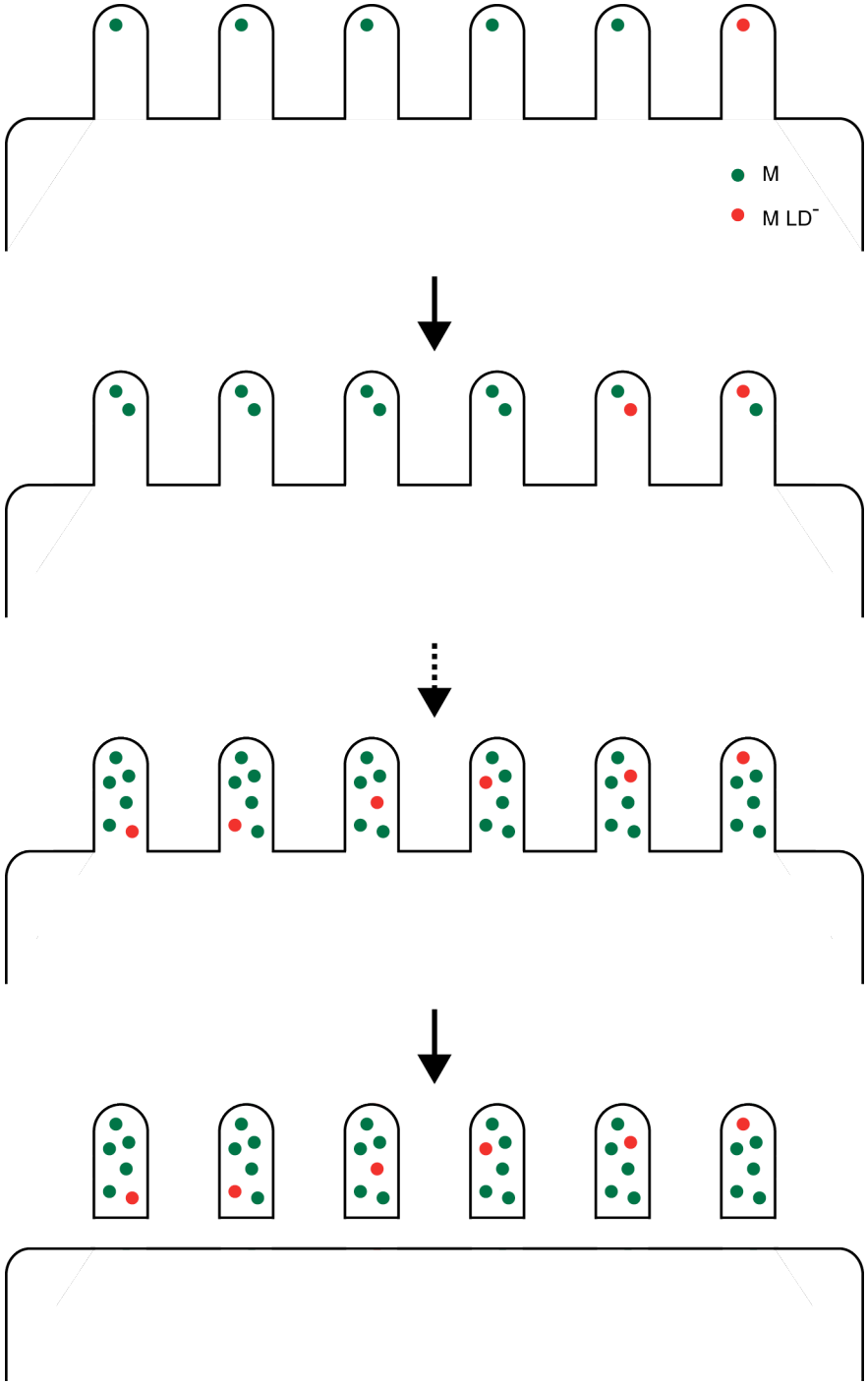

Figure 5.1. Late domains could mediate incorporation of M into particles.
If late domains are required for efficient assembly, then wild type M will be preferentially incorporated into particles over the late domain mutant (M LD^-). As assembly progresses, the particle composition will be biased for wild type M, and consequently the released particles will contain predominantly M with functional late domains.

An alternative model is that a threshold amount of late domains is required for efficient recruitment of the ESCRT pathway (Figure 5.2). In this case, NCM complexes would form with a range of M with and without late domains, but only the particles biased for M with functional late domains would successfully recruit the ESCRT pathway, fission, and be released. Since recruitment is mediated by protein-protein interactions, a higher number of late domains would increase the chance that the corresponding ESCRT protein binds to the assembly site. This would also imply that either recruitment of the ESCRT pathway by the viral proteins is inefficient or a large amount of ESCRT-0 complexes are required to lead to membrane fission. Recognition of ubiquitinated M by ESCRT-0 or Tsg101 may be difficult due to the condensed nature of the NCM complex and the fact that only the bottom of the NCM complex is accessible to the cytoplasm after assembly (68). The nonexclusive bias could be accounted for if the required threshold was < 100% or if late domains are only required in the M exposed to the cytoplasm. M at the tip of the bullet or inside the central "cigar" may be unable to directly interact with the ESCRT proteins. Therefore, there is no selection on these M molecules, and they are a random mix of wild type and mutant M.

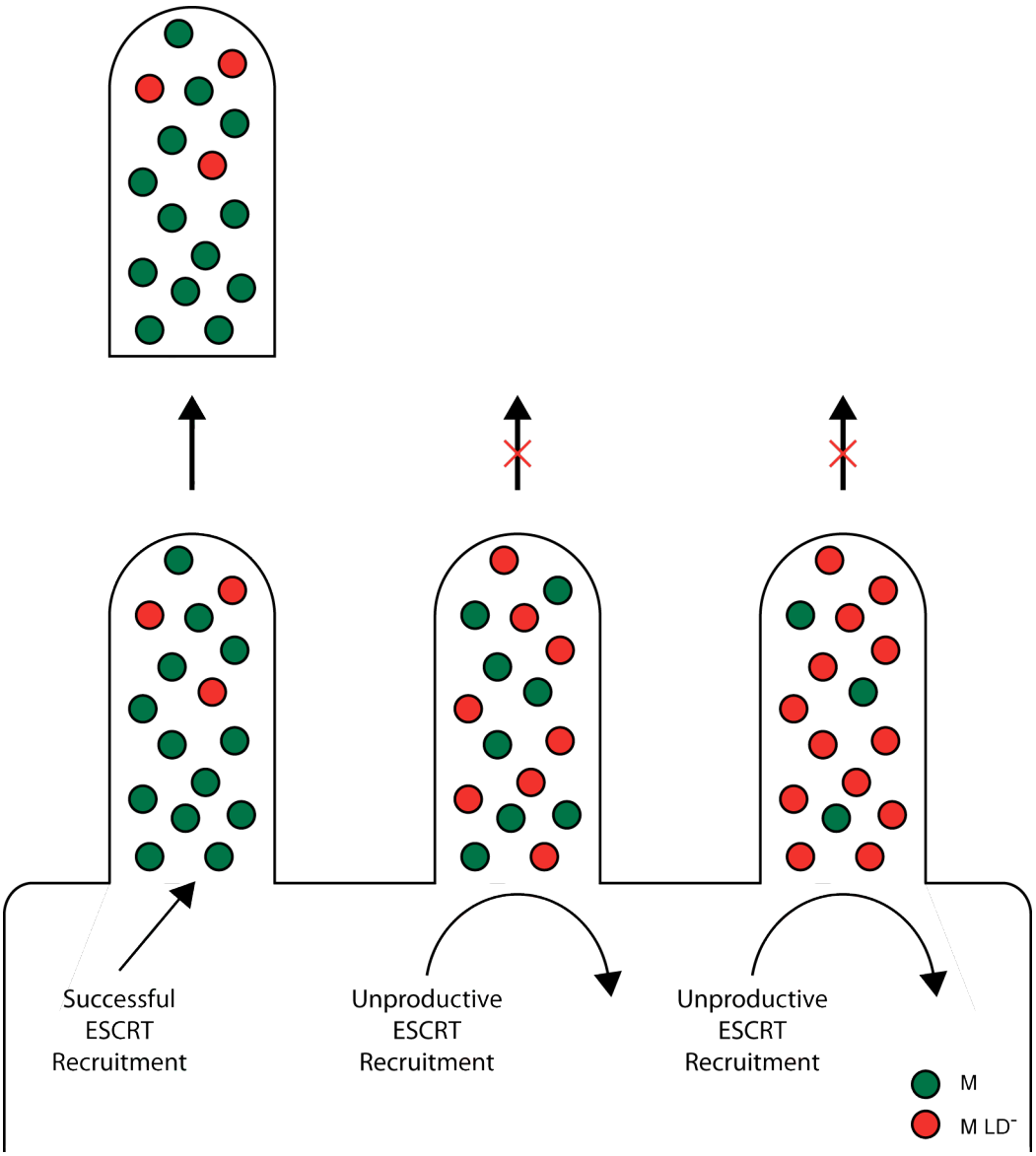

Figure 5.2. A threshold amount of late domains could be required for efficient fission.
If VSV particles assemble equally well with wild type M and a late domain mutant of M (M LD$^-$), then the NCM complexes at the plasma membrane will contain a range of each variant. If successful recruitment of the ESCRT pathway requires a high density of functional late domains, then only the particles that randomly assembled with a bias for wild type M will be released.

This threshold model would also have implications for the recruitment of the ESCRT pathway to cellular cargo. If a higher concentration of late domains leads to more efficient recruitment of the ESCRT pathway, this could be a way for cells to prioritize cargo. Many cargos are ubiquitinated for targeting to the ESCRT pathway (175). If the target is more heavily ubiquitinated, it would more efficiently recruit ESCRT-0 and more readily be incorporated into multivesicular bodies (MVBs). This could expedite metabolism of nutrients, autophagy, or degradation of toxins depending on the state of the cell. Regulation of these ubiquitin ligases could be a method to fine-tune the MVB pathway.

Both of these models could explain the presence of 2 late domains in M. These 2 motifs could mediate different stages of assembly as was found for MPMV Gag (171). While mutating only PSAP in M does not have a measurable effect (69, 70), the enhanced mutant phenotype in the PPPY PSAP double mutant suggests that it has a function (69). The 2 late domains may play different roles in VSV assembly like they do for MPMV (171), and thus are both required for efficient particle assembly and release. Alternatively, the late domains could function redundantly to recruit cellular proteins, *e.g.* AMOT or ESCRT proteins, which facilitated particle formation or fission. If a higher density of late domains mediates more efficient protein recruitment, then a greater number of late domains per molecule would also result in more efficient particle assembly and release.

Distinguishing between the mechanisms of how late domains enhance incorporation

The mechanism through which late domains mediate efficient incorporation of M into released particles would have profound effects on the understanding of VSV assembly and the involvement of the ESCRT pathway. The most direct way to address whether late domains affect

the composition of assembling particles or only applies a selection on the fully assembled virions would be through live cell imaging of the biogenesis of single VSV particles. If the formation of VSV particles could be observed, the incorporation of wild type M versus mutant M into assembling particles could be determined directly. However, the difficulty in imaging VSV assembly currently prevents this approach (Chapter 3). Alternatively, whether wild type M is incorporated into NCM complexes preferentially over M with late domain mutations could be tested *in vitro*. The affinity of wild type and mutant M for NCM complexes in the presence and absence of Nedd4 and Tsg101 could be measured to demonstrate whether the motifs or the ESCRT pathway affect NCM complex binding (98). How late domains facilitate M incorporation into released VSV particles would further the understanding of how viruses accomplish assembly and fission.

An N-terminal fusion to G does not abolish fusion activity

A fluorescent protein fusion to the N-terminus of G generates a replication competent virus (Chapter 3). This was unexpected since the ectodomain undergoes major conformational changes during fusion (164), suggesting that there are less restrictions on the N-terminus, consistent with the flexibility of the N-terminal region (176). The crystal structures of the pre-fusion (164) and post-fusion (165) conformations of G position the N-terminus near the periphery of the protein facing in between the monomers in the trimer but on opposite sides of G (Figure 3.8 B-C). During the structural reorganization that occurs when G is triggered (164), mCherry must move out of the way as well as around the monomer. The ability of G to mediate fusion in the presence of an N-terminal fusion suggests that this terminus does not play an essential role in the structure or function of G.

While VSV G-mCherry is viable, it is highly attenuated (Chapter 3). This could be due to an inefficiency of mCherry to move around the monomer leading to inhibition of the conformational change that leads to fusion. In addition, mCherry could inhibit the triggering of G or possibly cellular binding. However, the N-terminus is not near D268, the major pH sensor residue (177), or the canyon at the top of the trimer thought to be involved in ligand binding (164). Since G-mCherry contains a normal cytoplasmic tail and the sequences necessary for efficient budding (89, 90), it is possible that budding is not significantly altered. In this case, the decreased yield of infectious virus would be due to an increase in the particle to PFU ratio of VSV G-mCherry. The addition of mCherry likely inhibits the specific fusion activity of this G chimera.

Identity of the fluorescent protein can affect the functionality of the fusion protein

An interesting discovery was that a G fluorescent fusion is more genetically stable when fused to mCherry instead of eGFP (Chapter 3). After a few passages, VSV G-eGFP would spontaneously delete the majority of the fluorescent protein coding sequence while VSV G-mCherry was stable. The selective pressure on G-eGFP must be stronger than on G-mCherry, suggesting that G-eGFP is more defective.

Fluorophores are often chosen based on high photostability and intrinsic brightness, *i.e.* the product of the extinction coefficient and the quantum yield, but fusions to G have shown that these properties are sometimes not the most important criteria. G-eGFP is more genetically unstable than G-mCherry, and this must be due to a difference between eGFP and mCherry. These fluorophores are derived from different sources. The eGFP is a derivative of GFP which was isolated from the jellyfish *Aequorea victoria* (178), and the mCherry is a derivative of

mRFP1 which is a derivative of dsRED which was isolated from the coral *Discosoma sp* (179). Given the diverse origins, these proteins likely have distinct physical properties, such as flexibility, hydrophobicity, and surface charge density. One or more of these properties likely results in G-mCherry being more functional that G-eGFP. When testing new fluorescent protein fusions for functionality, eGFP is often chosen because of its desirable fluorescent properties (180) with the assumption that all fluorescent proteins are interchangeable. If this fusion protein is non-functional, it is often assumed that the insertion site is non-permissive. However, our results suggest that in some cases, the identity of the fluorescent protein can influence the functionality of the fusion protein.

Future Directions

Quantification of all viral proteins in single VSV particles

The highly order nature of VSV particles suggests an organized internal structure. While such a structure has been demonstrated for N and M (1), we have found that bullet-shaped particles package a variable amount of P, M, and G (Chapter 2, Chapter 3). Understanding the consistency in the incorporation of the other viral proteins would be informative about their packaging mechanisms. Since N coats the genomic RNA in regular intervals (38), a constant amount of N is expected to be packaged. However, it is possible that a variable amount of free N is also packaged. L is linked to the N-RNA through binding to P (35), and since a variable amount of P is packaged this variable incorporation likely extends to L as well.

Quantification of the contents of virions would also permit the identification of which proteins are co-packaged. A correlation in the amounts of proteins packaged would suggest that

their incorporation mechanisms are connected. The quantities of P and L are expected to be positively correlated since P is thought to mediate L incorporation (35). However, since more P is incorporated into particles than can bind to L (47, 99), a perfect or symmetrical correlation is not expected. The nonessential nature of G makes the identity of proteins that are co-packaged of particular interest. While the amounts of M and G in particles are positively correlated (Chapter 3), it is unknown whether the packaging of N and G are related, which would be predicted by the current model for assembly where association of G with N initiates this process (64).

The protein content of single VSV particles could be quantified through fluorescence microscopy as performed here (Chapter 2). While a functional fluorescent protein fusion to L has been generated (146), there are no reports of a functional fusion to N. Such a fusion could be generated through terminal fusions, rational design based on the crystal structures (38, 101, 181), or a forward genetics screen as was performed for M-eGFP (Chapter 2). Understanding the composition of single particles would advance the understanding of how viral proteins are packaged into VSV particles.

How can the VSV virion structure be maintained with a variable amount of M?

We have demonstrated that VSV particles contain a variable amount of M and that even with this variation the bullet-shaped structure is maintained (Chapter 2). What arrangement this inconsistent amount of M forms inside virions is unclear. While the averaged structure of particles display a discrete M helix (1), such a crystalline structure may not be formed in individual particles. To determine how M packs inside single particles, cryo-electron tomography (cryoET) can be used to determine if the M helix is fully occupied. Alternatively, cryo-electron microscopy (cryoEM) could generate class averages of a portion of the M helix to

determine if imperfections can be detected. In addition, a cryoEM reconstruction of the core could be generated. Alignment of the core independently of the N and M helixes would establish if a 3D model can be built and if the core is truly amorphous. This would determine whether a variable amount of protein can be packaged into this volume. These techniques could determine how M packs into single VSV virions.

How the M-eGFP fusion is organized inside virions is unclear for a number of reasons. While wild type M forms a ~1200 molecule helix inside particles (1), the average VSV M-eGFP particle contains only 800 ± 30 molecules of M-eGFP (Chapter 2), suggesting that this discrete helix cannot be fully occupied even if there were no M in the core. In addition, M-eGFP is twice the mass of wild type M, 53 kDa versus 26 kDa, but there is not enough space in virions between the membrane and N helix to accommodate this addition (1). These incongruities can be rectified by the measurement that VSV M-eGFP particles contain only 44 ± 2% the number of molecules of M. M-eGFP is double the mass, but ½ of the number of moles of M are incorporated into particles, suggesting that the eGFP domain is occupying an M position. Since M (78, 81, 82) and GFP (152) are both globular proteins of similar size, 26 and 27 kDa respectively, and eGFP is inserted near the N-terminus, the structure of M-eGFP may be 2 linked globular domains. It is possible that eGFP domain occupies the volume of an adjacent M molecule (Figure 5.3 A-C). If M-eGFP can occupy 2 positions of M, then only ~600 molecules of M-eGFP are needed to fill the helix. In this orientation, the ability of GFP to form antiparallel dimers (182) may facilitate the organization of M in the helix where the monomers alternate between facing the membrane and N (Figure 5.3 D), discussed in Chapter 1 CryoEM reconstruction of VSV virions. In this model, the M and eGFP domains could form a checkered-pattern (Figure 5.4 A-B) or sub-structures where the M from multiple M-eGFP are facing and interacting with each other (Figure

5.4 C-D). In the latter case, since the helix is driven by M-M and not eGFP-eGFP protein-protein interactions, these sub-structures would likely not form a regular array within the helix. This arrangement could contribute to generating “holes” in the helix volume and a variation in the amount of M that is incorporated. M-eGFP is likely not orientated radially since this would result in an increase in particle width, which was not observed (Figure 2.7). The orientation of M-eGFP in particles could also be determined with cryoET or cryoEM averages of a portion of the helix. Understanding how this M fusion packs would be informative about the structural requires for formation of the M helix and VSV assembly.

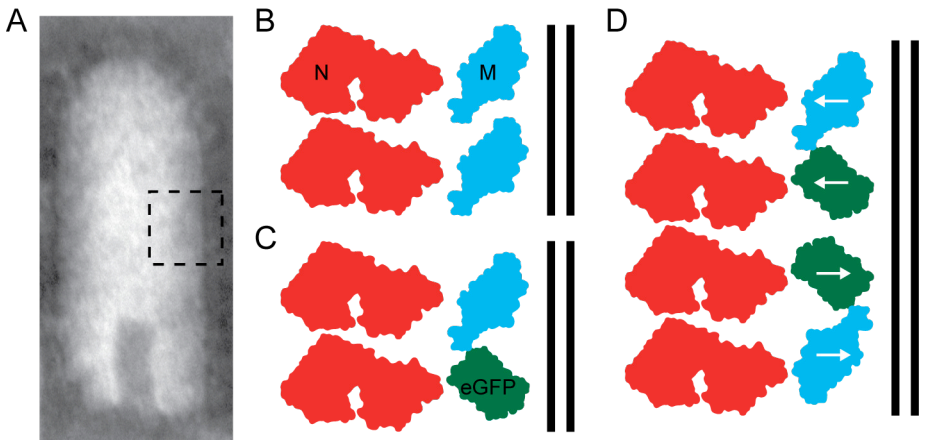

Figure 5.3. Model for orientation of M-eGFP relative to N and the membrane in virions. (A) The location of the schematic relative to a VSV virion is illustrated. (B) In wild type VSV virions, under the lipid bilayer (vertical black lines) are a helix of M (blue) and an inner helix of N (red) (1). (C) For VSV M-eGFP, the M helix may contain the M or eGFP domain of M-eGFP in each wild type M position. (D) Since GFP is able to form antiparallel dimers (182), M-eGFP may form dimers where 1 monomer is facing the membrane and the other is facing N.

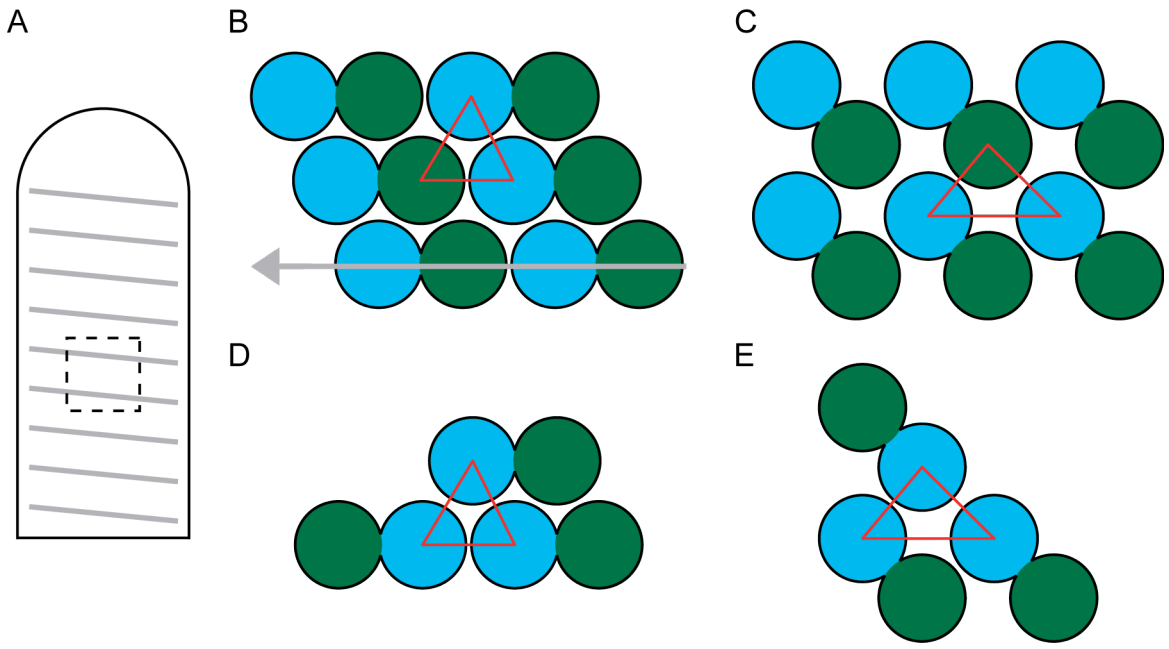

Figure 5.4. Models for packing of M-eGFP in the M-helix.
The M (blue) and eGFP (green) domains of M-eGFP could each be occupying a wild type M position. (A) The orientation of the schematic relative to the particle is illustrated, and the grey arrow denotes the direction of the left-handed helix (1). The triangularly packed lattice is shown in red. (B) The M-eGFP could be orientated head-tail in the direction of the helix or (C) the M and eGFP domains could form adjacent "rows" to allow M-M interactions in the direction of the helix. The M domains of multiple M-eGFP molecules could be orientated towards each other with eGFP orientated either parallel to the helix (D) or between "rows" (E).

Identification of VSV assembly events in live infected cells

In VSV infected cells, the majority of fluorescent M does not appear to be actively involved in assembly (Chapter 3). Perhaps the difficulty in identifying assembly events is in screening the cell surface for regions of interest. During assembly, the viral RNP is condensed into a compact regular structure (1), and detection of this compaction by förster resonance energy transfer (FRET) could identify assembling particles (138). Ratiometric FRET was used to identify putative condensation events at a single time point (Chapter 3). The images display low FRET efficiencies, and a concern with ratiometric FRET is whether these puncta are due to variations in the bleedthrough correction. Fluorescence lifetime imaging microscopy (FLIM) FRET is a more robust method of determining FRET since it measures the fluorescence lifetime, which is a property of the fluorophore and is independent of the fluorescent intensity (183). Combining FLIM FRET with a timecourse would demonstrate if these particles are still forming, *e.g.* increasing in fluorescent intensity, or if they are released into the supernatant, *e.g.* show rapid movement. FRET measurements could also be followed by fluorescence recovery after photobleaching (FRAP) analysis to determine if the puncta of high FRET have undergone fission. Combining FLIM FRET, FRAP, and time lapse imaging could facilitate screening cells for assembling particles.

An alternate method to screen for VSV assembly events is the colocalization with proteins that mediate a late step in assembly. The ESCRT pathway is a good candidate since these proteins mediate the final step of egress, *i.e.* fission, and associate with assembling particles (143). A number of stable fluorescent fusion cell lines with moderate expression levels have been isolated and used for studying the assembly of HIV-1 VLPs (143). We tried transfection of vacuolar protein sorting 4 (Vps4), the last protein to be recruited in the ESCRT

pathway (184), to screen for assembling particles (Chapter 3). However, transfection led to inconsistent expression levels. Stable cell lines would insure that all cells express a moderate level of the tagged protein and could aid in identification of which viral puncta are actively assembling.

Tracking M and G microdomains and their role in assembly in real time

M and G form microdomains at the plasma membrane that coalesce during assembly (34, 64). Microdomains of M are 50-100 nm in diameter (64) and of G are 100-150 nm in diameter (34). Both of these are below the diffraction limit of the light microscope, which are 188 nm for eGFP and 227 nm for mCherry, see equation below. However, the amalgamation of diffraction limited M and G puncta is not seen in infected cells. Since the microdomains are smaller than the resolution, a diffraction limited volume will contain protein that is not part of the microdomain. If the proteins in microdomains are not sufficiently denser than free protein, then the noise of the microscope would obscure the additional signal from the microdomain. Alternatively, the microdomains may be highly dynamic and undergoing continuous rearrangement. These situations would result in the microdomains not being observable on the total internal reflection fluorescence (TIRF) microscope.

$$\text{Resolution} = \frac{\lambda}{2\text{NA}} \qquad \text{NA} = n \sin\theta$$

λ is wavelength
n is the index of refraction
θ is the aperture angle

If the microdomains cannot be identified by intensity, then a different method would need to be used. Microdomains should diffuse slower due to their increased size and protein-protein interactions that hold them together. Diffusion of fluorescent proteins in live cells can be

measured with fluorescence correlation spectroscopy (FCS). This technique analyzes a single diffraction limited volume for the variation in fluorescent intensity over time (185) and calculates the 2D diffusion time (τ_D) (186). It can be performed at multiple locations in a single optical plane (186) to look for variations in τ_D, where higher values would indicate slower movement and a microdomain.

$$\frac{\langle (I(t) - \langle I \rangle)(I(t+\tau) - \langle I \rangle) \rangle}{\langle I \rangle^2} = G(\tau)$$

$$G(\tau) = \frac{1}{N}\left(1 + \tau / \tau_D\right)^{-1}$$

I(t) is the intensity at time t
$G(\tau)$ is the autocorrelation function
N is the average number of particles in the volume
τ is the delay time
τ_D is the diffusion time

While FCS analyzes a single point, image correlation spectroscopy (ICS) examines an entire field of view (187). This would allow for regions of slow diffusion to be identified as well as the determination of how fast microdomains move, assemble, and disassemble. This method has been used to illustrate the association of the ebola virus (EboV) virion protein 40 (VP40), the matrix protein, with the plasma membrane by the measurement of a slower diffusion (188). A related method, image cross-correlation spectroscopy (ICCS), determines the correlation between 2 fluorophores (187). This could identify regions where M and G are moving together, which would identify locations of particle assembly (64). This could be combined with a P-fusion to confirm colocalization with the viral RNP. In addition, correlative transmission electron microscopy (TEM) at the regions with high cross-correlation could confirm assembly through the presence of the electron-dense NCM complex. FCS and the related techniques could measure the dynamics and kinetics of M and G microdomains and their involvement in VSV assembly.

Involvement of late domains in the assembly of other viruses

Many enveloped viruses contain late domains to mediate fission (108), and it would be interesting to determine if they also show the biased incorporation of functional matrix protein over the late domain mutant. In order to perform the competition assay (Chapter 4), the matrix protein must compete for incorporation into a finite structure in the virus particle. Other (-) ssRNA viruses that contain late domains are the filovirus EboV (125), arenavirus lymphocytic choriomeningitis virus (LCMV) (126), and paramyxovirus Sendai virus (SeV) (123). However, EboV VP40 forms VLPs that vary in length (7), and LCMV (189) and SeV (190) form variable sized spherical particles. The pleomorphic nature of these virus families prevents them from working in the competition assay since they likely do not contain a finite amount of matrix protein. We assessed HIV-1 Gag VLPs for this criteria, but the particles are too pleomorphic (Chapter 4). However, mature HIV-1 particles contain Gag in a fullerene cone structure (191). Since this is a finite structure, HIV-1 may be amenable to the competition assay.

Application of studying competition between proteins with known genetic origin

The competition assay used to demonstrate the role of M late domains in the incorporation of M into released particles has a number of applications. Other M features may also be involved in packaging. While the subcellular location of phosphorylated M correlates with assembly, no essential function as been attributed to this modification (192, 193). Perhaps like late domains, phosphorylation affects the efficiency of assembly but is not required. Alternatively, competition for translocation could be studied. Since the nucleus is spatially separated from the cytoplasm, the ratio of wild type to mutant M at each location could be

compared. If M in released particles is more heavily phosphorylated, perhaps the unphosphorylated M is not transported to the plasma membrane where assembly occurs.

This method can also be applied to any protein that can be fluorescently tagged, such as P or L. The active form of these proteins are oligomers (47, 194), and the role of oligomerization in incorporation into particles is not known. The competition between monomers and oligomers for packaging could be examined. However, oligomerization would be an added complication when evaluating the role of other protein features. If the oligomers do not exchange, then the less efficient variant in hetero-oligomers would still be packaged. Conversely, if there is rapid exchange or there is a large efficiency difference, then competition variations could still be measured. This competition assay could also be applied to cellular proteins or other viruses, as long as the tagged proteins compete and the readout can be spatially or temporally isolated.

Application of fluorescent M to entry studies

The generation of a functional fluorescent protein fusion to M creates fluorescent virions, which have a number of uses in entry studies. This virus permits the tracking of particles during cellular binding, internalization, and uncoating, which can be used to investigate the transport and endosomal maturation that is required for VSV fusion. Internalized particles can be tracked by M, and hemi-fusion can be monitored by the dequenching of a lipid dye soaked into virions (195). Separation of M from the dequenched dye confirms pore formation and delivery of the internal components into the cytoplasm, and the location of fusion can be determined by the colocalization of these events with endosomal markers (195).

These methods to study the entry of VSV can also be applied to the study of other enveloped viruses since G in the VSV genome can be replaced with the glycoprotein from a number of different viruses, *e.g.* EboV (196), rabies virus (RabV) (197), or lassa virus (LasV) (196, 198), and the glycoprotein is sufficient for entry. VSV containing M-eGFP and the LasV glycoprotein (GP) was used to study the host factors required for LasV entry (198). M-eGFP permits the visualization of incoming particles, and the release of vesicle-bound puncta into the cytoplasm denotes that fusion has occurred (26). Conversely, the accumulation of M-eGFP inside vesicles illustrates that viral fusion is blocked. To test the involvement of lysosomal-associated membrane protein 1 (LAMP1) as a host factor, wild type and LAMP1 deficient cells were infected with VSV M-eGFP LasV GP. While M-eGFP is released into the cytoplasm of wild type cells, it localizes to vesicles in the mutant cells, demonstrating that binding of LasV GP to LAMP1 precedes membrane fusion (198). This M-release assay allows for the confirmation that fusion has occurred inside cells and can be used to assess which steps in entry are essential for achieving membrane fusion.

Perspectives

The *Rhabdoviridae* family displays a characteristic bullet-shape, but the mechanism through which this structure is generated is unknown. For VSV, this may be due to the assembly of protein helices inside the virion (1), although these helices may only be partially filled and contain a variable amount of protein. M is essential for condensation of the viral RNP into the bullet-shaped NCM complex, but this process may only require a small quantity of M. Formation of the NCM complex may proceed through at least 2 steps where a minor amount of M initiates this process but the N-RNA can rearrange itself into the bullet-shape that recruits the majority of

M. Viruses utilize host pathways in their replication cycles, but sometimes through a mechanism that is unexpected based on the cellular function. The ESCRT pathway may play a role in VSV assembly prior to fission, and it has also been found to be important for RNA replication by the non-enveloped brome mosaic virus (199). Future studies of viral assembly will benefit greatly from fluorescent fusions to viral proteins and fluorescence microscopy. Protein interactions as well as their functional outcome can be examined with high spatial and temporal resolutions in live cells, providing the ability to address previously unanswerable questions.

References

1. **Ge P, Tsao J, Schein S, Green TJ, Luo M, Zhou ZH.** 2010. Cryo-EM model of the bullet-shaped vesicular stomatitis virus. Science **327**:689-693.

2. **Pringle CR.** 1991. The order *Mononegavirales*. Archives Virology **117**:137-140.

3. **Waterson AP, Jensen KE, Tyrrell DA, Horne RW.** 1961. The structure of parainfluenza 3 virus. Virology **14**:374-378.

4. **Gould AR, Hyatt AD, Lunt R, Kattenbelt JA, Hengstberger S, Blacksell SD.** 1998. Characterisation of a novel lyssavirus isolated from Pteropid bats in Australia. Virus Res **54**:165-187.

5. **Li Y, Luo L, Schubert M, Wagner RR, Kang CY.** 1993. Viral liposomes released from insect cells infected with recombinant baculovirus expressing the matrix protein of vesicular stomatitis virus. J Virol **67**:4415-4420.

6. **Justice PA, Sun W, Li Y, Ye Z, Grigera PR, Wagner RR.** 1995. Membrane vesiculation function and exocytosis of wild-type and mutant matrix proteins of vesicular stomatitis virus. J Virol **69**:3156-3160.

7. **Noda T, Sagara H, Suzuki E, Takada A, Kida H, Kawaoka Y.** 2002. Ebola virus VP40 drives the formation of virus-like filamentous particles along with GP. J Virol **76**:4855-4865.

8. **Lawson ND, Stillman EA, Whitt MA, Rose JK.** 1995. Recombinant vesicular stomatitis viruses from DNA. Proc Natl Acad Sci U S A **92**:4477-4481.

9. **Whelan SP, Ball LA, Barr JN, Wertz GT.** 1995. Efficient recovery of infectious vesicular stomatitis virus entirely from cDNA clones. Proc Natl Acad Sci U S A **92**:8388-8392.

10. **King AMQ, Adams MJ, Carstens EB, Lefkowitz EJ.** 2014. Virus taxonomy: classification and nomenclature of viruses: Ninth Report of the International Committee on Taxonomy of Viruses.

11. **Sun X, Yau VK, Briggs BJ, Whittaker GR.** 2005. Role of clathrin-mediated endocytosis during vesicular stomatitis virus entry into host cells. Virology **338**:53-60.

12. **White J, Matlin K, Helenius A.** 1981. Cell fusion by Semliki Forest, influenza, and vesicular stomatitis viruses. J Cell Biol **89**:674-679.

13. **Blumenthal R, Bali-Puri A, Walter A, Covell D, Eidelman O.** 1987. pH-dependent fusion of vesicular stomatitis virus with Vero cells. Measurement by dequenching of octadecyl rhodamine fluorescence. J Biol Chem **262**:13614-13619.

14. **Emerson SU, Wagner RR.** 1972. Dissociation and reconstitution of the transcriptase and template activities of vesicular stomatitis B and T virions. J Virol **10**:297-309.

15. **Knipe DM, Baltimore D, Lodish HF.** 1977. Separate pathways of maturation of the major structural proteins of vesicular stomatitis virus. J Virol **21**:1128-1139.

16. **Newcomb WW, Brown JC.** 1981. Role of the vesicular stomatitis virus matrix protein in maintaining the viral nucleocapsid in the condensed form found in native virions. J Virol **39**:295-299.

17. **Schloemer RH, Wagner RR.** 1975. Cellular adsorption function of the sialoglycoprotein of vesicular stomatitis virus and its neuraminic acid. J Virol **15**:882-893.

18. **Finkelshtein D, Werman A, Novick D, Barak S, Rubinstein M.** 2013. LDL receptor and its family members serve as the cellular receptors for vesicular stomatitis virus. Proc Natl Acad Sci U S A **110**:7306-7311.

19. **Schlegel R, Willingham MC, Pastan IH.** 1982. Saturable binding sites for vesicular stomatitis virus on the surface of Vero cells. J Virol **43**:871-875.

20. **Carneiro FA, Bianconi ML, Weissmuller G, Stauffer F, Da Poian AT.** 2002. Membrane recognition by vesicular stomatitis virus involves enthalpy-driven protein-lipid interactions. J Virol **76**:3756-3764.

21. **Schlegel R, Tralka TS, Willingham MC, Pastan I.** 1983. Inhibition of VSV binding and infectivity by phosphatidylserine: is phosphatidylserine a VSV-binding site? Cell **32**:639-646.

22. **Kalvodova L, Sampaio JL, Cordo S, Ejsing CS, Shevchenko A, Simons K.** 2009. The lipidomes of vesicular stomatitis virus, semliki forest virus, and the host plasma membrane analyzed by quantitative shotgun mass spectrometry. J Virol **83**:7996-8003.

23. **Jemielity S, Wang JJ, Chan YK, Ahmed AA, Li W, Monahan S, Bu X, Farzan M, Freeman GJ, Umetsu DT, Dekruyff RH, Choe H.** 2013. TIM-family proteins promote infection of multiple enveloped viruses through virion-associated phosphatidylserine. PLoS Pathog **9**:e1003232.

24. **Mire CE, White JM, Whitt MA.** 2010. A spatio-temporal analysis of matrix protein and nucleocapsid trafficking during vesicular stomatitis virus uncoating. PLoS Pathog **6**:e1000994.

25. **Le Blanc I, Luyet PP, Pons V, Ferguson C, Emans N, Petiot A, Mayran N, Demaurex N, Faure J, Sadoul R, Parton RG, Gruenberg J.** 2005. Endosome-to-cytosol transport of viral nucleocapsids. Nat Cell Biol **7**:653-664.

26. **Rigaut KD, Birk DE, Lenard J.** 1991. Intracellular distribution of input vesicular stomatitis virus proteins after uncoating. J Virol **65**:2622-2628.

27. **Katz FN, Lodish HF.** 1979. Transmembrane biogenesis of the vesicular stomatitis virus glycoprotein. J Cell Biol **80**:416-426.

28. **Doms RW, Keller DS, Helenius A, Balch WE.** 1987. Role for adenosine triphosphate in regulating the assembly and transport of vesicular stomatitis virus G protein trimers. J Cell Biol **105**:1957-1969.

29. **Kreis TE, Lodish HF.** 1986. Oligomerization is essential for transport of vesicular stomatitis viral glycoprotein to the cell surface. Cell **46**:929-937.

30. **McSharry JJ, Wagner RR.** 1971. Carbohydrate composition of vesicular stomatitis virus. J Virol **7**:412-415.

31. **Reading CL, Penhoet EE, Ballou CE.** 1978. Carbohydrate structure of vesicular stomatitis virus glycoprotein. J Biol Chem **253**:5600-5612.

32. **Hammond C, Helenius A.** 1994. Folding of VSV G protein: sequential interaction with BiP and calnexin. Science **266**:456-458.

33. **Doms RW, Ruusala A, Machamer C, Helenius J, Helenius A, Rose JK.** 1988. Differential effects of mutations in three domains on folding, quaternary structure, and intracellular transport of vesicular stomatitis virus G protein. J Cell Biol **107**:89-99.

34. **Brown EL, Lyles DS.** 2003. Organization of the vesicular stomatitis virus glycoprotein into membrane microdomains occurs independently of intracellular viral components. J Virol **77**:3985-3992.

35. **Emerson SU, Schubert M.** 1987. Location of the binding domains for the RNA polymerase L and the ribonucleocapsid template within different halves of the NS phosphoprotein of vesicular stomatitis virus. Proc Natl Acad Sci U S A **84**:5655-5659.

36. **Naito S, Ishihama A.** 1976. Function and structure of RNA polymerase from vesicular stomatitis virus. J Biol Chem **251**:4307-4314.

37. **Patton JT, Davis NL, Wertz GW.** 1984. N protein alone satisfies the requirement for protein synthesis during RNA replication of vesicular stomatitis virus. J Virol **49**:303-309.

38. **Green TJ, Zhang X, Wertz GW, Luo M.** 2006. Structure of the vesicular stomatitis virus nucleoprotein-RNA complex. Science **313**:357-360.

39. **Sleat DE, Banerjee AK.** 1993. Transcriptional activity and mutational analysis of recombinant vesicular stomatitis virus RNA polymerase. J Virol **67**:1334-1339.

40. **Ogino T, Banerjee AK.** 2007. Unconventional mechanism of mRNA capping by the RNA-dependent RNA polymerase of vesicular stomatitis virus. Mol Cell **25**:85-97.

41. **Li J, Rahmeh A, Morelli M, Whelan SP.** 2008. A conserved motif in region v of the large polymerase proteins of nonsegmented negative-sense RNA viruses that is essential for mRNA capping. J Virol **82**:775-784.

42. **Li J, Fontaine-Rodriguez EC, Whelan SP.** 2005. Amino acid residues within conserved domain VI of the vesicular stomatitis virus large polymerase protein essential for mRNA cap methyltransferase activity. J Virol **79**:13373-13384.

43. **Li J, Wang JT, Whelan SP.** 2006. A unique strategy for mRNA cap methylation used by vesicular stomatitis virus. Proc Natl Acad Sci U S A **103**:8493-8498.

44. **Rahmeh AA, Li J, Kranzusch PJ, Whelan SP.** 2009. Ribose 2'-O methylation of the vesicular stomatitis virus mRNA cap precedes and facilitates subsequent guanine-N-7 methylation by the large polymerase protein. J Virol **83**:11043-11050.

45. **Hunt DM, Mehta R, Hutchinson KL.** 1988. The L protein of vesicular stomatitis virus modulates the response of the polyadenylic acid polymerase to S-adenosylhomocysteine. J Gen Virol **69 (Pt 10)**:2555-2561.

46. **Emerson SU, Yu Y.** 1975. Both NS and L proteins are required for in vitro RNA synthesis by vesicular stomatitis virus. J Virol **15**:1348-1356.

47. **Rahmeh AA, Schenk AD, Danek EI, Kranzusch PJ, Liang B, Walz T, Whelan SP.** 2010. Molecular architecture of the vesicular stomatitis virus RNA polymerase. Proc Natl Acad Sci U S A **107**:20075-20080.

48. **Morin B, Rahmeh AA, Whelan SP.** 2012. Mechanism of RNA synthesis initiation by the vesicular stomatitis virus polymerase. Embo J **31**:1320-1329.

49. **Pattnaik AK, Wertz GW.** 1990. Replication and amplification of defective interfering particle RNAs of vesicular stomatitis virus in cells expressing viral proteins from vectors containing cloned cDNAs. J Virol **64**:2948-2957.

50. **Pattnaik AK, Wertz GW.** 1991. Cells that express all five proteins of vesicular stomatitis virus from cloned cDNAs support replication, assembly, and budding of defective interfering particles. Proc Natl Acad Sci U S A **88**:1379-1383.

51. **Pattnaik AK, Ball LA, LeGrone AW, Wertz GW.** 1992. Infectious defective interfering particles of VSV from transcripts of a cDNA clone. Cell **69**:1011-1020.

52. **Ball LA, White CN.** 1976. Order of transcription of genes of vesicular stomatitis virus. Proc Natl Acad Sci U S A **73**:442-446.

53. **Iverson LE, Rose JK.** 1981. Localized attenuation and discontinuous synthesis during vesicular stomatitis virus transcription. Cell **23**:477-484.

54. **Barr JN, Whelan SP, Wertz GW.** 1997. cis-Acting signals involved in termination of vesicular stomatitis virus mRNA synthesis include the conserved AUAC and the U7 signal for polyadenylation. J Virol **71**:8718-8725.

55. **Stillman EA, Whitt MA.** 1997. Mutational analyses of the intergenic dinucleotide and the transcriptional start sequence of vesicular stomatitis virus (VSV) define sequences required for efficient termination and initiation of VSV transcripts. J Virol **71**:2127-2137.

56. **Heinrich BS, Cureton DK, Rahmeh AA, Whelan SP.** 2010. Protein expression redirects vesicular stomatitis virus RNA synthesis to cytoplasmic inclusions. PLoS Pathog **6**:e1000958.

57. **Das SC, Nayak D, Zhou Y, Pattnaik AK.** 2006. Visualization of intracellular transport of vesicular stomatitis virus nucleocapsids in living cells. J Virol **80**:6368-6377.

58. **Whelan SP, Wertz GW.** 1999. The 5' terminal trailer region of vesicular stomatitis virus contains a position-dependent cis-acting signal for assembly of RNA into infectious particles. J Virol **73**:307-315.

59. **Black BL, Lyles DS.** 1992. Vesicular stomatitis virus matrix protein inhibits host cell-directed transcription of target genes in vivo. J Virol **66**:4058-4064.

60. **Gaudier M, Gaudin Y, Knossow M.** 2001. Cleavage of vesicular stomatitis virus matrix protein prevents self-association and leads to crystallization. Virology **288**:308-314.

61. **Gaudin Y, Sturgis J, Doumith M, Barge A, Robert B, Ruigrok RW.** 1997. Conformational flexibility and polymerization of vesicular stomatitis virus matrix protein. J Mol Biol **274**:816-825.

62. **Ye Z, Sun W, Suryanarayana K, Justice P, Robinson D, Wagner RR.** 1994. Membrane-binding domains and cytopathogenesis of the matrix protein of vesicular stomatitis virus. J Virol **68**:7386-7396.

63. **Lenard J, Vanderoef R.** 1990. Localization of the membrane-associated region of vesicular stomatitis virus M protein at the N terminus, using the hydrophobic, photoreactive probe 125I-TID. J Virol **64**:3486-3491.

64. **Swinteck BD, Lyles DS.** 2008. Plasma membrane microdomains containing vesicular stomatitis virus M protein are separate from microdomains containing G protein and nucleocapsids. J Virol **82**:5536-5547.

65. **Chong LD, Rose JK.** 1994. Interactions of normal and mutant vesicular stomatitis virus matrix proteins with the plasma membrane and nucleocapsids. J Virol **68**:441-447.

66. **Capone J, Ghosh HP.** 1984. Association of the nucleocapsid protein N of vesicular stomatitis virus with phospholipid vesicles containing the matrix protein M. Can J Biochem Cell Biol **62**:1174-1180.

67. **Watanabe R, Lamb RA.** 2010. Influenza virus budding does not require a functional AAA+ ATPase, VPS4. Virus Res **153**:58-63.

68. **Jayakar HR, Murti KG, Whitt MA.** 2000. Mutations in the PPPY motif of vesicular stomatitis virus matrix protein reduce virus budding by inhibiting a late step in virion release. J Virol **74**:9818-9827.

69. **Obiang L, Raux H, Ouldali M, Blondel D, Gaudin Y.** 2012. Phenotypes of vesicular stomatitis virus mutants with mutations in the PSAP motif of the matrix protein. J Gen Virol **93**:857-865.

70. **Irie T, Licata JM, Jayakar HR, Whitt MA, Bell P, Harty RN.** 2004. Functional analysis of late-budding domain activity associated with the PSAP motif within the vesicular stomatitis virus M protein. J Virol **78**:7823-7827.

71. **Coulon P, Deutsch V, Lafay F, Martinet-Edelist C, Wyers F, Herman RC, Flamand A.** 1990. Genetic evidence for multiple functions of the matrix protein of vesicular stomatitis virus. J Gen Virol **71 (Pt 4)**:991-996.

72. **Ahmed M, Lyles DS.** 1998. Effect of vesicular stomatitis virus matrix protein on transcription directed by host RNA polymerases I, II, and III. J Virol **72**:8413-8419.

73. **Her LS, Lund E, Dahlberg JE.** 1997. Inhibition of Ran guanosine triphosphatase-dependent nuclear transport by the matrix protein of vesicular stomatitis virus. Science **276**:1845-1848.

74. **Faria PA, Chakraborty P, Levay A, Barber GN, Ezelle HJ, Enninga J, Arana C, van Deursen J, Fontoura BM.** 2005. VSV disrupts the Rae1/mrnp41 mRNA nuclear export pathway. Mol Cell **17**:93-102.

75. **von Kobbe C, van Deursen JM, Rodrigues JP, Sitterlin D, Bachi A, Wu X, Wilm M, Carmo-Fonseca M, Izaurralde E.** 2000. Vesicular stomatitis virus matrix protein inhibits host cell gene expression by targeting the nucleoporin Nup98. Mol Cell **6**:1243-1252.

76. **Brown JA, Bharathi A, Ghosh A, Whalen W, Fitzgerald E, Dhar R.** 1995. A mutation in the Schizosaccharomyces pombe rae1 gene causes defects in poly(A)+ RNA export and in the cytoskeleton. J Biol Chem **270**:7411-7419.

77. **Powers MA, Forbes DJ, Dahlberg JE, Lund E.** 1997. The vertebrate GLFG nucleoporin, Nup98, is an essential component of multiple RNA export pathways. J Cell Biol **136**:241-250.

78. **Quan B, Seo HS, Blobel G, Ren Y.** 2014. Vesiculoviral matrix (M) protein occupies nucleic acid binding site at nucleoporin pair (Rae1 * Nup98). Proc Natl Acad Sci U S A **111**:9127-9132.

79. **Rajani KR, Pettit Kneller EL, McKenzie MO, Horita DA, Chou JW, Lyles DS.** 2012. Complexes of vesicular stomatitis virus matrix protein with host Rae1 and Nup98 involved in inhibition of host transcription. PLoS Pathog **8**:e1002929.

80. **Yuan H, Yoza BK, Lyles DS.** 1998. Inhibition of host RNA polymerase II-dependent transcription by vesicular stomatitis virus results from inactivation of TFIID. Virology **251**:383-392.

81. **Gaudier M, Gaudin Y, Knossow M.** 2002. Crystal structure of vesicular stomatitis virus matrix protein. Embo J **21**:2886-2892.

82. **Graham SC, Assenberg R, Delmas O, Verma A, Gholami A, Talbi C, Owens RJ, Stuart DI, Grimes JM, Bourhy H.** 2008. Rhabdovirus matrix protein structures reveal a novel mode of self-association. PLoS Pathog **4**:e1000251.

83. **Bornholdt ZA, Noda T, Abelson DM, Halfmann P, Wood MR, Kawaoka Y, Saphire EO.** 2013. Structural rearrangement of ebola virus VP40 begets multiple functions in the virus life cycle. Cell **154**:763-774.

84. **Connor JH, McKenzie MO, Lyles DS.** 2006. Role of residues 121 to 124 of vesicular stomatitis virus matrix protein in virus assembly and virus-host interaction. J Virol **80**:3701-3711.

85. **Raux H, Obiang L, Richard N, Harper F, Blondel D, Gaudin Y.** 2010. The matrix protein of vesicular stomatitis virus binds dynamin for efficient viral assembly. J Virol **84**:12609-12618.

86. **Jayakar HR, Whitt MA.** 2002. Identification of two additional translation products from the matrix (M) gene that contribute to vesicular stomatitis virus cytopathology. J Virol **76**:8011-8018.

87. **Glodowski DR, Petersen JM, Dahlberg JE.** 2002. Complex nuclear localization signals in the matrix protein of vesicular stomatitis virus. J Biol Chem **277**:46864-46870.

88. **Kaptur PE, McCreedy BJ, Jr., Lyles DS.** 1992. Sites of in vivo phosphorylation of vesicular stomatitis virus matrix protein. J Virol **66**:5384-5392.

89. **Schnell MJ, Buonocore L, Boritz E, Ghosh HP, Chernish R, Rose JK.** 1998. Requirement for a non-specific glycoprotein cytoplasmic domain sequence to drive efficient budding of vesicular stomatitis virus. Embo J **17**:1289-1296.

90. **Robison CS, Whitt MA.** 2000. The membrane-proximal stem region of vesicular stomatitis virus G protein confers efficient virus assembly. J Virol **74**:2239-2246.

91. **Takada A, Robison C, Goto H, Sanchez A, Murti KG, Whitt MA, Kawaoka Y.** 1997. A system for functional analysis of Ebola virus glycoprotein. Proc Natl Acad Sci U S A **94**:14764-14769.

92. **Desfosses A, Ribeiro EA, Jr., Schoehn G, Blondel D, Guilligay D, Jamin M, Ruigrok RW, Gutsche I.** 2013. Self-organization of the vesicular stomatitis virus nucleocapsid into a bullet shape. Nat Commun **4**:1429.

93. **Newcomb WW, Tobin GJ, McGowan JJ, Brown JC.** 1982. In vitro reassembly of vesicular stomatitis virus skeletons. J Virol **41**:1055-1062.

94. **Gopalakrishna Y, Lenard J.** 1985. Sequence alterations in temperature-sensitive M-protein mutants (complementation group III) of vesicular stomatitis virus. J Virol **56**:655-659.

95. **Lyles DS, McKenzie MO, Kaptur PE, Grant KW, Jerome WG.** 1996. Complementation of M gene mutants of vesicular stomatitis virus by plasmid-derived M protein converts spherical extracellular particles into native bullet shapes. Virology **217**:76-87.

96. **Mebatsion T, Weiland F, Conzelmann KK.** 1999. Matrix protein of rabies virus is responsible for the assembly and budding of bullet-shaped particles and interacts with the transmembrane spike glycoprotein G. J Virol **73**:242-250.

97. **Lyles DS, McKenzie MO.** 1998. Reversible and irreversible steps in assembly and disassembly of vesicular stomatitis virus: equilibria and kinetics of dissociation of nucleocapsid-M protein complexes assembled in vivo. Biochemistry **37**:439-450.

98. **Flood EA, Lyles DS.** 1999. Assembly of nucleocapsids with cytosolic and membrane-derived matrix proteins of vesicular stomatitis virus. Virology **261**:295-308.

99. **Thomas D, Newcomb WW, Brown JC, Wall JS, Hainfeld JF, Trus BL, Steven AC.** 1985. Mass and molecular composition of vesicular stomatitis virus: a scanning transmission electron microscopy analysis. J Virol **54**:598-607.

100. **Barge A, Gaudin Y, Coulon P, Ruigrok RW.** 1993. Vesicular stomatitis virus M protein may be inside the ribonucleocapsid coil. J Virol **67**:7246-7253.

101. **Green TJ, Luo M.** 2009. Structure of the vesicular stomatitis virus nucleocapsid in complex with the nucleocapsid-binding domain of the small polymerase cofactor, P. Proc Natl Acad Sci U S A **106**:11713-11718.

102. **Hodges J, Tang X, Landesman MB, Ruedas JB, Ghimire A, Gudheti MV, Perrault J, Jorgensen EM, Gerton JM, Saffarian S.** 2013. Asymmetric packaging of polymerases within vesicular stomatitis virus. Biochem Biophys Res Commun **440**:271-276.

103. **Green TJ, Macpherson S, Qiu S, Lebowitz J, Wertz GW, Luo M.** 2000. Study of the assembly of vesicular stomatitis virus N protein: role of the P protein. J Virol **74**:9515-9524.

104. **Kranzusch PJ, Whelan SP.** 2011. Arenavirus Z protein controls viral RNA synthesis by locking a polymerase-promoter complex. Proc Natl Acad Sci U S A **108**:19743-19748.

105. **Lyles DS, McKenzie M, Parce JW.** 1992. Subunit interactions of vesicular stomatitis virus envelope glycoprotein stabilized by binding to viral matrix protein. J Virol **66**:349-358.

106. **Gottlinger HG, Dorfman T, Sodroski JG, Haseltine WA.** 1991. Effect of mutations affecting the p6 gag protein on human immunodeficiency virus particle release. Proc Natl Acad Sci U S A **88**:3195-3199.

107. **Demirov DG, Orenstein JM, Freed EO.** 2002. The late domain of human immunodeficiency virus type 1 p6 promotes virus release in a cell type-dependent manner. J Virol **76**:105-117.

108. **Chen BJ, Lamb RA.** 2008. Mechanisms for enveloped virus budding: can some viruses do without an ESCRT? Virology **372**:221-232.

109. **Votteler J, Sundquist WI.** 2013. Virus budding and the ESCRT pathway. Cell Host Microbe **14**:232-241.

110. **Martin-Serrano J, Eastman SW, Chung W, Bieniasz PD.** 2005. HECT ubiquitin ligases link viral and cellular PPXY motifs to the vacuolar protein-sorting pathway. J Cell Biol **168**:89-101.

111. **Babst M, Katzmann DJ, Snyder WB, Wendland B, Emr SD.** 2002. Endosome-associated complex, ESCRT-II, recruits transport machinery for protein sorting at the multivesicular body. Dev Cell **3**:283-289.

112. **Kay BK, Williamson MP, Sudol M.** 2000. The importance of being proline: the interaction of proline-rich motifs in signaling proteins with their cognate domains. Faseb J **14**:231-241.

113. **Huang X, Poy F, Zhang R, Joachimiak A, Sudol M, Eck MJ.** 2000. Structure of a WW domain containing fragment of dystrophin in complex with beta-dystroglycan. Nat Struct Biol **7**:634-638.

114. **Harty RN, Brown ME, McGettigan JP, Wang G, Jayakar HR, Huibregtse JM, Whitt MA, Schnell MJ.** 2001. Rhabdoviruses and the cellular ubiquitin-proteasome system: a budding interaction. J Virol **75**:10623-10629.

115. **Harty RN, Paragas J, Sudol M, Palese P.** 1999. A proline-rich motif within the matrix protein of vesicular stomatitis virus and rabies virus interacts with WW domains of cellular proteins: implications for viral budding. J Virol **73**:2921-2929.

116. **Pornillos O, Alam SL, Davis DR, Sundquist WI.** 2002. Structure of the Tsg101 UEV domain in complex with the PTAP motif of the HIV-1 p6 protein. Nat Struct Biol **9**:812-817.

117. **Katzmann DJ, Babst M, Emr SD.** 2001. Ubiquitin-dependent sorting into the multivesicular body pathway requires the function of a conserved endosomal protein sorting complex, ESCRT-I. Cell **106**:145-155.

118. **Strack B, Calistri A, Craig S, Popova E, Gottlinger HG.** 2003. AIP1/ALIX is a binding partner for HIV-1 p6 and EIAV p9 functioning in virus budding. Cell **114**:689-699.

119. **McCullough J, Fisher RD, Whitby FG, Sundquist WI, Hill CP.** 2008. ALIX-CHMP4 interactions in the human ESCRT pathway. Proc Natl Acad Sci U S A **105**:7687-7691.

120. **Lee S, Joshi A, Nagashima K, Freed EO, Hurley JH.** 2007. Structural basis for viral late-domain binding to Alix. Nat Struct Mol Biol **14**:194-199.

121. **Morita E, Sandrin V, McCullough J, Katsuyama A, Baci Hamilton I, Sundquist WI.** 2011. ESCRT-III protein requirements for HIV-1 budding. Cell Host Microbe **9**:235-242.

122. **Morita E, Colf LA, Karren MA, Sandrin V, Rodesch CK, Sundquist WI.** 2010. Human ESCRT-III and VPS4 proteins are required for centrosome and spindle maintenance. Proc Natl Acad Sci U S A **107**:12889-12894.

123. **Irie T, Shimazu Y, Yoshida T, Sakaguchi T.** 2007. The YLDL sequence within Sendai virus M protein is critical for budding of virus-like particles and interacts with Alix/AIP1 independently of C protein. J Virol **81**:2263-2273.

124. **Martin-Serrano J, Zang T, Bieniasz PD.** 2001. HIV-1 and Ebola virus encode small peptide motifs that recruit Tsg101 to sites of particle assembly to facilitate egress. Nat Med **7**:1313-1319.

125. **Harty RN, Brown ME, Wang G, Huibregtse J, Hayes FP.** 2000. A PPxY motif within the VP40 protein of Ebola virus interacts physically and functionally with a ubiquitin ligase: implications for filovirus budding. Proc Natl Acad Sci U S A **97**:13871-13876.

126. **Perez M, Craven RC, de la Torre JC.** 2003. The small RING finger protein Z drives arenavirus budding: implications for antiviral strategies. Proc Natl Acad Sci U S A **100**:12978-12983.

127. **Garrus JE, von Schwedler UK, Pornillos OW, Morham SG, Zavitz KH, Wang HE, Wettstein DA, Stray KM, Cote M, Rich RL, Myszka DG, Sundquist WI.** 2001. Tsg101 and the vacuolar protein sorting pathway are essential for HIV-1 budding. Cell **107**:55-65.

128. **Henne WM, Buchkovich NJ, Emr SD.** 2011. The ESCRT pathway. Dev Cell **21**:77-91.

129. **Lu Q, Hope LW, Brasch M, Reinhard C, Cohen SN.** 2003. TSG101 interaction with HRS mediates endosomal trafficking and receptor down-regulation. Proc Natl Acad Sci U S A **100**:7626-7631.

130. **Teo H, Gill DJ, Sun J, Perisic O, Veprintsev DB, Vallis Y, Emr SD, Williams RL.** 2006. ESCRT-I core and ESCRT-II GLUE domain structures reveal role for GLUE in linking to ESCRT-I and membranes. Cell **125**:99-111.

131. **Teis D, Saksena S, Emr SD.** 2008. Ordered assembly of the ESCRT-III complex on endosomes is required to sequester cargo during MVB formation. Dev Cell **15**:578-589.

132. **Babst M, Katzmann DJ, Estepa-Sabal EJ, Meerloo T, Emr SD.** 2002. Escrt-III: an endosome-associated heterooligomeric protein complex required for mvb sorting. Dev Cell **3**:271-282.

133. **Stuchell-Brereton MD, Skalicky JJ, Kieffer C, Karren MA, Ghaffarian S, Sundquist WI.** 2007. ESCRT-III recognition by VPS4 ATPases. Nature **449**:740-744.

134. **Azmi IF, Davies BA, Xiao J, Babst M, Xu Z, Katzmann DJ.** 2008. ESCRT-III family members stimulate Vps4 ATPase activity directly or via Vta1. Dev Cell **14**:50-61.

135. **Hermida-Matsumoto L, Resh MD.** 2000. Localization of human immunodeficiency virus type 1 Gag and Env at the plasma membrane by confocal imaging. J Virol **74**:8670-8679.

136. **Larson DR, Johnson MC, Webb WW, Vogt VM.** 2005. Visualization of retrovirus budding with correlated light and electron microscopy. Proc Natl Acad Sci U S A **102**:15453-15458.

137. **Muller B, Daecke J, Fackler OT, Dittmar MT, Zentgraf H, Krausslich HG.** 2004. Construction and characterization of a fluorescently labeled infectious human immunodeficiency virus type 1 derivative. J Virol **78**:10803-10813.

138. **Jouvenet N, Bieniasz PD, Simon SM.** 2008. Imaging the biogenesis of individual HIV-1 virions in live cells. Nature **454**:236-240.

139. **Ivanchenko S, Godinez WJ, Lampe M, Krausslich HG, Eils R, Rohr K, Brauchle C, Muller B, Lamb DC.** 2009. Dynamics of HIV-1 assembly and release. PLoS Pathog **5**:e1000652.

140. **Jouvenet N, Simon SM, Bieniasz PD.** 2009. Imaging the interaction of HIV-1 genomes and Gag during assembly of individual viral particles. Proc Natl Acad Sci U S A **106**:19114-19119.

141. **Muranyi W, Malkusch S, Muller B, Heilemann M, Krausslich HG.** 2013. Super-resolution microscopy reveals specific recruitment of HIV-1 envelope proteins to viral assembly sites dependent on the envelope C-terminal tail. PLoS Pathog **9**:e1003198.

142. **Bleck M, Itano MS, Johnson DS, Thomas VK, North AJ, Bieniasz PD, Simon SM.** 2014. Temporal and spatial organization of ESCRT protein recruitment during HIV-1 budding. Proc Natl Acad Sci U S A **111**:12211-12216.

143. **Jouvenet N, Zhadina M, Bieniasz PD, Simon SM.** 2011. Dynamics of ESCRT protein recruitment during retroviral assembly. Nat Cell Biol **13**:394-401.

144. **Ku PI, Bendjennat M, Ballew J, Landesman MB, Saffarian S.** 2014. ALIX is recruited temporarily into HIV-1 budding sites at the end of gag assembly. PLoS One **9**:e96950.

145. **Schott DH, Cureton DK, Whelan SP, Hunter CP.** 2005. An antiviral role for the RNA interference machinery in Caenorhabditis elegans. Proc Natl Acad Sci U S A **102**:18420-18424.

146. **Ruedas JB, Perrault J.** 2009. Insertion of enhanced green fluorescent protein in a hinge region of vesicular stomatitis virus L polymerase protein creates a temperature-sensitive virus that displays no virion-associated polymerase activity in vitro. J Virol **83**:12241-12252.

147. **Dalton KP, Rose JK.** 2001. Vesicular stomatitis virus glycoprotein containing the entire green fluorescent protein on its cytoplasmic domain is incorporated efficiently into virus particles. Virology **279**:414-421.

148. **Das SC, Panda D, Nayak D, Pattnaik AK.** 2009. Biarsenical labeling of vesicular stomatitis virus encoding tetracysteine-tagged m protein allows dynamic imaging of m protein and virus uncoating in infected cells. J Virol **83**:2611-2622.

149. **Naeve CW, Kolakofsky CM, Summers DF.** 1980. Comparison o;f vesicular stomatitis virus intracellular and virion ribonucleoproteins. J Virol **33**:856-865.

150. **Kozak M.** 1986. Bifunctional messenger RNAs in eukaryotes. Cell **47**:481-483.

151. **Black BL, Rhodes RB, McKenzie M, Lyles DS.** 1993. The role of vesicular stomatitis virus matrix protein in inhibition of host-directed gene expression is genetically separable from its function in virus assembly. J Virol **67**:4814-4821.

152. **Ormo M, Cubitt AB, Kallio K, Gross LA, Tsien RY, Remington SJ.** 1996. Crystal structure of the Aequorea victoria green fluorescent protein. Science **273**:1392-1395.

153. **Schnell MJ, Buonocore L, Kretzschmar E, Johnson E, Rose JK.** 1996. Foreign glycoproteins expressed from recombinant vesicular stomatitis viruses are incorporated efficiently into virus particles. Proc Natl Acad Sci U S A **93**:11359-11365.

154. **Lyles DS, McKenzie MO.** 1997. Activity of vesicular stomatitis virus M protein mutants in cell rounding is correlated with the ability to inhibit host gene expression and is not correlated with virus assembly function. Virology **229**:77-89.

155. **Zhang W, Jiang Y, Wang Q, Ma X, Xiao Z, Zuo W, Fang X, Chen YG.** 2009. Single-molecule imaging reveals transforming growth factor-beta-induced type II receptor dimerization. Proc Natl Acad Sci U S A **106**:15679-15683.

156. **Gather MC, Yun SH.** 2014. Bio-optimized energy transfer in densely packed fluorescent protein enables near-maximal luminescence and solid-state lasers. Nat Commun **5**:5722.

157. **Buchholz UJ, Finke S, Conzelmann KK.** 1999. Generation of bovine respiratory syncytial virus (BRSV) from cDNA: BRSV NS2 is not essential for virus replication in tissue culture, and the human RSV leader region acts as a functional BRSV genome promoter. J Virol **73**:251-259.

158. **Cureton DK, Massol RH, Saffarian S, Kirchhausen TL, Whelan SP.** 2009. Vesicular stomatitis virus enters cells through vesicles incompletely coated with clathrin that depend upon actin for internalization. PLoS Pathog **5**:e1000394.

159. **Lyles DS, Puddington L, McCreedy BJ, Jr.** 1988. Vesicular stomatitis virus M protein in the nuclei of infected cells. J Virol **62**:4387-4392.

160. **Massol RH, Boll W, Griffin AM, Kirchhausen T.** 2006. A burst of auxilin recruitment determines the onset of clathrin-coated vesicle uncoating. Proc Natl Acad Sci U S A **103**:10265-10270.

161. **Ohno S, Ohtake N.** 1987. Immunocytochemical study of the intracellular localization of M protein of vesicular stomatitis virus. Histochem J **19**:297-306.

162. **McCreedy BJ, Jr., Lyles DS.** 1989. Distribution of M protein and nucleocapsid protein of vesicular stomatitis virus in infected cell plasma membranes. Virus Res **14**:189-205.

163. **Baumgartel V, Ivanchenko S, Dupont A, Sergeev M, Wiseman PW, Krausslich HG, Brauchle C, Muller B, Lamb DC.** 2011. Live-cell visualization of dynamics of HIV budding site interactions with an ESCRT component. Nat Cell Biol **13**:469-474.

164. **Roche S, Rey FA, Gaudin Y, Bressanelli S.** 2007. Structure of the prefusion form of the vesicular stomatitis virus glycoprotein G. Science **315**:843-848.

165. **Roche S, Bressanelli S, Rey FA, Gaudin Y.** 2006. Crystal structure of the low-pH form of the vesicular stomatitis virus glycoprotein G. Science **313**:187-191.

166. **Shu X, Shaner NC, Yarbrough CA, Tsien RY, Remington SJ.** 2006. Novel chromophores and buried charges control color in mFruits. Biochemistry **45**:9639-9647.

167. **Lingappa VR, Katz FN, Lodish HF, Blobel G.** 1978. A signal sequence for the insertion of a transmembrane glycoprotein. Similarities to the signals of secretory proteins in primary structure and function. J Biol Chem **253**:8667-8670.

168. **McCombs RM, Melnick MB, Brunschwig JP.** 1966. Biophysical studies of vesicular stomatitis virus. J Bacteriol **91**:803-812.

169. **Maupin P, Pollard TD.** 1983. Improved preservation and staining of HeLa cell actin filaments, clathrin-coated membranes, and other cytoplasmic structures by tannic acid-glutaraldehyde-saponin fixation. J Cell Biol **96**:51-62.

170. **Goodwin JS, Kenworthy AK.** 2005. Photobleaching approaches to investigate diffusional mobility and trafficking of Ras in living cells. Methods **37**:154-164.

171. **Gottwein E, Bodem J, Muller B, Schmechel A, Zentgraf H, Krausslich HG.** 2003. The Mason-Pfizer monkey virus PPPY and PSAP motifs both contribute to virus release. J Virol **77**:9474-9485.

172. **Mercenne G, Alam SL, Arii J, Lalonde MS, Sundquist WI.** 2015. Angiomotin functions in HIV-1 assembly and budding. Elife **4**:

173. **Wills JW, Cameron CE, Wilson CB, Xiang Y, Bennett RP, Leis J.** 1994. An assembly domain of the Rous sarcoma virus Gag protein required late in budding. J Virol **68**:6605-6618.

174. **Chong LD, Rose JK.** 1993. Membrane association of functional vesicular stomatitis virus matrix protein in vivo. J Virol **67**:407-414.

175. **Carlton J.** 2010. The ESCRT machinery: a cellular apparatus for sorting and scission. Biochem Soc Trans **38**:1397-1412.

176. **Baquero E, Albertini AA, Raux H, Buonocore L, Rose JK, Bressanelli S, Gaudin Y.** 2015. Structure of the Low pH Conformation of Chandipura Virus G Reveals Important Features in the Evolution of the Vesiculovirus Glycoprotein. PLoS Pathog **11**:e1004756.

177. **Ferlin A, Raux H, Baquero E, Lepault J, Gaudin Y.** 2014. Characterization of pH-sensitive molecular switches that trigger the structural transition of vesicular stomatitis virus glycoprotein from the postfusion state toward the prefusion state. J Virol **88**:13396-13409.

178. **Prasher DC, Eckenrode VK, Ward WW, Prendergast FG, Cormier MJ.** 1992. Primary structure of the Aequorea victoria green-fluorescent protein. Gene **111**:229-233.

179. **Shaner NC, Campbell RE, Steinbach PA, Giepmans BN, Palmer AE, Tsien RY.** 2004. Improved monomeric red, orange and yellow fluorescent proteins derived from Discosoma sp. red fluorescent protein. Nat Biotechnol **22**:1567-1572.

180. **Shaner NC, Steinbach PA, Tsien RY.** 2005. A guide to choosing fluorescent proteins. Nat Methods **2**:905-909.

181. **Leyrat C, Yabukarski F, Tarbouriech N, Ribeiro EA, Jr., Jensen MR, Blackledge M, Ruigrok RW, Jamin M.** 2011. Structure of the vesicular stomatitis virus N(0)-P complex. PLoS Pathog **7**:e1002248.

182. **Yang F, Moss LG, Phillips GN, Jr.** 1996. The molecular structure of green fluorescent protein. Nat Biotechnol **14**:1246-1251.

183. **Chen Y, Mills JD, Periasamy A.** 2003. Protein localization in living cells and tissues using FRET and FLIM. Differentiation **71**:528-541.

184. **Adell MA, Teis D.** 2011. Assembly and disassembly of the ESCRT-III membrane scission complex. FEBS Lett **585**:3191-3196.

185. **Rika J, Binkert T.** 1989. Direct measurement of a distinct correlation function by fluorescence cross correlation. Phys Rev A **39**:2646-2652.

186. **Needleman DJ, Xu Y, Mitchison TJ.** 2009. Pin-hole array correlation imaging: highly parallel fluorescence correlation spectroscopy. Biophys J **96**:5050-5059.

187. **Kolin DL, Wiseman PW.** 2007. Advances in image correlation spectroscopy: measuring number densities, aggregation states, and dynamics of fluorescently labeled macromolecules in cells. Cell Biochem Biophys **49**:141-164.

188. **Adu-Gyamfi E, Digman MA, Gratton E, Stahelin RV.** 2012. Investigation of Ebola VP40 assembly and oligomerization in live cells using number and brightness analysis. Biophys J **102**:2517-2525.

189. **Dalton AJ, Rowe WP, Smith GH, Wilsnack RE, Pugh WE.** 1968. Morphological and cytochemical studies on lymphocytic choriomeningitis virus. J Virol **2**:1465-1478.

190. **Loney C, Mottet-Osman G, Roux L, Bhella D.** 2009. Paramyxovirus ultrastructure and genome packaging: cryo-electron tomography of sendai virus. J Virol **83**:8191-8197.

191. **Briggs JA, Wilk T, Welker R, Krausslich HG, Fuller SD.** 2003. Structural organization of authentic, mature HIV-1 virions and cores. Embo J **22**:1707-1715.

192. **Clinton GM, Burge BW, Huang AS.** 1978. Effects of phosphorylation and pH on the association of NS protein with vesicular stomatitis virus cores. J Virol **27**:340-346.

193. **Kaptur PE, McKenzie MO, Wertz GW, Lyles DS.** 1995. Assembly functions of vesicular stomatitis virus matrix protein are not disrupted by mutations at major sites of phosphorylation. Virology **206**:894-903.

194. **Gao Y, Lenard J.** 1995. Multimerization and transcriptional activation of the phosphoprotein (P) of vesicular stomatitis virus by casein kinase-II. Embo J **14**:1240-1247.

195. **van der Schaar HM, Rust MJ, Chen C, van der Ende-Metselaar H, Wilschut J, Zhuang X, Smit JM.** 2008. Dissecting the cell entry pathway of dengue virus by single-particle tracking in living cells. PLoS Pathog **4**:e1000244.

196. **Garbutt M, Liebscher R, Wahl-Jensen V, Jones S, Moller P, Wagner R, Volchkov V, Klenk HD, Feldmann H, Stroher U.** 2004. Properties of replication-competent vesicular stomatitis virus vectors expressing glycoproteins of filoviruses and arenaviruses. J Virol **78**:5458-5465.

197. **Piccinotti S, Kirchhausen T, Whelan SP.** 2013. Uptake of rabies virus into epithelial cells by clathrin-mediated endocytosis depends upon actin. J Virol **87**:11637-11647.

198. **Jae LT, Raaben M, Herbert AS, Kuehne AI, Wirchnianski AS, Soh TK, Stubbs SH, Janssen H, Damme M, Saftig P, Whelan SP, Dye JM, Brummelkamp TR.** 2014. Virus entry. Lassa virus entry requires a trigger-induced receptor switch. Science **344**:1506-1510.

199. **Diaz A, Zhang J, Ollwerther A, Wang X, Ahlquist P.** 2015. Host ESCRT Proteins Are Required for Bromovirus RNA Replication Compartment Assembly and Function. PLoS Pathog **11**:e1004742.

200. **Ahmed M, McKenzie MO, Puckett S, Hojnacki M, Poliquin L, Lyles DS.** 2003. Ability of the matrix protein of vesicular stomatitis virus to suppress beta interferon gene expression is genetically correlated with the inhibition of host RNA and protein synthesis. J Virol **77**:4646-4657.

201. **Whitlow ZW, Connor JH, Lyles DS.** 2006. Preferential translation of vesicular stomatitis virus mRNAs is conferred by transcription from the viral genome. J Virol **80**:11733-11742.

202. **Lee AS, Burdeinick-Kerr R, Whelan SP.** 2013. A ribosome-specialized translation initiation pathway is required for cap-dependent translation of vesicular stomatitis virus mRNAs. Proc Natl Acad Sci U S A **110**:324-329.

203. **Connor JH, Lyles DS.** 2002. Vesicular stomatitis virus infection alters the eIF4F translation initiation complex and causes dephosphorylation of the eIF4E binding protein 4E-BP1. J Virol **76**:10177-10187.

204. **Inoue M, Tokusumi Y, Ban H, Kanaya T, Shirakura M, Tokusumi T, Hirata T, Nagai Y, Iida A, Hasegawa M.** 2003. A new Sendai virus vector deficient in the matrix gene does not form virus particles and shows extensive cell-to-cell spreading. J Virol **77**:6419-6429.

205. **Mitra R, Baviskar P, Duncan-Decocq RR, Patel D, Oomens AG.** 2012. The human respiratory syncytial virus matrix protein is required for maturation of viral filaments. J Virol **86**:4432-4443.

206. **Cathomen T, Mrkic B, Spehner D, Drillien R, Naef R, Pavlovic J, Aguzzi A, Billeter MA, Cattaneo R.** 1998. A matrix-less measles virus is infectious and elicits extensive cell fusion: consequences for propagation in the brain. Embo J **17**:3899-3908.

207. **Dubochet J, Adrian M, Richter K, Garces J, Wittek R.** 1994. Structure of intracellular mature vaccinia virus observed by cryoelectron microscopy. J Virol **68**:1935-1941.

Appendix A

Generation and recovery of VSV ΔM

Abstract

The vesicular stomatitis virus (VSV) matrix protein (M) has a number of roles in the VSV replication cycle. During assembly, M mediates localization of the nucleocapsid protein (N) to membranes and condensation of the viral ribonucleoprotein (RNP) into the condensed nucleocapsid-matrix protein (NCM) complex, but M also inhibits host RNA synthesis and nuclear-cytoplasmic transport of host messenger RNPs. Investigation of which steps in assembly require M and the importance of host shutoff on the initiation and progression of infection in the context of physiological VSV protein levels requires a virus with M deleted. We generate a clone where the M coding sequence is replaced with eGFP (VSV ΔM eGFP). This virus could be recovered and passaged when M was expressed *in trans* from a VSV genomic analog but not from T7 or host RNA polymerase II. This proof of principle for the generation and amplification of VSV ΔM eGFP will allow for further optimization of the production of this virus and the study of the direct and indirect roles of M in VSV infection.

Introduction

In vesicular stomatitis virus (VSV) infected cells, the matrix protein (M) mediates the assembly of viral particles as well has host shutoff. Assembly of virions requires the colocalization of M, the viral ribonucleoprotein (RNP), and the glycoprotein (G) at the plasma membrane. M facilitates the association of the viral RNP with membranes (65, 66) and is required for the condensation of the viral RNP into the bullet-shaped nucleocapsid-matrix protein (NCM) complex (16). Prior to the initiation of assembly, M and G form independent microdomains at the plasma membrane (34, 64). However, a small amount of M may be in the G microdomains since M stabilizes G trimers (105). While the formation of G microdomains does not require M (34), the presence of M may be important for the translocation of the viral RNP to G that occurs during assembly (64).

Efficient expression of viral genes requires host shutoff by M. Partial disruption of this function leads to decreased viral RNA synthesis (71) and delayed production of viral proteins (200). M mediates host shutoff through the inhibition of host transcription (72) as well as nuclear export (73). Since VSV mRNA is capped (40, 41) and methylated (42-44) to appear identical to host mRNA, preferential translation of viral genes could be partly due to the absence of cellular mRNA. Although, transcripts produced from the VSV genome are more efficiently translated (201) and ribosomal subunit rpL40 plays a role in selectively translating VSV mRNA (202). The importance of host shutoff on the preferential expression of viral genes and how this affects the establishment and progression of VSV infection is not completely understood.

Determination of which stages of the VSV replication cycle are critically dependent on M can be established with a VSV ΔM. While temperature-sensitive mutants of M have been generated, these often affect only 1 function of M (71) and only partially inhibit the function

(203). Successful recovery of VSV ΔM has not been reported. However, ΔM mutants have been generated for a number of related viruses. Rabies virus (RabV), another member of the family *Rhabdoviridae*, with M deleted from the genome could be recovered by including M in the initial recovery and passaged by expression of M *in trans* from a T7 driven plasmid (96). Sendai virus (SeV) (204) and human respiratory syncytial virus (hRSV) (205), of the family *Paramyxoviridae*, could also be recovered by expressing M *in trans*. The initial recovery provided M from a T7 driven plasmid, and the viruses were passaged in inducible cell lines expressing M. In contrast, deletion of M from measles virus, another paramyxovirus, generates a replication competent virus (206). The success of generating ΔM clones of related viruses suggests that *in trans* complementation of M for VSV could be possible.

In this study, we successfully recover virus from a VSV ΔM cDNA through complementation of M from a VSV genomic analog. Expression of M from a T7 or cellular promoter was insufficient to support spread of this virus. While further optimization of complementation conditions is required, the generation of VSV ΔM will allow for the identification of processes in infected cells that require M.

Results

Successful recovery of VSV ΔM from cDNA

Starting from an infectious VSV cDNA backbone, the M coding sequence was replaced with eGFP (VSV ΔM eGFP) to permit tracking of viral infection (Figure A.1 A). During recovery of this virus, M was expressed *in trans* from the VSV genomic analog 3' Leader (Le)-M-G-Trailer (Tr) 5' (LMGT), and $eGFP^+$ plaques were observed. In contrast, using a T7 promoter for expression of M instead of LMGT did not lead to spread of eGFP signal. VSV ΔM eGFP was passaged by including 3' Le-M-mCherry-Tr 5' (LMCT) and the *trans*-acting replication machinery nucleocapsid protein (N), phosphoprotein (P), and large polymerase protein (L) as a source for M (Figure A.1 B). Infected cells were positive for a reverse transcriptase-dependent viral genome product (Figure A.1 C-D). However, only a titre of 10^4 plaque forming units (PFUs) per mL could be achieved.

LMCT expressed by exogenous N, P, and L can support passaging of VSV ΔM eGFP

Expression of M from a range of promoters was tested for the ability to support spread of VSV ΔM eGFP (Figure A.2). Expression of M with the M51R mutation from a cytomegalovirus promoter did not support VSV spread. This mutant of M was used since the M51R mutation decreases M mediated host shutoff (71), which would inhibit the RNA polymerase II (RNAP II) expression of M from this plasmid. Expression of M from a T7 promoter and T7 from a vaccinia virus (vTF7-3) also did not support spread of eGFP. While coinfection with LMCT genomic analog particles was also insufficient to form eGFP plaques, passaging was supported by combining vTF7-3, N, P, L, and LMCT prior to infection with VSV ΔM eGFP. In this infection, LMCT could be introduced from the cDNA or from recovered genomic analog particles.

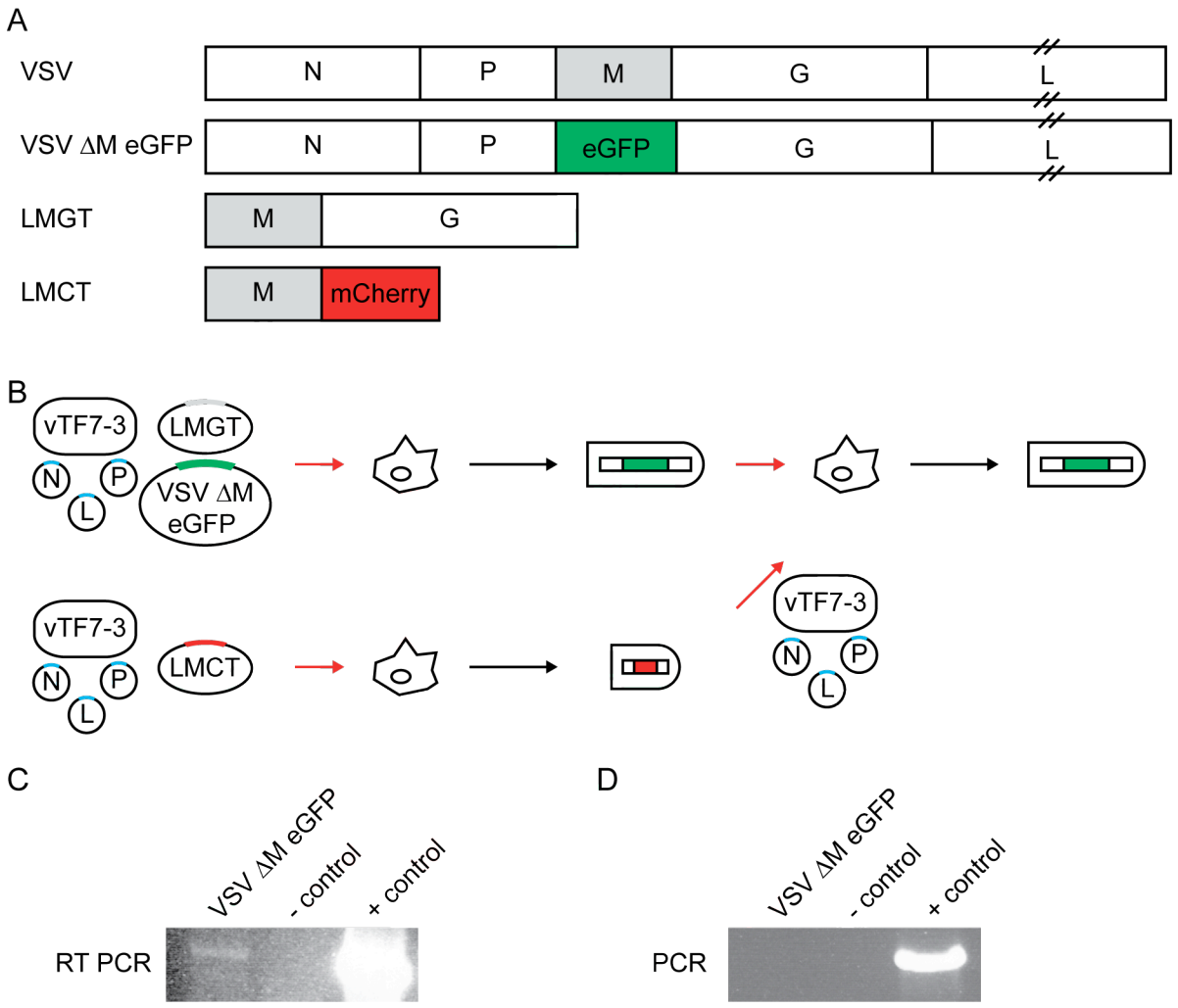

Figure A.1. Generation and recovery of VSV ΔM eGFP.
(A) Schematic of the VSV ΔM eGFP genome and genomic analogs. (B) Schematic of strategy for passaging VSV ΔM eGFP. T7 expressing vaccinia virus (vTF7-3) with N, P, L, and LMGT were used (red arrow) in the initial recovery of VSV ΔM eGFP. LMCT particles could be generated (black arrow) and were used to passage VSV ΔM eGFP. RT PCR (C) and PCR (D) of infected cell RNA with primers that amplify the genomic region between P and G.

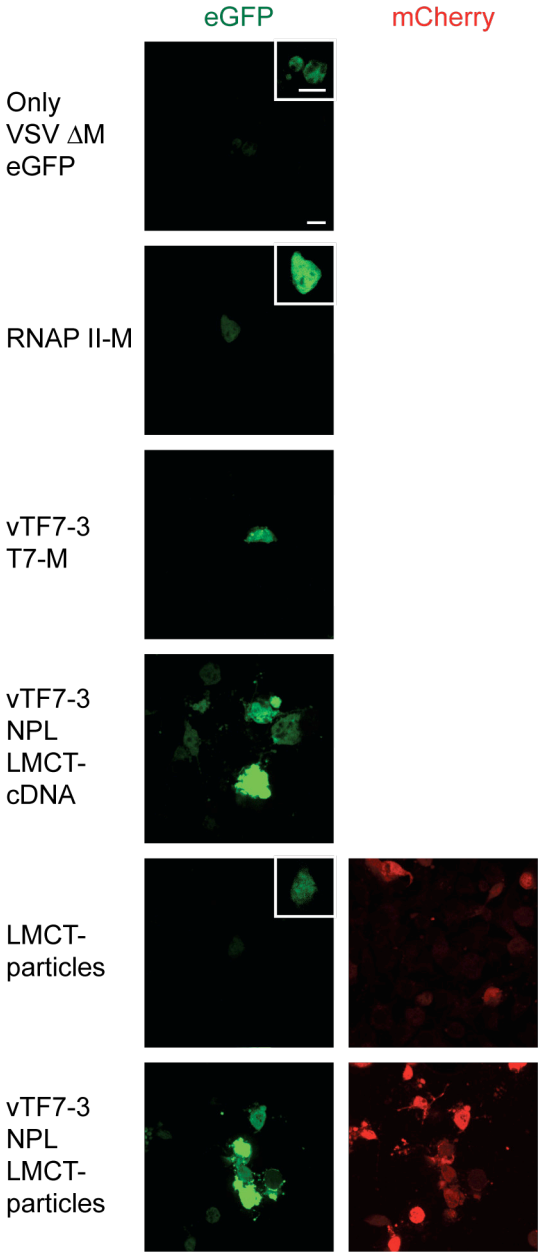

Figure A.2. Expression methods for M that support spread of VSV ΔM eGFP.
Confocal images of BsrT7 cells infected with VSV ΔM eGFP and expressing M from a range of sources. Vaccinia virus (vTF7-3) was used as a source of T7. For infections with LMCT genomic analog particles, the mCherry channel is also shown. Raw images were acquired under the same microscope settings and renormalized to the same values. The inset is a crop of the $eGFP^+$ cell renormalized to highlight expression. Scale bars represent 20 μm.

Discussion

Successful recovery and passaging of VSV ΔM eGFP

VSV with M deleted from the genome could be successfully recovered and passaged by complementation with an M expressing VSV genomic analog. Like RabV ΔM (96), VSV ΔM eGFP is not replication competent. Amplification of this VSV mutant could be complemented by the LMCT genomic analog but not expression of M M51R from RNAP II or M from T7. A possible reason why RNAP II did not support amplification is that complementation requires very high expression levels of M. Viral promoters are more efficient than RNAP II. However, T7 was also not sufficient. Perhaps efficient production of VSV particles requires low levels of M early in infection when replication of the VSV genome is being initiated but high later on when the genome concentration has reached the appropriate level for assembly. Since the LMCT genomic analog is replicated by the VSV replication machinery, M expression will increase exponentially as infection progresses, which would result in relatively low levels at the start of infection but high levels later on. If M expression is too high early in infection, perhaps the cell dies, due to the cytotoxic nature of M (72, 154), before VSV replication can occur. In contrast once genome replication is taking place, high M levels would be necessary for assembly.

Coinfection of VSV ΔM eGFP and the LMCT genomic analog particles did not appear to complement replication in the absence of exogenous N, P, and L expression. However, this could be due to infection with an insufficient amount of genomic analog. The titre of LMCT particles was assayed for by titration on cells expressing N, P, and L. Coinfection was then performed at MOI 1 to minimize amplification of the LMCT genomic analog over VSV ΔM eGFP. The poisson distribution predicts that 63% of cells will be infected at this MOI. Identification of LMCT infection by mCherry expression suggests that this is not the case in the absence of

exogenously expressed replication machinery (Figure A.2). It is possible that high expression levels of N, P, and L prior to infection enhance the efficiency of initiating replication of the incoming genome. Therefore, the measured titre would overestimate the amount of successful LMCT infections that would occur in the absence of exogenously expressed replication machinery. Using a much higher MOI could further test the ability of LMCT genomic analog particles to complement VSV ΔM eGFP.

An indirect role of M in the establishment of viral infection

Expression of M may play an indirect role in the establishment of VSV infection. Higher eGFP expression and more $eGFP^+$ cells were observed when VSV ΔM eGFP was complemented than when it was used for infection alone (Figure A.2). Since M mediates host shutoff (59), the lack of M and consequently this shutoff will lead to the decreased expression of viral genes (71). This decreased expression would delay genome replication since replication is dependent on the expression of N (37). Delayed VSV replication could increase the chance of degradation of the incoming particle by the cell, which would prevent infection and lead to a decrease in the number of infected cells. This would suggest that early expression of M and the associated host shutoff are important for establishing infection. Alternatively, the decreased amount of eGFP expression could lead to infected cells producing less eGFP signal than the background, leading to infected cells appearing uninfected.

Further development and uses

In order for VSV ΔM eGFP to be useful, it would need to be isolated from the genomic analog and vaccinia virus. Full length VSV can be isolated from these particles through gradient

purification (90) since the genomic analog is smaller due to the shorter genome (153) and vaccinia virus virions are larger (207). However, this would require that the yield of VSV ΔM eGFP is sufficiently high to observe on the gradient. Alternatively, a genomic analog that does not generate infectious particles, *e.g.* the genomic analog is flanked by Le and Le-complement instead of Tr (58), could be transfected into cells for the expression of M. Expression of this genomic analog and exogenous replication machinery could be driven by T7 from a stable cell line (157). The supernatant from these infections would only contain VSV ΔM eGFP. Complementation from cellular expression of M would be ideal since no additional viruses would be present. However, an inducible stable cell line for M, as was used for SeV (204) and hRSV (205), may not work due to the host shutoff functions of VSV M (71).

VSV ΔM eGFP would allow for a number of questions about assembly to be asked. Assembly is thought to proceed by recruitment of the viral RNP to G microdomains and then subsequent recruitment of M (64). While M and G microdomains to not colocalize (64), some M may be present with G since M stabilizes G trimers (105). This M may play a role in recruiting the viral RNP since M mediates the association of the viral RNP with lipids (65, 66). With VSV ΔM eGFP, it could be asked how far assembly will proceed in the absence of M. Does the viral RNP still get recruited to G microdomains? Do the G-viral RNP complexes accumulate at the plasma membrane?

This virus would also allow for analysis of the relationship of the other viral proteins with host shutoff. It could be asked how important newly synthesized M is for initiating and maintaining efficient replication. Is host shutoff by M important for establishing successful infection? Do other viral proteins cause host shutoff? While the functions of M have been

studied in both the context and absence of other viral proteins, the effect of the absence of M on VSV replication and assembly at physiological protein concentrations is unknown.

Materials and Methods

Cells and viruses.

BsrT7 cells and VSV clones were maintained as previously described (Chapter 2 Materials and Methods). The M51R mutation in M was generated previously (Chapter 2 Materials and Methods) and was cloned into pcDNA3.1 (Life Technologies Corporation; Carlsbad, CA). Recovery of VSV ΔM eGFP was performed as previously described (9), but included LMGT. For passaging VSV ΔM eGFP, BsrT7 cells were infected with T7 expressing vaccinia virus (vTF7-3), transfected with N, P, and L, and then infected with LMCT genomic analog particles and VSV ΔM eGFP.

RT PCR and PCR

Cellular RNA was extracted from VSV ΔM eGFP infected cells 24 hpi with QIAzol (Qiagen; Venlo, Netherlands). RT PCR was performed with the OneStep RT-PCR kit (Qiagen), and PCR was performed with Taq (Invitrogen, Life Technologies Corporation; Carlsbad, CA).

Confocal microscopy

Confocal images were taken on the same microscope as previously described for immunofluorescence (Chapter 2 Materials and Methods).

Appendix B

Lassa virus entry requires a trigger-induced receptor switch

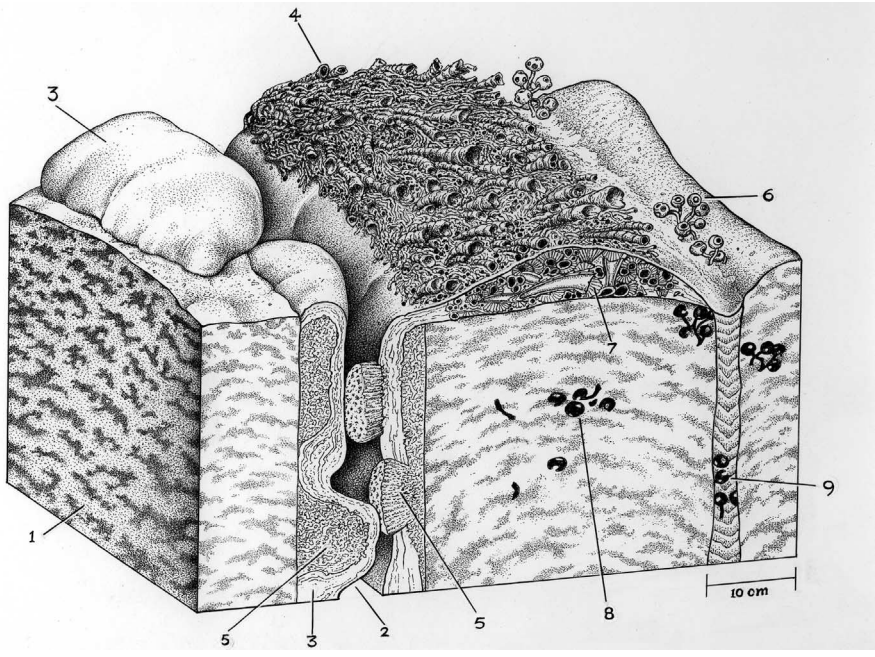

Fig. 2. Reconstruction of a late Ediacaran reef. 1, Thrombolite; **2**, Neptunian dyke; **3**, stromatolite; **4**, *Cloudina*; **5**, *Namapoikia*; **6**, *Namacalathus*; **7**, cement botryoids; **8**, trapped *Namacalathus*; **9**, sediment. [Image copyright: J. Sibbick]

differentiation of metazoans into the distinct open surface and cryptic biotas so characteristic of Phanerozoic and modern reefs (Fig. 2). *Cloudina* possessed additional features, such as the ability for interindividual skeletal cementation that enabled elevated growth above a substrate and mutual support to form an open framework with high mechanical strength and potential resistance to predation. These paleoecological characteristics are all consistent with competitive strategies and antipredation traits and support the views that both skeletonization and reef-building in metazoans was promoted by the rise of substrate competitors and bilaterian predators and that such a selective pressure was a strong driving evolutionary force by the Ediacaran.

REFERENCES AND NOTES

1. S. Bengtson, *Paleontol. Soc. Pap.* **10**, 67 (2004).
2. M. D. Brasier, in *The Precambrian-Cambrian Boundary*, J. W. Cowie, M. D. Brasier, Eds. (Oxford Univ. Press, Oxford, 1989), pp. 117–165.
3. S. W. F. Grant, *Am. J. Sci.* **290-A**, 261–294 (1990).
4. J. Gehling, J. K. Rigby, *J. Paleontol.* **70**, 185 (1996).
5. A. E. Kontorovich *et al.*, *Russ. Geol. Geophys.* **49**, 932–939 (2008).
6. J. P. Grotzinger, W. Watters, A. H. Knoll, *Paleobiology* **26**, 334–359 (2000).
7. R. A. Wood, J. P. Grotzinger, J. A. D. Dickson, *Science* **296**, 2383–2386 (2002).
8. P. D. Kruse, A. Yu. Zhuravlev, N. P. James, *Palaios* **10**, 291 (1995).
9. S. Bengtson, S. Conway Morris, *Topics in Geobiology* **20**, 447–481 (1992).
10. G. B. H. Germs, *Am. J. Sci.* **272**, 752–761 (1972).
11. I. Cortijo, M. M. Mus, S. Jensen, T. Palacios, *Precambrian Res.* **176**, 1–10 (2010).
12. L. V. Warren *et al.*, *Terra Nova* **23**, 382–389 (2011).
13. H. Hua, B. R. Pratt, L.-Z. Zhang, *Palaios* **18**, 454–459 (2003).
14. H. Hua, Z. Chen, X. L. Yuan, L.-Z. Zhang, S. H. Xiao, *Geology* **33**, 277 (2005).
15. A. Seilacher, *Palaios* **14**, 86 (1999).
16. Y. Cai *et al.*, *Gondwana Res.* **25**, 1008–1018 (2014).
17. R. A. Wood, *Earth Sci. Rev.* **106**, 184–190 (2011).
18. B. Z. Saylor, A. J. Kaufman, J. P. Grotzinger, F. Urban, *J. Sediment. Res.* **68**, 1223–1235 (1998).
19. J. P. Grotzinger, *Commun. Geol. Surv. Namibia* **11**, 77 (2002).
20. For details, see supplementary text on *Science* Online.
21. G. M. Narbonne, S. Xiao, G. Shields, "The Ediacaran Period," in *The Geologic Time Scale 2012*, F. Gradstein, J. Ogg, G. Ogg, Eds. (Elsevier, Boston, 2012), pp. 427–449.
22. G. M. Narbonne, B. Z. Saylor, J. P. Grotzinger, *J. Paleontol.* **71**, 953–967 (1997).
23. For details, see materials and methods on *Science* Online.
24. A. H. Knoll, *Rev. Mineral. Geochem.* **54**, 329–356 (2003).
25. S. Bengtson, Y. Zhao, *Science* **257**, 367–369 (1992).
26. G. J. Vermeij, *A Natural History of Shells* (Princeton Univ. Press, Princeton, NJ, 1993).
27. J. B. C. Jackson, in *Biotic Interactions in Recent and Fossil Benthic Communities*, M. Tevesz, P. W. McCall, Eds. (Plenum, New York, 1983), vol. 39.
28. M. L. Droser, J. G. Gehling, *Science* **319**, 1660–1662 (2008).
29. R. Wood, *Reef Evolution* (Oxford Univ. Press, Oxford, 1999).

ACKNOWLEDGMENTS

A.M.P. acknowledges funding from a University of Edinburgh, School of Geosciences Scholarship and the International Centre for Carbonate Reservoirs. R.W., R.T., and A.M.P. acknowledge support from Natural Environment Research Council (NERC) project "Re-inventing the planet: the Neoproterozoic revolution in oxygenation, biogeochemistry and biological complexity" (NE/I005978/1). F.B. thanks the Laidlaw Trust for fieldwork support. We thank the Geological Survey of Namibia; C. Husselmann for access to Driedoornvlagte; M. Hall for technical support; and A. Yu. Zhuravlev, B. MacGabhann, and S. Brusatte for comments and discussion. All data are available online in the supplementary materials on *Science* Online.

SUPPLEMENTARY MATERIALS

www.sciencemag.org/content/344/6191/1504/suppl/DC1
Materials and Methods
Supplementary Text
Figs. S1 to S4
References (*30*–*39*)

14 March 2014; accepted 2 June 2014
10.1126/science.1253393

VIRUS ENTRY

Lassa virus entry requires a trigger-induced receptor switch

Lucas T. Jae,[1] Matthijs Raaben,[1,2] Andrew S. Herbert,[3] Ana I. Kuehne,[3] Ariel S. Wirchnianski,[3] Timothy K. Soh,[2] Sarah H. Stubbs,[2] Hans Janssen,[1] Markus Damme,[4] Paul Saftig,[4] Sean P. Whelan,[2]* John M. Dye,[3]* Thijn R. Brummelkamp[1,5,6]*

Lassa virus spreads from a rodent to humans and can lead to lethal hemorrhagic fever. Despite its broad tropism, chicken cells were reported 30 years ago to resist infection. We found that Lassa virus readily engaged its cell-surface receptor α-dystroglycan in avian cells, but virus entry in susceptible species involved a pH-dependent switch to an intracellular receptor, the lysosome-resident protein LAMP1. Iterative haploid screens revealed that the sialyltransferase ST3GAL4 was required for the interaction of the virus glycoprotein with LAMP1. A single glycosylated residue in LAMP1, present in susceptible species but absent in birds, was essential for interaction with the Lassa virus envelope protein and subsequent infection. The resistance of *Lamp1*-deficient mice to Lassa virus highlights the relevance of this receptor switch in vivo.

Lassa virus binds to glycosylated α-dystroglycan (α-DG) at the cell surface to enter cells (*1*, *2*). Over 30 years ago, it was reported that Lassa virus infects a broad suite of cells from different species, with the exception of chicken (*3*). This was recapitulated by a recombinant vesicular stomatitis virus (VSV) that enters cells using the Lassa virus glycoprotein (rVSV-GP-LASV) (*4*). Because wild-type VSV was unaffected, this indicated a defect in Lassa glycoprotein (GP)–mediated entry (fig. S1A). Birds, however, generate glycosylated α-DG (*5*), and the Lassa envelope protein recognized avian α-DG (fig. S1, B and C).

To identify host factors affecting virus entry independent of α-DG binding, we carried out a haploid screen in receptor-deficient cells. For this, we made use of their incomplete resistance phenotype (fig. S2). This showed that neither α-DG nor factors glycosylating α-DG acted as host factors under these conditions (Fig. 1A; fig. S3, A and B; and tables S1 and S2) (*6*). Instead, we found genes involved in glycosylation, Golgi function, and heparan sulfate biosynthesis. The latter were not identified in wild-type cells (fig. S3C and tables S1 and S3) (*4*), suggesting that in the absence of α-DG, Lassa virus used heparan sulfate, a commonly used virus attachment factor (*7*). The lysosomal transmembrane protein LAMP1 and factors involved in *N*-glycosylation and sialylation, including the α-2,3-sialyltransferase ST3GAL4, stood out in both genotypes. Cells deficient for *LAMP1* or *ST3GAL4* were comparably resistant to wild-type Lassa virus as those lacking α-DG (Fig. 1B and fig. S4, A and B). Expression of human but not chicken LAMP1 sensitized chicken fibroblasts to infection with rVSV-GP-LASV (Fig. 1C and fig. S4C) and imposed virus susceptibility in *LAMP1*-deficient human cells (Fig. 1D and fig. S5). This requirement for LAMP1 was specific for Lassa virus and not shared by the related lymphocytic choriomeningitis virus (fig. S6). Thus, LAMP1 and ST3GAL4 were important for Lassa virus infection independent of α-DG, and host factor function of human LAMP1 was not shared by its chicken ortholog.

Because LAMP1 deficiency neither causes pronounced phenotypes in mice (*8*) nor detectably impaired the endo-lysosomal compartment in cultured cells (fig. S7), we asked whether the

[1]Netherlands Cancer Institute, Plesmanlaan 121, 1066 CX, Amsterdam, Netherlands. [2]Department of Microbiology and Immunobiology, Harvard Medical School, 77 Avenue Louis Pasteur, Boston, MA 02115, USA. [3]U.S. Army Medical Research Institute of Infectious Diseases, 1425 Porter Street, Fort Detrick, MD 21702–5011, USA. [4]Biochemisches Institut, Christian Albrechts-Universität Kiel, 24118 Kiel, Germany. [5]CeMM Research Center for Molecular Medicine of the Austrian Academy of Sciences, 1090 Vienna, Austria. [6]Cancer Genomics Center (CGC.nl), Plesmanlaan 121, 1066 CX, Amsterdam, Netherlands.
***Corresponding author. E-mail: t.brummelkamp@nki.nl (T.R.B.); john.m.dye1.civ@mail.mil (J.M.D.); sean_whelan@hms.harvard.edu (S.P.W.)**

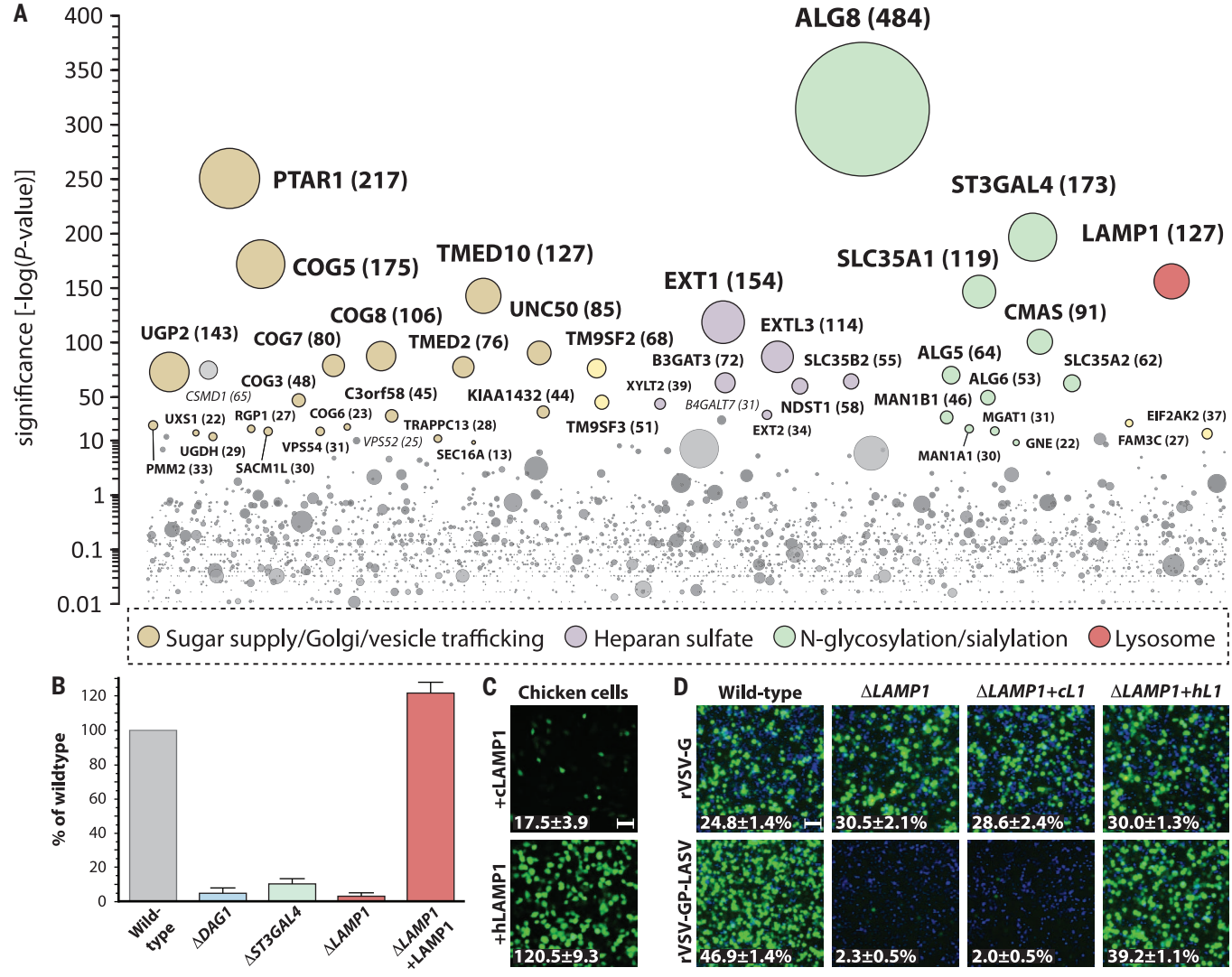

Fig. 1. Human LAMP1 is an α-DG–independent host factor for Lassa virus and bypasses an infection barrier in avian cells. (**A**) Haploid genetic screen for host factors required for infection with rVSV-GP-LASV in cells lacking α-DG. The *y* axis indicates the significance of enrichment of gene-trap insertions in particular genes as compared with nonselected control cells. Solid circles represent genes, and their size corresponds to the number of insertion sites identified in the virus-selected cell population. Hits were colored if they passed the statistical criteria described in (*6*). Significant hits were grouped by function horizontally, and data are displayed until −log(*P*) = 0.01. (**B**) HAP1 cell lines with nuclease-generated mutations in the corresponding genes were exposed to wild-type Lassa virus and stained with antibodies specific for viral antigens to measure infected cells. *LAMP1*-deficient cells were complemented with human LAMP1 cDNA. (**C**) Chicken fibroblasts were transduced with retroviruses expressing chicken (c) or human (h) LAMP1 and challenged with rVSV-GP-LASV. Average number (±SD) of infected cells per field (eGFP-positive) is indicated. (**D**) Wild-type or *LAMP1*-deficient HAP1 cells transduced with retroviruses expressing cLAMP1 or hLAMP1 (L1) were exposed to rVSV-G or rVSV-GP-LASV. Percentage (±SD) of infected cells (expressing eGFP) is indicated. Scale bars, 50 μm.

Lassa virus envelope protein could bind to LAMP1. As the majority of LAMP1 is localized in the acidic interior of lysosomes (*9*, *10*), these experiments were carried out at neutral and acidic pH. Immobilized Flag-tagged Lassa-GP bound α-DG at neutral pH, but this interaction was lost at acidic pH, at which Lassa-GP instead strongly bound to LAMP1 (Fig. 2A and fig. S8, A and B). Lassa-GP molecules that had previously bound α-DG were capable of subsequent binding to LAMP1 (fig. S8C). Likewise, intact virions were captured by the luminal region of LAMP1 at acidic but not at neutral pH (fig. S9). Last, this interaction was observed for both human and mouse LAMP1 but not chicken LAMP1 or human LAMP2 (Fig. 2B and fig. S10).

Virus particles containing enhanced green fluorescent protein (eGFP) fused to the VSV matrix protein (MeGFP, allowing direct visualization of incoming fluorescent virions) were internalized in cells lacking *LAMP1* or *ST3GAL4* (fig. S11) but accumulated in vesicles of *LAMP1*-deficient cells (Fig. 2C). In wild-type cells, fusion of viral and cellular membranes leads to release of MeGFP protein into the cytoplasm (*11*), but in *LAMP1*-deficient cells, MeGFP remained localized to vesicles (figs. S12 and 13), suggesting that the association of Lassa-GP with LAMP1 precedes membrane fusion. In agreement with this, LAMP1 interacted with Lassa-GP in a prefusion configuration when the GP1 subunit of the viral envelope protein is still part of the complex (*12*, *13*) but not when GP1 was fully released from GP2 by low pH (Fig. 2D and fig. S14). To test whether Lassa-GP–mediated membrane fusion was affected by LAMP1, we carried out cell-cell fusion experiments in the presence of a LAMP1 mutant that localizes to the cell surface (LAMP1d384) (fig. S15A) (*9*). Expression of this mutant led to increased syncytia formation as a consequence of membrane fusion (Fig. 2E and fig. S15, B and C). This activity of LAMP1 was independent of α-DG (fig. S15D). Thus, Lassa virus likely engages α-DG at the cell surface, enters the endocytic pathway and binds to LAMP1 upon reaching the acidic interior of lysosomes, before membrane fusion.

To test this model, we engineered an artificial virus infection scenario. Cells in which α-DG was knocked out that expressed LAMP1d384 were largely resistant to rVSV-GP-LASV under normal conditions, but lowering the extracellular pH during virus exposure led to productive infection (fig. S16, A to E). Lassa virus entry normally depends on acidification of endosomes (*14*) and is sensitive to bafilomycin (*15*). The engineered entry route was, however, bafilomycin-insensitive (fig. S16, F and G). Thus, the requirement for α-DG could be bypassed by rerouting LAMP1 to the cell surface and triggering binding to Lassa-GP.

Besides LAMP1, the screens identified the α-2,3-sialyltransferase ST3GAL4 as an α-DG–independent host factor. Because targets modified by this enzyme could display genetic interactions, we searched for host factors depending on ST3GAL4. *ST3GAL4*-deficient cells were mutagenized and selected with rVSV-GP-LASV. Like experiments in wild-type cells, this screen identified *DAG1* and its modifiers (*4*). As expected, the disrupted *ST3GAL4* locus did not act as a host factor under

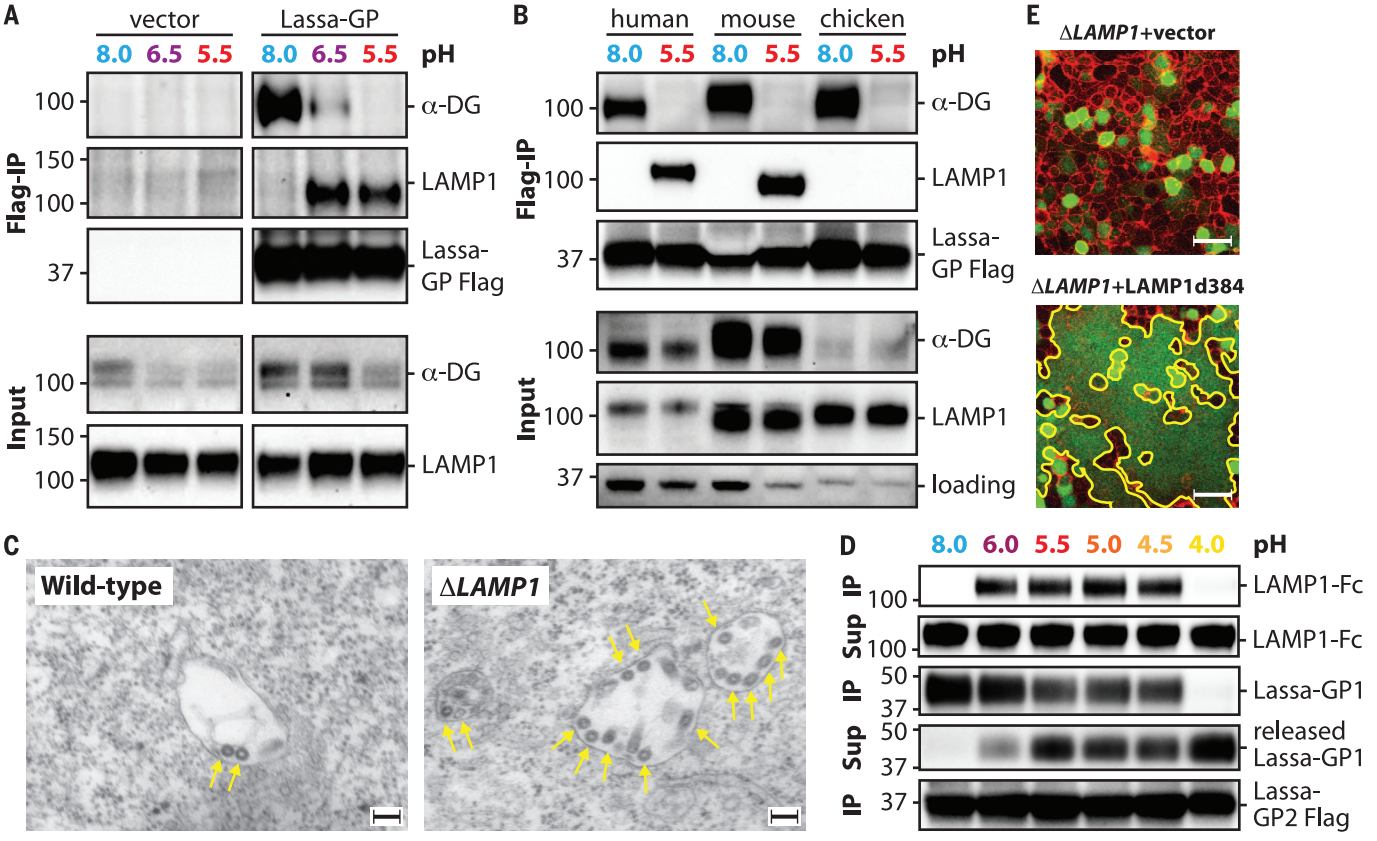

Fig. 2. Lassa-GP undergoes a pH-induced switch to engage LAMP1. (**A**) Flag-tagged Lassa-GP was immobilized on beads and incubated with cell lysates from human embryonic kidney (HEK) 293T cells at the indicated pH. Bound proteins were subjected to immunoblot analysis, and uncoated beads served as a control. IP, immunoprecipitation. (**B**) Flag-tagged Lassa-GP was immobilized on beads and incubated with lysates from human, mouse, and chicken cells at the indicated pH. Bound proteins were subjected to immunoblot analysis. (**C**) Electron micrographs of wild-type and *LAMP1*-deficient HEK-293T cells that were infected with rVSV-GP-LASV. *LAMP1*-deficient cells show an accumulation of the bullet-shaped viral particles (arrows) in intracellular vesicles. Scale bars, 100 nm. (**D**) Flag-tagged Lassa-GP was immobilized on beads and incubated with purified LAMP1-Fc at the indicated pH. Complexes (IP) were precipitated and subjected to immunoblot analysis. The supernatant (Sup) was analyzed for the release of Lassa-GP1. (**E**) *LAMP1*-deficient (top) or LAMP1d384-expressing HEK-293T cells (bottom) were transfected with expression vectors for Lassa-GP and GFP and exposed to pH 5.5. Cell boundaries were visualized with fluorescent wheat germ agglutinin (red). Large, homogenous green fluorescent area results from Lassa-GP–induced syncytia formation (yellow outline). Scale bars, 50 μm.

these conditions, but neither did *LAMP1* (Fig. 3A; figs. S3, C and D, and S17A, and tables S1 and S4). Therefore, we investigated a putative biochemical connection between them. LAMP1 is glycosylated (*16*) with both N- and O-glycans (*17*). LAMP1 derived from *ST3GAL4*-deficient cells showed reduced binding to lectins that preferentially capture α-2,3–linked sialic acid (fig. S17, B and C) (*18*) and lost its ability to bind to Lassa-GP (Fig. 3B). Thus, LAMP1 was only able to act as a host factor in the context of *ST3GAL4* proficiency.

LAMP1 consists of three luminal domains: a membrane-proximal domain, an O-glycosylated hinge region, and a distal domain. The distal domain contains 11 *N*-glycosylation sites (UniProt, P11279) and was sufficient to support rVSV-GP-LASV infection by itself (fig. S18). Reconciling that genes for *N*-glycosylation and sialylation acted as host factors and that LAMP1 derived from *ST3GAL4*-mutant cells was not recognized by Lassa-GP, we speculated that one of these glycosylation sites was important for host factor function. Indeed, we found that only Asn^{76} was essential for VSV-GP-LASV infectivity (Fig. 3C). This residue is present in LAMP1 from species susceptible to Lassa virus but absent in birds (Fig. 3D) (*16*). Substitution of this amino acid in human LAMP1 for the respective avian residue ($Asn^{76}Ser$) was sufficient to block infection (fig. S19) and binding to Lassa-GP (Fig. 3E). Reciprocally, insertion of a region surrounding human Asn^{76} into chicken LAMP1 converted the avian protein into a host factor (fig. S20). Thus, we identified the sialyltransferase ST3GAL4 as a critical enzyme required for LAMP1 to function as a host factor and mapped the interaction between sialylated LAMP1 and Lassa-GP to a single glycosylated amino acid present in sensitive species but absent in birds.

Because Lassa virus has a rodent reservoir, we examined whether LAMP1 is required for the propagation of wild-type Lassa virus in vivo. After intraperitoneal injection, virus was cleared in mice in which *Lamp1* was knocked out, whereas infection was manifest in all organ samples taken from wild-type or heterozygous animals (Fig. 4A and fig. S21).

Here, we have shown that Lassa virus entry requires a pH-regulated engagement of α-DG and LAMP1, both of which need to be glycosylated. However, the glycan structures that are needed for host factor function are unrelated and constructed by distinct enzymes (Fig. 4B and fig. S22). Unlike in rodents (*19*), the human upper airway mainly contains α-2,6–linked sialic acid moieties rather than α-2,3–linked sugars (*20*) generated by enzymes such as ST3GAL4. It has been proposed that this is an adaptation to evade pathogens like avian influenza (*21*), but it may also limit human-to-human spread of Lassa virus (*22*). Lassa virus has been described as a "late-penetrating"

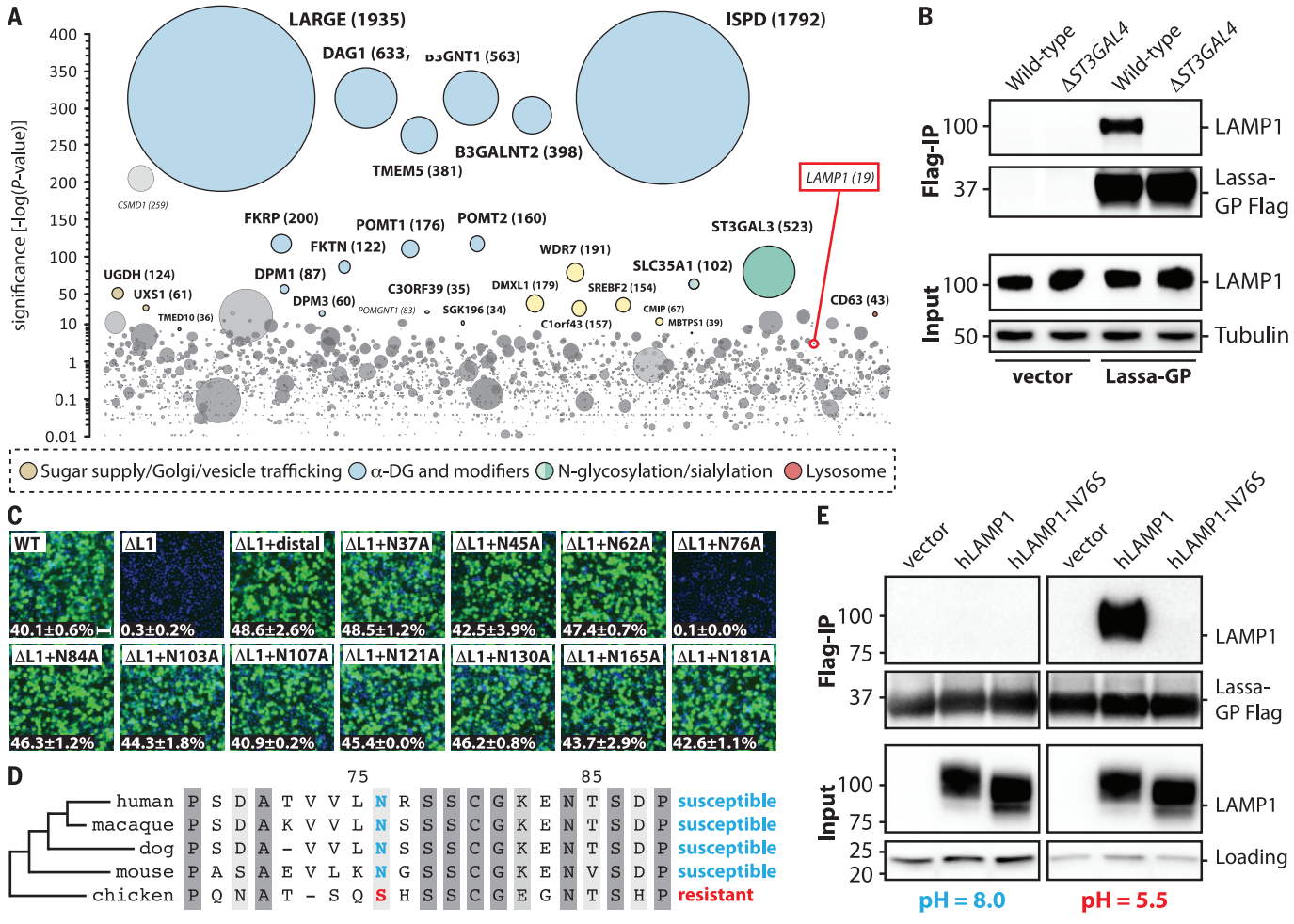

Fig. 3. Binding of Lassa-GP to LAMP1 depends on ST3GAL4, and LAMP1-Asn^{76} is critical for host factor function. (**A**) Haploid genetic screen pointing out genetic interactions between *ST3GAL4* and other Lassa entry factors. *ST3GAL4*-deficient cells were mutagenized and exposed to rVSV-GP-LASV. Gene-trap insertion sites were mapped in the resistant cell population, and data was analyzed as in Fig. 1A. (**B**) Flag-tagged Lassa-GP was immobilized on beads and incubated with cell lysates from wild-type and *ST3GAL4*-deficient HAP1 cells at pH 5.5. Bound proteins were subjected to immunoblot analysis. (**C**) Wild-type (WT) and *LAMP1*-deficient (ΔL1) HAP1 cells complemented with cDNAs expressing the distal domain of LAMP1 containing mutations at the indicated glycosylation sites were exposed to rVSV-GP-LASV. Percentage (±SD) of infected cells (eGFP-positive) is shown. (**D**) Comparison of LAMP1 polypeptides from indicated species highlights Asn^{76} as a marker of susceptibility to Lassa virus infection. (**E**) Flag-tagged Lassa-GP was immobilized on beads and incubated with lysates from *LAMP1*-deficient HEK-293T cells expressing human LAMP1 or "chickenized" LAMP1 carrying the $Asn^{76}Ser$ substitution at the indicated pH.

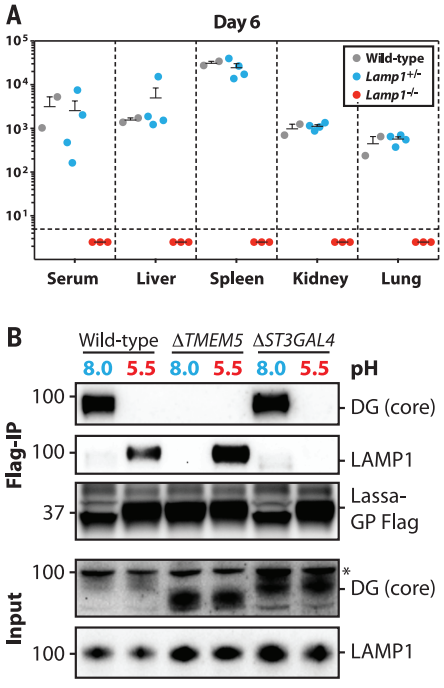

Fig. 4. *Lamp1* knockout mice are resistant to wild-type Lassa virus, and the receptors require distinct glycosyltransferases. (**A**) Lassa virus propagation in *Lamp1*$^{+/+}$, *Lamp1*$^{+/-}$, and *Lamp*$^{-/-}$ mice. Mice were injected intraperitoneally with wild-type Lassa virus, and viral titers (*y* axis, plaque-forming units/mL) were determined after 6 days in the indicated tissues. The horizontal line marks the detection limit. (**B**) Flag-tagged Lassa-GP was immobilized on beads and incubated with cell lysates from wild-type, *TMEM5*-, or *ST3GAL4*-deficient cells at the indicated pH. The glycosyltransferase TMEM5 is needed to generate an epitope on α-DG that is recognized by Lassa-GP (*4*). Bound proteins were subjected to immunoblot analysis. Asterisk indicates nonspecific background band.

virus (*23*) that requires low pH (*24*). Our findings rationalize these observations and emphasize the emergence of intracellular receptors for virus entry.

REFERENCES AND NOTES

1. S. Kunz *et al.*, *J. Virol.* **79**, 14282–14296 (2005).
2. W. Cao *et al.*, *Science* **282**, 2079–2081 (1998).
3. I. S. Lukashevich, R. F. Maryankova, F. M. Fidarov, *Acta Virol.* **27**, 282–285 (1983).
4. L. T. Jae *et al.*, *Science* **340**, 479–483 (2013).
5. F. Saito *et al.*, *FEBS Lett.* **579**, 2359–2363 (2005).
6. Materials and methods are available as supplementary materials on *Science* Online.
7. W. Zhu, J. Li, G. Liang, *Biomed. Environ. Sci.* **24**, 81–87 (2011).
8. N. Andrejewski *et al.*, *J. Biol. Chem.* **274**, 12692–12701 (1999).
9. J. Rohrer, A. Schweizer, D. Russell, S. Kornfeld, *J. Cell Biol.* **132**, 565–576 (1996).
10. T. Nishi, M. Forgac, *Nat. Rev. Mol. Cell Biol.* **3**, 94–103 (2002).
11. J. E. Carette *et al.*, *Nature* **477**, 340–343 (2011).
12. C. Di Simone, M. J. Buchmeier, *Virology* **209**, 3–9 (1995).
13. J. York, D. Dai, S. M. Amberg, J. H. Nunberg, *J. Virol.* **82**, 10932–10939 (2008).
14. J. H. Nunberg, J. York, *Viruses* **4**, 83–101 (2012).
15. E. J. Bowman, A. Siebers, K. Altendorf, *Proc. Natl. Acad. Sci. U.S.A.* **85**, 7972–7976 (1988).
16. M. Heffernan, S. Yousefi, J. W. Dennis, *Cancer Res.* **49**, 6077–6084 (1989).
17. S. R. Carlsson, P. O. Lycksell, M. Fukuda, *Arch. Biochem. Biophys.* **304**, 65–73 (1993).
18. W. C. Wang, R. D. Cummings, *J. Biol. Chem.* **263**, 4576–4585 (1988).
19. A. Ibricevic *et al.*, *J. Virol.* **80**, 7469–7480 (2006).
20. M. de Graaf, R. A. Fouchier, *EMBO J.* **33**, 823–841 (2014).
21. K. Shinya *et al.*, *Nature* **440**, 435–436 (2006).
22. W. H. Haas *et al.*, *Clin. Infect. Dis.* **36**, 1254–1258 (2003).
23. P. Y. Lozach, J. Huotari, A. Helenius, *Curr. Opin. Virol.* **1**, 35–43 (2011).
24. F. L. Cosset *et al.*, *J. Virol.* **83**, 3228–3237 (2009).

ACKNOWLEDGMENTS

We thank T. Sixma, A. Perrakis, E. von Castelmur, D. Lefeber, and members of the Brummelkamp group for discussion; M. Rusch for mouse breeding; S. Kunz for a plasmid encoding Lassa-GP; E. Ollmann-Saphire for an Fc-fusion vector; R. Schoepp for GP1 antibodies; and M. Verheije for DF1 cells. This work was supported by CGC.nl, Nederlandse Organisatie voor Wetenschappelijk Onderzoek Vidi grant 91711316, and European Research Council (ERC) Starting Grant (ERC-2012-StG 309634) to T.R.B.; Deutsche Forschungsgemeinschaft (DFG SPP1580 and GRK1459) to P.S.; and NIH grants AI081842 and AI109740 to S.P.W. J.M.D was supported by the Defense Threat Reduction Agency (CB3947). The HAP1 cells that were used are distributed under a materials transfer agreement. Opinions, interpretations, conclusions, and recommendations are those of the author and are not necessarily endorsed by the U.S. Army. T.R.B. is a cofounder and shareholder of Haplogen GmbH, a company involved in haploid genetics. Sequencing data are accessible at www.ncbi.nlm.nih.gov/sra (accession SRP041566).

SUPPLEMENTARY MATERIALS

www.sciencemag.org/content/344/6191/1506/suppl/DC1
Materials and Methods
Figs. S1 to S22
Tables S1 to S4
References (*25*–*44*)

20 February 2014; accepted 30 May 2014
10.1126/science.1252480

MEMBRANE TRAFFICKING

Nucleoside diphosphate kinases fuel dynamin superfamily proteins with GTP for membrane remodeling

Mathieu Boissan,[1,2,3,4]* Guillaume Montagnac,[1,2]† Qinfang Shen,[5] Lorena Griparic,[5] Jérôme Guitton,[6,7] Maryse Romao,[1,8] Nathalie Sauvonnet,[9] Thibault Lagache,[10] Ioan Lascu,[11] Graça Raposo,[1,8] Céline Desbourdes,[12,13] Uwe Schlattner,[12,13] Marie-Lise Lacombe,[3,4] Simona Polo,[14,15] Alexander M. van der Bliek,[5] Aurélien Roux,[16] Philippe Chavrier[1,2]*

Dynamin superfamily molecular motors use guanosine triphosphate (GTP) as a source of energy for membrane-remodeling events. We found that knockdown of nucleoside diphosphate kinases (NDPKs) NM23-H1/H2, which produce GTP through adenosine triphosphate (ATP)–driven conversion of guanosine diphosphate (GDP), inhibited dynamin-mediated endocytosis. NM23-H1/H2 localized at clathrin-coated pits and interacted with the proline-rich domain of dynamin. In vitro, NM23-H1/H2 were recruited to dynamin-induced tubules, stimulated GTP-loading on dynamin, and triggered fission in the presence of ATP and GDP. NM23-H4, a mitochondria-specific NDPK, colocalized with mitochondrial dynamin-like OPA1 involved in mitochondria inner membrane fusion and increased GTP-loading on OPA1. Like OPA1 loss of function, silencing of NM23-H4 but not NM23-H1/H2 resulted in mitochondrial fragmentation, reflecting fusion defects. Thus, NDPKs interact with and provide GTP to dynamins, allowing these motor proteins to work with high thermodynamic efficiency.

The 100-kD dynamin guanosine triphosphatase (GTPase) promotes uptake of cell-surface receptors both by clathrin-dependent and -independent pathways (*1*, *2*). Dynamin polymerizes into helix around the neck of endocytic pits and induces guanosine triphosphate (GTP) hydrolysis–driven membrane fission (*3*–*7*). Typical of molecular motors, dynamin has a low affinity for GTP and a high basal GTP-hydrolysis rate, which can be further stimulated by dynamin polymerization (*8*, *9*). This maximizes chemical energy gain and kinetics of hydrolysis, respectively, which in vivo depend on high concentration ratios of adenosine triphosphate/adenosine diphosphate (ATP/ADP) or GTP/guanosine diphosphate (GDP). The cellular concentrations of GTP and GDP are at least a factor of 10 lower than those of ATP and ADP, and GTP/GDP ratios could thus decrease much more rapidly at elevated workload, both of which make GTP not an ideal substrate for high-turnover, energy-dependent enzymes. Paradoxically, dynamin GTPases are among the most powerful molecular motors described (*7*).

Studies in *Drosophila* identified a genetic interaction between dynamin and *Awd* (*10*–*12*). Awd belongs to the family of nucleoside diphosphate kinases (NDPKs), which catalyze synthesis of nucleoside triphosphates, including GTP, from corresponding nucleoside diphosphates and ATP (*13*). The most abundant human NDPKs are the highly related cytosolic proteins NM23-H1 and -H2. NM23-H4, another NDPK-family member, localizes exclusively at the mitochondrial inner membrane (*14*, *15*). Mitochondrial

www.sciencemag.org/content/344/6191/1506/suppl/DC1

Supplementary Material for

Lassa virus entry requires a trigger-induced receptor switch

Lucas T. Jae, Matthijs Raaben, Andrew S. Herbert, Ana I. Kuehne, Ariel S. Wirchnianski, Timothy K. Soh, Sarah H. Stubbs, Hans Janssen, Markus Damme, Paul Saftig, Sean P. Whelan,* John M. Dye,* Thijn R. Brummelkamp*

*Corresponding author. E-mail: t.brummelkamp@nki.nl (T.R.B.); john.m.dye1.civ@mail.mil (J.M.D.); sean_whelan@hms.harvard.edu (S.P.W.)

Published 27 June 2014, *Science* **344**, 1506 (2014)
DOI: 10.1126/science.1252480

This PDF file includes:

Other Supplementary Material for this manuscript includes the following:
(available at www.sciencemag.org/content/344/6191/1506/suppl/DC1)

Tables S2 to S4 as separate Excel files

Materials and Methods:

Cells

HAP1 cells (*11*) and isogenic knockout derivatives were cultured in IMDM supplemented with 10% fetal calf serum (FCS), penicillin–streptomycin and L-glutamine. HEK-293T cells and knockout derivatives, Vero cells (American Type Culture Collection, Manassas, Virginia, USA), mouse embryonic fibroblasts (MEFs) and chicken embryonic fibroblasts (Cell Lines Service GmbH, Eppelheim, Germany) were cultured in DMEM supplemented with 10% FCS, penicillin–streptomycin and L-glutamine. DF1 chicken fibroblasts (kind gift from Dr. M. Verheije) were grown in DMEM supplemented with 10% FCS, penicillin–streptomycin, L-glutamine and 1mM sodium pyruvate. HAP1 cells and isogenic knockout clones were utilized for haploid genetic screens (see below) and follow-up experiments. HEK-293T cells and isogenic knockout derivatives were used for the generation of recombinant retroviruses (see below), production of Flag-tagged Lassa virus glycoprotein (Lassa-GP) and LAMP1 proteins, as well as follow-up experiments. Vero cells were used for the amplification of rVSV-GP-LASV and rVSV-G. Chicken embryo fibroblasts and DF1 chicken fibroblast cells were used for follow-up experiments.

Recombinant vesicular stomatitis viruses (rVSVs)

Generation of recombinant vesicular stomatitis virus (rVSV) expressing eGFP and the Lassa virus glycoprotein (rVSV-GP-LASV), the LCMV glycoprotein (rVSV-GP-LCMV) or the eGFP-expressing control virus (rVSV-G) have been described previously (*4, 26*). A functional fluorescent VSV M protein was constructed by introducing the eGFP coding sequence in between Arg^{39}-Gly^{40} of VSV M. MeGFP was cloned into pVSV-G and pVSV-LASV-GP (*4*) replacing the native VSV M sequence and replication-competent fluorescent virus (rVSV-LASV-GP-MeGFP) was recovered as described previously (*27*).

Infectivity assays with rVSV, rVSV-GP-LASV and rVSV-GP-LCMV

Cells were challenged with ca. 6.7 x 10^6 plaque forming units (PFU)/ml (multiplicity of infection (MOI) ≈ 2) of the respective virus and infectivity was assessed by the fraction of eGFP-positive cells 4-6h after challenge using a fluorescence microscope (Zeiss,

Oberkochen, Germany). The average number of eGFP-positive cells ± standard-deviation (SD) per field was calculated using ImageJ. In some experiments, cell nuclei were visualized by staining with Hoechst33342 (Invitrogen, Carlsbad, California, USA) or 4',6-diamidino-2-phenylindole (DAPI, Invitrogen) and the percentage of infected cells per field was calculated using the ratio of eGFP-positive cells and nucleus counts.

Infectivity assays with wild-type LCMV

Wild-type and *LAMP1*-deficient cells were infected with LCMV-Armstrong (kind gift of Allan Zajac, University of Alabama-Birmingham) at an MOI of 3 and infection was allowed to proceed for 16h at 34°C. Cells were pretreated with 100nM bafilomycin A1 or mock-treated for 1h before infection. Where applicable bafilomycin A1 was maintained present throughout the infection. Cells were then fixed with 4% para-formaldehyde (PFA) and immunofluorescence was performed using anti-LCMV polyclonal antisera. Secondary antibodies were coupled to Alexa Fluor 488 and nuclei were visualized using a DAPI stain.

Internalization assays with rVSV-GP-LASV-MeGFP

Cells grown on coverslips coated with poly-L-lysine (Sigma-Aldrich, St. Louis, Missouri, USA) were inoculated with gradient-purified rVSV-GP-LASV-MeGFP (MOI ≈ 300) at 4°C for 30min to allow binding of virus particles to the cell surface. Cells were subsequently incubated for 2h at 37°C in the presence of 10mM NH_4Cl to allow accumulation of internalized viral particles. Cells were washed with citric acid buffer (pH 3.0) to remove residual surface-bound virus and fixed in 2% PFA. The cellular plasma membrane was labeled by incubation of cells with 1µg/ml wheat germ agglutinin (WGA) conjugated to Alexa Fluor 568 (Molecular Probes, Invitrogen) in PBS for 15min at room temperature. After washing with PBS, cells were mounted onto glass slides and fluorescence was monitored by spinning-disk confocal microscopy (Zeiss). Representative images were collected with Slidebook 4.2 software (Intelligent Imaging Innovations).

LysoTracker staining

MEFs were plated on live cell imaging chambers and incubated in normal DMEM the day before imaging. Cells were washed with PBS before incubation with LysoTracker (LysoTracker® Red DND-99, Invitrogen) diluted 1:2000 in DMEM at 37°C for 30min. Before imaging, cells were washed 3x with PBS to remove excess dye.

DQ Red BSA degradation

MEFs were plated on coverslips the day before the experiment. The cells were incubated with the BODIPY labeled bovine serum albumin in DMEM at a final concentration of 50µg/ml for 5 hours. Cells were subsequently 3x washed with PBS, fixed with 4% PFA for 15min and imaged with a confocal microscopy.

Transferrin uptake

MEFs were plated on coverslips the day before the experiment. Cells were pulse-labeled with Alexa Fluor 488 conjugated Transferrin (Invitrogen) at 50 µg/ml for 30min at 37°C. After pulse cells were washed 2x with PBS and chased for the indicated time with medium lacking conjugated Transferrin and subsequently washed 2x with PBS and fixed with 4% PFA for 15min.

Endosomal fusion assay

MEFs were plated on coverslips the day before the experiment. The cells were incubated in FITC-labelled Dextran with a molecular weight of 3000 Dalton (Invitrogen) (0.5 µg/ml in DMEM) for 16h, washed 3x with PBS and subsequently chased in DMEM for 3h to ensure transport to lysosomes. Cells were then stained for Lamp2 by immunofluorescence, fixed and mounted onto glass slides.

Antibodies used for immunofluorescence

The following antibodies were used: Lamp1 (clone 1D4B) and Lamp2 (clone Abl93) (Developmental Studies Hybridoma Bank, created by the NICHD of the NIH and maintained at The University of Iowa, Department of Biology, Iowa City, IA 52242), Ctsd (*28*), Lbpa (clone 6C4, gift from Jean Gruenberg), EEA1 (Cell Signaling

Technology, Danvers, Massachusetts, USA), Rab7 (Cell Signaling Technology). For detection of cells infected with Influenza A virus (strain WSN) an anti-NP antibody was used (kind gift from C. de Haan).

Confocal microscopy

Photographs were acquired with an FV1000 confocal laser scanning microscope (Olympus) equipped with an oil immersion objective (U Plan S Apo 100×, N.A. 1.40) and Olympus Fluoview Software (3.0a) and a Leica-Microsystems microscope. Representative images were acquired with LCS software (Leica-Microsystems, Vienna, Austria).

MeGFP protein release assay

Cells grown on coverslips were pre-treated with 10µg/ml puromycin (Invivogen, San Diego, California, USA) for 30min (in the presence or absence of 100nM bafilomycin A1) and inoculated with rVSV-GP-LASV-MeGFP or rVSV-MeGFP control virus at an MOI of ≈ 300. Puromycin and bafilomycin A1 were maintained throughout the experiment. After incubation for 4h at 37°C, cells were washed twice with PBS and fixed with 2% PFA in PBS for 15min at room temperature. Cells were washed with PBS and mounted onto glass slides after which MeGFP localization images were acquired. To visualize the cell membrane, cells were stained with Alexa Fluor 647 labeled wheat germ agglutinin (WGA, Invitrogen, Molecular Probes).

Flow cytometry

Cells were detached using PBS supplemented with 5mM EDTA prior to incubation with murine antibodies directed against glycosylated α-DG (IIH6-C4, Millipore, Billerica, Massachusetts, USA) or against LAMP1 (H4A3, Santa Cruz biotechnology, Dallas, Texas, USA) in PBS 5% bovine serum albumin (BSA). Primary antibodies were labeled with a goat anti-mouse antibody coupled to Alexa Fluor 568 (Invitrogen). Samples were measured on a BD Fortessa flow-cytometer (BD, Franklin Lakes, NewJersey, USA). Fluorescence-activated cell sorting was carried out on a BD FACS Aria flow-cytometer

(BD). Data was analyzed and assembled using FlowJo (TreeStar Inc, Ashland, Oregon, USA).

Genome engineering

HAP1 cells with a disrupted *DAG1*, *LAMP1* or *ST3GAL4* locus were generated previously (*4*). In HEK-293T cells *DAG1*, *LAMP1* or both loci in combination were targeted using transcription activator-like effector nucleases targeting exonic sequences within these genes as described before (*4*). HEK-293T cells were subcloned and individual subclones were analyzed for the absence of the respective gene products by immunoblot analysis.

Immunoblot analysis

Proteins from cell pellets or lysates were denatured using sample buffer containing 100mM dithiothreitol (DTT) and 2% sodium dodecyl sulfate (SDS), separated by SDS-polyacrylamid-gel-electrophoresis (SDS-PAGE) and transferred onto polyvinylidene fluoride (PVDF) membranes (Millipore) by wet Western blotting. Membranes were subsequently blocked using PBS 0.1% Tween-20 supplemented with 5% BSA or non-fat milk powder. Glycosylated α-DG of different species was detected using the IIH6-C4 antibody (Millipore). The peptide backbone of dystroglycan (core) was visualized using the GTX105038 antibody (GeneTex, San Antonio, Texas, USA). Flag-tagged Lassa-GP was detected with the anti-Flag M2 antibody (Sigma-Aldrich). Human LAMP1 was detected using antibody AB2971 (Millipore). In experiments including mouse and/or chicken LAMP1, an antibody capable of detecting human, chicken and mouse LAMP1 (ab79821, Abcam, Cambridge, UK) was used. HA-tagged proteins were visualized using antibody H6908 (Sigma-Aldrich). Fc-fusion proteins were detected with horseradish peroxidase (HRP)-conjugated anti-rabbit antibodies (Invitrogen). eIF4G of different species was visualized using antibody #2498 (Cell Signaling Technology). Tubulin was detected using the B-7 antibody (Santa Cruz biotechnology). Lassa-GP1 was detected using a mouse monoclonal antibody (kind gift from R. Schoepp). Human LAMP2 was detected using a specific antibody (Abcam). Primary antibodies were detected using HRP-conjugated anti-mouse (Bio-Rad, Hercules, California, USA and Rockland,

Gilbertsville, Pennsylvania, USA) or anti-rabbit (Invitrogen) secondary antibodies. Antibody-bound proteins were visualized using enhancer and peroxide solutions (Thermo-Scientific, Waltham, Massachusetts, USA) and a gel imaging system (Bio-Rad).

Cloning of genes and retroviral transduction of cells

HAP1 cDNA was generated using the SuperScript® III First-Strand Synthesis System (Invitrogen). Human LAMP1 cDNA was amplified from this library using primers (5'-gatcGAATTCaccatggcggcccccggcagcgcc-3' and 5'-gatcCTCGAGctagatagtctggtagcctgc-3') and cloned into the retroviral expression vector pMX-IRES-BLAST using EcoRI and XhoI restriction enzymes. Human LAMP1d384 was generated from the wild-type cDNA using an altered reverse primer (5'-gatcCTCGAGctagatagtctggtagccgtgactcctcttcctgccgac-3'). Chicken LAMP1 cDNA was gene-synthesized based on the Ensembl transcript ENSGALT00000027170 and cloned into pMX-IRES-BLAST. HA-tagged variants of human and chicken LAMP1 were created by gene-synthesis of variants, C-terminally encoding a short linker followed by a triple HA tag as present in the pCMV6-AC-3HA vector (Addgene) and XhoI site (AAVYPYDVPDYAGYPYDVPDYAGSYPYDVPDYAVGSLE) and cloned into an altered version of the pMX-IRES-BLAST vector in which the IRES sequence was previously replaced with a 2A sequence (pMX-2A-BLAST), creating a single open reading frame containing the cloned genes and the blasticidin resistance cassette. pMX-2A-BLAST was generated by ligation of a gene-synthesized blasticidin cassette in which the translation start site (ATG) was replaced by a self-cleaving P2A sequence (GSGATNFSLLKQAGDVEENPGP, (*29*)) into pMX-IRES-BLAST using NotI and SalI. Domain mutants of human LAMP1 (LAMP1distal, LAMP1Δdistal and LAMP1Δhinge) were generated by gene-synthesis and cloned into pMX-2A-BLAST using EcoRI and XhoI. For generation of LAMP1distal, amino acids 1-197 of the human protein, comprising the membrane-distal ordered domain and three additional adjacent amino acids for flexibility, were fused to amino acids 381-417, encompassing the transmembrane region and lysosomal targeting sequence and two adjacent amino acids. LAMP1Δdistal was generated by deleting amino acids 29-197 from the full-length

sequence. For the generation of LAMP1Δhinge, amino acids 198-217 comprising the proline-rich hinge region were deleted from the full-length protein.

Asparagine-mutants of LAMP1distal were generated by gene-synthesis (replacing the asparagine-encoding triplets with GCA, encoding alanine) and cloned into the pMX-2A-BLAST vector using EcoRI and XhoI. 'Chickenized' human LAMP1-N76S was generated from the wild-type cDNA by introduction of a point mutation in the sequence by overlap-extension PCR using the following internal primers: 5'-ctgccatcagatgccacagtggtgctcTCAcgcagctcctgtggaaaagagaac-3' and 5'-gttctcttttccacaggagctgcgTGAgagcaccactgtggcatctgatggcag-3'. 'Humanized' chicken LAMP1 was generated by gene-synthesis introducing residues 63-101 of human LAMP1 into the chicken protein at the corresponding position. 'Chickenized' human and 'humanized' chicken LAMP1 were cloned into pMX-IRES-BLAST using EcoRI and XhoI restriction enzymes. Full length human LAMP2 was cloned from the HAP1 cDNA library using primer sequences 5'- gcaacgGGATCCaccatggtgtgcttccgcctcttc-3' and 5'-gcaacgCTCGAGaaattgctcatatccagcatgatg-3' and cloned into pMX-2A-BLAST using BamHI and XhoI.

A retroviral expression vector encoding LAMP2-RFP was constructed as follows: Overlap-extension PCR was performed to C-terminally ligate RFP to the human LAMP2 coding sequence. A 6x alanine-linker was introduced as a spacer. The first PCR was performed with the following primers: 5'-gcaacgGGATCCatggtgtgcttccgcctcttc-3' and 5'-gctgctgcagcagcagatctaaattgctcatatccagcatgatg-3'. The second PCR was carried out with the following primers: 5'-agatctgctgctgcagcagctgctatggtgagcaagggcgagga-3' and 5'-gcaacgGTCGACttacttgtacagctcgtccatg-3'. The resulting PCR product was cloned into pBABE-PURO using BamHI and SalI.

Retroviral vectors were transfected into HEK-293T cells together with pAdvantage (Clontech, Mountain View, California, USA) and the packaging plasmids pCMV-VSV-G and pGAG-POL. Virus was harvested 48h post transfection, filtered and applied to the respective cells. Transduced cells were selected with blasticidin S (Invivogen) or puromycin (Invivogen).

Cloning of constructs to direct the expression of Fc-fusion proteins

LAMP1-Fc and LAMP2-Fc expression plasmids were generated by overlap-extension PCR of DNA fragments encoding LAMP1 and LAMP2 extracellular parts (human LAMP1; residues Ala^{29}–Ser^{351} (PCR1), chicken LAMP1; residues Ser^{17}–Ser^{377} (PCR2), human LAMP1distal; residues Ala^{29}–Ser^{140} (PCR3), chicken LAMP1distal; residues Ser^{17}–Ser^{185} (PCR4), human LAMP2; residues Leu^{29}-Q^{342} (PCR5)) and a fragment encoding the Fc domain of rabbit IgG1 (PCR6-10). The resulting products were cloned (using BglII and BamHI restriction enzymes) into a phCMV soluble expression vector (a kind gift from Dr. E. Ollmann-Saphire), introducing an IgK signal sequence at the N-terminus. Sequences of the overlap-extension primers: 5'-gcaacgAGATCTcgagcagcaatgtttatggtgaaaaatggc-3' and 5'-cgctgttctctgcgccttcgtgacacg-3' (PCR1) with 5'-aggcgttttcagagaacagcgagacacactac-3' and 5'-ggtttaGGATCCtttacccgg-3' (PCR6); 5'-gcaacgAGATCTtcctcttcatttgacgtgagaga-3' and 5'-cgctgttctcgttttcatccagctgacattctt-3' (PCR2) with 5'-tggatgaaaacgagaacagcgagacacactac-3' and 5'-ggtttaGGATCCtttacccgg-3' (PCR7); 5'-gcaacgAGATCTcgagcagcaatgtttatggtgaaaaatggc-3' and 5'-cgctgttctcggaaggcctgtcttgttcaca-3' (PCR3) with 5'-cgctgttctcggaaggcctgtcttgttcaca-3' and 5'-ggtttaGGATCCtttacccgg-3' (PCR8); 5'-gcaacgAGATCTtcctcttcatttgacgtgagaga-3' and 5'-cgctgttctcagagaccatatcttccctacatt-3' (PCR4) with 5'-atatggtctctgagaacagcgagacacacta-3' and 5'-ggtttaGGATCCtttacccgg-3' (PCR9); 5'-gcaacgAGATCTcgagcattggaacttaatttgacagattcag-3' and 5'-cgctgttctcctgaaatgctccagacactgaa-3' (PCR5) with 5'-gagcatttcaggagaacagcgagacacactac-3' and 5'-ggtttaGGATCCtttacccgg-3' (PCR10) Fc-fusion proteins were expressed by transfection of the plasmids into HEK-293T cells and affinity purified from the culture supernatant using protein A sepharose beads (GE Healthcare, Little Chalfont, UK).

Immunoprecipitations

Flag-tagged Lassa-GP was produced in HEK-293T cells engineered to lack both α-DG and LAMP1. Cells were transiently transfected with pCAGGS-LASV-GP-Flag (kindly provided by Dr. S. Kunz) and lysates were prepared 48h post transfection in NETN buffer (50mM Tris-HCl, 150mM NaCl, 1mM EDTA, 0.5% NP-40) adjusted to pH 8.0,

7.4, 6.5, 6.0, 5.5, 5.0, 4.5 or 4.0 and supplemented with cOmplete protease inhibitor cocktail (Roche, Basel, Switzerland). Lysates were sonicated and Lassa-GP was immobilized on anti-Flag M2 agarose beads (Sigma-Aldrich). Beads were washed and incubated with whole cell lysates prepared in NETN buffer adjusted to the respective pHs. After incubation beads were washed with NETN buffer adjusted to the respective pH. Bound proteins were eluted and subjected to immunoblot analysis. For incubation of Flag-tagged GP with cells, beads were washed and bound proteins were eluted using 3xFlag peptide (Sigma Aldrich) and added to cells that were harvested in PBS containing 10% FCS. Flag-GP was incubated with the cells at 4°C for 1h and subsequently cells were pelleted and washed 3 times with PBS.

Lectin bead protein capture and PNGase F treatment

Cells were lysed in Lectin lysis buffer (50mM Tris-HCl pH 7.4, 150mM NaCl, 1% Triton-X 100, 2mM $CaCl_2$, 2mM $MgCl_2$) complemented with cOmplete protease inhibitor cocktail and samples were sonicated. Lysates were supplemented with 1% β-mercaptoethanol, 1% NP-40 and 0.5% SDS, boiled and incubated with 40μg/ml PNGase F or mock-treated at 37°C. Lysates were then incubated with Maackia amurensis lectin (MAA) agarose beads (US Biological, Salem, Massachusetts, USA) or Sambucus Nigra lectin (SNA) agarose beads (Vector Labs, Burlingame, California, USA). Beads were washed bound proteins were subjected to SDS-PAGE and immunoblot analysis (see above).

Fc-pull-down assays

Lysates from Lassa-GP transfected HEK-293T cells (see above) were incubated with protein A sepharose bead-bound Fc fusion proteins and incubated for 2h at 4°C under slow rotation. Beads were washed four times with lysis buffer after which proteins were taken up in sample buffer and subjected SDS-PAGE and immunoblot analysis (see above).

Radiolabeling and capture of recombinant rVSV-GP-LASV

Vero cells were cultured in T150 flasks and inoculated with rVSV-GP-LASV (MOI ≈ 3). 2.5h post inoculation the medium was replaced with methionine-free and cysteine-free medium containing 10µg/ml Actinomycin D (labeling medium). 3.5h post inoculation the medium was replaced with labeling medium supplemented with 200 µCi ^{35}S-Met/Cys. Virus was propagated O/N at 34°C. Rabiolabeled virus was harvested, filtered through a 0.2µm filter, pelleted and resuspended in NTE buffer (10mM Tris-HCl pH 7.4, 100mM NaCl, 1mM EDTA) O/N on ice. 5µg of radiolabeled virus was incubated for 2h with protein A sepharose bead-bound LAMP1-Fc in neutral (pH 8.0) or acidic (pH 5.5) medium under slow rotation. Beads were washed four times and subjected to SDS gel electrophoresis under reducing conditions. Gels were dried and radiolabeled proteins were detected using a Typhoon 9400 imager (GE Healthcare).

Electron microscopy (EM)

Cells were fixed in Karnovsky's fixative (2% paraformaldehyde + 2.5% glutaraldehyde in 0.1M cacodylate buffer at pH 7.2). Postfixation was performed with 1% osmiumtetroxide in 0.1M cacodylatebuffer. After washing, pellets were stained en bloc with Ultrastain 1 (Leica, Vienna, Austria), followed by an ethanol dehydration series. Finally, the cells were embedded in a mixture of DDSA/NMA/Embed-812 (EMS, Hatfield, Pennsylvania, USA), sectioned and stained with Ultrastain 2 (Leica) and analyzed with a CM10 electron microscope (FEI, Eindhoven, Netherlands).

Cell-cell fusion assays (polykarion assays)

HEK-293T cells and genome-engineered derivatives were transduced with empty vector or human LAMP1d384 and selected with blasticidin S. Selected cells were then transiently transfected with an expression vector for GFP together with pCAGGS-LASV-GP-Flag or an empty vector. 48h post transfection, the pH was dropped to 5.5 for 5min. 1h later cells were incubated with fluorescent wheat germ agglutinin (WGA) to visualize cell boundaries and examined for membrane fusion events by confocal microscopy. Fused cells lack intercellular WGA staining and instead show increased homogenously GFP-positive areas as a result of mixing of their cytoplasms.

The fusion index was calculated by comparing the number of unfused cells (as determined by WGA staining) per field in mock versus Lassa-GP transfected cells of the respective genotype.

rVSV-GP-LASV infectivity assays at acidic pH and bafilomycin treatment

HAP1 or HEK-293T cells of the respective genotypes were seeded prior to infection and, where applicable, pre-treated with 100nM bafilomycin A1 or mock-treated with DMSO for 1.5h. rVSV-GP-LASV was diluted to 6.7 x 10^6 PFU/ml in regular IMDM medium or IMDM adjusted to pH 5.5 and added to the cells (MOI ≈ 2). In some experiments, 100nM bafilomycin A1 was added along with the virus and maintained throughout the experiment. Virus containing medium was removed 2h post challenge and cells were scored for infection with rVSV-GP-LASV 4-7h post infection by eGFP expression using a fluorescence microscope.

Alignment of LAMP1 polypeptides from different species

Human LAMP1 (ENSGALT00000027170, Ensembl), LAMP1 from Rhesus macaque (I0FRN0, UniProt), from dog (F1Q260, UniProt), mouse (P11438, UniProt) and chicken (P05300, UniProt) were aligned and phylogenetically related using UniProt. In multi-species comparison, identity (dark grey) and similarity (light grey) were indicated.

Haploid genetic screens

The generation of gene-trap retrovirus and mutagenesis have been described previously (*4*). Approximately 10^8 mutagenized HAP1 cells or mutagenized HAP1 cells engineered to lack *DAG1* or *ST3GAL4* were used for the respective screens. Non-engineered mutagenized HAP1 cells were selected with ca. 4.5 x 10^4 PFU/ml of rVSV-GP-LASV (MOI ≈ 0.1) in the presence of 5mM NH_4Cl. Mutagenized HAP1 cells lacking *DAG1* or *ST3GAL4* were exposed to higher titers (ca. 6.7 x 10^6 PFU/ml, MOI ≈ 12.5) of rVSV-GP-LASV for selection. Following selection, the surviving colonies were expanded to ca. 3 × 10^7 total cells and their genomic DNA was isolated using a QIAamp DNA mini kit (Qiagen, Venlo, Netherlands).

Sequence analysis of gene-trap insertion sites

Recovery of gene-trap insertion sites from unselected control cells and cells selected with rVSV-GP-LASV has been described previously (*4*). For rVSV-GP-LASV-selected mutagenized HAP1 cells lacking *DAG1* or *ST3GAL4* enzymatic digest of the recovered genomic DNA was omitted. Processing of sequencing data from virus-selected populations was carried out as described before (*4*) with the exception that close read filtering (two reads on the same strand being within 2bp from one another) was omitted. For every gene, enrichment of inactivating gene-trap insertions in the rVSV-GP-LASV-selected populations over an unselected control data set (*4*) was assessed by applying a one-sided Fisher's exact test. Genes with *P*-value $\leq 10^{-4}$ were considered enriched (tables S2-4, first tab). Furthermore, genes found enriched for insertion sites had to pass a second statistical test. Enriched genes needed to show a significant bias ($P \leq 0.05$, binomial test) for gene-trap insertions in sense orientation of the affected gene (disruptive) versus insertions in antisense orientation (see tables S2-4, second tab). Because gene-trap insertions in exons are expected to disrupt the gene regardless of their orientation, this test could only be applied to genes for which the majority of insertions (≥70%) mapped to intronic regions. Genes for which less than 70% of the insertions affected introns could only be tested for enrichment of disruptive insertions compared to the unselected control dataset (see above), but were therefore required to meet a stricter cut-off ($P \leq 10^{-20}$, see tables S2-4, third tab). All *P*-values were corrected for false discovery rate (FDR). If the reported *P*-value was smaller than what the software (R) could report, its numerical value was set to the smallest non-zero normalized floating-point number R was capable of listing on the computer used for data analysis (ca. 10^{-314}).

HAP1 infections with wild-type Lassa virus

HAP1 cells, seeded in 96 well black plates (Greiner Bio-One Cellcoat®), were incubated with Lassa virus, Josiah strain, at MOI ≈ 1 in a Biosafety Level 4 (BSL4) laboratory located at USAMRIID. Following 1h absorption, virus inoculum was removed and cells were washed once with PBS. Fresh HAP1 cell culture media was added to each well and cells were incubated at 37°C, 5% CO_2, 80% humidity. Following 48h incubation, cells were washed once with PBS and submerged in 10% formalin prior to removal from the

BSL4 laboratory. Formalin was removed and cells were washed 3 times with PBS. Cells were blocked by adding 3% BSA/PBS to each well and incubating at 37°C for 2h. Lassa GP-specific mAb 52-161-6 was added to each well and incubated at room temperature for 2h. Cells were washed 3 times with PBS prior to addition of goat anti-mouse IgG-Alexa Fluor 488 (Invitrogen, Molecular Probes®) secondary antibody. Following 1h incubation with secondary antibody, cells were washed 3 times prior to addition of Hoechst 33342 (Invitrogen, Molecular Probes®) diluted in PBS. Cells were imaged and Lassa virus infected cells enumerated using the Operetta High Content Imaging System (PerkinElmer, Waltham, Massachusetts, USA) and Harmony® High Content Imaging and Analysis Software (PerkinElmer).

Mouse injections and tissue titer analysis

$Lamp1^{-/-}$ (n=9), $Lamp1^{+/-}$ (n=12), and wild-type ($Lamp1^{+/+}$, n=8) mice, 13-16 weeks of age, were inoculated intraperitoneally with 100 PFU of Lassa virus, Josiah strain. Subsets of mice from each knockout group and wild-type group were euthanized on days 3 and 6 post infection and blood, liver, spleen, kidneys, and lungs were collected. Blood samples were allowed to clot prior to centrifugation and serum fraction was collected for viral titer determination. Tissue samples were weighed and appropriate volumes of Minimal Essential Medium (MEM)/2% FBS were added to yield 10% tissue homogenates. Following homogenization using a gentleMACS™ Dissociator (Miltenyi Biotec, Bergisch Gladbach, Germany), homogenates were centrifuged and supernatants collected for viral titer determination. Half of each organ was placed in 10% formalin for immunohistochemical analysis and hematoxylin and eosin (H&E) staining.

Viral titers were determined by plaque assay using Vero cells maintained in MEM/5%FBS. Serum and tissue samples were serially diluted in MEM/5%FBS and added to confluent monolayers of Vero cells. Following 1h incubation at 37°C, 5% CO_2, 80% humidity, cells were overlaid with a mixture of 1 part 1% agarose (Seakem, Lonza, Basel, Switzerland) and 1 part 2X Eagle basal medium (EBME)/5% FBS and incubated at 37°C, 5% CO_2, 80% humidity for 7 days. Cells were again overlaid with a mixture of 1 part 1% agarose (Seakem) and 1 part 2X EBME/30mM HEPES/5% FBS/5% Neutral Red and incubated for 1-2 more days before enumerating the number of plaque forming units

per milliliter. Research was conducted under an IACUC approved protocol in compliance with the Animal Welfare Act, PHS Policy, and other Federal statutes and regulations relating to animals and experiments involving animals. The facility where this research was conducted is accredited by the Association for Assessment and Accreditation of Laboratory Animal Care, International and adheres to principles stated in the Guide for the Care and Use of Laboratory Animals, National Research Council, 2011.

Fig S1

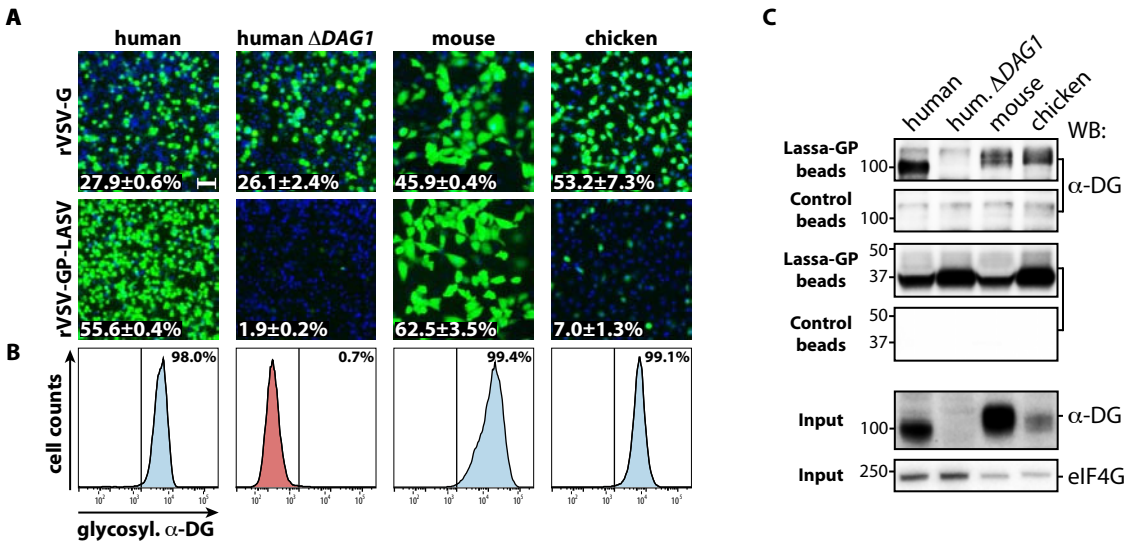

Figure S1. Chicken fibroblasts are resistant to infection with rVSV-GP-LASV although Lassa-GP interacts with avian α-DG. (A) Infection of wild-type and *DAG1*-deficient HAP1 cells as well as chicken and mouse fibroblasts with replication-competent recombinant vesicular stomatitis viruses that expresses enhanced green fluorescent protein (eGFP) as an infection marker, and the VSV (VSV-G, control) or Lassa virus glycoprotein (rVSV-GP-LASV). Percentage (±SD) of infected cells (eGFP-positive) is indicated. **(B)** Detection of glycosylated α-DG at the cell surface using a specific antibody (IIH6). Percentage of positive cells is indicated. **(C)** Lassa-GP carrying a Flag-tag on the C-terminus (joining it to the GP2 subunit of the viral protein) was immobilized on beads containing anti-Flag antibody and incubated with lysates from cells described in panel (A). Bound proteins were subjected to immunoblot analysis. Beads without Lassa-GP served as a control.

Fig S2

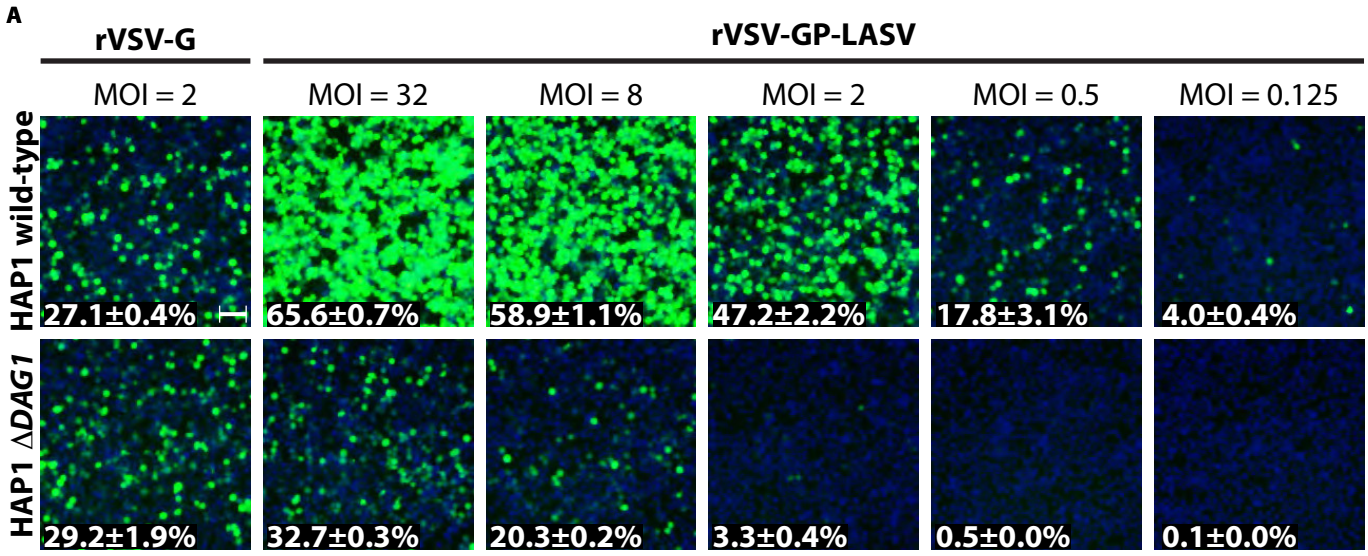

Figure S2. Residual susceptibility of α-DG-deficient cells to rVSV-GP-LASV infection. Wild-type and *DAG1*-deficient HAP1 cells were challenged with rVSV-GP-LASV at the indicated multiplicity of infection (MOI). rVSV-G served as a control. Resistance of *DAG1*-deficient cells to rVSV-GP-LASV could be overcome by high titers of rVSV-GP-LASV. Percentage (±SD) of infected cells (eGFP-positive) is indicated.

Fig S3

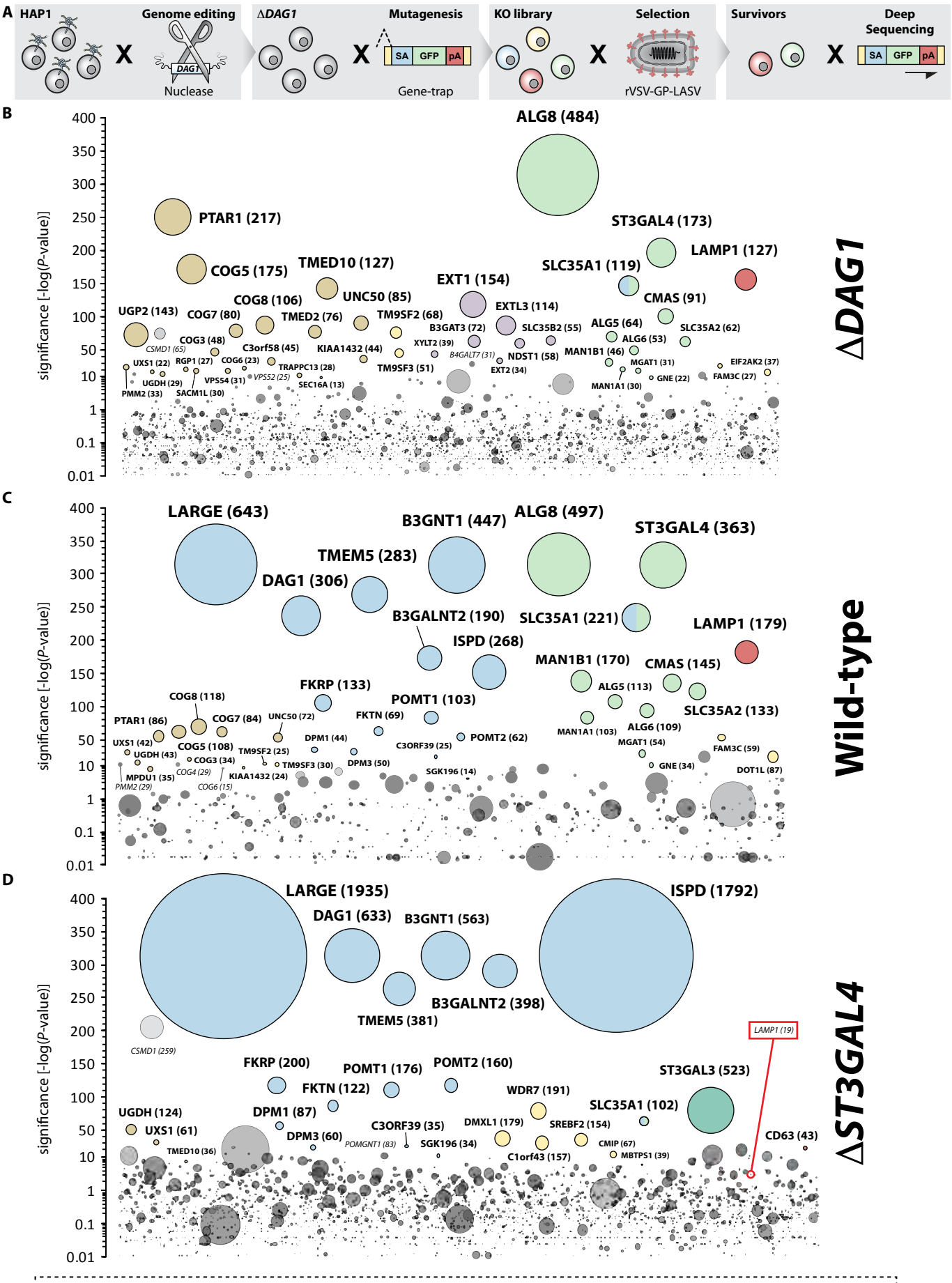
A
HAP1
Genome editing
DAG1
Nuclease
ΔDAG1
Mutagenesis
SA
GFP
pA
Gene-trap
KO library
Selection
rVSV-GP-LASV
Survivors
Deep Sequencing
B
significance [-log(P-value)]
ALG8 (484)
PTAR1 (217)
ST3GAL4 (173)
LAMP1 (127)
COG5 (175)
TMED10 (127)
SLC35A1 (119)
EXT1 (154)
UNC50 (85)
COG8 (106)
CMAS (91)
EXTL3 (114)
UGP2 (143)
COG7 (80)
TMED2 (76)
TM9SF2 (68)
B3GAT3 (72)
SLC35B2 (55)
ALG5 (64)
SLC35A2 (62)
COG3 (48)
ALG6 (53)
XYLT2 (39)
C3orf58 (45)
KIAA1432 (44)
NDST1 (58)
MAN1B1 (46)
UXS1 (22)
RGP1 (27)
COG6 (23)
TRAPPC13 (28)
TM9SF3 (51)
MGAT1 (31)
EIF2AK2 (37)
UGDH (29)
VPS54 (31)
SEC16A (13)
GNE (22)
FAM3C (27)
PMM2 (33)
SACM1L (30)
MAN1A1 (30)
ΔDAG1
C
significance [-log(P-value)]
LARGE (643)
B3GNT1 (447)
ALG8 (497)
ST3GAL4 (363)
TMEM5 (283)
DAG1 (306)
B3GALNT2 (190)
SLC35A1 (221)
LAMP1 (179)
ISPD (268)
MAN1B1 (170)
CMAS (145)
FKRP (133)
ALG5 (113)
COG8 (118)
POMT1 (103)
SLC35A2 (133)
PTAR1 (86)
COG7 (84)
UNC50 (72)
FKTN (69)
ALG6 (109)
MAN1A1 (103)
UXS1 (42)
COG5 (108)
DPM1 (44)
POMT2 (62)
MGAT1 (54)
FAM3C (59)
UGDH (43)
TM9SF2 (25)
C3ORF39 (25)
COG3 (34)
GNE (34)
DOT1L (87)
TM9SF3 (30)
DPM3 (50)
MPDU1 (35)
COG4 (29)
KIAA1432 (24)
SGK196 (14)
PMM2 (29)
COG6 (15)
Wild-type
D
significance [-log(P-value)]
LARGE (1935)
ISPD (1792)
DAG1 (633)
B3GNT1 (563)
B3GALNT2 (398)
TMEM5 (381)
CSMD1 (259)
LAMP1 (19)
FKRP (200)
POMT1 (176)
POMT2 (160)
ST3GAL3 (523)
FKTN (122)
WDR7 (191)
UGDH (124)
DPM1 (87)
SLC35A1 (102)
C3ORF39 (35)
DMXL1 (179)
SREBF2 (154)
UXS1 (61)
DPM3 (60)
CD63 (43)
POMGNT1 (83)
SGK196 (34)
CMIP (67)
TMED10 (36)
C1orf43 (157)
MBTPS1 (39)
ΔST3GAL4
Sugar supply/Golgi/vesicle trafficking
Heparan sulfate / α-DG and modifiers
N-glycosylation/sialylation
Lysosome

Figure S3. Iterative haploid genetic screens identify host factor interdependencies in Lassa virus entry. (A) Workflow for genetic screens in nuclease-engineered haploid cells carrying disruptive mutations in the respective loci. Nuclease-edited cells were subjected to gene-trap mutagenesis, creating a knock-out (KO) library and subsequently selected with rVSV-GP-LASV. Gene-trap insertion sites were recovered from surviving cells and analyzed by deep sequencing. **(B)** Genes enriched for disruptive mutations in α-DG-deficient cells selected with rVSV-GP-LASV. This representation is identical to the one in Fig. 1A but included here to facilitate side-by-side comparison of the screens in different genetic backgrounds. **(C)** Genes enriched for disruptive mutations in wild-type control cells selected with rVSV-GP-LASV. This screen is similar to a screen that has been published by our group (*4*) but has been carried out in parallel to the screens in the modified genetic backgrounds. **(D)** Genes enriched for disruptive mutations in *ST3GAL4*-deficient cells selected with rVSV-GP-LASV. This representation is identical to the one shown in Fig. 3A but included for side-by-side comparison. All haploid genetic screens were analyzed as described in Fig. 1A and in the supplementary materials. For full gene names see table S1.

Fig S4

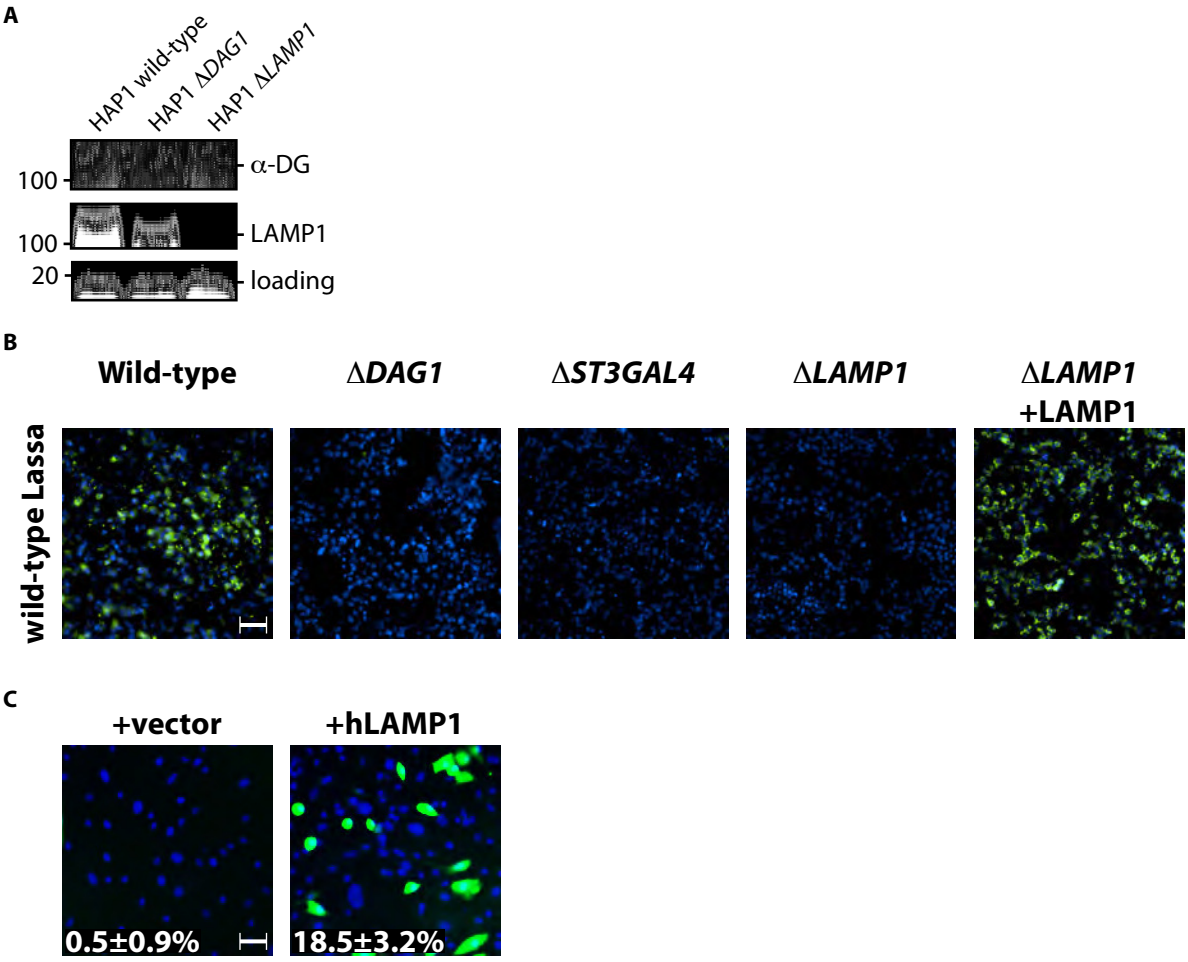

Figure S4. Human LAMP1 and ST3GAL4 are important host factors for Lassa virus entry. (A) Immunoblot analysis of α-DG and LAMP1 protein expression in HAP1 cells engineered to lack dystroglycan (Δ*DAG1*) or LAMP1 (Δ*LAMP1*) using specific antibodies. **(B)** HAP1 cells engineered to lack *ST3GAL4* or *LAMP1* were as resistant to wild-type Lassa virus as HAP1 cells lacking the reported Lassa receptor α-DG. Re-introduction of LAMP1 restored susceptibility to wild-type Lassa virus. Infected cells were visualized using an antibody directed against Lassa-GP (green). **(C)** Primary chicken embryo fibroblast cells were naturally resistant to infection with rVSV-GP-LASV but became susceptible upon heterologous expression of human LAMP1 (hLAMP1). Percentage (±SD) of infected cells (eGFP-positive) is indicated. Scale bars: 50μm.

Fig S5

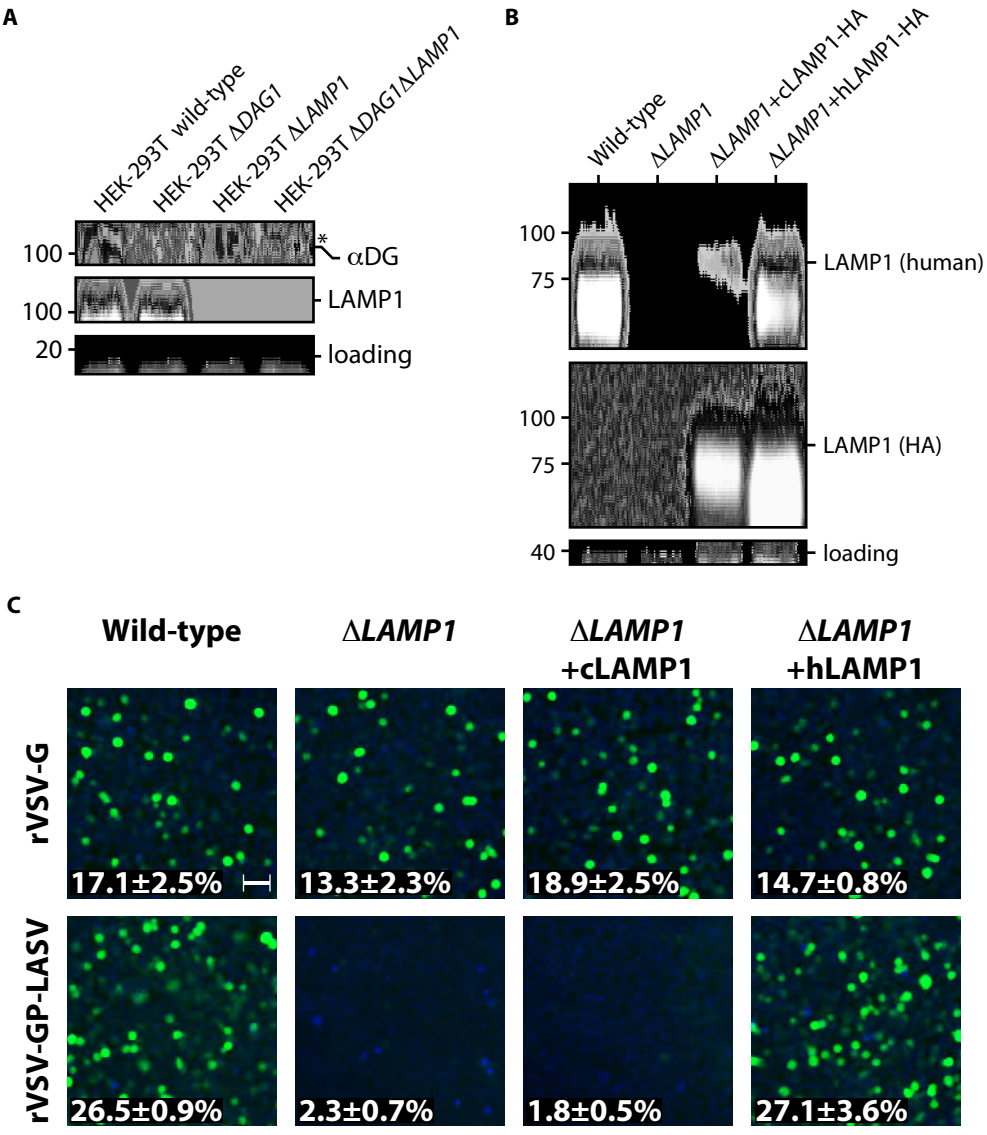
A
HEK-293T wild-type
HEK-293T ΔDAG1
HEK-293T ΔLAMP1
HEK-293T ΔDAG1ΔLAMP1
100
αDG
100
LAMP1
20
loading
B
Wild-type
ΔLAMP1
ΔLAMP1+cLAMP1-HA
ΔLAMP1+hLAMP1-HA
100
75
LAMP1 (human)
100
75
LAMP1 (HA)
40
loading
C
Wild-type
ΔLAMP1
ΔLAMP1 +cLAMP1
ΔLAMP1 +hLAMP1
rVSV-G
17.1±2.5%
13.3±2.3%
18.9±2.5%
14.7±0.8%
rVSV-GP-LASV
26.5±0.9%
2.3±0.7%
1.8±0.5%
27.1±3.6%

Figure S5. Human but not chicken LAMP1 restores susceptibility to rVSV-GP-LASV in *LAMP1*-deficient human cells. (A) Immunoblot analysis of α-DG and LAMP1 protein expression in HEK-293T cells engineered to lack α-DG (Δ*DAG1*), LAMP1 (Δ*LAMP1*) or both (Δ*DAG*1Δ*LAMP1)* using specific antibodies. * = non-specific background band. **(B)** Detection of chicken LAMP1 (cLAMP1) and human LAMP1 (hLAMP1) in retrovirus-transduced human cells using antibodies specific for human LAMP1 or a C-terminal HA-tag present on both recombinant proteins. **(C)** Wild-type or *LAMP1*-deficient HEK-293T cells were transduced with retroviruses expressing cLAMP1 or hLAMP1 and exposed to rVSV-G or rVSV-GP-LASV. Percentage (±SD) of infected cells (eGFP-positive) is indicated. Scale bar: 50μm.

Fig S6

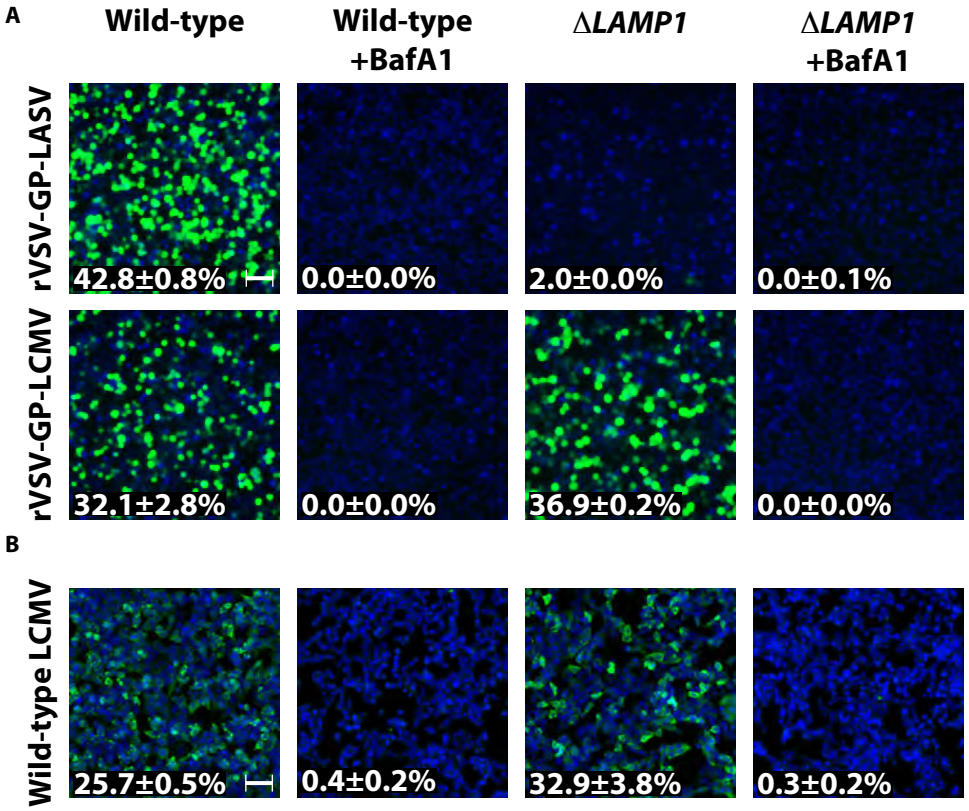

Figure S6. LAMP1 does not act as an essential host factor for lymphocytic choriomeningitis virus (LCMV). (A) Wild-type and *LAMP1*-deficient HAP1 cells were challenged with rVSV expressing the glycoprotein of lymphocytic choriomeningitis virus (rVSV-GP-LCMV) in the presence or absence of bafilomycin A1 (BafA1). rVSV-GP-LASV served as a control. **(B)** The cells shown in panel (A) were infected with wild-type LCMV in the presence or absence of bafilomycin A1 and stained with an antibody directed against the nucleoprotein (NP, green) to visualize infected cells. Percentage (±SD) of infected cells (eGFP-positive) is indicated. Scale bars: 50µm.

Fig S7

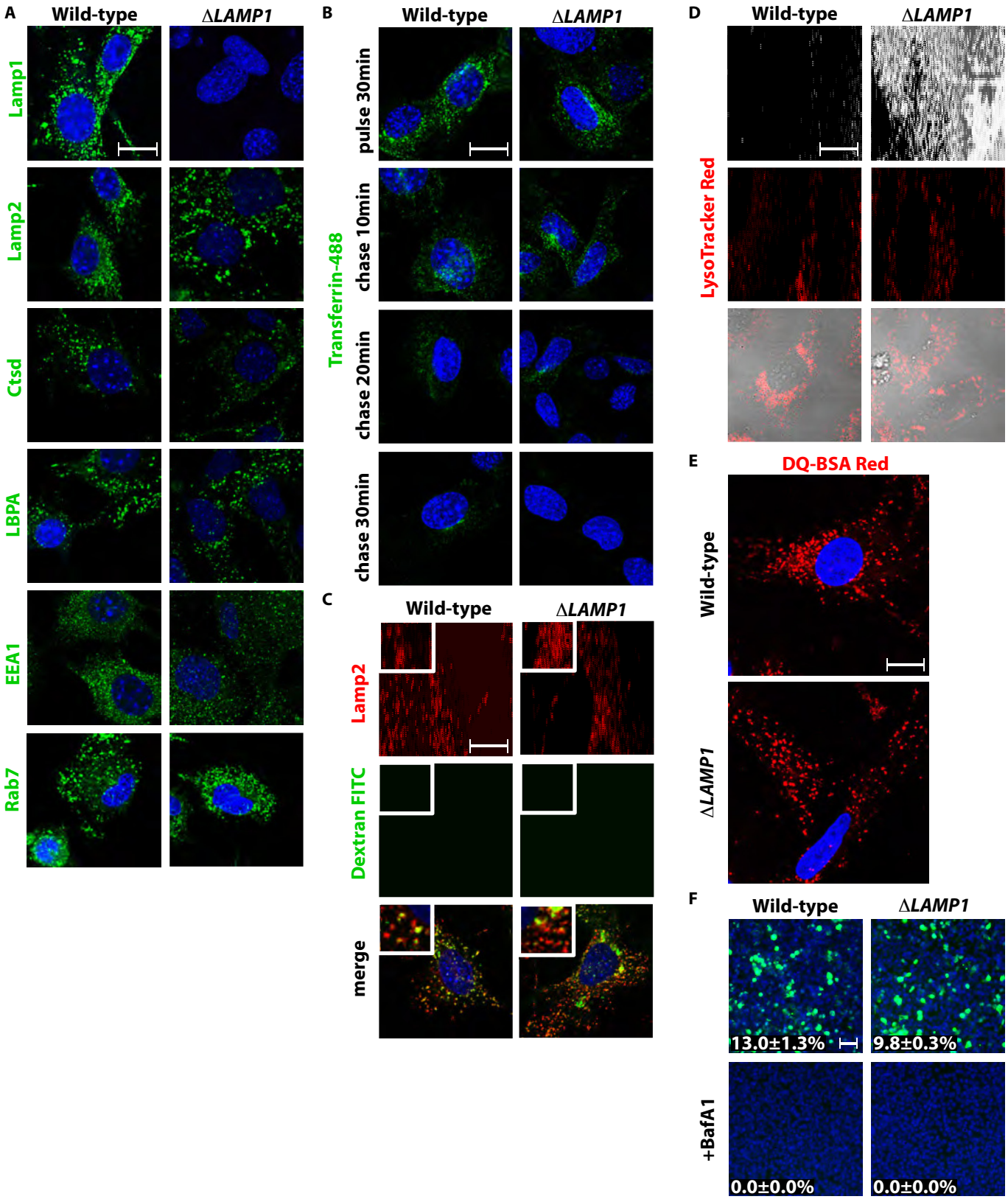
A
Wild-type
ΔLAMP1
Lamp1
Lamp2
Ctsd
LBPA
EEA1
Rab7
B
Wild-type
ΔLAMP1
pulse 30min
Transferrin-488
chase 10min
chase 20min
chase 30min
C
Wild-type
ΔLAMP1
Lamp2
Dextran FITC
merge
D
Wild-type
ΔLAMP1
LysoTracker Red
E
DQ-BSA Red
Wild-type
ΔLAMP1
F
Wild-type
ΔLAMP1
13.0±1.3%
9.8±0.3%
+BafA1
0.0±0.0%
0.0±0.0%

Figure S7. Cells deficient of *Lamp1* do not display major differences in endo/lysosomal properties and the endocytic pathway. (A) Wild-type (+/+) and *Lamp1*-deficient (-/-) mouse embryonic fibroblasts (MEF) showed no gross differences for the lysosomal markers Lamp2, cathepsin D (Ctsd), the early endosomal marker early endosomal antigen 1 (EEA1), Rab7 or the late endosomal marker lysobisphosphatidic acid (LBPA). Scale bar: 15μm. **(B)** Endocytosis and recycling of Alexa Fluor 488 labeled Transferrin is similar in wild-type (+/+) and *Lamp1*-deficient (-/-) MEFs. MEFs were pulsed for 30min with labeled Transferrin and chased in medium without labeled Transferrin for 10, 20 and 30min respectively. Scale bar: 15μm. **(C)** Fusion of endosomes with lysosomes was not impaired in *Lamp1*-deficient (-/-) MEFs as determined by incubation and uptake of FITC labeled Dextran (molecular weight 3000 Da) for 16h (green), followed by a 3h chase to ensure quantitative delivery of labeled Dextran to lysosomes followed by immunofluorescence staining for Lamp2 (red). A similar co-localization pattern was observed in cells of both genotypes. Scale bar: 15μm. **(D)** Lysosomes from wild-type (+/+) and *Lamp1*-deficient (-/-) MEFs were properly acidified as determined by LysoTracker Red staining followed by confocal live cell imaging. Scale bar: 15μm. **(E)** Degradative capacity of late endosomes/lysosomes was unaffected in *Lamp1*-deficient MEFs as determined by DQ-BSA degradation. Comparable release of the BODIPY-fluorophore from BSA was apparent in MEFs from both genotypes. **(F)** Wild-type and *LAMP1*-deficient HAP1 cells were exposed to Influenza A virus (WSN) in the absence or presence of bafilomycin A1 and stained using antibodies against Influenza A virus nucleoprotein. Percentage (±SD) of infected cells (Alexa Fluor 488 positive) is indicated. Scale bar: 50μm.

Fig S8

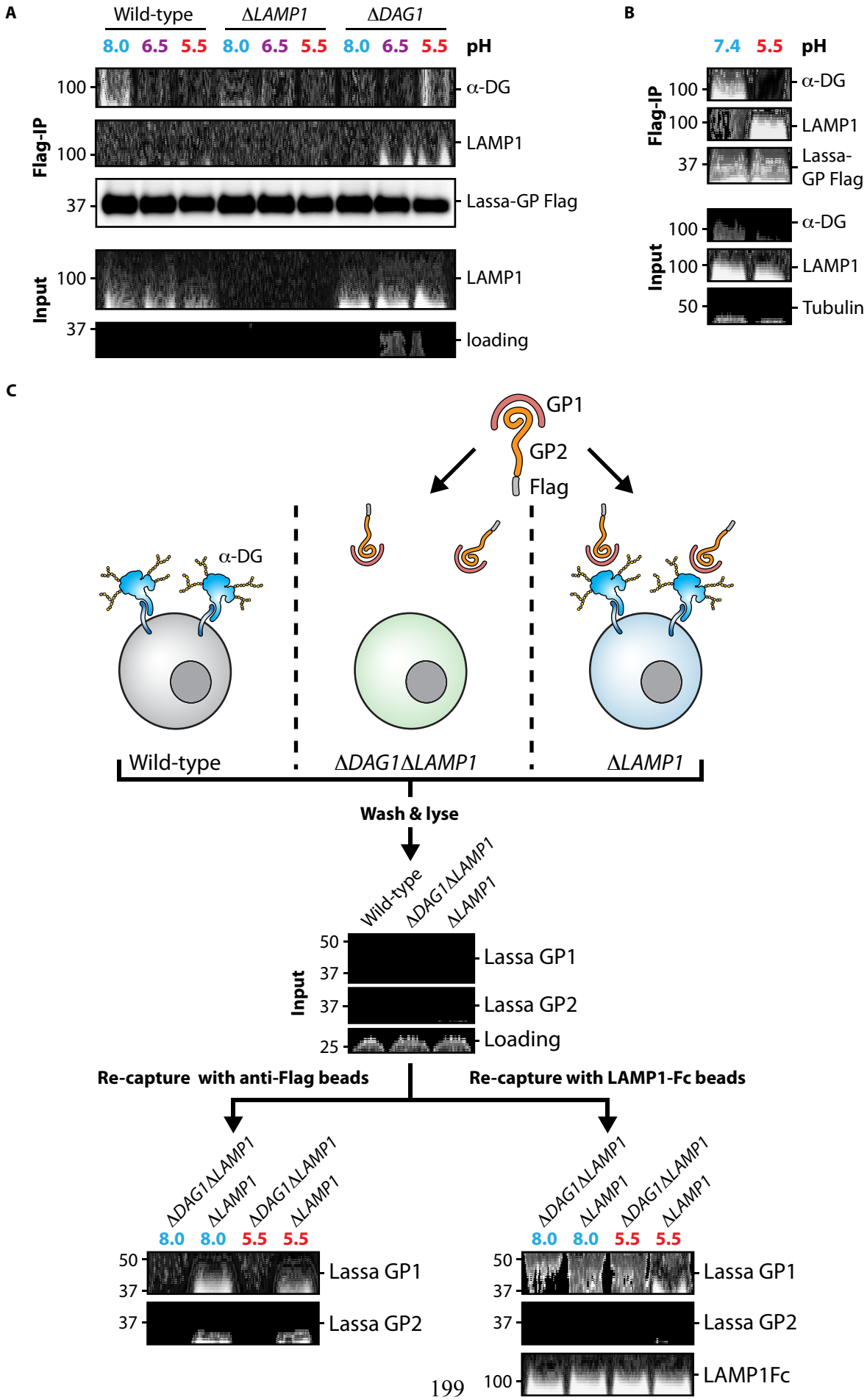
A
Wild-type
ΔLAMP1
ΔDAG1
8.0 6.5 5.5 8.0 6.5 5.5 8.0 6.5 5.5
pH
Flag-IP
100
α-DG
100
LAMP1
37
Lassa-GP Flag
Input
100
LAMP1
37
loading
B
7.4 5.5
pH
Flag-IP
100
α-DG
100
LAMP1
37
Lassa-GP Flag
Input
100
α-DG
100
LAMP1
50
Tubulin
C
GP1
GP2
Flag
α-DG
Wild-type
ΔDAG1ΔLAMP1
ΔLAMP1
Wash & lyse
Wild-type
ΔDAG1ΔLAMP1
ΔLAMP1
Input
50
Lassa GP1
37
37
Lassa GP2
25
Loading
Re-capture with anti-Flag beads
Re-capture with LAMP1-Fc beads
ΔDAG1ΔLAMP1
ΔLAMP1
ΔDAG1ΔLAMP1
ΔLAMP1
8.0 8.0 5.5 5.5
50
Lassa GP1
37
37
Lassa GP2
ΔDAG1ΔLAMP1
ΔLAMP1
ΔDAG1ΔLAMP1
ΔLAMP1
8.0 8.0 5.5 5.5
50
Lassa GP1
37
37
Lassa GP2
100
LAMP1Fc

Figure S8. Lassa-GP undergoes a pH-dependent engagement of α-DG and human LAMP1 that is not due to competition and α-DG-bound glycoprotein can subsequently bind LAMP1. (A) Flag-tagged Lassa-GP was immobilized on beads and incubated with cell lysates from wild-type, *LAMP1*-deficient, or *DAG1*-deficient HEK-293T cells at the indicated pH. Protein complexes were subjected to immunoblot analysis. **(B)** Lassa-GP was immobilized as described in panel (A) and mixed with cell lysates from HAP1 wild-type cells at the indicated pH. Complexes were analyzed by immunoblot analysis. **(C)** Flag-tagged Lassa-GP was purified with anti-Flag beads and subsequently eluted using a Flag peptide. Eluted Lassa-GP was then incubated with HEK-293T cells lacking LAMP1 or LAMP1 and α-DG on ice followed by extensive washing. Cell-bound Lassa-GP was analyzed for the presence of the GP1 and GP2 subunit by immunoblotting (middle) or re-captured using anti-Flag beads (left) or immobilized LAMP1-Fc (right) at the indicated pH. Precipitated Lassa-GP complexes were analyzed for the presence of GP1 and GP2 by immunoblotting. Wild-type HEK-293T (not exposed to Lassa-GP) cells served as a control.

Fig S9

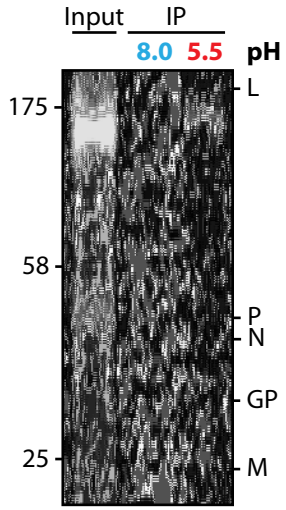

Figure S9. Intact virions can interact with LAMP1 at acidic but not at neutral pH. rVSV-GP-LASV was propagated in the presence of ^{35}S-labelled methionine and cysteine. Radiolabeled virus was purified and exposed to Fc-tagged LAMP1 immobilized on beads at pH 8.0 and 5.5. Bound viral particles were analyzed by immunoblot analysis.

Fig S10

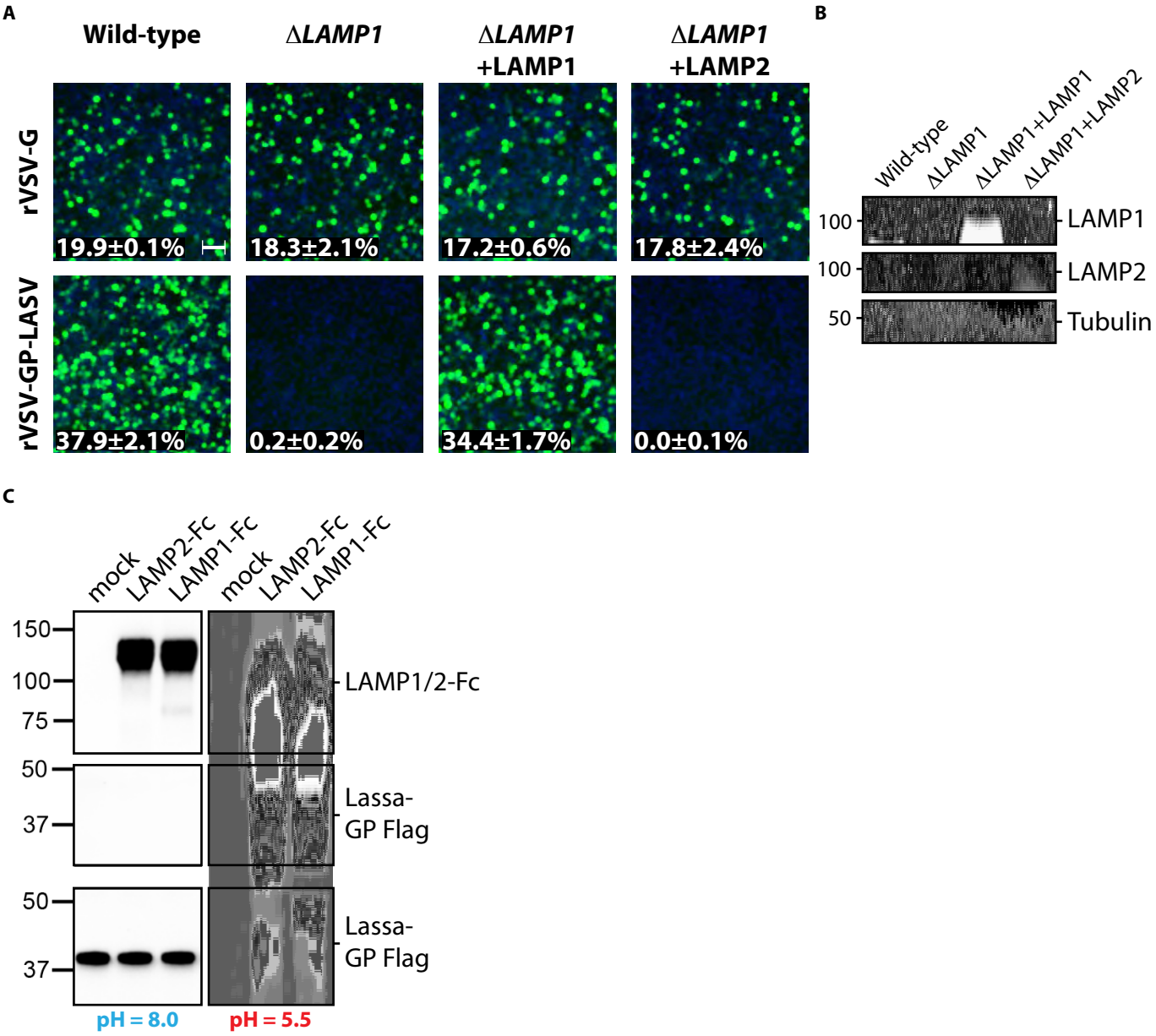
A
Wild-type
ΔLAMP1
ΔLAMP1 +LAMP1
ΔLAMP1 +LAMP2
rVSV-G
rVSV-GP-LASV
19.9±0.1%
18.3±2.1%
17.2±0.6%
17.8±2.4%
37.9±2.1%
0.2±0.2%
34.4±1.7%
0.0±0.1%
B
Wild-type
ΔLAMP1
ΔLAMP1+LAMP1
ΔLAMP1+LAMP2
100
LAMP1
100
LAMP2
50
Tubulin
C
mock
LAMP2-Fc
LAMP1-Fc
mock
LAMP2-Fc
LAMP1-Fc
150
100
75
LAMP1/2-Fc
50
37
Lassa-GP Flag
50
37
Lassa-GP Flag
pH = 8.0
pH = 5.5

Figure S10. LAMP1 but not LAMP2 acts as a host factor and interacts with Lassa-GP at low pH. (A) *LAMP1*-deficient HAP1 cells were transduced with retroviruses expressing human LAMP1 or LAMP2 and challenged with rVSV-GP-LASV or rVSV-G. Wild-type and *LAMP1*-deficient HAP1 cells served as a control. Percentage (±SD) of infected cells (eGFP-positive) is indicated. **(B)** Immunoblot analysis of the cells described in panel (A) showing expression of LAMP proteins. **(C)** Fc-tagged human LAMP1 or LAMP2 were immobilized on beads and mixed with lysates of HEK-293T cell transfected with Flag-tagged Lassa-GP at the respective pH. Bound complexes were subjected to immunoblot analysis. LAMP proteins were visualized with an antibody directed against their Fc tag. Beads containing neither LAMP1-Fc nor LAMP2-Fc served as a control.

Fig S11

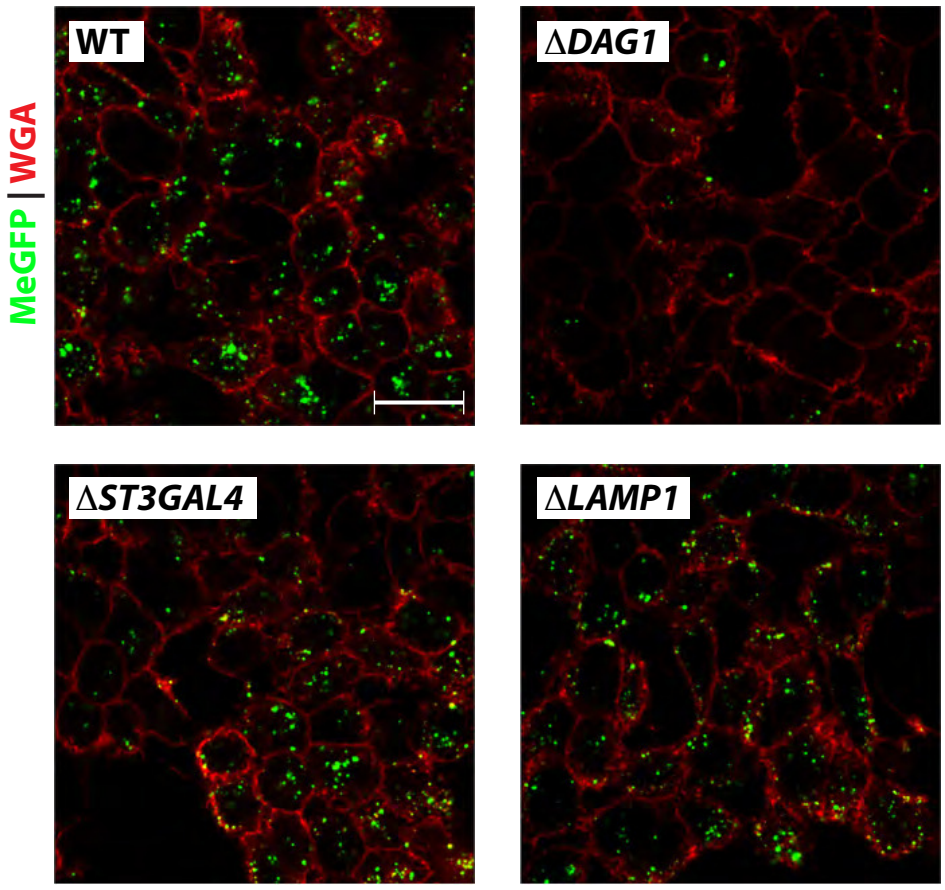

Figure S11. Early internalization of virus particles carrying eGFP fused to the VSV matrix (M) protein (rVSV-MeGFP-GP-LASV) depends on α-DG but not on ST3GAL4 or LAMP1. Confocal immunofluorescence analysis of wild-type, *DAG1*-deficient, *ST3GAL4*-deficient and *LAMP1*-deficient HAP1 cells challenged with virus carrying a VSV matrix protein fused to eGFP (rVSV-MeGFP-GP-LASV). Infection was carried out in the presence of 10mM NH_4Cl to trap intracellular viral particles. Cells were fixed 2h post virus inoculation and non-internalized virus was removed by a brief acid wash. Cells were co-stained with Alexa Fluor 568 labeled wheat germ agglutinin (WGA) to visualize the plasma membrane. Scale bar: 100µm.

Fig S12

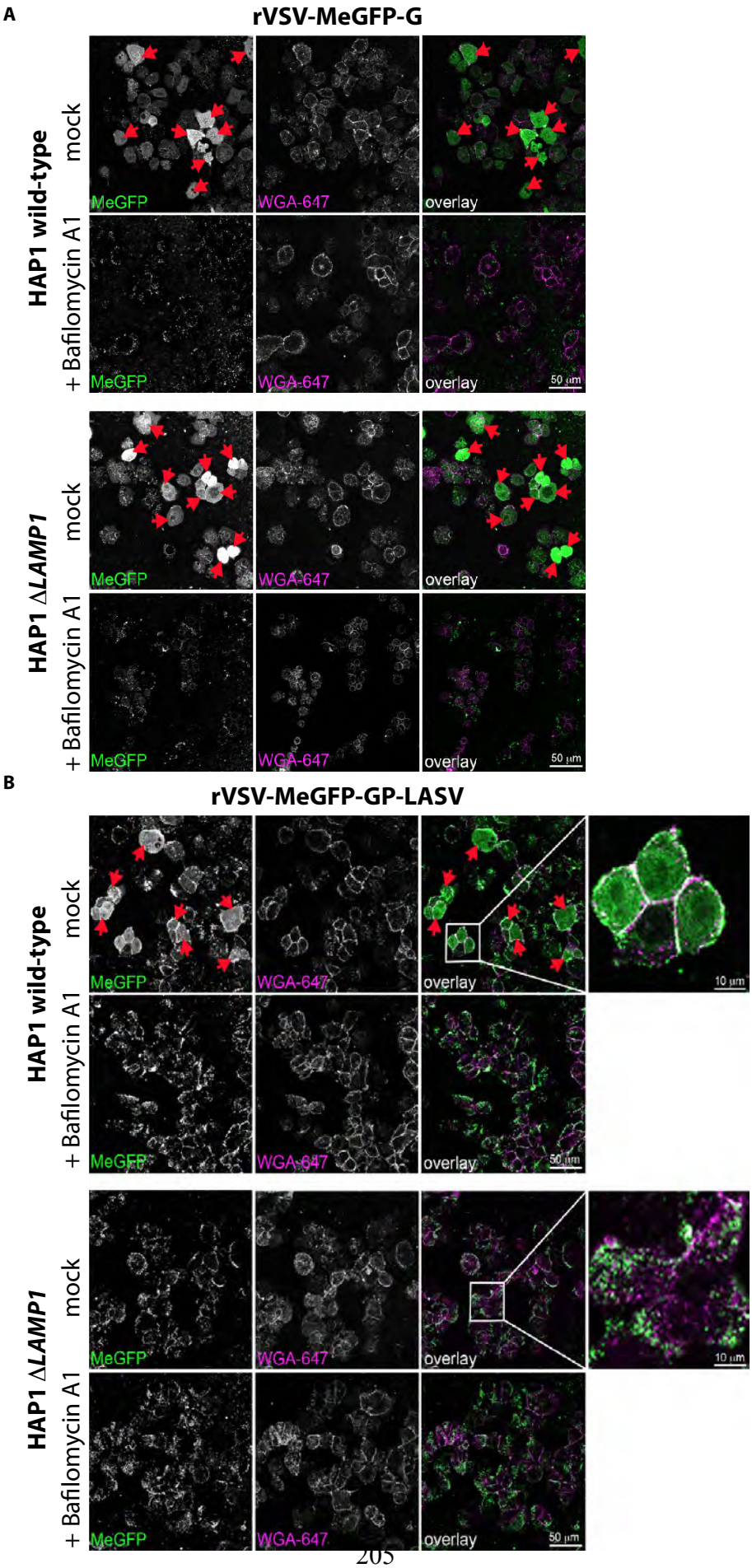
A
rVSV-MeGFP-G
HAP1 wild-type
mock
+ Bafilomycin A1
HAP1 ΔLAMP1
mock
+ Bafilomycin A1
MeGFP
WGA-647
overlay
50 µm
B
rVSV-MeGFP-GP-LASV
HAP1 wild-type
mock
+ Bafilomycin A1
HAP1 ΔLAMP1
mock
+ Bafilomycin A1
MeGFP
WGA-647
overlay
10 µm
50 µm

Figure S12. Release of the viral matrix protein requires LAMP1 and acidification of endosomes. Wild-type and *LAMP1*-deficient HAP1 cells grown on coverslips and pre-treated for 30min with the translation inhibitor puromycin (10ug/ml) in the absence or presence of bafilomyicin A1 (100nM), were inoculated with rVSV-MeGFP-GP-LASV or with the rVSV-MeGFP-G control virus at high multiplicity of infection (MOI ≈ 300). Bafilomycin A1 and puromycin were maintained in the inoculum throughout the experiment. Cells were washed and fixed 4h post virus inoculation and subsequently stained with Alexa Fluor 647 labeled wheat germ agglutinin (WGA) to highlight the cell membrane. **(A)** Diffusion of MeGFP (indicated by the red arrows) into the cytoplasm is apparent in wild-type and *LAMP1*-deficient cells for rVSV-MeGFP-G, which could be completely blocked by bafilomycin A1. **(B)** In contrast to the control virus, rVSV-MeGFP-GP-LASV displayed diffuse MeGFP only in wild-type cells and required acidification of endosomes. In *LAMP1*-deficient cells, the MeGFP signal was restricted to the cell surface and intracellular vesicles. Scale bars are indicated.

Fig S13

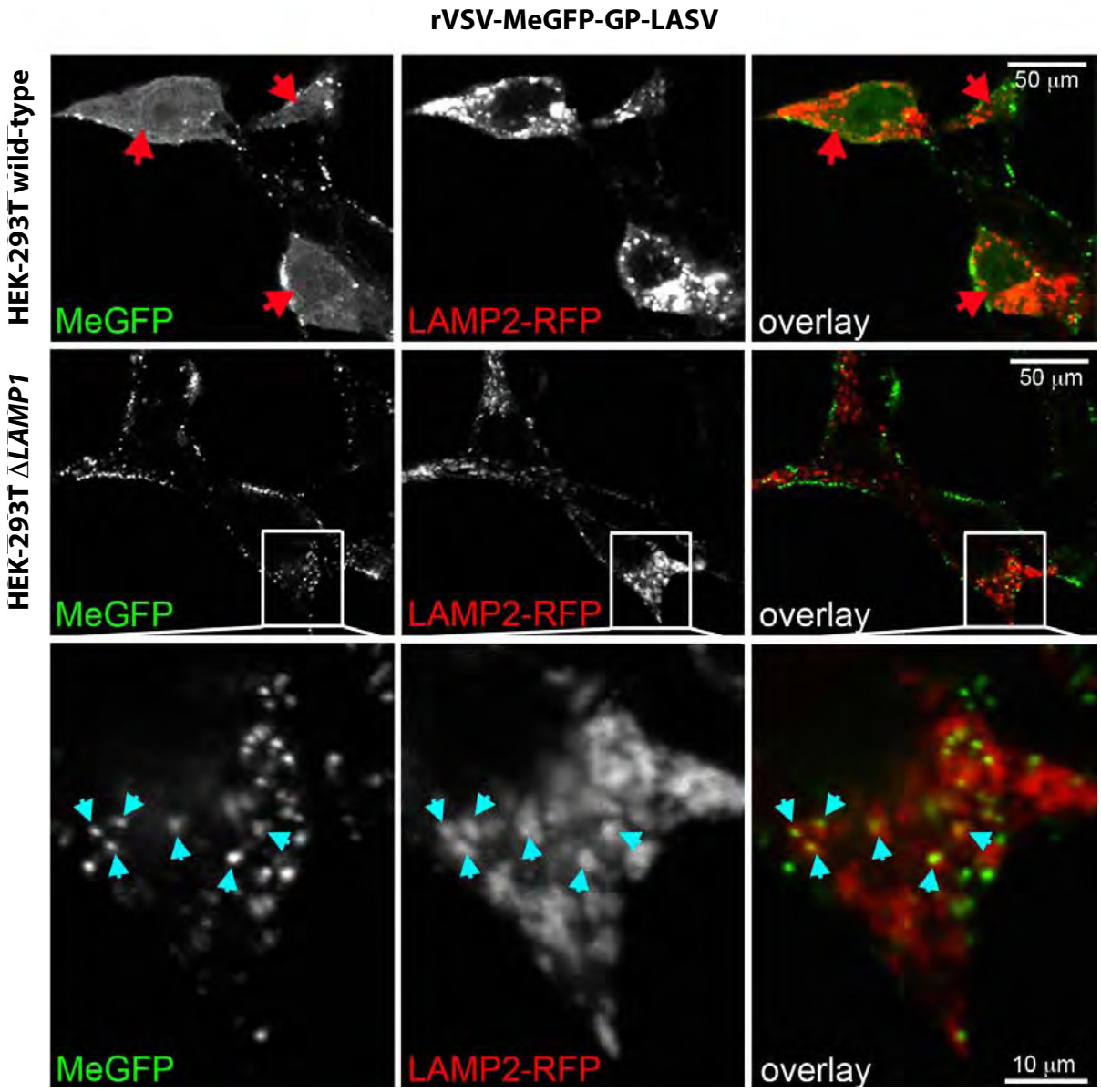

Figure S13. Absence of LAMP1 leads to blockade of virus in LAMP2-positive vesicles. High-resolution confocal immunofluorescence analysis of wild-type and *LAMP1*-deficient HEK-293T cells inoculated with rVSV-MeGFP-GP-LASV. Cells were transduced to stably express LAMP2-RFP. While diffusion of MeGFP into the cytoplasm is apparent in wild-type cells (red arrows, (11)), *LAMP1*-deficient cells displayed retention of viral particles in LAMP2-positive compartments (blue arrows).

Fig S14

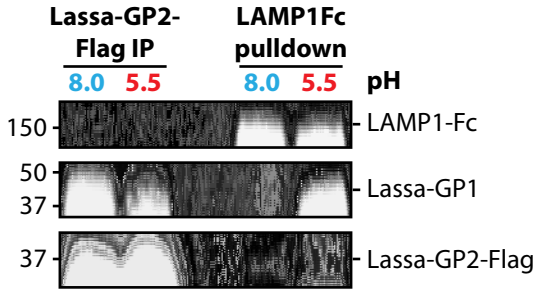

Figure S14. The complex of Lassa-GP bound to LAMP1 contains the GP1 subunit. Flag-tagged Lassa-GP was incubated with anti-Flag beads or immobilized LAMP1-Fc at the indicated pH. Bound complexes were analyzed for the presence of GP1 and GP2 by immunoblotting.

Fig S15

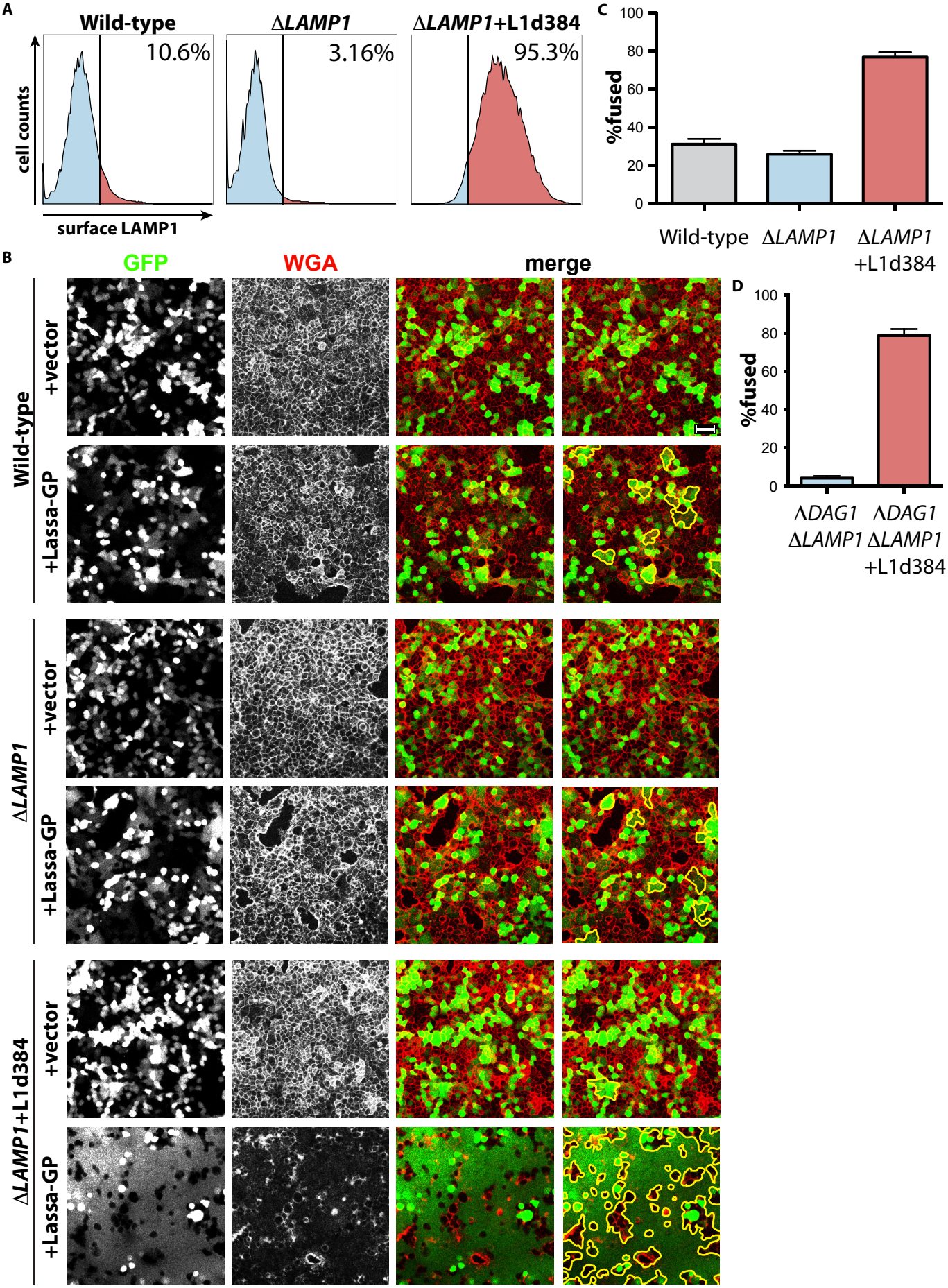
A
Wild-type
ΔLAMP1
ΔLAMP1+L1d384
10.6%
3.16%
95.3%
cell counts
surface LAMP1
C
%fused
100
80
60
40
20
0
Wild-type
ΔLAMP1
ΔLAMP1 +L1d384
B
GFP
WGA
merge
Wild-type
+vector
+Lassa-GP
ΔLAMP1
+vector
+Lassa-GP
ΔLAMP1+L1d384
+vector
+Lassa-GP
D
%fused
100
80
60
40
20
0
ΔDAG1 ΔLAMP1
ΔDAG1 ΔLAMP1 +L1d384

Figure S15. LAMP1d384 localizes to the cell surface and stimulates membrane fusion mediated by Lassa-GP. (A) Flow-cytometric analysis of LAMP1 on the cell surface in wild-type, *LAMP1*-deficient and *LAMP1*-deficient cells expressing LAMP1d384 (Δ*LAMP1*+L1d384), which localizes to the cell surface. Percentage of non-permeabilized cells that were positive for LAMP1 signal at the cell surface is indicated. **(B)** The cells described in panel (A) were transfected with GFP and an empty vector or a vector directing the expression of Lassa-GP and subsequently exposed to pH 5.5. Transfeced cells express GFP (first column) and cell boundaries were visualized with fluorescent wheat germ agglutinin (WGA, second column). The large, homogenous green fluorescent areas result from syncytia formation (yellow outlines, last column). Representative images of multiple experiments are shown. Scale bar: 50μm. **(C)** Quantification of Lassa-GP mediated syncytia formation in the cells described in panels (A) and (B). Percentage of fused cells in indicated. **(D)** Quantification of Lassa-GP mediated syncytia formation in the absence of endogenous α-DG and LAMP1. Percentage of fused cells is shown.

Fig S16

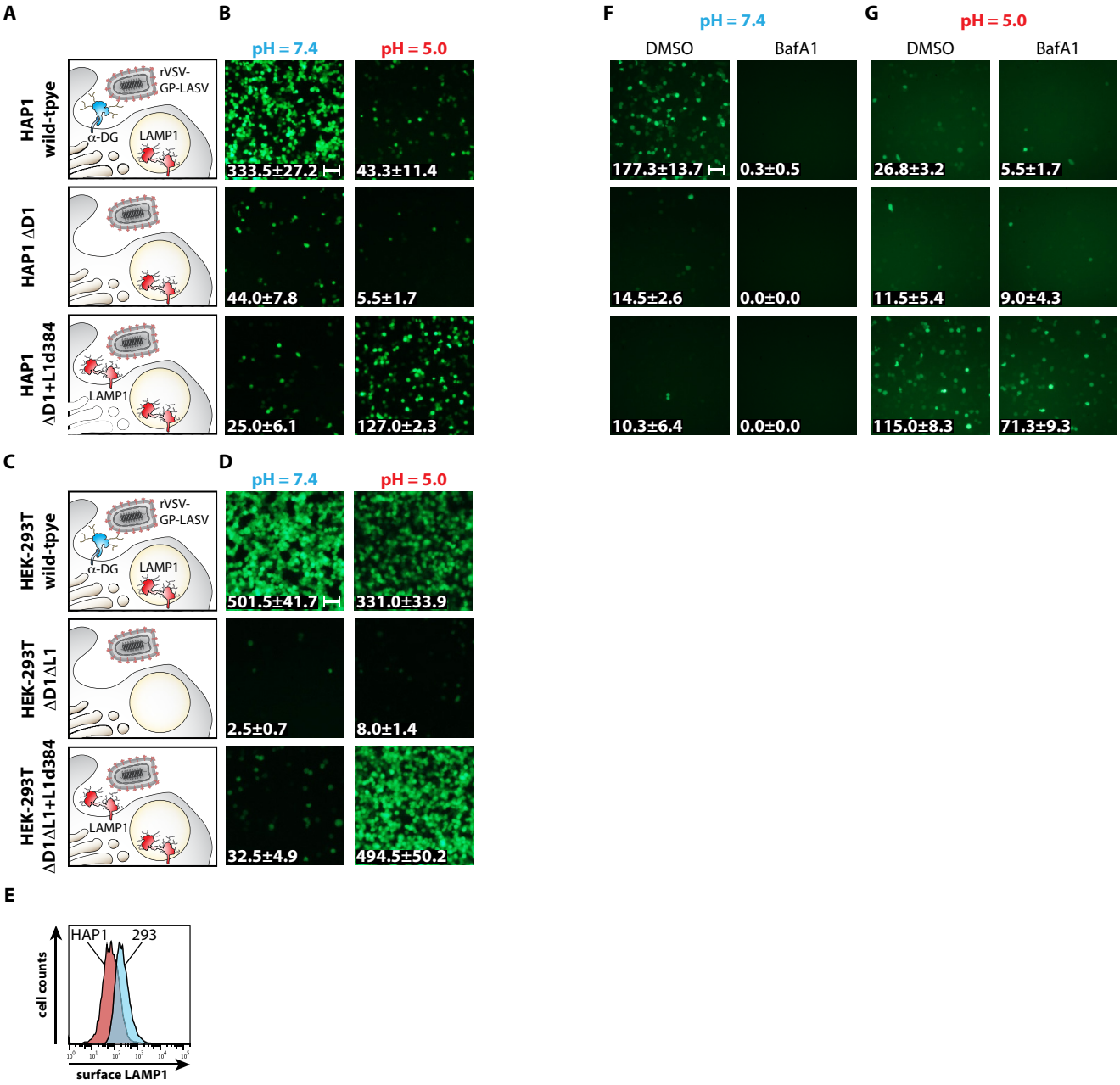
A
B
pH = 7.4
pH = 5.0
HAP1 wild-tpye
rVSV-GP-LASV
α-DG
LAMP1
333.5±27.2
43.3±11.4
HAP1 ΔD1
44.0±7.8
5.5±1.7
HAP1 ΔD1+L1d384
25.0±6.1
127.0±2.3
F
pH = 7.4
DMSO
BafA1
177.3±13.7
0.3±0.5
14.5±2.6
0.0±0.0
10.3±6.4
0.0±0.0
G
pH = 5.0
DMSO
BafA1
26.8±3.2
5.5±1.7
11.5±5.4
9.0±4.3
115.0±8.3
71.3±9.3
C
D
pH = 7.4
pH = 5.0
HEK-293T wild-tpye
rVSV-GP-LASV
α-DG
LAMP1
501.5±41.7
331.0±33.9
HEK-293T ΔD1ΔL1
2.5±0.7
8.0±1.4
HEK-293T ΔD1ΔL1+L1d384
LAMP1
32.5±4.9
494.5±50.2
E
HAP1
293
cell counts
surface LAMP1

Figure S16. Re-routing of LAMP1 to the cell surface allows entry of rVSV-GP-LASV at acidic pH in the absence of α-DG and is insensitive to bafilomycin. (A) Schematic outline of the engineered entry route in wild-type, α-DG-deficient (ΔD1) and α-DG-deficient HAP1 cells stably expressing LAMP1d384 (ΔD1+L1d384). **(B)** Cells described in panel (A) were exposed to rVSV-GP-LASV for 2h at neutral or acidic pH and subsequently the medium was replaced. **(C, D)** As in panel (A, B) using HEK-293 cells of the indicated genotypes. **(E)** Higher expression of LAMP1 on the cell surface in wild-type HEK-293T cells compared to HAP1 cells potentially contributes to higher infectivity with rVSV-GP-LASV at acidic pH. **(F, G)** Cells described in panel (A) were exposed to rVSV-GP-LASV at the indicated pH in the presence or absence of bafilomycin A1 (exposure time for G was slightly longer to compensate for reduced fitness of cells in acidified medium). Average number (±SD) of infected cells per field (eGFP-positive) is indicated. Scale bars: 50μm.

Fig S17

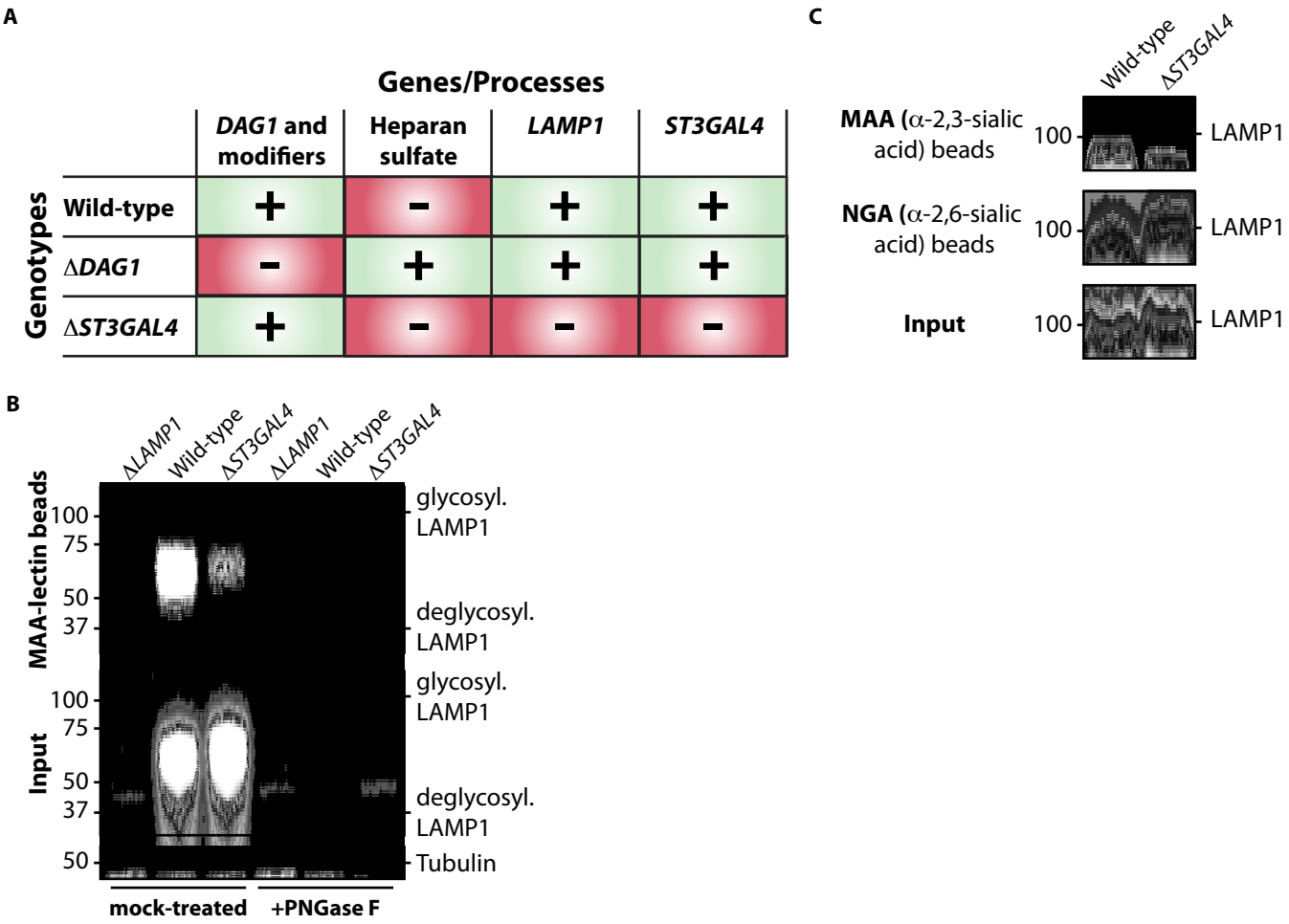

Figure S17. HAP1 cells modify LAMP1 with both α-2,3- and α-2,6-linked sialic acid. (A) Table summarizing clusters of genes enriched for disruptive mutations in haploid genetic screens in different genotypes. **(B)** Cell lysates of wild-type and *ST3GAL4*-deficient HAP1 cells were exposed to beads coated with Maackia amurensis (MAA)-lectin and captured proteins were subjected to immunoblot analysis. Lysates derived from *LAMP1*-deficient HAP1 cells and PNGase F-treated lysates served as control. **(C)** Cell lysates of wild-type and *ST3GAL4*-deficient HAP1 cells were captured using lectin beads specific for α-2,3-linked sialic acid (MAA) or α-2,6-linked sialic acid (NGA) and subjected to immunoblot analysis. LAMP1 was detected using an antibody that does not rely on the glycosylation status of its target.

Fig S18

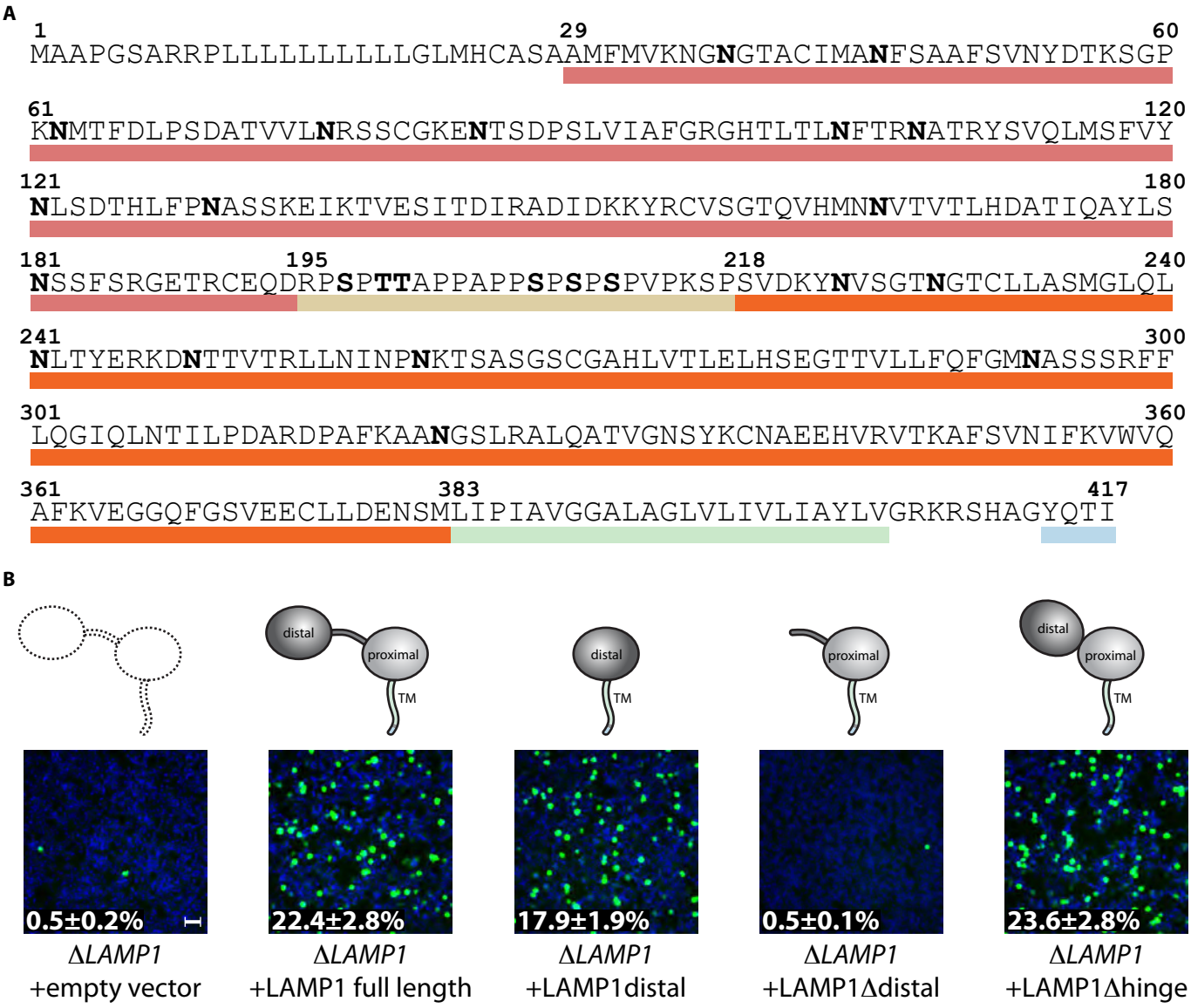
A
1 29 60
MAAPGSARRPLLLLLLLLLLGLMHCASAAMFMVKNGNGTACIMANFSAAFSVNYDTKSGP
61 120
KNMTFDLPSDATVVLNRSSCGKENTSDPSLVIAFGRGHTLTLNFTRNATRYSVQLMSFVY
121 180
NLSDTHLFPNASSKEIKTVESITDIRADIDKKYRCVSGTQVHMNNVTVTLHDATIQAYLS
181 195 218 240
NSSFSRGETRCEQDRPSPTTAPPAPPSPSPSPVPKSPSVDKYNVSGTNGTCLLASMGLQL
241 300
NLTYERKDNTTVTRLLNINPNKTSASGSCGAHLVTLELHSEGTTVLLFQFGMNASSSRFF
301 360
LQGIQLNTILPDARDPAFKAANGSLRALQATVGNSYKCNAEEHVRVTKAFSVNIFKVWVQ
361 383 417
AFKVEGGQFGSVEECLLDENSMLIPIAVGGALAGLVLIVLIAYLVGRKRSHAGYQTI
B
distal
proximal
TM
distal
TM
proximal
TM
distal
proximal
TM
0.5±0.2%
22.4±2.8%
17.9±1.9%
0.5±0.1%
23.6±2.8%
ΔLAMP1
+empty vector
ΔLAMP1
+LAMP1 full length
ΔLAMP1
+LAMP1distal
ΔLAMP1
+LAMP1Δdistal
ΔLAMP1
+LAMP1Δhinge

Figure S18. The membrane-distal domain of LAMP1 is sufficient to support rVSV-GP-LASV infection. (A) Amino acid sequence, domain organization and known/predicted glycosylation sites of human LAMP1 (UniProt, P11279, (*25*)). The membrane-distal domain is indicated in red and the membrane-proximal domain in orange. These domains are connected via a proline-rich hinge region indicated in brown. The C-terminus contains the transmembrane region (TM, green) and lysosomal targeting sequence (blue). **(B)** *LAMP1*-deficient HEK-293T cells were transduced with retroviruses expressing full-length human LAMP1 or the indicated LAMP1 mutants and exposed to rVSV-GP-LASV. LAMP1distal contains amino acids 1-197 attached to amino acids 381-417, connecting the folded distal domain and C-terminus via the five adjacent amino acids (RPSSM). Percentage (±SD) of infected cells (eGFP-positive) is indicated. Scale bar: 50μm.

Fig S19

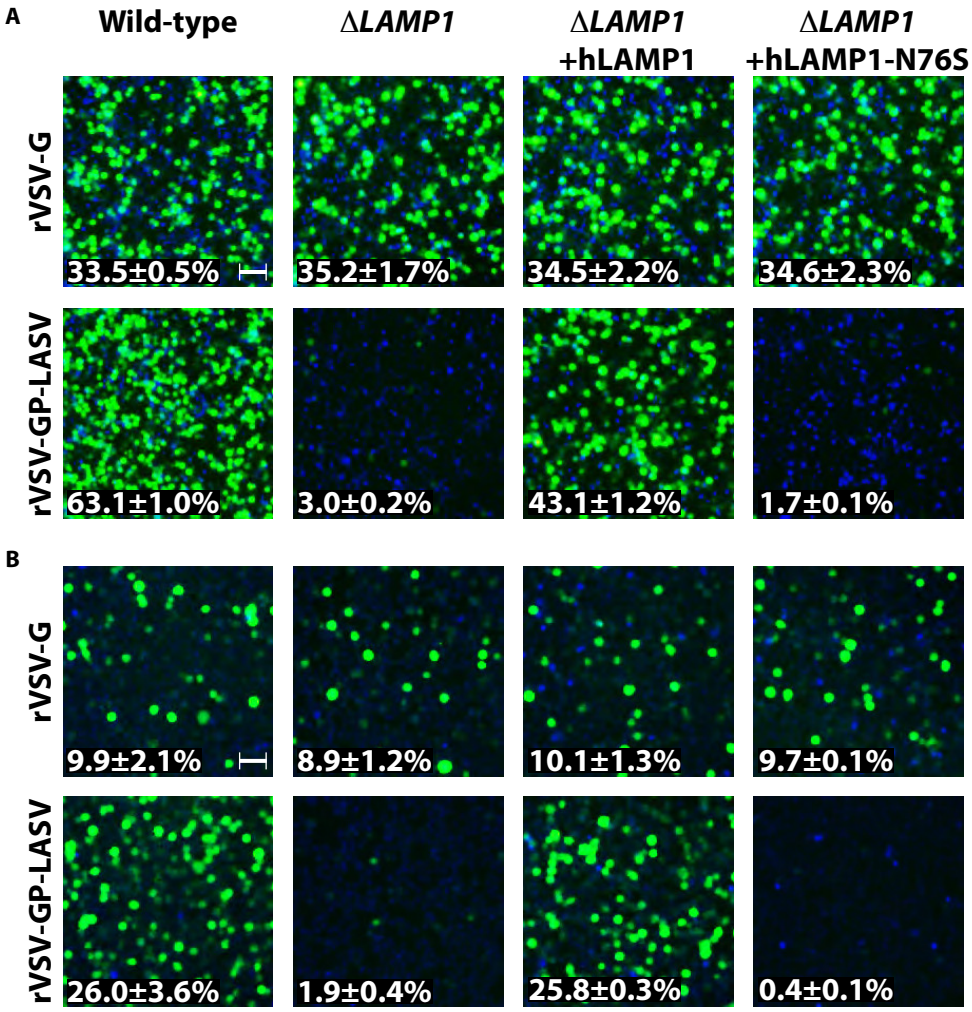

Figure S19. A single glycosylation site, Asn^{76}, present in human LAMP1 but absent in chicken LAMP1, is essential for supporting Lassa-GP-mediated infection. (A) *LAMP1*-deficient HAP1 cells were transduced with retroviruses expressing wild-type human LAMP1 or a 'chickenized' human LAMP1 mutant lacking the N-glycosylation site at Asn76 (N76S) and exposed to rVSV-G or rVSV-GP-LASV. Infected cells express eGFP. **(B)** As in panel (A) but using HEK-293T cells of the respective genotypes. Percentage (±SD) of infected cells (eGFP-positive) is indicated. Scale bars: 50µm.

Fig S20

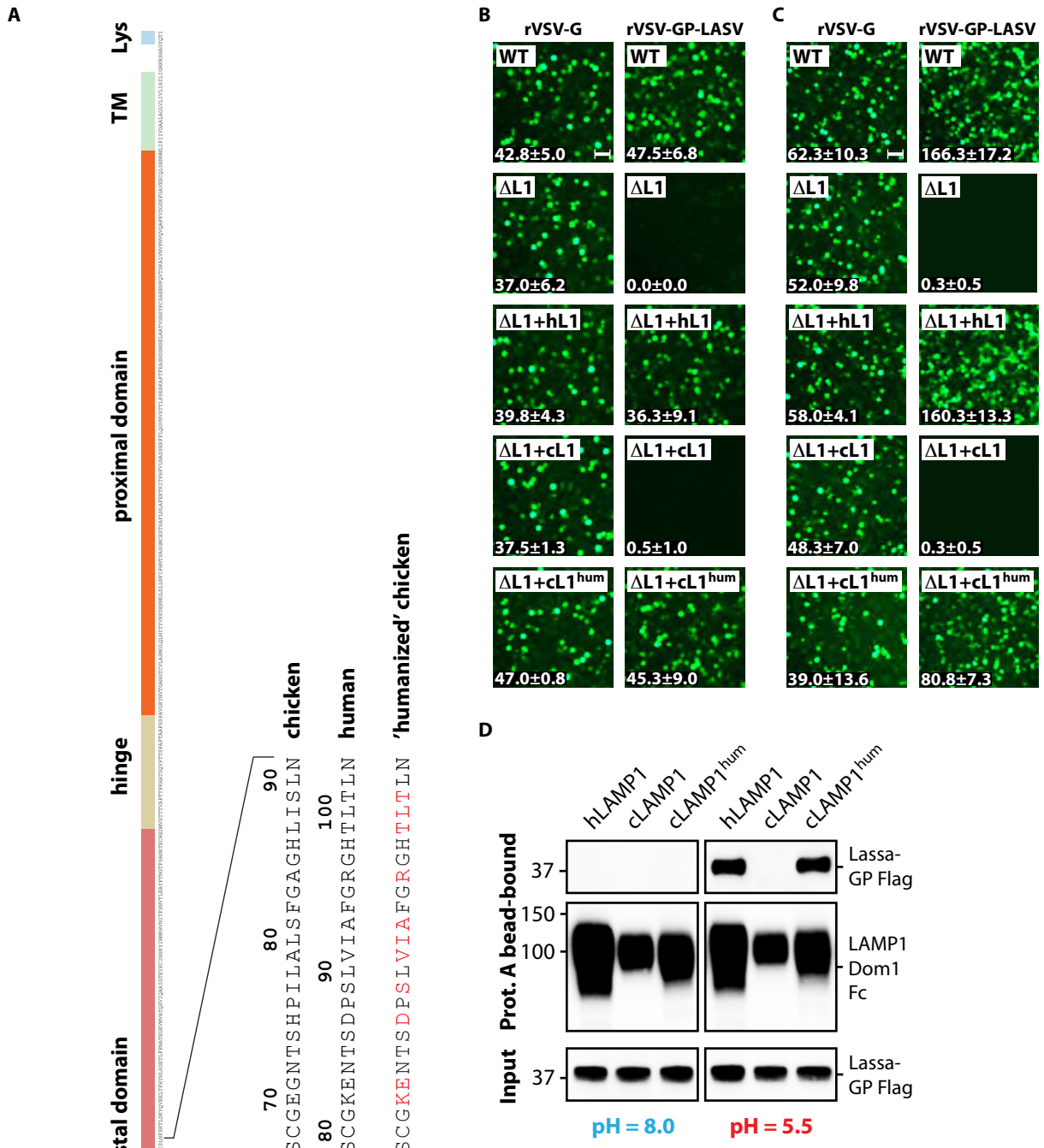
A
Lys
TM
proximal domain
hinge
distal domain
chicken
human
'humanized' chicken
B
rVSV-G
rVSV-GP-LASV
WT
42.8±5.0
47.5±6.8
ΔL1
37.0±6.2
0.0±0.0
ΔL1+hL1
39.8±4.3
36.3±9.1
ΔL1+cL1
37.5±1.3
0.5±1.0
ΔL1+cL1hum
47.0±0.8
45.3±9.0
C
rVSV-G
rVSV-GP-LASV
WT
62.3±10.3
166.3±17.2
ΔL1
52.0±9.8
0.3±0.5
ΔL1+hL1
58.0±4.1
160.3±13.3
ΔL1+cL1
48.3±7.0
0.3±0.5
ΔL1+cL1hum
39.0±13.6
80.8±7.3
D
hLAMP1
cLAMP1
cLAMP1hum
Prot. A bead-bound
Input
37
150
100
Lassa-GP Flag
LAMP1 Dom1 Fc
pH = 8.0
pH = 5.5

Figure S20. 'Humanization' of chicken LAMP1. (A) The 414 amino acid sequence of chicken LAMP1 and its principal domains are shown. For the magnified region an alignment of chicken and human LAMP1 is depicted. Below is the resulting sequence of 'humanized' chicken LAMP1, where deviating amino acids are highlighted in red. Asn^{76} of the human protein and its corresponding residue in chicken LAMP1 (Ser^{64}) are shaded in grey. **(B, C)** *LAMP1*-deficient HEK-293T cells (B) or HAP1 cells (C) were transduced with retroviruses expressing human LAMP1 (hL1), chicken LAMP1 (cL1) or a 'humanized' chicken LAMP1 (cL1hum) and exposed to rVSV-G or rVSV-GP-LASV. Average number (±SD) of infected cells per field (eGFP-positive) is indicated. Scale bars: 50μm. **(D)** Fc-tagged human, chicken or 'humanized' chicken LAMP1 distal domain proteins were immobilized on beads and incubated with cell lysates from HEK-293T cells at the indicated pH. Bound complexes were isolated and subjected to immunoblot analysis.

Fig S21

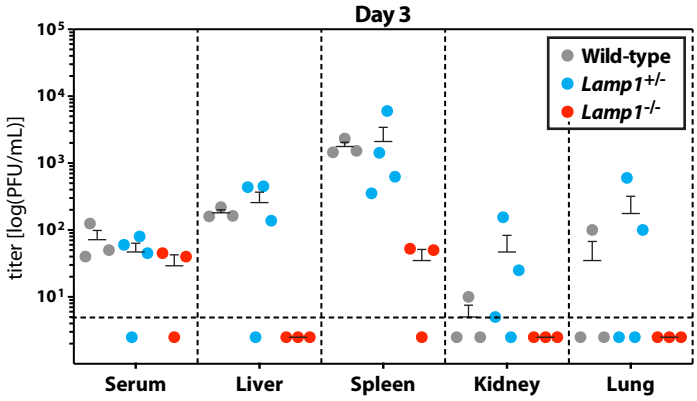

Figure 21. Viral titres in mice 3 days after exposure to wild-type Lassa virus. Wild-type, heterozygous and homozygous *Lamp1* knockout mice were injected intraperitoneally with 100 plaque forming units (PFU) of wild-type Lassa virus and viral titers were determined three days post injection in the indicated tissues. The detection limit is highlighted by the horizontal dashed line.

Fig S22

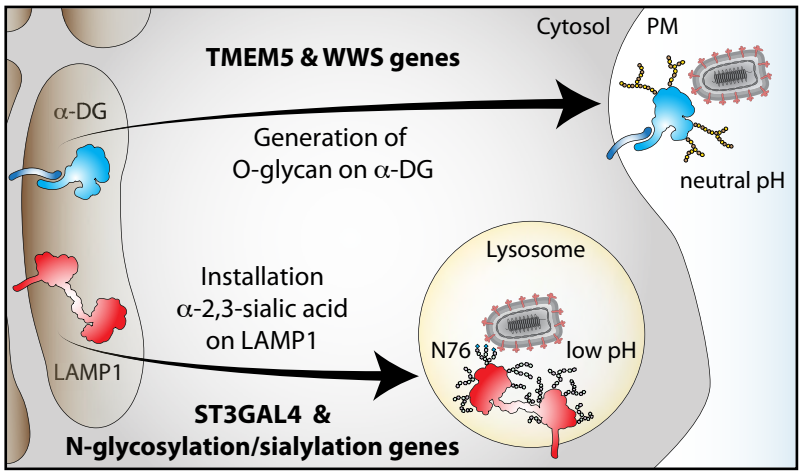

Figure S22. Schematic outline of Lassa virus entry requiring a switch from the first glycosylated receptor to the second. Distinct sets of enzyme are needed to modify α-DG, which is recognized by Lassa virus on the cell surface, and LAMP1, which is recognized subsequently in the interior of the cell. PM = plasma membrane.

Legends to Supplementary Tables

Table S1. Genes identified in haploid genetic screens for Lassa virus entry. Comparison of haploid genetic screens performed using rVSV-GP-LASV in wild-type (WT), *DAG1*-deficient (ΔD) or *ST3GAL4*-deficient (ΔS) HAP1 cells. Full gene names and corresponding gene symbols are indicated in the first two columns. Genes are grouped by biological processes (third column) and for some cases a reference (REF, fourth column) for its involvement in the respective process is provided. The last columns denote in which of the three haploid genetic screens the respective gene stood out as a significant hit (dots).

Table S2. Results of haploid genetic screen for Lassa virus entry in *DAG1*-deficient HAP1 cells. Table listing gene-trap insertions predicted to inactivate the respective gene that were mapped in *DAG1*-deficient HAP1 cells selected with rVSV-GP-LASV. Insertions were compared to unselected HAP1 control cells and the significance of enrichment was calculated using a one-sided Fisher's exact test followed by FDR-correction of the *P*-values. For every gene, the percentage of intronic (as opposed to exonic) insertions is given, as this was used for categorization of genes for statistic criteria (see materials and methods). Furthermore, per gene, the number of gene-trap insertions in sense-orientation of the gene (predicted to disrupt transcription of the gene) is compared to the number of gene-trap insertions in anti-sense orientation (predicted not to affect gene function) using a binomial test and FDR-correction of *P*-values. Genes in which the majority (70% or more) of gene-trap insertions mapped to intronic regions were colored orange and intron-poor genes (less than 70% of gene-trap insertions mapping to introns) were colored purple if they passed the respective statistical criteria described under experimental procedures in the materials and methods.

Table S3. Results of haploid genetic screen for Lassa virus entry in wild-type HAP1 cells. Table listing gene-trap insertions predicted to inactivate the respective gene that were mapped in wild-type HAP1 cells selected with rVSV-GP-LASV. Insertions were

compared to unselected HAP1 control cells and the significance of enrichment was calculated using a one-sided Fisher's exact test followed by FDR-correction of the *P*-values. For every gene, the percentage of intronic (as opposed to exonic) insertions is given, as this was used for categorization of genes for statistic criteria (see materials and methods). Furthermore, per gene, the number of gene-trap insertions in sense-orientation of the gene (predicted to disrupt transcription of the gene) is compared to the number of gene-trap insertions in anti-sense orientation (predicted not to affect gene function) using a binomial test and FDR-correction of *P*-values. Genes in which the majority (70% or more) of gene-trap insertions mapped to intronic regions were colored orange and intron-poor genes (less than 70% of gene-trap insertions mapping to introns) were colored purple if they passed the respective statistical criteria described under experimental procedures in the materials and methods.

Table S4. Results of haploid genetic screen for Lassa virus entry in *ST3GAL4*-deficient HAP1 cells. Table listing gene-trap insertions predicted to inactivate the respective gene that were mapped in *ST3GAL4*-deficient HAP1 cells selected with rVSV-GP-LASV. Insertions were compared to unselected HAP1 control cells and the significance of enrichment was calculated using a one-sided Fisher's exact test followed by FDR-correction of the *P*-values. For every gene, the percentage of intronic (as opposed to exonic) insertions is given, as this was used for categorization of genes for statistic criteria (see materials and methods). Furthermore, per gene, the number of gene-trap insertions in sense-orientation of the gene (predicted to disrupt transcription of the gene) is compared to the number of gene-trap insertions in anti-sense orientation (predicted not to affect gene function) using a binomial test and FDR-correction of *P*-values. Genes in which the majority (70% or more) of gene-trap insertions mapped to intronic regions were colored orange and intron-poor genes (less than 70% of gene-trap insertions mapping to introns) were colored purple if they passed the respective statistical criteria described under experimental procedures in the materials and methods.

Table S1. Genes identified in haploid genetic screens for Lassa virus entry.

SYMBOL	GENE NAME	PROCESS	REF	ΔD	WT	ΔS
UGP2	UDP-glucose pyrophosphorylase 2	sugar supply		•		
MPDU1	mannose-P-dolichol utilization defect 1	sugar supply			•	
PMM2	phosphomannomutase 2	sugar supply		•		
UXS1	UDP-glucuronate decarboxylase 1	sugar supply		•	•	•
UGDH	UDP-glucose 6-dehydrogenase	sugar supply		•	•	•
PTAR1	protein prenyltransferase alpha subunit repeat containing 1	Golgi/vesicle trafficking	(*4*)	•	•	
COG3	component of oligomeric golgi complex 3	Golgi/vesicle trafficking		•	•	
COG5	component of oligomeric golgi complex 5	Golgi/vesicle trafficking		•	•	
COG6	component of oligomeric golgi complex 6	Golgi/vesicle trafficking		•		
COG7	component of oligomeric golgi complex 7	Golgi/vesicle trafficking		•	•	
COG8	component of oligomeric golgi complex 8	Golgi/vesicle trafficking		•	•	
TMED10	transmembrane emp24-like trafficking protein 10 (yeast)	Golgi/vesicle trafficking	(*30-32*)	•		•
TMED2	transmembrane emp24 domain trafficking protein 2	Golgi/vesicle trafficking	(*30-31, 33*)	•		
UNC50	unc-50 homolog (C. elegans)	Golgi/vesicle trafficking	(*34*)	•	•	
KIAA1432/ RIC1	KIAA1432	Golgi/vesicle trafficking	(*35*)	•	•	
C3orf58/ GoPro49	chromosome 3 open reading frame 58	Golgi/vesicle trafficking	(*36*)	•		
TRAPPC13/ C5orf44	trafficking protein particle complex 13	Golgi/vesicle trafficking	(*37-38*)	•		
SEC16A	SEC16 homolog A (S. cerevisiae)	Golgi/vesicle trafficking	(*39-40*)	•		
VPS54	vacuolar protein sorting 54 homolog (S. cerevisiae)	Golgi/vesicle trafficking	(*41-42*)	•		
SACM1L	SAC1 suppressor of actin mutations 1-like (yeast)	Golgi/vesicle trafficking	(*43*)	•		
RGP1	RGP1 retrograde golgi transport homolog (S. cerevisiae)	Golgi/vesicle trafficking	(*44*)	•		
XYLT2	xylosyltransferase II	heparan sulfate		•		
B3GAT3	beta-1,3-glucuronyltransferase 3 (glucuronosyltransferase I)	heparan sulfate		•		
EXT1	exostosin glycosyltransferase 1	heparan sulfate		•		
EXT2	exostosin glycosyltransferase 2	heparan sulfate		•		
EXTL3	exostosin-like glycosyltransferase 3	heparan sulfate		•		
NDST1	N-deacetylase/N-sulfotransferase (heparan glucosaminyl) 1	heparan sulfate		•		
SLC35B2	solute carrier family 35 (adenosine 3'-phospho 5'-phosphosulfate transporter), member B2	heparan sulfate		•		
DAG1	dystroglycan 1 (dystrophin-associated glycoprotein 1)	α-DG glycosylation			•	•
LARGE	like-glycosyltransferase	α-DG glycosylation			•	•
TMEM5	transmembrane protein 5	α-DG glycosylation			•	•
B3GNT1	UDP-GlcNAc:betaGal beta-1,3-N-acetylglucosaminyltransferase 1	α-DG glycosylation			•	•
B3GALNT2	beta-1,3-N-acetylgalactosaminyltransferase 2	α-DG glycosylation			•	•
ISPD	isoprenoid synthase domain containing	α-DG glycosylation			•	•
DPM1	dolichyl-phosphate mannosyltransferase polypeptide 1, catalytic subunit	α-DG glycosylation			•	•

Table S1 (continued).

SYMBOL	GENE NAME	PROCESS	REF	ΔD	WT	ΔS
DPM3	dolichyl-phosphate mannosyltransferase polypeptide 3	α-DG glycosylation			•	•
FKTN	fukutin	α-DG glycosylation			•	•
FKRP	fukutin related protein	α-DG glycosylation			•	•
POMT1	protein-O-mannosyltransferase 1	α-DG glycosylation			•	•
POMT2	protein-O-mannosyltransferase 2	α-DG glycosylation			•	•
GTDC2/ C3orf39	glycosyltransferase-like domain containing 2	α-DG glycosylation			•	•
SGK196/ POMK	protein kinase-like protein SgK196	a-DG glycosylation			•	•
SLC35A1	solute carrier family 35 (CMP-sialic acid transporter), member A1	α-DG glycosylation/ sialylation		•	•	•
ALG5	ALG5, dolichyl-phosphate beta-glucosyltransferase	N-glycosylation/ sialylation		•	•	
ALG6	ALG6, alpha-1,3-glucosyltransferase	N-glycosylation/ sialylation		•	•	
ALG8	ALG8, alpha-1,3-glucosyltransferase	N-glycosylation/ sialylation		•	•	
MAN1A1	mannosidase, alpha, class 1A, member 1	N-glycosylation/ sialylation		•	•	
MAN1B1	mannosidase, alpha, class 1B, member 1	N-glycosylation/ sialylation		•	•	
MGAT1	mannosyl (alpha-1,3-)-glycoprotein beta-1,2-N-acetylglucosaminyltransferase	N-glycosylation/ sialylation		•	•	
GNE	glucosamine (UDP-N-acetyl)-2-epimerase/N-acetylmannosamine kinase	N-glycosylation/ sialylation		•	•	
SLC35A2	solute carrier family 35 (UDP-galactose transporter), member A2	N-glycosylation/ sialylation		•	•	
CMAS	cytidine monophosphate N-acetylneuraminic acid synthetase	N-glycosylation/ sialylation		•	•	
ST3GAL4	ST3 beta-galactoside alpha-2,3-sialyltransferase 4	N-glycosylation/ sialylation		•	•	
ST3GAL3	ST3 beta-galactoside alpha-2,3-sialyltransferase 3	N-glycosylation/ sialylation				•
LAMP1	lysosomal-associated membrane protein 1	lysosome		•	•	
CD63	CD63 molecule	lysosome				•
EIF2AK2/ PKR	eukaryotic translation initiation factor 2-alpha kinase 2	other		•		
FAM3C	family with sequence similarity 3, member C	other		•	•	
TM9SF2	transmembrane 9 superfamily member 2	other		•	•	
TM9SF3	transmembrane 9 superfamily member 3	other		•	•	
DOT1L	DOT1-like histone H3K79 methyltransferase	other			•	
WDR7	WD repeat domain 7	other				•
DMXL1	Dmx-like 1	other				•
C1orf43	chromosome 1 open reading frame 43	other				•
SREBF2	sterol regulatory element binding transcription factor 2	other				•
CMIP	c-Maf inducing protein	other				•
MBTPS1	membrane-bound transcription factor peptidase, site 1	other				•

Δ**D** = Δ*DAG1* screen; **WT** = Wild-type screen; Δ**S** = Δ*ST3GAL4* screen

1. S. Kunz, J. M. Rojek, M. Kanagawa, C. F. Spiropoulou, R. Barresi, K. P. Campbell, M. B. Oldstone, Posttranslational modification of α-dystroglycan, the cellular receptor for arenaviruses, by the glycosyltransferase LARGE is critical for virus binding. *J. Virol.* **79**, 14282–14296 (2005). Medline doi:10.1128/JVI.79.22.14282-14296.2005

2. W. Cao, M. D. Henry, P. Borrow, H. Yamada, J. H. Elder, E. V. Ravkov, S. T. Nichol, R. W. Compans, K. P. Campbell, M. B. Oldstone, Identification of α-dystroglycan as a receptor for lymphocytic choriomeningitis virus and Lassa fever virus. *Science* **282**, 2079–2081 (1998). Medline doi:10.1126/science.282.5396.2079

3. I. S. Lukashevich, R. F. Maryankova, F. M. Fidarov, Reproduction of Lassa virus in different cell cultures. *Acta Virol.* **27**, 282–285 (1983). Medline

4. L. T. Jae, M. Raaben, M. Riemersma, E. van Beusekom, V. A. Blomen, A. Velds, R. M. Kerkhoven, J. E. Carette, H. Topaloglu, P. Meinecke, M. W. Wessels, D. J. Lefeber, S. P. Whelan, H. van Bokhoven, T. R. Brummelkamp, Deciphering the glycosylome of dystroglycanopathies using haploid screens for lassa virus entry. *Science* **340**, 479–483 (2013). Medline doi:10.1126/science.1233675

5. F. Saito, M. Blank, J. Schröder, H. Manya, T. Shimizu, K. P. Campbell, T. Endo, M. Mizutani, S. Kröger, K. Matsumura, Aberrant glycosylation of α-dystroglycan causes defective binding of laminin in the muscle of chicken muscular dystrophy. *FEBS Lett.* **579**, 2359–2363 (2005). Medline doi:10.1016/j.febslet.2005.03.033

6. Materials and methods are available as supplementary materials on *Science* Online.

7. W. Zhu, J. Li, G. Liang, How does cellular heparan sulfate function in viral pathogenicity? *Biomed. Environ. Sci.* **24**, 81–87 (2011). Medline

8. N. Andrejewski, E. L. Punnonen, G. Guhde, Y. Tanaka, R. Lüllmann-Rauch, D. Hartmann, K. von Figura, P. Saftig, Normal lysosomal morphology and function in LAMP-1-deficient mice. *J. Biol. Chem.* **274**, 12692–12701 (1999). Medline doi:10.1074/jbc.274.18.12692

9. J. Rohrer, A. Schweizer, D. Russell, S. Kornfeld, The targeting of Lamp1 to lysosomes is dependent on the spacing of its cytoplasmic tail tyrosine sorting motif relative to the membrane. *J. Cell Biol.* **132**, 565–576 (1996). Medline doi:10.1083/jcb.132.4.565

10. T. Nishi, M. Forgac, The vacuolar (H+)-ATPases—Nature's most versatile proton pumps. *Nat. Rev. Mol. Cell Biol.* **3**, 94–103 (2002). Medline doi:10.1038/nrm729

11. J. E. Carette, M. Raaben, A. C. Wong, A. S. Herbert, G. Obernosterer, N. Mulherkar, A. I. Kuehne, P. J. Kranzusch, A. M. Griffin, G. Ruthel, P. Dal Cin, J. M. Dye, S. P. Whelan, K. Chandran, T. R. Brummelkamp, Ebola virus entry requires the cholesterol transporter Niemann-Pick C1. *Nature* **477**, 340–343 (2011). Medline doi:10.1038/nature10348

12. C. Di Simone, M. J. Buchmeier, Kinetics and pH dependence of acid-induced structural changes in the lymphocytic choriomeningitis virus glycoprotein complex. *Virology* **209**, 3–9 (1995). Medline doi:10.1006/viro.1995.1225

13. J. York, D. Dai, S. M. Amberg, J. H. Nunberg, pH-induced activation of arenavirus membrane fusion is antagonized by small-molecule inhibitors. *J. Virol.* **82**, 10932–10939 (2008). Medline doi:10.1128/JVI.01140-08

14. J. H. Nunberg, J. York, The curious case of arenavirus entry, and its inhibition. *Viruses* **4**, 83–101 (2012). Medline doi:10.3390/v4010083

15. E. J. Bowman, A. Siebers, K. Altendorf, *Proc. Natl. Acad. Sci. U.S.A.* **85**, 7972–7976 (1988).

16. M. Heffernan, S. Yousefi, J. W. Dennis, Molecular characterization of P2B/LAMP-1, a major protein target of a metastasis-associated oligosaccharide structure. *Cancer Res.* **49**, 6077–6084 (1989). Medline

17. S. R. Carlsson, P. O. Lycksell, M. Fukuda, Assignment of O-glycan attachment sites to the hinge-like regions of human lysosomal membrane glycoproteins lamp-1 and lamp-2. *Arch. Biochem. Biophys.* **304**, 65–73 (1993). Medline doi:10.1006/abbi.1993.1322

18. W. C. Wang, R. D. Cummings, The immobilized leukoagglutinin from the seeds of Maackia amurensis binds with high affinity to complex-type Asn-linked oligosaccharides containing terminal sialic acid-linked α-2,3 to penultimate galactose residues. *J. Biol. Chem.* **263**, 4576–4585 (1988). Medline

19. A. Ibricevic, A. Pekosz, M. J. Walter, C. Newby, J. T. Battaile, E. G. Brown, M. J. Holtzman, S. L. Brody, Influenza virus receptor specificity and cell tropism in mouse and human airway epithelial cells. *J. Virol.* **80**, 7469–7480 (2006). Medline doi:10.1128/JVI.02677-05

20. M. de Graaf, R. A. Fouchier, Role of receptor binding specificity in influenza A virus transmission and pathogenesis. *EMBO J.* **33**, 823–841 (2014). Medline doi:10.1002/embj.201387442

21. K. Shinya, M. Ebina, S. Yamada, M. Ono, N. Kasai, Y. Kawaoka, Avian flu: Influenza virus receptors in the human airway. *Nature* **440**, 435–436 (2006). Medline doi:10.1038/440435a

22. W. H. Haas, T. Breuer, G. Pfaff, H. Schmitz, P. Köhler, M. Asper, P. Emmerich, C. Drosten, U. Gölnitz, K. Fleischer, S. Günther, Imported Lassa fever in Germany: Surveillance and management of contact persons. *Clin. Infect. Dis.* **36**, 1254–1258 (2003). Medline doi:10.1086/374853

23. P. Y. Lozach, J. Huotari, A. Helenius, Late-penetrating viruses. *Curr. Opin. Virol.* **1**, 35–43 (2011). Medline doi:10.1016/j.coviro.2011.05.004

24. F. L. Cosset, P. Marianneau, G. Verney, F. Gallais, N. Tordo, E. I. Pécheur, J. ter Meulen, V. Deubel, B. Bartosch, Characterization of Lassa virus cell entry and neutralization with Lassa virus pseudoparticles. *J. Virol.* **83**, 3228–3237 (2009). Medline doi:10.1128/JVI.01711-08

25. S. Wilke, J. Krausze, K. Büssow, Crystal structure of the conserved domain of the DC lysosomal associated membrane protein: Implications for the lysosomal glycocalyx. *BMC Biol.* **10**, 62 (2012). Medline doi:10.1186/1741-7007-10-62

26. S. Cherry, T. Doukas, S. Armknecht, S. Whelan, H. Wang, P. Sarnow, N. Perrimon, Genome-wide RNAi screen reveals a specific sensitivity of IRES-containing RNA viruses to host translation inhibition. *Genes Dev.* **19**, 445–452 (2005). Medline doi:10.1101/gad.1267905

27. S. P. Whelan, L. A. Ball, J. N. Barr, G. T. Wertz, Efficient recovery of infectious vesicular stomatitis virus entirely from cDNA clones. *Proc. Natl. Acad. Sci. U.S.A.* **92**, 8388–8392 (1995). Medline doi:10.1073/pnas.92.18.8388

28. M. Claussen, B. Kübler, M. Wendland, K. Neifer, B. Schmidt, J. Zapf, T. Braulke, Proteolysis of insulin-like growth factors (IGF) and IGF binding proteins by cathepsin D. *Endocrinology* **138**, 3797–3803 (1997). Medline

29. J. H. Kim, S. R. Lee, L. H. Li, H. J. Park, J. H. Park, K. Y. Lee, M. K. Kim, B. A. Shin, S. Y. Choi, High cleavage efficiency of a 2A peptide derived from porcine teschovirus-1 in human cell lines, zebrafish and mice. *PLOS ONE* **6**, e18556 (2011). Medline doi:10.1371/journal.pone.0018556

30. R. Blum, P. Feick, M. Puype, J. Vandekerckhove, R. Klengel, W. Nastainczyk, I. Schulz, Tmp21 and p24A, two type I proteins enriched in pancreatic microsomal membranes, are members of a protein family involved in vesicular trafficking. *J. Biol. Chem.* **271**, 17183–17189 (1996). Medline doi:10.1074/jbc.271.29.17183

31. M. Bremser, W. Nickel, M. Schweikert, M. Ravazzola, M. Amherdt, C. A. Hughes, T. H. Söllner, J. E. Rothman, F. T. Wieland, Coupling of coat assembly and vesicle budding to packaging of putative cargo receptors. *Cell* **96**, 495–506 (1999). Medline doi:10.1016/S0092-8674(00)80654-6

32. K. Sohn, L. Orci, M. Ravazzola, M. Amherdt, M. Bremser, F. Lottspeich, K. Fiedler, J. B. Helms, F. T. Wieland, A major transmembrane protein of Golgi-derived COPI-coated vesicles involved in coatomer binding. *J. Cell Biol.* **135**, 1239–1248 (1996). Medline doi:10.1083/jcb.135.5.1239

33. M. A. Stamnes, M. W. Craighead, M. H. Hoe, N. Lampen, S. Geromanos, P. Tempst, J. E. Rothman, An integral membrane component of coatomer-coated transport vesicles defines a family of proteins involved in budding. *Proc. Natl. Acad. Sci. U.S.A.* **92**, 8011–8015 (1995). Medline doi:10.1073/pnas.92.17.8011

34. S. Chantalat, R. Courbeyrette, F. Senic-Matuglia, C. L. Jackson, B. Goud, A. Peyroche, A novel Golgi membrane protein is a partner of the ARF exchange factors Gea1p and Gea2p. *Mol. Biol. Cell* **14**, 2357–2371 (2003). Medline doi:10.1091/mbc.E02-10-0693

35. G. V. Pusapati, G. Luchetti, S. R. Pfeffer, Ric1-Rgp1 complex is a guanine nucleotide exchange factor for the late Golgi Rab6A GTPase and an effector of the medial Golgi Rab33B GTPase. *J. Biol. Chem.* **287**, 42129–42137 (2012). Medline doi:10.1074/jbc.M112.414565

36. M. Takatalo, E. Järvinen, S. Laitinen, I. Thesleff, R. Rönnholm, Expression of the novel Golgi protein GoPro49 is developmentally regulated during mesenchymal differentiation. *Dev. Dyn.* **237**, 2243–2255 (2008). Medline doi:10.1002/dvdy.21646

37. M. C. Bassik, M. Kampmann, R. J. Lebbink, S. Wang, M. Y. Hein, I. Poser, J. Weibezahn, M. A. Horlbeck, S. Chen, M. Mann, A. A. Hyman, E. M. Leproust, M. T. McManus, J. S. Weissman, A systematic mammalian genetic interaction map reveals pathways underlying ricin susceptibility. *Cell* **152**, 909–922 (2013). Medline doi:10.1016/j.cell.2013.01.030

38. C. Choi, M. Davey, C. Schluter, P. Pandher, Y. Fang, L. J. Foster, E. Conibear, Organization and assembly of the TRAPPII complex. *Traffic* **12**, 715–725 (2011). Medline doi:10.1111/j.1600-0854.2011.01181.x

39. P. L. Connerly, M. Esaki, E. A. Montegna, D. E. Strongin, S. Levi, J. Soderholm, B. S. Glick, Sec16 is a determinant of transitional ER organization. *Curr. Biol.* **15**, 1439–1447 (2005). Medline doi:10.1016/j.cub.2005.06.065

40. P. Watson, A. K. Townley, P. Koka, K. J. Palmer, D. J. Stephens, Sec16 defines endoplasmic reticulum exit sites and is required for secretory cargo export in mammalian cells. *Traffic* **7**, 1678–1687 (2006). Medline doi:10.1111/j.1600-0854.2006.00493.x

41. H. Liewen, I. Meinhold-Heerlein, V. Oliveira, R. Schwarzenbacher, G. Luo, A. Wadle, M. Jung, M. Pfreundschuh, F. Stenner-Liewen, Characterization of the human GARP (Golgi associated retrograde protein) complex. *Exp. Cell Res.* **306**, 24–34 (2005). Medline doi:10.1016/j.yexcr.2005.01.022

42. F. J. Pérez-Victoria, G. A. Mardones, J. S. Bonifacino, Requirement of the human GARP complex for mannose 6-phosphate-receptor-dependent sorting of cathepsin D to lysosomes. *Mol. Biol. Cell* **19**, 2350–2362 (2008). Medline doi:10.1091/mbc.E07-11-1189

43. H. M. Rohde, F. Y. Cheong, G. Konrad, K. Paiha, P. Mayinger, G. Boehmelt, The human phosphatidylinositol phosphatase SAC1 interacts with the coatomer I complex. *J. Biol. Chem.* **278**, 52689–52699 (2003). Medline doi:10.1074/jbc.M307983200

44. S. Siniossoglou, S. Y. Peak-Chew, H. R. Pelham, Ric1p and Rgp1p form a complex that catalyses nucleotide exchange on Ypt6p. *EMBO J.* **19**, 4885–4894 (2000). Medline doi:10.1093/emboj/19.18.4885